UNIVERSITY OF SOUTHAMPTON

FACULTY OF ENGINEERING AND PHYSICAL SCIENCES

Computational Engineering and Design Group

Numerical Investigation of Oscillating Flapping Foils for Energy Harvesting in Freestream and Ground Effect

by

Sarah A'fifah Abdullah Sani

Thesis for the degree of Doctor of Philosophy

December 2021

UNIVERSITY OF SOUTHAMPTON

ABSTRACT

FACULTY OF ENGINEERING AND PHYSICAL SCIENCES

Computational Engineering and Design Group

Thesis for the degree of Doctor of Philosophy

NUMERICAL INVESTIGATION OF FLAPPING FOILS FOR ENERGY HARVESTING IN FREESTREAM AND GROUND EFFECT

by Sarah A'fifah Abdullah Sani

In recent years, as an alternative to rotary wind turbines, flapping foils or oscillating airfoils are under increasingly active investigation to extract energy from wind/water. The aim of this research is to investigate numerically the role of flapping foils on the performance of energy harvesting in freestream and in ground effect. Their potentials for the generation of electric power are studied here using two- and three-dimensional, unsteady Navier-Stokes solver (Ansys Fluent) with a dynamic mesh and sliding interface, in both laminar and turbulent flows. The performance efficiency and mean power coefficient are investigated here for different geometry modifications, namely thickness distribution (NACA0012, NACA0015 and NACA0018) and trailing edge shape modification (sharp, blunt and round) at a low and a high Reynolds numbers ($Re = 1100$ and 5×10^5) and under different operational parameters, to explore the effect of geometry change on the energy harvesting performance efficiency. The purpose of the truncation process is to eliminate the sharp and steep curvature at the trailing edge portion which may in turn reduces the adverse pressure gradient caused in that area, and thus helps in delaying flow separation. Modifying the airfoil trailing edge and thickness are found to have influence on the lift coefficient, especially for a high Reynolds number, and that the blunt trailing edge has a better efficiency (7% improvement) than the sharp and rounded trailing edges. For all simulations which have been carried out for the 2D single oscillating airfoils, the highest efficiency performance is found to occur at reduced frequencies $f^* = 0.14 - 0.18$. This increase in efficiency is mainly due to the LEVs (leading edge vortices) and a better synchronization between C_Y and V_Y (i.e., good timing in the sign switch of C_Y and V_Y). This study is then extended to multiple oscillating bodies to investigate the interaction effect on the power extraction for the two objects in tandem, which are airfoil-airfoil, and cylinder-airfoil. From this study, it is observed that the multiple configurations of airfoil-airfoil interaction (for low inter airfoil distance) can generate up to 30% higher efficiency more than the optimal single oscillating airfoil, and the use of airfoil-airfoil interaction with blunt trailing edge airfoil is found

to have a better energy harvesting/efficiency for the two oscillating bodies, with a total efficiency of more than 5% in comparison to the sharp airfoil-airfoil. Finally, for the cylinder-airfoil interaction, the efficiency performance is found to decrease when compared to the two airfoils interaction.

Next, a parametric study on the ground effect has been conducted to optimise the power efficiency. The effects of Reynolds numbers at laminar and turbulent flows, the location of airfoil pitching axis, the distance between the airfoil pitching axis and the ground, the amplitude and frequency of oscillation on power extraction by the flapping wing were examined using URANS. From this study, it is found that in all the cases there is an increase in the peak lift coefficient, as height decreases. However, the improvement in power efficiency in ground effect is found to be depended mainly on the perfect synchronization of the heaving velocity and the instantaneous lift that happens at $0.12 < f^* < 0.2$. For lower and higher reduced frequencies, the increase in lift is not always reflected in a better power efficiency, as the motion of the airfoil and the forces are not well synchronized. Finally, a turbulent case with a higher Reynolds number was also evaluated in ground effect, and it found that an improvement of more than 8% in the energy efficiency was observed in comparison to its freestream case.

Finally, the 2D simulation has been extended to the 3D simulation at a low and a high aspect ratios of 3.5 and 7. In addition, the effect of trailing edge geometry variation was investigated. From these results, it is found that the 2D case over-predict the power efficiency as compared to the 3D case, which is about 22% and 10% efficiency drop for aspect ratios of 3.5 and 7, respectively for the laminar case, and this is due to the well-known limits of the 2D models which do not take into account the 3D effects like tip vortex. Increasing the aspect ratio of the wing leads to a higher contribution to efficiency from heaving, as expected. Turbulent flow also shows a similar efficiency drop in both aspect ratios. In addition, the effect of the aspect ratio on efficiency from pitching is found to be negligible for laminar flow but quite significant for turbulent flow. The 3D geometrical shape variation has also been investigated, where the results of NACA0015 sharp trailing edge has been compared to NACA0018 blunt trailing edge in both laminar and turbulent flow, and the results of the study are found to agree with the 2D results where NACA0018 blunt trailing edge gives slightly better efficiency. Thus, it may be concluded that, the aspect ratio, 3D effects and geometrical shape modification have influence on the power efficiency in both laminar and turbulent flows.

Table of Contents

List of Tables

List of Figures

DECLARATION OF AUTHORSHIP

I, **Sarah A'fifah Binti Abdullah Sani**

declares that this thesis and the work presented in it are my own and has been generated by me as the result of my own original research.

INVESTIGATION OF OSCILLATING NONLINEAR FLUID-STRUCTURE INTERACTION SYSTEMS FOR ENERGY HARVESTING

I confirm that:

1. This work was done wholly or mainly while in candidature for a research degree at this University;
2. Where any part of this thesis has previously been submitted for a degree or any other qualification at this University or any other institution, this has been clearly stated;
3. Where I have consulted the published work of others, this is always clearly attributed;
4. Where I have quoted from the work of others, the source is always given. With the exception of such quotations, this thesis is entirely my own work;
5. I have acknowledged all main sources of help;
6. Where the thesis is based on work done by myself jointly with others, I have made clear exactly what was done by others and what I have contributed myself;
7. Parts of this work have been published as:

Signed: .....

Date: 14th December 2021

Acknowledgements

IN THE NAME OF ALLAH , THE MOST GRACIOUS, THE MOST MERCIFUL.

First of all, Alhamdulillah I am grateful to Allah for providing me with the health and blessings to undertake this task.

I would like to express my sincere thanks and deepest gratitude to my supervisors Dr. Kamal Djidjeli for his continuous guidance and valuable advice that helped me throughout completing this thesis. Besides, I also very thankful to my co-supervisor, Prof. Dr. Jing Tang Xing for his support and belief in me.

Thanks to the International Islamic University Malaysia (IIUM) and Ministry of Higher Education of Malaysia (MOHE) for their financial support in my research.

I would also like to thank all people that have helped me over the duration of my study at University of Southampton, in particular to Tauseef Ahmed who are always be by side during my though time.

Last but not least, I would like to thank my family, especially my father, mother and sisters who continues pray the best for me.

Definitions and Abbreviations

Roman Symbols

b	Airfoil span
c	Airfoil chord
C_L	Lift coefficient
C_M	Moment coefficient
C_P	Output power coefficient
$C_{P\theta}$	Output power coefficient from pitching motion
C_Y	Instantaneous vertical force
$\bar{C}_P$	Mean output power coefficient
$\bar{C}_{P\ upstream}$	Mean output power coefficient for upstream body in tandem arrangement
$\bar{C}_{P\ downstream}$	Mean output power coefficient for downstream body in tandem arrangement
$\bar{C}_{P\ total}$	Total mean output power coefficient for upstream and downstream bodies in tandem arrangement
$\bar{C}_{Ph}$	Mean output power coefficient, time-averaged over a cycle of flapping motion from heaving motion
$\bar{C}_{P\theta}$	Mean output power coefficient, time-averaged over a cycle of flapping motion from pitching motion
$\hat{C}_M$	Maximum values of moment's coefficient
$\hat{C}_X$	Maximum values of drag's coefficient
$\bar{C}_Y$	Mean values of lift's coefficient
d	Total vertical distance swept by the leading or trailing edge of the airfoil
w	Angular velocity
f	Flapping frequency, $f = \frac{2\pi}{w}$
f^*	Non-dimensional flapping frequency, $f^* = \frac{fc}{U_\infty}$
g	Acceleration due to gravity
$h(t)$	Heaving motion of the airfoil
H_0	Non-dimensional heave amplitude

I	Unit tensor
L_x	Distance between upstream and downstream bodies in tandem arrangement
M	Moment, measured about the airfoil pivot point
p	Pressure of the fluid
$\bar{P}$	Averaged output power
$P(t)$	Instantaneous output power
$P_h(t)$	Output power from heaving motion
$P_\theta(t)$	Output power from pitching motion
Re	Reynolds number
St	Strouhal number
t	Time
T	Period of flapping motion
u_i	Velocity of a flow particle *i*
$\bar{u}_i$	Time-averaged component of the velocity of flow particle *i*
u'_i	Fluctuating component of the velocity of flow particle *i*
$\bar{u}_j$	Time-averaged component of the velocity of flow particle *j*
u'_j	Fluctuating component of the velocity of flow particle *j*
U_x	Inlet *x* velocity
U_y	Inlet *y* velocity
U_∞	Free-stream velocity
v	Velocity vector
x_p	Distance from the airfoil leading edge to the pivot point.
Δy	The normal distance of first layer from the solid surface
y^+	Non-dimensional wall distance
Y	Vertical force, measure normal to the free-stream flow (positive downwards)
$V_{\text{eff}}(t)$	Effective upstream velocity
V_{max}	Maximum effective velocity

$V_Y(t)$	Vertical velocity of the airfoil about the pivot point

Greek Symbols

$\alpha(t)$	Angel of attack
$\alpha_{\max}$	Maximum angle of attack achieved throughout the oscillating cycle
η	Power extraction efficiency
$\eta_{upstream}$	Power extraction efficiency of upstream body in tandem arrangement
$\eta_{downstream}$	Power extraction efficiency of downstream body in tandem arrangement
η_{total}	Total power extraction efficiency of upstream and downstream body in tandem arrangement
χ	Feathering parameter
$\theta(t)$	Pitching motion of the airfoil about the pivot point
$\dot{\theta}(t)$	Pitching angular velocity of the airfoil about the pivot point
θ_0	Pitching amplitude
ω	Angular frequency of flapping motion, $\omega = 2\pi f$
ρ	Density of the fluid
τ	Stress tensor
Γ	Circulation
κ	Turbulent kinetic energy
μ	Viscosity of the fluid
ϕ	Phase angle between the pitch and heave motions
ψ_{1-2}	Phase difference between the motions of upstream and downstream bodies in tandem arrangement
δ	Boundary layer thickness

Abbreviations

2D, 3D	Two or Three-Dimensional
AR	Aspect Ratio
AUV	Autonomous Underwater Vehicle
CFD	Computational Fluid Dynamics
FV	Finite Volume

MAV	Micro Aerial Vehicle
RANS	Reynolds-Averaged Navier-Stokes
SA	Spalart-Allmaras
SIMPLE	Semi-Implicit Method for Pressure-Linked Equations
SST	Shear Stress Transport
ts	Time steps
UDF	User Defined Function

Chapter 1: Introduction

1.1 Motivation of Research

Burning fossil fuel to produce electricity continue to be the major energy resource to the world (World Energy Council, 2016). The rapid progress in industrial and social development in the last hundred years have led to a sharp increase in the amount of fuel being burnt such that more carbon dioxide is emitted than the amount that can be absorbed by plant. This increased amount of carbon dioxide in the atmosphere has led to the phenomenon of climate change, which is threatening the human being and environment.

The growing concern for the increasing levels of carbon dioxide being released in the atmosphere due to burning of fossil fuel has intensified the urge to use renewable sources of energy. This proposition has been strengthened by concerns for the depletion of the finite supply of fossil fuel. For instance, oil deposits are estimated to last until 2052 while the supply for natural gas will approximately last until 2060 (IPCC, 2014). Hence, conversion from fossil fuel to renewable source of energy can contribute to the improvement of the environmental sustainability and human wellbeing.

By 2015, only 9.6% of the global energy consumption was obtained from renewable sources, with almost three per cent of which being attributed to wind, solar, geothermal and biofuel source. Hydropower also contributes a significant proportion of the global energy consumption with 6.8% (World Energy Council, 2016).

Existing technologies, which take benefit of these power sources, rely mainly on rotary machines (Ashraf *et al.*, 2011). There are many turbine farms have been constructed all over the world. Currently, 85,000 big wind turbines are spinning on earth (50,000 only in Europe) (Carcangiu, 2008). However, there are some of the drawbacks of using rotary machine. Other than the excessive space that they take, which could impact the local wildlife, the rotary turbine also require an average velocity of 2.5-3.6 m/s to be financial viable, while most of the currents flow at lower speeds (Westwood, 2004).

In recent past years, there have been tremendous research efforts to develop rather nonconventional renewable resources from design and scale perspective. One such

technology includes the green energy production through the innovative concept of flapping foils. As an alternative to rotary turbines, flapping foil systems or oscillating airfoils are under increasingly active investigation. Moreover, the oscillating airfoil turbines promise some key potential advantages than the rotary turbines including lower foil velocity (and hence lower noise and wildlife impact), more effective small-scale and shallow water operation (Shyy and Liu, 2007). In addition, the geometry structure of the oscillating airfoil is much simpler and easier to manufacture as compared to the twisted rotor blade of the rotary turbine (Xiao and Zhu, 2014). Other than that, the oscillating airfoil also provides a better filling factor when compared to the rotary turbine as shown in Figure 1.1.

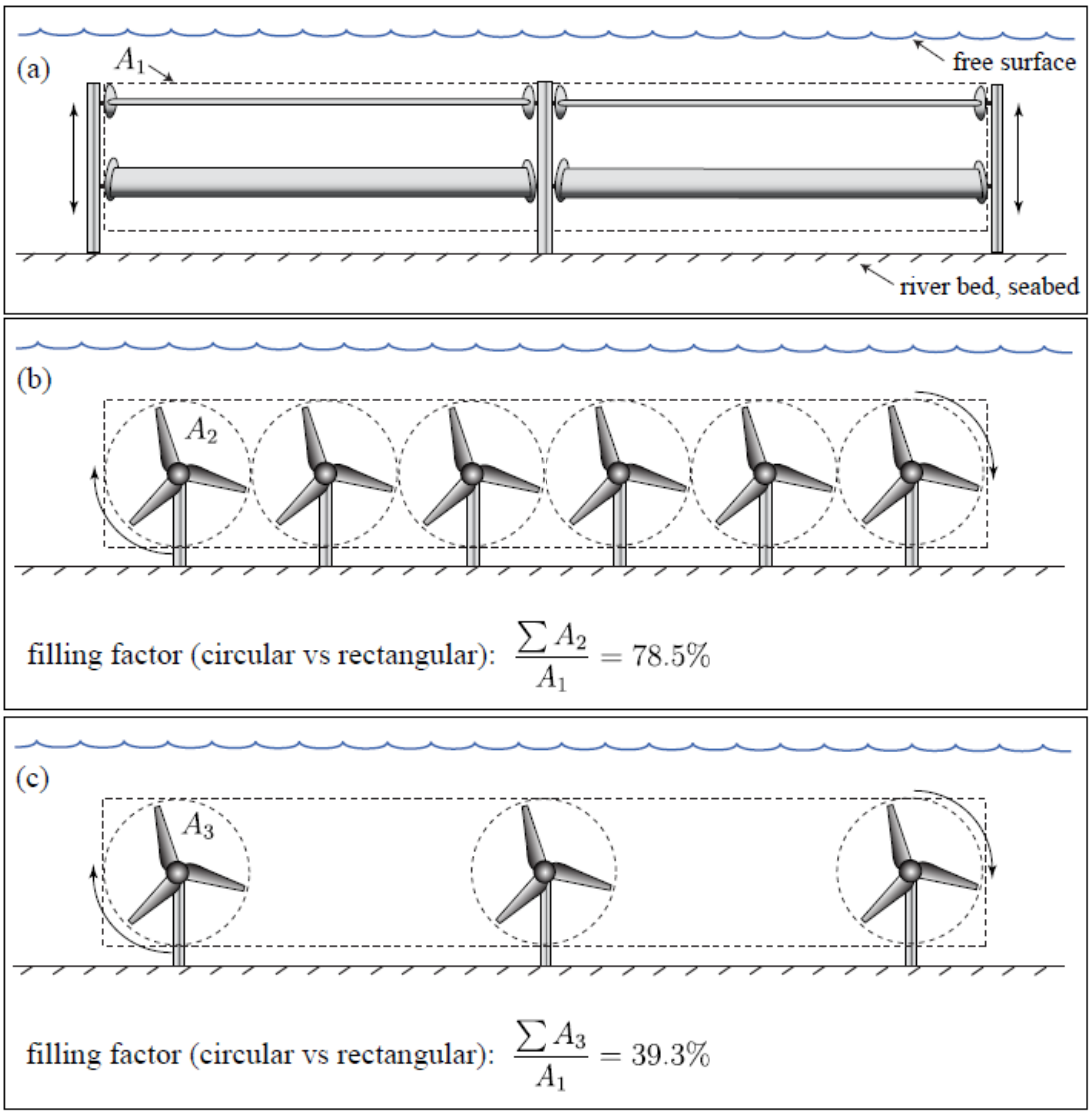

Figure 1. 1: Rectangular extraction plane versus the rotary extraction plane (Kinsey, 2011)

From this figure, it is shown that two rectangular extraction plane can sweep more area as compared to an array of rotary turbine placing too close to each other (Figure 1.1 b), which can only cover up to 78.5% area of rectangular. Unfortunately, this packed turbine is

unrealistic since the EMEC (European Marine Energy Centre) has fixed the guidelines that specify the lateral spacing between devices should be two and a half times the rotor diameter (Legrand and Ltd., 2009) which is equivalent to Figure 1.1 c. Hence, even less area can be covered by the rotary turbine.

This oscillating airfoil device can be installed for wind and hydrokinetic energy extraction. However the use as hydrokinetic turbine is more appealing since water has greater energy density and much better energy predictability, and are particularly suited in shallow water or in ocean floor.

At the beginning, the flapping foil mechanism was used as a thrust generator for micro air vehicles (MAV) or autonomous underwater vehicles (AUV). With the growing importance of renewable energy, the interest in this novel concept has been used in the past few years for energy harvesting. One notable phenomenon is the involvement of industry in developing full-scale prototypes including, e.g. the Oscillating Marine Current Energy Converter initially developed by The Engineering Business Ltd. (The Engineering Business Ltd Technical Report, 2005) and further improved by Pulse Tidal Ltd. (http://www.pulsetidal.com), the BioSTREAM device which is developed by BioPower Systems Pty Ltd., Sydney, Australia (Kloos et al. , 2009), the European Marine Energy Centre LDT (EMEC) [http://www.emec.org.uk/marine-energy/tidal-devices/], and the DualWingGenerator which is an active wing rotation modelled on the bionic SmartBird and developed by Festo Company (https://www.festo.com/group/en/cms/10222.htm).

The idea of using flapping foil to extract energy from the surrounding fluid was inspired from the observation of dolphins and sharks who are able to swim at high speeds by extracting energy from the surrounding water (Xiao *et al.*, 2012) and from the observation of insects such as the small fly which is able to fly for long distances (Lehmann, 2009). The fluid mechanics of many swimming and flying animals involves the generation and shedding of vortices into the wake (Dickinson et al., 2000). Observation of the behaviour of such aquatic animals, insects and birds have led to a better understanding of the surrounding flow characteristics that result in their forward propulsion and in the extraction of energy to remain in flight for long periods of time. In flapping foil aerodynamics the vortices are shed and form either a periodic or chaotic wake pattern, depending on the kinematics, notably advance ratio and dimensionless flapping amplitude (Thaweewat et al., 2009, Lentink et al., 2008). McKinney and DeLaurier (McKinney, W., DeLaurier, 1981) were the first to propose this concept in 1981 and was further investigated by Jones et al. (D. and F, 1997). Since then,

various experimental and analytical studies have been carried out based on this flapping motion to analyse the aerodynamic forces produced and to study the wing-wake interaction that takes place during the flapping process (Dumas, G., Kinsey, 2006; Kinsey and Dumas, 2008a; Kinsey *et al.*, 2011a; Campobasso and Drofelnik, 2012; Liu, Xiao and Cheng, 2013; Wu, Qiu, Shu, Zhao, Wu, *et al.*, 2015). However, the study of flapping foil for power generation is still largely remained unexplored. Hence, in this study, we will focus on the oscillating foils under power extraction regime with the aim of improving efficiency. Understanding the underlying physics of flapping foils in fluid is essential to improve the efficiency of existing devices and to pave the way for the development of future novel energy-efficient flapping foil devices which can extract energy from wind, streams, rivers, and tidal flows.

1.2 Mechanism of Oscillatory Energy Harvesting System

The fundamental motion along with the governing equations to describe the motion of the oscillating foil has been discussed below. Moreover, the key influential parameter of oscillating foil dynamics is also summarized here.

1.2.1 Motion Description

Flow over oscillating foil has been analysed by using 2D and 3D symmetrical rigid section. The flapping motion of a foil, which is based on the translational and rotational motion, can be classified into three main modes of motion, namely:

i. Pure heaving motion, $h(t)$ (Figure 1.2 (a)).
ii. Pure pitching motion, $\theta(t)$ around the pivot point x_p from the leading edge of an airfoil (Figure 1.2 (b)).
iii. Simultaneously heaving-pitching motion around the pivot point x_p (Figure 1.2 (c)).

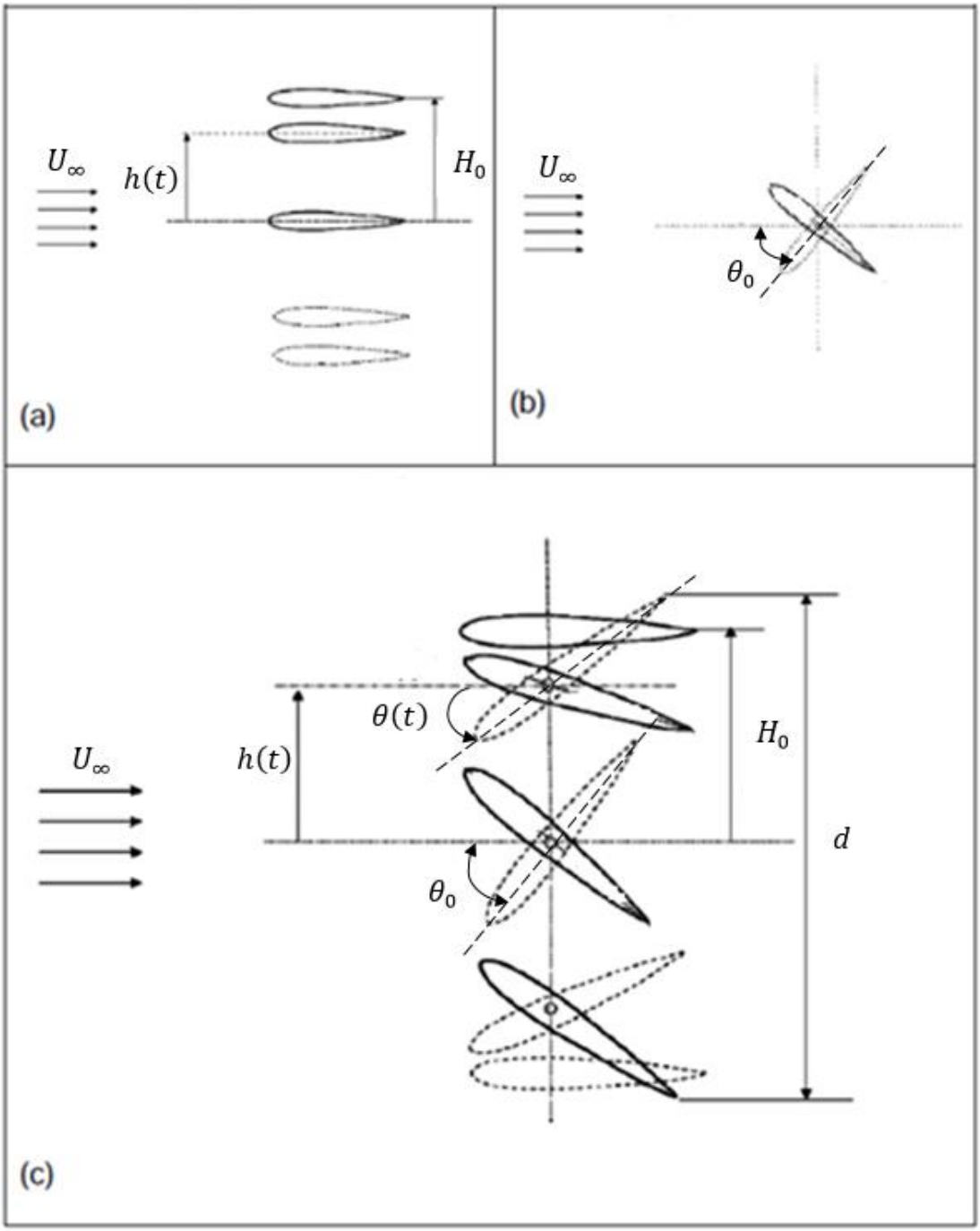

Figure 1. 2: Airfoil undergoing (a) pure heaving, (b) pure pitching, and (c) combine heaving and pitching motion (Ashraf, 2010)

In this study, the combined pitch and heave case of foil motion are considered in detail. For flapping foil operating in free stream velocity U_∞, the pitch and heave motion is mathematically expressed as sinusoidal functions:

$$\theta(t) = \theta_0 \sin(\omega t) \rightarrow \dot{\theta}(t) = \theta_0 \omega \cos(\omega t) \tag{1.1}$$

$$h(t) = H_0 \sin(\omega t + \phi) \rightarrow V_Y(t) = \dot{h}(t) = H_0 \omega \cos(\omega t + \phi) \quad (1.2)$$

where θ_0 and H_0 are the pitching and heaving amplitudes, respectively, $\dot{\theta}$ is the pitching velocity, V_Y the heaving velocity, ω is the angular frequency $(\omega = 2\pi f)$, f is the oscillating frequency and ϕ is the phase angle between the pitch and heave motion.

1.2.2 Oscillating Foil - Operating Regimes

The general operating cycle of an oscillating airfoil can be divided into the following two different regimes, namely propulsion and power extraction. In the last decade, there has been increasing and intense interest in the aerodynamics of flapping foils for propulsion (D. and F, 1997; Dippold, 2003; Grue, Mo and Palm, 2006; Platzer, M.F., Young, J., Lai, 2008; Ashraf, Young and Lai, 2011; Ashraf, Young and S. Lai, 2012; Peng and Chen, 2012) compared to the use for power generator.

In Figure 1.3, the resultant force ***R*** is first constructed from typical lift and drag forces (right-hand side), and then decomposed into X and Y components (left-hand side). In the power extraction regimes, the resultant aerodynamics force ***R*** has a vertical component Y, which is in the same direction as the vertical displacement of the airfoil; therefore, the flow performs positive work and power is extracted from the flow because no negative work is involved with respect to the horizontal component X (Figure 1.4) (Kinsey & Dumas, 2008b). This is exactly the case of interest in our work here since our airfoil is actually not moving horizontally, but only pitching and heaving into a uniform flow from left to right of speed U_∞. On the other hand, in the propulsion regime, a foil works on the fluid through the vertical component of the resultant force opposing its vertical displacement which results in a net propulsive force (X toward the left) in the horizontal direction (Figure 1.4).

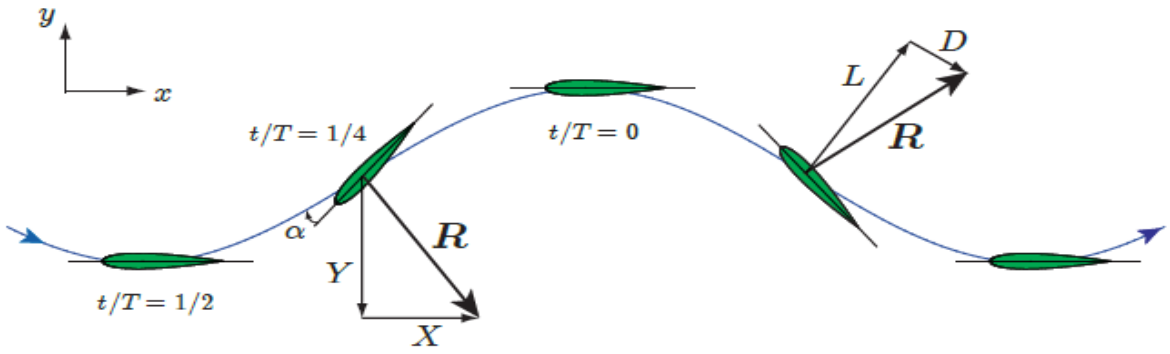

Figure 1. 3: Power extraction regime of an oscillating airfoil (Kinsey and Dumas, 2008b)

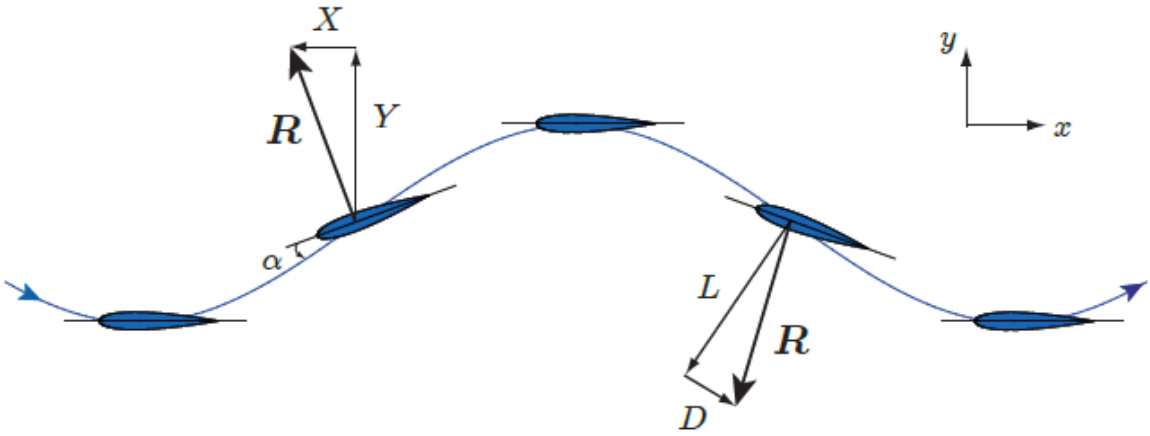

Figure 1. 4: Propulsion regime for an oscillating airfoil (Kinsey and Dumas, 2008b)

Further, the foil experiences an effective angle of attack α and an effective upstream velocity V_{eff}, expressed as follows (Kinsey and Dumas, 2008a):

$$\alpha(t) = \tan^{-1}\left(\frac{-V_Y(t)}{U_\infty}\right) - \theta(t) \tag{1.3}$$

$$V_{\text{eff}}(t) = \sqrt{U_\infty^2 + V_Y(t)^2} \tag{1.4}$$

Their maximum values in the cycle are expected to have a major impact on the peak forces generated and on the possibility of dynamic-stall occurrence. The maximum effective angle of attack $\alpha_{\max}$ reached in one cycle is approximated by the modulus of its quarter-period value $(\alpha_{T/4})$ (Kinsey and Dumas, 2008a):

$$\alpha_{\max} \approx |\alpha_{T/4}| = \left|\tan^{-1}\left(\frac{\omega H_0}{U_\infty}\right) - \theta_0\right| \tag{1.5}$$

The maximum effective velocity also occurs at the quarter-period:

$$V_{\max} = V_{\text{eff}}(T/4) = \sqrt{U_\infty^2 + (\omega H_0)^2} \tag{1.6}$$

The effect of foil on the flow regimes is identified by feathering parameter χ, which is defined as (Anderson *et al.*, 1998):

$$\chi = \frac{\theta_0}{\tan^{-1}\left(\frac{\omega H_0}{U_\infty}\right)} \tag{1.7}$$

Based on a simple quasi-steady argument, one can show that, $\chi < 1, \alpha_{T/4} > 0$ is associated with propulsion regime, whereas $\chi > 1, \alpha_{T/4} < 0$ correspond to power extraction regime and $\chi = 1, \alpha_{T/4} = 0$ related to feathering limit regime (Kinsey and Dumas, 2008a). The feathering limit regime refers to a special case of oscillating airfoil in which neither thrust is produced nor power is extracted. The motion imposed and upstream flow condition on the airfoil for feathering limit is shown in Figure 1.5.

Figure 1. 5: Feathering regime of an oscillating airfoil (Kinsey and Dumas, 2008b)

Other than looking at the sign of the forces that the flow generates on the moving airfoil, it is often one can identify which regime an oscillating airfoil belongs to by just looking at it wake vortices.

In the case of power extraction, the wake behind the oscillating airfoil will always experience a drag-producing wake. This means, the drag coefficient C_X will remain positive throughout the overall cycle. This type of wake vortices was presented by the (Von Karman, T., Burgers, 1934) where the vortices are arranged in a manner such that the upper row of vortices consists of clockwise vortices and the lower row of anti-clockwise vortices (Figure 1.6a). Hence, the velocity induced by the wake vortices is in the negative direction which results in a deficit of the net momentum of the flow downstream the body.

On the other hand, for propulsion case, the wake vortices transform into a reverse Von Karman vortex street, i.e. the upper row of vortices becomes anti-clockwise and the lower row clockwise as shown in Figure 1.6b. Now, the velocity induced by the wake vortices is in the same direction as the flow, thereby causing an excess of momentum downstream of the body. Due to this added momentum, the velocity profile downstream of the body appears jet-like and the body experiences thrust.

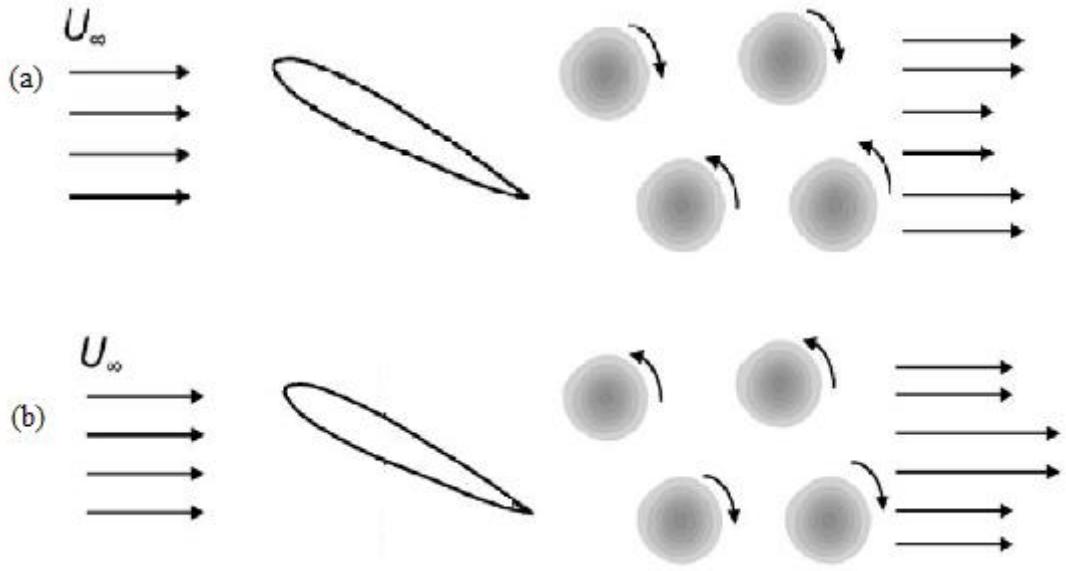

Figure 1. 6: Instantaneous vorticity field with direction of wake-vortices induced velocities for (a) power-extraction case, and (b) propulsion case (Ashraf, 2010)

1.2.3 Extracted Power and Efficiency

To quantify the value of extracted power, the time-averaged method is used, where it defines as integrating the instantaneous power extracted in one cycle. The instantaneous power extracted from the flow comes from the sum of a heaving contribution $P_h(t) = Y(t)V_Y(t)$ and a pitching contribution $P_\theta(t) = M(t)\dot{\theta}(t)$, where $Y(t)$ is the vertical component of aerodynamic force; $M(t)$ is the torque about the pitching axis x_p. The instance power extraction and the time-averaged extracted power can be expressed as (Kinsey and Dumas, 2008a):

$$P(t) = P_h(t) + P_\theta(t) \tag{1.8}$$

$$\bar{P} = \frac{1}{T}\int_{t}^{t+T} P(t)\, dt \tag{1.9}$$

As the research work includes different layouts of flapping foils for the modified foil geometries, the use of power coefficient C_P provides better comparison. The power coefficient C_P is defineds as the ratio of the extracted power P to the total available power in free stream. Hence, the non-dimensional instantaneous power coefficient is defined as:

$$\begin{aligned} C_P &= \frac{P}{\frac{1}{2}\rho U_\infty^3 bc} = \frac{2}{\rho U_\infty^3 bc}\left[Y(t)V_Y(t) + M(t)\dot{\theta}(t)\right] \\ &= \frac{1}{U_\infty}\left[C_L(t)V_Y(t) + C_M(t)\dot{\theta}(t)c\right] \end{aligned} \tag{1.10}$$

Where b is an airfoil span, c is the chord length, ρ is density of fluid, $C_L(t)$ is the instantaneous lift coefficient and $C_M(t)$ is the instantaneous moment coefficient. These coefficients can be expressed as:

$$C_L(t) = \frac{Y(t)}{\frac{1}{2}\rho U_\infty^2 bc} \tag{1.11}$$

$$C_M(t) = \frac{M(t)}{\frac{1}{2}\rho U_\infty^2 bc^2} \tag{1.12}$$

Thus, the time-averaged extracted power in one cycle can be calculated and its non-dimensional form can be expressed as follow:

$$\bar{C_P} = \frac{1}{T}\int_{t}^{t+T} C_P(t)\, dt = \frac{\bar{P}}{\frac{1}{2}\rho U_\infty^3 bc} \tag{1.13}$$

$$\bar{C_P} = \bar{C}_{Ph} + \bar{C}_{P\theta} = \frac{1}{U_\infty T}\left[\int_{t}^{t+T} C_L(t)\, V_Y(t) + C_M(t)\dot{\theta}(t)c\right] dt \tag{1.14}$$

or

$$\bar{C_P} = \bar{C}_{Ph} + \bar{C}_{P\theta} = \frac{1}{U_\infty}\int_{0}^{1}\left\{C_L(t)V_Y(t) + C_M(t)\dot{\theta}(t)c\right\} d(t/T) \tag{1.15}$$

Similarly, the power extraction efficiency η can be induced from the time-averaged extracted power. It is represented as the ratio of the total extracted power to the total incoming flow energy flux within the swept area.

$$\eta = \frac{\bar{P}}{\frac{1}{2}\rho U_\infty^3 bd} = \frac{\bar{P}_h + \bar{P}_\theta}{\frac{1}{2}\rho U_\infty^3 bd} = \frac{\bar{C}_P \frac{1}{2}\rho U_\infty^3 bc}{\frac{1}{2}\rho U_\infty^3 bd} = \bar{C}_P \frac{c}{d} \tag{1.16}$$

Where ρ is the density of fluid; b is the foil span; c is the chord length; and d is the overall vertical extent of the foil motion. Power extraction efficiency is defined as the portion of flow energy flux within the swept area extracted by the system.

1.2.4 Dimensional analysis

The chord-based Reynolds number is applied to both propulsion and energy-extraction regimes. This fundamental relation can have a large impact on the boundary layer dynamics of these systems.

The oscillation frequency, $f = {}^{2\pi}/_{W}$, is an important governing parameter in the operation of all oscillating-foils, but is non-dimensionalised differently for propulsion and energy-extraction regimes. For propulsive cases, the Strouhal number, St, is defined as

$$St = {}^{fL}/_{U_\infty}$$

where f is the frequency of vortex shedding, L is the characteristic length and U_∞ is the flow velocity. The Strouhal number provides suitable scaling for propulsive cases, where it has been observed that the oscillation frequency for fins and tails in nature nearly universally collapse into a range of Strouhal numbers between $0.2 < St < 0.4$ (Rohr et al., 2004 & Saadat et al., 2017). At these frequencies the oscillating-foil applies periodic disturbances to the fluid corresponding to dominant frequency of the most unstable mode of the wake, leading to an amplification of unsteady forces (Richards, 2013).

Although the Strouhal number could also be applied to energy-extraction applications, better scaling has been found with the reduced frequency, f^*, defined as

$$f^* = {}^{fc}/_{U_\infty}$$

Here, the chord length of the foil is used as the characteristic length scale. Research by Simpson, (2009) found that similitude in vortex modes and efficiency for energy-extraction was possible with the use of reduced frequency, but this scaling failed when the Strouhal

number was used. It has become standard in the context of energy-extraction applications to therefore use the reduced frequency.

1.3 Thesis Outline

This section provides the snapshot of the research work outlined as following chapters.

Chapter 1 briefly introduces the motivation behind the research study, and describe the mathematical model of oscillatory motion.

Chapter 2 mainly highlights the state of existing literature in the field of energy harvesting using flapping foils including the gap in the literature and outline the research objectives.

Chapter 3 presents an overview of the numerical approach used in this study. It introduces the numerical method; the unsteady Reynolds averaged Navier-stokes equations, the solver employed in this study (ANSYS Fluent), as well as the mesh generation by the Pointwise software.

Chapter 4 examines the numerical study of 2D single and multiple bodies operating in power extraction regime. For the single foil, this study explores the effect of the geometrical shape variations (thickness distribution and trailing edge shape modifications) and its correlation with the foil kinematic parameters and the flow fields around the foil at low and high Reynolds numbers on the performance efficiency. For the multiple bodies' configuration, the efficiency performance of the interaction between two bodies is analysed, including airfoil-airfoil interaction, and airfoil-cylinder interaction. In addition, the effect of trailing edge geometry variation was investigated.

Chapter 5 deals with ground effects on the performance characteristics of oscillatory foils. The focus of this chapter is to explore different mechanisms that are beneficial to maximise the power efficiency.

Chapter 6 extends the work to 3D flapping foils, where the 3D effect, low and high aspect ratios and the geometrical shape variations are investigated for energy harvesting performance efficiency. For this study, aspect ratios 3.5c and 7c have been examined for NACA 0015 and NACA 0018 airfoils.

Finally, the major conclusion and findings of this study are summarised and recommendation for future work is outlined in Chapter

Chapter 2: Literature Review

In this chapter, a review on the current improvement of energy harvesting and flow interaction with the oscillating component is described. Also, the literature of various experimental, analytical and computational approaches employed to study flapping foil aerodynamics are given and the gaps in the previous research are identified as a justification of this study.

2.1 Basic Design of Oscillating Foil for Energy Harvesting

Energy harvesting devices based on the oscillating foils have been classified into three categories (Figure 2.1) namely (i) prescribed motion, (ii) semi-passive motion and (iii) fully passive motion.

i. *Prescribed motion*

In the absence of the actuation mechanism these devices are mainly theoretical. However, these idealised models are simple and easier to formulate mathematically, and thus are preferred in existing theoretical and numerical studies. The results obtained can provide some useful theoretical insights and guidance for real devices design at preliminary stage. Because of the specified pitching and heaving motion, the power generation for this type of device is equal to the available aero-/hydro-dynamic power input into the system. Most of the analysis of the oscillating motion of energy harvesting devices has been conducted in this mode (Kinsey and Dumas, 2008a; Ashraf *et al.*, 2009, 2011; Zhu, 2011; Campobasso and Drofelnik, 2012; Usoh *et al.*, 2012; Xiao *et al.*, 2012; Le, Ko and Byun, 2013, Xiao and Zhu, 2014), by prescribing a frequency, amplitude of pitch and heave mode. This mode of motion has also been used in the current study. This approach has been broadly used as the mathematical model to represent the extraction efficiency is simplified greatly. Moreover, the results obtained can provide some useful theoretical insight and guidance for real devices design at preliminary stage.

ii. *Semi-passive motion*

Semi-activated systems are characterized by prescribing the pitching motion and allowing the time-dependent forces and moments acting on the body to induce the plunging motion of the oscillating body. As a result, the foil undergoes heaving

oscillations which may be used for energy extraction. The existing flapping type energy harvesters in industry are often based on this design. Hence, energy input is needed to activate the pitching motion, whereas energy harvesting is achieved through the resulting heaving motion generated by fluid dynamic lifting forces. Such systems have been examined in literature (Isogai et al., 2003; Shimizu, Isogai and Obayashi, 2008; Zhu and Peng, 2009; Abiru, H., Yoshitake, 2011; Huxham, Cochard and Patterson, 2012, Wu et al., 2014, Deng et al., 2015, Javed et al., 2018) as these provide a more realistic overview of the energy extraction efficiency of oscillating bodies. Zhu and Peng (2009) examined the vorticity control mechanism around the foil. They proposed that energy harvesting capacity could be increased if leading edge vortex is partially recovered after being detached from the airfoil. (Abiru, H., Yoshitake, 2011) who studied the semi-activated energy extraction system by using a spring-dashpot model (Figure 2.1(b)) observed that in such systems a positive net energy extraction efficiency is obtained only if the energy during the heaving motion is greater than the energy required to active the pitching motion. Wu et al. (2014) carried out a detailed investigation of wall effects on energy extraction performance. Deng et al. (2015) studied the inertial effects on semi-passive foil energy harvesters, and Javed et al. (2018) investigated the effect of low Reynolds numbers on energy extraction performance of semi-passive flapping foil.

iii. *Fully passive motion*

Fully passive systems depend on the instabilities present in the flow to induce motion in the energy extraction devices or in other words the pitch and heave motions are generated directly by fluid forces. Thus, these systems do not require an actuation system and therefore all the energy extracted from the system can be used for the generation of electricity. Previous studies which have used this system are (Jones, Davids and Platzer, 1999; Jones, K. D., Linsey, K., Platzer, 2003; Platzer, M.F., Young, J., Lai, 2008; Peng and Zhu, 2009; Young, J., Ashraf, M. A., Lai, J. C. S., Platzer, 2010; Kinsey *et al.*, 2011a; Zhu, 2012; Young *et al.*, 2013, Ghasemi et al., 2016). Young et. al. (Young, J., Ashraf, M. A., Lai, J. C. S., Platzer, 2010; Young *et al.*, 2013) have showed that, the promising efficiencies reported for prescribed motion and semi-passive motion studies by (Kinsey and Dumas, 2008a; Ashraf, M. A., Young, J., Lai, 2009) could be replicated with the fully flow driven motion. Young et al. (2013) proposed a flywheel and linkage mechanism to

constraint the pitching motion of foil with heave motion. They observed that controlling the timing and location of leading edge vortex and its interaction with trailing edge can result in significant improvement in the efficiency of the system. Similar model of a tethered undersea kite was studied by Ghasemi et al. (2016) for power generation. In other fully passive systems, pitch and heave motions of the foil are independent of each other and oscillation amplitudes are controlled using linear and rotational springs and dampers (e.g. Peng and Zhu (2009), Zhu (2012)).

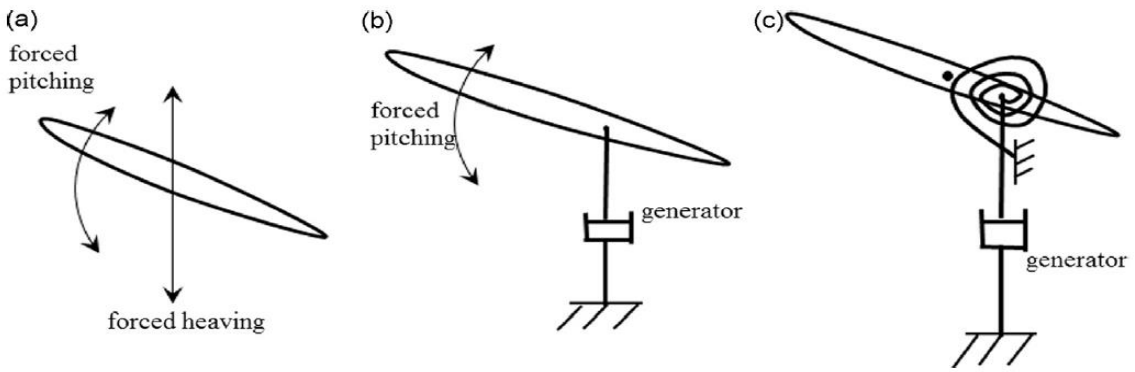

Figure 2. 1: Schematics (a) a system with fully prescribed motion, (b) a system with semi-passive motion, (c) a system with fully passive motion (Xiao and Zhu, 2014)

2.2 Influence of Parameters on Energy Harvesting using Oscillating foils

From the description in section 1.2, it is clear that the oscillating airfoil system operate under two motions which are known as heaving and pitching motion. Since 1981, Mckinney and Delaurie has applied these two motions in the energy harvester oscillating system and the development of these two motions have been studied extensively previously in the oscillating airfoil for propellers (Anderson et al. 1998, Read et al. 2003).

Hence, to assess the feasibility of using oscillating foils to harvest energy from renewable sources, studies have been carried out to assess the optimum efficiency that is produced when varying parameters such as the oscillating frequency, the heaving and pitching amplitudes, the location of the pitching axis, the shape of the foil, the magnitude of the Reynolds number, the aspect ratio (AR) of the foil and the use of multiple configurations. The efficiency obtained from these studies is often compared to the Betz efficiency (59%)

which is the maximum theoretical efficiency of wind turbines as calculated from the actuator disc theory.

Oscillating Frequency

The effect of oscillating frequency in the power extraction region is the same as in the propulsion region in which, when other parameters have been fixed, the efficiency of the system will increase proportionally with the frequency *f*. After it reach the peak value, the efficiency will decrease if the frequency is further increase (Campobasso *et al.*, 2013). The same phenomena can be observed in the present study. Moreover, Dumas and Kinsey (Dumas, G., Kinsey, 2006; Kinsey and Dumas, 2008a) have shown that the oscillating frequency determines whether the heaving velocity of the foil is in synchronization with the vertical force acting on it. When the frequency is set such that both parameters are positive or both are negative, energy is extracted throughout the whole cycle. In the case when the two parameters are synchronised for only a small portion of the cycle, the energy extracted during the synchronized region is consumed when they are out of sync. Such a synchronization between the pitching amplitude and the pitching moment is also valid. In addition, by varying the oscillating frequency, Zhu and Peng (Zhu and Peng, 2009) have shown that, at the optimum frequency, interaction between the leading edge vortices and the surface of the airfoil takes place close to the trailing edge. The low pressure generated as a result of this interaction will produce a pitching moment. Maximum energy efficiency is achieved when the direction of this pitching moment corresponds to the motion of the airfoil. A performance comparison between various non-sinusoidal motions was performed by Lu et al. (2014, 2015) and Xie et al. (2014, 2016), and their results showed that a suitable combination of non-sinusoidal heaving motions and non-sinusoidal pitching motions provides superior energy extraction performance, and a relatively large oscillating frequency and pitching amplitude should be used for optimal energy extraction performance.

Heaving Amplitude

The heaving amplitude influences the area through which the foil oscillates thereby affecting the power available. This implies that increasing the heaving amplitude will result in an increase in the power coefficient (Kinsey and Dumas, 2008a, Xiao et al., 2012). However, this trend is not always true for efficiency especially when the heaving amplitude already reach one chord length (c). This is because, by increasing the heave amplitude, the swept area (d) will keep increasing while from Equation (1.16), the relationship between

efficiency and total swept area is inversely proportional, hence this contributes to the efficiency decrease.

Pitching Amplitude

The energy extracted from the flow by the heaving motion is generally higher that that extracted through the pitching motion (Dumas, G., Kinsey, 2006; Kinsey and Dumas, 2008a; Xie, Lu and Zhang, 2014). However, Zhu, Haase et al. (Zhu, Haase and Wu, 2009a) have shown that increasing the pitching amplitude does increase the efficiency of the system. This was confirmed by Zhu and Peng (Zhu and Peng, 2009) who used computational simulations to exhibit how the pitching amplitude influences the location where the leading edge vortices interact with the airfoil. At low pitching amplitudes the flow remains attached to its surface throughout the entire cycle while at higher amplitudes, flow separation takes place causing shedding of leading edge vortices. For maximum efficiency, the pitching amplitude is such that vortices interact with the airfoil surface as close to the trailing edge as possible. Furthermore, the direction of the pitching moment induced on the airfoil should match the instantaneous pitching motion. This is comparable to the effects that varying the oscillating frequency has on the shedding of leading edge vortices as described by Xie, Lu et al. (Xie, Lu and Zhang, 2014).

By using numerical modelling, Xie, Lu et al. (Xie, Lu and Zhang, 2014) have shown that for an airfoil having a particular Strouhal number, there is an optimum amplitude beyond which the efficiency of the system decreases. A negative correlation is also found between the Strouhal number, there is an optimum pitching amplitude beyond which the efficiency of the system decreases. A negative correlation is also found between the Strouhal number and the pitching amplitude so that as the Strouhal number increases, the maximum pitching amplitude decreases $\left(\theta_{0max} = 25°\text{for } St = \frac{0.8\pi c}{H_0}, \theta_{0max} = 15°\text{for } St = \frac{1.48\pi c}{H_0}\right.$ and $\left.\theta_{0max} = 10° \text{ for } St = \frac{2\pi c}{H_0}\right)$. The best energy extraction performance presented by Xie, Lu et al. (Xie, Lu and Zhang, 2014) was achieved for a pitching amplitude in the range of $5 - 10°$ and a Strouhal number in the range of $\left(2.4 - 4 \times \frac{\pi c}{H_0}\right)$ at which the mean power coefficient was found to be equal to 0.9.

Pitching Axis

The location of the pitching axis is considered an important parameter in maximizing the energy efficiency of the system. For most of the oscillating foil system, the pitching axis is

located at one third or one quarter chord length from the leading edge (Kinsey and Dumas, 2008a). This is because the location of the pitching axis has been shown to be attributed to the shedding of leading edge vortices. Foils pitching about a point closer to the leading edge shed vortices at an earlier period within the cycle. Similar to that described for the oscillating frequency, the shedding of the vortices can influence the synchronization between the plunging velocity and the vertical force acting on the foil thereby influencing the efficiency of the system.

Airfoil Shape

At the moment, the existing study related to different airfoil shapes focusses on laminar flow field (Linsey, 2002; Kinsey and Dumas, 2008a; Usoh *et al.*, 2012). The one that commonly cited in literature is the study that has been carried out by Kinsey and Dumas (Kinsey and Dumas, 2008a) (Re = 1100) on three symmetric airfoils – NACA0002, NACA0015 and NACA0020. The conclusion they have made is that the correlation between the efficiency of energy extraction and the thickness of the airfoil was weak. Earlier study by Linsey (Linsey, 2002) performed a very limited comparison of NACA0010, 0014 and 0018 foils. He found a measurable effect on power and efficiency by reducing the foil thickness. He has concluded that thickness distribution does affect the efficiency performance, with the thinner airfoil performing better. However, this study has ignored the flow separation because of the viscous effect and only consider the inviscid flow. Hence, it is believed that the validity of this conclusion may not be justified. Le et al. (2013) investigated the effect of corrugation combined with camber of the foil. They found that the best corrugated section (008-100) provided approximately 6% more efficiency than a NACA0012 section, but was still inferior to a NACA0008 section.

Although some factors which influence the energy harvesting performance of the flapping foil generator (including foil kinematics, flow physics effects, flapping motions, etc) have been widely discussed, only a few brief studies have been done to examine whether foil thickness might have any impact on the power generation efficiency. In addition, the studies on the effects of foil shapes for other NACA series on energy harvesting performance and its mechanical mechanism are also lacking.

Reynolds Number

Most of the existing studies focus on the performance of semi-passive oscillating foils at low Reynolds numbers (~1000). As pointed out by Deng et al. (2015), the results at low Reynolds number cannot be directly applied to actual engineering projects. A few groups have

computationally explored moderate and higher Reynolds numbers, including Jones, Linsey et al. (2003), Dumas and Kinsey (2008a), Ashraf et al. (2011), Xiao et al. (2012), Campobasso et al. (2013), Kinsey and Dumas (2015), and Javed et al. (2018). Jones, Linsey et al. (Jones, K. D., Linsey, K., Platzer, 2003), investigated the effect of increasing the Reynolds number of 1×10^4 and 2×10^6 for a NACA0015 airfoil, and have shown that increasing the Reynolds number of the system increases the energy extracted from the flow. This result was validated by Dumas and Kinsey (Kinsey and Dumas, 2008a) who have shown that increasing the Reynolds number from 500 to 10,000 can result in a 10% increase in the energy efficiency of the system. Ashraf et al. (2011), Xiao et al. (2012) explored non-sinusoidal effects at moderate Reynolds numbers of 10,000-20,000 using a two-dimensional Navier-Stokes solver. At much higher Reynolds numbers, Campobasso et al. (2013) compared low (Re = 1100) and high (Re = $1.5 * 10^6$) Reynolds number results of a pitching and heaving foil using a compressible Navier-Stokes solver with a $k - \omega$ Shear stress transport model, and found that the two regimes offer different dynamics in terms of optimal parameters for energy harvesting. Kinsey and Dumas (2015) used an unsteady Reynolds Averaged Navier-Stokes (RANS) model with a Spalart-Allmaras turbulence closure for two-dimensional and three-dimensional hydrofoils to investigate tip effects and found good agreement with experimental results from a 2 kW prototype with two-foils in a tandem configuration. Javed et al. (2018) investigated the effect of low to moderate Reynolds numbers ranging from 5000 to 50,000, on energy extraction performance of semi-passive flapping foil using a meshfree method**.** They found that net power extracted by the system increases at high Reynolds numbers. Moreover, re-attachment of leading edge separation vortex plays an important role in the overall system performance.

The increase of power efficiency at high Reynolds number is believed to be caused by the presence of large flow separation due to dynamic stall which creates more lift and power (Jones, K. D., Linsey, K., Platzer, 2003). Moreover, the different characteristics of the turbulent and laminar boundary layers are also contributing to the higher efficiency as the Reynolds number increases. The additional effective viscosity associated with the turbulence model delayed the formation of leading edge vortices (LEV), so that a much larger leading-edge suction was maintained during the up and downstrokes, which is beneficial to energy extraction during these portions of the flapping cycle. The later formation of the LEV meant that it was not convicted as far aft by the time of the pitch reversal compared to the laminar case, and so the interaction with the trailing edge was also quite different (Young *et al.*, 2013).

To conduct computational studies at high Reynolds number using CFD software such as Fluent, turbulence models must be used. The choice of the turbulence model is largely influenced by the state of the flow. For oscillating foils, the turbulence model used should provide reliable results for unsteady flows with large boundary layer separation and vortex shedding.

Three-Dimensional Effect

The real foil always has a limited aspect ratio and thus the three dimensional flow structure can be generated due to the end effect. Taira and Colonius (2009) used direct numerical simulations (DNS) to investigate the wake structures of rectangular plates with different aspect ratios and non-rectangular plates under the state of inclination. von Ellenrieder et al., 2003; and Parker et al., 2007 performed experiments to discuss the effect of amplitude and frequency of an oscillating finite-span wing on three-dimensional vortex structure at low Reynolds number. Except for rectangular plate, there are many studies on oscillating plates of other shapes, such as the circular disk (Yang et al., 2014; Tian et al. 2017a,b), the elliptic disk (Dong et al., 2006; Yilmaz and Rockwell, 2012; Harbig et al., 2013; Wang et al., 2016) and the trapezoidal plate (Green et al., 2011). However, Zhang (2017) specially pointed out that the problems on how to make an oscillating foil generate maximum thrust and have energy harvesting efficiency up to the optimal state are still unclear.

For the 3D simulations with varying aspect ratios, most of the previous studies focused mainly on the thrust/propulsion, i.e., to understand how flapping low-aspect-ratio foils work for propulsion (Triantafyllou et al. 1991, Dong et al. 2006, Bleischwitz et al. 2015). For the energy harvesting, Simpson, Licht et al. (Simpson *et al.*, 2008), Simpson, Hover et al. (Triantafyllou *et al.*, 2008) and Haase et al. (Zhu, Haase and Wu, 2009a) have shown that increasing the aspect ratio of the airfoil has a positive effect on the energy efficiency of the system. Using water-based experiments for airfoils having aspect ratios of 4.1, 5.9 and 7.9, Simpson, Lich et al. (Simpson *et al.*, 2008) reported that a maximum efficiency of $52 \pm 3\%$ is achieved with the airfoil having an aspect ratio of 7.9 for a Strouhal number of 0.5 while Simpson, Hover et al. (Triantafyllou *et al.*, 2008) reported a maximum efficiency of $43 \pm 3\%$ for an airfoil under the same conditions but with a Strouhal number of 0.4.

Zhu, Haase et al. (Zhu, Haase and Wu, 2009a) investigated the system at lower Strouhal number ($St < 0.12$) in order to be able to use the 2D thin-plate model and the 3D boundary-element model which assumes negligible leading-edge separation. Using this technique, the maximum efficiency was calculated to be equal to $\frac{\pi c \theta_0 \omega}{4U_\infty}$ where *c* is the chord

length of the airfoil, θ_0 is the pitching amplitude, ω is the angular frequency and U_∞ is the free-stream velocity. Using this analysis, a foil having a pitching amplitude of 30°, aspect ratio of 10 and impinging free-stream velocity of $2ms^{-1}$ has a maximum efficiency of 25% which is much lower than the Betz efficiency. Hence, for both cases it has been shown that the increase in the energy efficiency of the system achieved through an increase in the aspect ratio is less compared to that produced when considering other parameters.

Kim et al. (Kim et al. 2017) investigated the energy harvesting performance and the flow structures of a 3D hydrofoil oscillating in pitch and heave experimentally in a water flume for different aspect ratios, Kinsey et al. (Kinsey *et al.*, 2011b) designed, built and experimentally tested a hydrokinetic turbine using oscillating hydrofoils to extract energy from water currents/tidal, and Deng et al. (Deng et al. 2015) investigated numerically the effect of variation of the aspect ratio and the structure of pitching motions on the energy extraction efficiency and wake topology of flapping hydrofoils in laminar flow.

Multiple Configurations

The majority of studies are concentrated on single foil devices. A few works discussed the multiple foils in tandem or parallel configuration. The propulsive performance of tandem flapping wings has been studied by Akhtar et al. (2007), Gong et al. (2015), Gravish et al. (2015), Pan et al. (2016) and Muscutt et al. (2017). In addition, Kumar and Hu (2010) investigated flow structures in wakes of tandem flapping wings. Peng et al. (2018a,b) studied the propulsion efficiency of two or more self-propelled flapping flexible wings. For the energy harvesting, the efficiency of oscillating foils in tandem or parallel configuration has been investigated by some researchers (e.g., Kinsey and Dumas (2012) and Karbasian et al. (2015).

In 2002, Lindsey (Linsey, 2002) suggested in his experiment study that operating oscillating airfoil in tandem configuration might have a positive impact on the efficiency performance. The same suggestion has been given by Jones (Jones, K. D., Linsey, K., Platzer, 2003) and Platzer (Platzer *et al.*, 2008). Lefrancois (2008) has investigated the power extraction performance of dual-foil turbine in both parallel and tandem configurations. He run the numerical simulation by using an in-house Lagrangian vortex method at low Reynold number $(Re = 1100)$. He found that tandem configuration give better efficiency as compared to parallel configuration which are 41% and 31% respectively. This happened due to the overall system sweeping area, *d*. For tandem configuration, the total sweeping area is

the same as single airfoil, whereas for parallel configuration, it is not and the sweeping area is more. Hence, it is effecting the calculation of efficiency as shown in Equation (1.16).

In 2011, Ashraf, Young et al. (Ashraf *et al.*, 2011) have conducted numerical simulations and shown that by using a tandem configuration, the energy efficiency of the multiple-foil configuration was increased to 59% when compared to the efficiency extracted by a single airfoil.

Kinsey and Dumas (2012) have further simulated tandem configurations to determine optimum spacing and phase between upstream and downstream airfoils. They found that a parameter global phase shift (i.e. combination of airfoil spacing, L_x and phase, ϕ) allowed predictions of different favourable spatial configurations. They also emphasised the critical role in terms of power extraction performance played by the downstream airfoil position relative to the upstream airfoil.

Later in 2013, Liu, Xiao et al. (Liu, Xiao and Cheng, 2013) have also shown that placing wings in twin configuration have a positive effect on the increase in energy efficiency of the system. The maximum efficiency is found to increase by decreasing the gap between the two airfoils as a result of a stronger vortex interaction.

Karakas and Fenercioglu (2017) experimentally investigated the inter-foil phase effects on power generation of a two-foil fixed set of kinematics and obtained an optimal inter-foil phase of 135^o from the observation of wake-foil interactions through an inter-foil phase variation of -180^o to +180^o. Numerical work from Ma et al. (2019) has coupled the motion of the leading and trailing foils in passive tandem arrays and noted how the inter-foil distance impact the system dynamics.

Ground Effect

One of the parameters that is beneficial for a wing to enhance the lift generation and reduce the drag formation is the ground effect (the wings that placed close to the ground). This behaviour is usually explained by two fundamental changes. The first one is the limitation of the trailing wing tip vortices imposed by the ground, which decrease the downwash intensity cause by those vortices, leading to an increase in the effective angle of attack of the wing and a reduction in the induced drag. The second modification is the presence of an effective air cushion that leads to an additional lift (Cui and Zhang, 2010). This is explained by the venturi-type phenomenon that modifies the pressure on the lower surface of the wing, which is closer to the ground, due to the modification in the area ratio. These both effects

lead to increase in the lift-to-drag ratio. However, it is important to remember that all the simulations carried out in the present work (for ground effect) are in two-dimension (Molina and Zhang, 2011; Truong *et al.*, 2013; Wu, Yang, *et al.*, 2015; Molina, Zhang and Alomar, 2016), therefore only the venturi effect will be felt. A great number of fields take advantage of this effect, such as racing cars and 'wing-in-ground' craft, which can operate with more efficiency than conventional aircraft. However, usually the aim on each application is different: for ground effect racer cars, the objective is to increase the generation of lower pressure under the wing close to ground, whereas the aircraft application is more focus on the desirable increase of the lift-to-drag ratio, increasing the overall performance.

Most of the studies related to ground effect are largely focused on fixed wings. Only few works are about the ground effect on flapping/oscillating wings. Maryossef and Levy (Moryossef and Levy, 2004) numerically investigated this field analysing the flow field around vertically oscillating airfoil (only heaving, no pitching) close to the ground. Their conclusion is that, when the airfoil is close to the ground and it is subjected to low frequency oscillation, the viscous effect become dominant, however, at high frequencies the inviscid behaviour is acceptable. Gao and Lu (Gao *et al.*, 2008) studied the ground effect applied to insect wing on a normal hovering flight (rotating and translating horizontally) using an immersed boundary-lattice Boltzmann method at $Re = 1100$. They used an elliptic foil to investigate how parameters such as the distance between the foil and surface, the phase difference between rotation and translation and the amplitude of oscillating rotation would affect the aerodynamic forces. They observed three different force regimes: force enhancement, force reduction and force recovery. The first type is when the clearance between the airfoil and the ground is small enough, in which the lift force is increased. As the clearance increases, the flow enters in the force reduction, in which the lift force is remarkably reduced. The force recovery is denominated in the region where the force recovers to the level without ground effect, when the clearance continuous to increase. An experimental study by (Truong *et al.*, 2013) investigated the aerodynamic performance of the beetle take-off with considering the ground effect. They observed an increase of 18.4% in the total vertical force production for the first stroke and 8.6% for the second stroke.

The study of ground effect on flapping foil for energy harvesting is very limited. One of the study by Zhu et al. (Zhu, Haase and Wu, 2009b) using the force pitching model investigate numerically the flow around oscillating foils in 3D applying nonlinear boundary-element model. They found that the presence of the ground increases the heaving response and notably enhances both the power and efficiency. The research findings of (Molina

2011a, 2011b), in case of purely plunging airfoils under the influence of ground classified the response of aerodynamic coefficients in three different regimes by varying the ground clearance between airfoil and the ground. The numerical findings indicate that maximum downforce is obtained at high effective angles of attacks. The downward force initially increases following a reduction as the ground clearance is further reduced from a critical value.

A heaving airfoil can improve the performance in the force reduction region at certain frequencies (Molina and Zhang 2011a). The pitching motion could also prove useful to reduce the loss of downforce in the force reduction region. It is also of capital importance to study the case of combined pitching and heaving, because both motions usually appear simultaneously.Very limited information is available on the ground effect related to flapping wings

Recently, Wu et al. (Wu, Yang, *et al.*, 2015) investigated the ground effect on the power extraction by flapping wing based biomimetic energy generator in a laminar flow numerically using the immersed boundary-lattice Boltzmann. In their simulation, a NACA0015 airfoil was placed in a laminar flow imposed a harmonic heave and pitch motions at $Re = 1100$. By changing the clearance between the airfoil and the ground, the amplitude and frequency of motion, the power extraction was systematically evaluated. Compared to the situation without ground effect, they obtained an improvement in the maximum efficiency of 28.6%. They also concluded that most of the increase from the proximity of the ground came from the heaving motion rather than pitching motion.

Therefore, it is clear that there is a lack of information on the influence of the ground effect in the energy extraction of flapping wings; and on the understanding of how some key parameters would change the energy extraction efficiency when the wing is in close proximity to the ground. The only paper available has only worked with the laminar flow.

Shape Flexibility

Up till now, most of the work on rotatory wing structures or oscillating foils for energy extraction are for rigid structures. Recent studies conducted on the wing flexibility for propulsion performance have shown that flexibility could improve the aerodynamic efficiency in flapping wing significantly. Yamamoto et al. (Yamamoto et al. 1995) have studied the propulsion performance of a flapping foil with the front part rigid and the rear part flexible, and it was reported as much as 27% increase in propulsion efficiency compared with a rigid foil. Heathcote et al (Heathcote, Martin and Gursul, 2004) , and Mazaheri &

Ebrahimi (Mazaheri *et al.*, 2012) carried out experiments on the wing flexibility using heaving-only airfoils or membranous wing, and found that both chordwise and spanwise deformations can have positive impact on the thrust performance of the wing. In 2014, Cleave *et al.* (Cleaver *et al.*, 2014) studied experimentally the thrust enhancement due to flexible trailing-edge of plunging foils (short thin plates attached to the foil have been tested for a wide range of flexibilities), and found up to 28% more thrust than the rigid case. Recently, Bleischwitz & Ganapathisubramani (Bleischwitz, Kat and Ganapathisubramani, 2015, 2016) performed an experimental study on the FSI of membrane wings near the ground. They found that ,higher aspect-ratio wings exploit better the benefit of wing flexibility with a gain of 60% for an AR (Aspect Ratio) of 2 and 31% for an AR of 1 (compared to rigid flat plates) for propulsion. In addition, membrane wings in ground effect are found to be up to 30% more efficiency than rigid flat plates. In the area of animal propulsion, previous studies on the role of flexibility of insect and bat wings suggest that some degree of flexibility can achieve a higher level of aerodynamics propulsive thrust; and this could have interesting implications to design, e.g., for micro aerial vehicle (MAV) and autonomous underwater vehicles (AUV) [Sfakiotakis et al. 1999, Triantafyllou et al. 2004, Fish et al. 2006]. In contrast to various studies on foil flexibility for performance enhancement in thrust, there are only a few studies on the effects of foil flexibility on the performance of flapping foil power generation.

For this work, however this effect was initially planned but has not been considered due to time constraint. In this thesis, we have to compromise on this parameter since the computational involvement is also expensive and need comprehensive work due to mesh distortion arising from flexible oscillating foil in heaving and pitching.

2.3 Numerical approach

Nowadays, Computational Fluid Dynamics (CFD) based on high fidelity methods is the main method used for researches on the dynamics of flapping foils or plates. However, low fidelity methods developed earlier are still used today. For example, the panel method is one of the widely used methods in early days (Jones and Platzer, 1997; Jones et al., 1999). Guglielmini and Blondeaux (2004) solved governing equations of an oscillating foil using a stream-function vorticity formulation for a two-dimensional problem. This method is also adopted recently (Zhu et al., 2009a; Zhu, 2011, 2012). Andersen et al. (2017) performed the numerical simulations of wake structure of a flapping foil in 2D flow using the particle vortex method (PVM). This method has been described and validated by Walther and Larsen

(1997), Larsen and Walther (1997), Rasmussen et al. (2010) and Hejlesen et al. (2015). The use of low-order methods are more attractive given their low computational cost (despite the accuracy drawbacks due to using laminar models), and high fidelity CFD methods are more desirable for their higher accuracy despite the increased computational load. Due to maturity of computer technology, CFD has become the main method to investigate fluid problems. The implementation of CFD is mainly based on using some commercial or open-source codes, such as Fluent, CFX, StarCCM+ and OpenFOAM, most of which are based on finite volume method (FVM) and a few of which are based on finite element method (FEM) and finite difference method (FDM). Boiron et al. (2012) used the FEM to simulate the flow around the foil and then compared the hydrodynamics of a flapping foil through experimental and numerical methods. Yu et al. (2012, 2013) used an unsteady compressible Navier-Stokes (N–S) solver with high-order spectral difference (SD) method to investigate the wake structure and the effects of foil thickness and kinematics on flapping foil propulsion. Medjroubi et al. (2011, 2012) simulated the 2D unsteady flow around a heaving NACA0012 airfoil using the spectral element method (SEM), which reproduced well the wake flow behind the heaving foil. Wu et al. (2014, 2015a,b,c) used the immersed boundary-lattice Boltzmann method (IB-LBM) to simulate the flow over the foil and the energy extraction performance. Yu et al. (2017) investigated the effect of kinematic parameters on the propulsion performance of an oscillating foil using FVM with the Spalart-Allmaras (S-A) turbulence model. Javed et al. (2018) used the hybrid approach based on meshfree RBF and Cartesian finite difference method to study the effect of low Reynolds numbers on energy extraction performance of semi-passive flapping foil. For the numerical study of an oscillating foil, moving mesh method is an essential issue for solving these types of problems.

2.3.1 Turbulence models

There are three kinds of methods to simulate the turbulence flow of flapping foils, namely Direct Numerical Simulation (DNS), Large Eddy Simulation (LES) and Reynolds-Averaged Navier-Stokes (RANS). Based on the literature review, RANS is the early method used to solve the issues of turbulence. For flapping foils, as the flow is unsteady, URANS (unsteady RANS) has been used for a wide range of Re. The use of DNS can accurately get all information of turbulence and do not consider the closeness of the equations, but it is limited to low Re and simple boundary problems due to its high demand on computational resources. Actually, LES is superior to RANS/URANS in terms of model construction and is computationally more efficient than DNS (although its computational cost is still high),

but its development is not yet mature and is only used for simple shear and tube flows. For energy harvesting, at the moment there are very limited research on using DNS and LES, and they are used with low Reynolds numbers (Ribeiro et al., 2018, Zhongying et al, 2019), and coarse meshes. Amongst the turbulence models used for flapping foil are the single-equation Spalart-Allmaras (S-A) turbulence model, k-ε turbulence model, k-ω two-equations SST turbulence model and zero-equation Baldwin–Lomax (B-L) algebraic turbulence model. Tuncer and Kaya, (2005, 2007) used the B-L algebraic turbulence model to optimise the thrust and propulsion efficiency of flapping foils using different methods. Münch et al. (2010) proposed a method using SST k-ω and k-ε turbulence model that can predict fluid-structure coupling for a rigid hydrofoil with forced and free pitching motions. Kinsey and Dumas (2012) carried out a numerical research based on 2D unsteady RANS simulations using S-A model and analysed the different tandem configuration for two oscillating foils within a hydrokinetic turbine to maximise the energy harvesting efficiency. Liu et al. (2013) used a bio-inspired flexible flapping foil to discuss the energy harvesting performance, using k-ω turbulence model for unsteady RANS closure. Lu et al. (2013a,b) used SST k-ω model to investigate the effects of asymmetric sinusoidal motion on pitching airfoil aerodynamics.

For our simulations, the unsteady-RANS is used as it offers improved predictions of flow separation under adverse pressure gradients, which is mainly the case for oscillating foils.

2.4 Importance of this Study/Contribution

From the survey of the literature review of this emerging field of study, it has been found that the majority of the work is mainly focused on the standard 2D rigid foil devices for energy harvesting at low and intermediate Reynolds number. In this study, numerical simulations using CFD have been carried out on oscillating bodies in 2D and 3D to reveal the flow aerodynamics and their potential for power extraction efficiency. Mainly, we have explored the effect of trailing edge geometry modifications, ground effect, and 3D effects on the potential energy harvesting performance and efficiency of oscillating foil system at low and high Reynolds numbers. The following ‘gaps’ have been identified and they will be investigated in this thesis.

- The effect of geometrical shape modifications on energy harvesting potential. At the moment, studies on foil shape are mainly focussed on different thickness distribution for laminar flow. This study explores the effect of different foil thicknesses (NACA0012, NACA0015 and NACA0018) and different trailing edge shapes

modification at laminar and turbulent flow fields, under different operational parameters, on the energy harvesting performance efficiency. For the modified foils, three different trailing edge modifications (blunt, round and sharp) are proposed for the oscillating foils in this work. These three NACA profiles were chosen (NACA0012, NACA0015 and NACA0018) as they provide benefit in structural rigidity.

This work is inspired from the previous study on trailing edge modifications for lift performance/thrust of airfoil and hydrofoil (Ramjee et al. 1986, Law et al. 1987, Thompson and Whitelaw 1988, Gomez and Pinilla 2006, Murcia and Pinilla 2011). Ramjee et al. (1986) run a simulation of NACA 0012 with trailing edge modifications and the numerical results obtained are validated by his own experiments. The trailing edge was truncated by 5%, 10%, 15%, and 20% of chord length and found that the modifications influenced the lift force. He stated that by increasing the bluntness, the maximum lift coefficient increased to the point when 15% of chord length was being cut, and beyond that, the lift coefficient is decreased. The truncation was also found to affect the foil lift and drag ratio in the same result as the lift force is affected. Lift and drag ratio are improved when 15% of truncation was applied and decreased if any further length was being cut off. These results are adopted in this work for choosing the cut off length for modifying the foil model. Other researchers have shown also that allowing modifications at the trailing edge of NACA profiles influences the behaviour of both lift and drag coefficients. These studies are focused mainly on the lift enhancement/thrust, and no study, however, is done on the effect of the shape modifications of the airfoil on the power extraction efficiency. In this work, we investigate the effect of trailing edge modifications on energy harvesting performance potential for oscillating foils.

- At the moment the majority of studies are concentrated on single foil devices. Few works discussed the multiple foils in tandem or parallel configuration. This study looks at the effect of flapping foils operating in tandem with different configurations (including geometry shape modifications) on energy harvesting. Other than investigating the effect of kinematics parameters, distance between two bodies and trailing edge geometry modification, this study has also explored the effect of bluff body (cylinder) and the foil in tandem configuration which has not been studied before.
- The effect of near ground on energy efficiency performance. The previous studies are mainly focused on lift enhancement in laminar flow field. This work looks at the

effect of near ground on the potential energy harvesting at low and high Reynolds numbers with the optimal geometrical airfoil being considered.

- The 3D effect and geometric modifications potential on the energy efficiency performance. Due to the complexities of three-dimensional flow, the studies of foils are still focused on two-dimensional structures at low or moderate Reynolds number. This has been far from the real applications, where the effects of three-dimensionality, should be considered. The use of 2D simulation normally over-predicts the performance of the system since it does not include the 3D effect. Hence, this study on the 3D simulation of oscillating foils is to allow for more accurate prediction of energy harvesting. In addition to the study of different aspect ratios (AR), we have also extended the study of geometrical variation effect in 2D to 3D.

2.5 Aim and Objectives

The aim of this research is to investigate numerically the role of fluid-structure interaction dynamic systems on the performance of energy harvesting (through its nonlinear characteristics) of oscillating foils. To achieve this aim, it is anticipated that the following objectives will be fulfilled:

1. Explore the effect of geometry shape variations (including thickness distribution and trailing edge shape modifications) and the impact of different kinematics on the flow behaviour and energy harvesting performance of single 2D oscillating foils (with a combined heave and pitch motio
2. n), for laminar and turbulent flows.
3. Investigate the influence of multiple oscillating bodies configurations for different arrangements (including airfoil-airfoil and cylinder-airfoil interactions) and shape modifications on energy harvesting performance and power optimisation.
4. Explore the effect of near ground on the energy efficiency increase of oscillating foils in laminar and turbulent flows.
5. Investigate the influence of 3D effects, aspect ratios and geometry shape variations on oscillating foils for energy harvesting extraction.

Chapter 2

Chapter 3: Methodology

This chapter contains the details of the numerical methodology that is used in the present study. All solutions are based on computational analysis known as Computational Fluid Dynamic (CFD). The numerical analysis was conducted by commercial code ANSYS Fluent (V.14.5) and another commercial software known as Pointwise which has been used as the pre-processing meshing tool.

3.1 Structure of CFD Code

An overview of the CFD techniques used to tackle the fluid flow problems is given in (Versteeg and Malalasekera, 2007). In order to gives the user the possibility of easy setup to their problem, all commercial CFD packages include a friendly user interfaces to input problem parameters and to examine the results. The necessary computational tools required to carry out these steps can be classified into three categories: (i) pre-processor, (ii) solver and (iii) post-processor (Ferziger and Peric, 1999; Versteeg and Malalasekera, 2007).

i. *Pre-processor*

In the first stage of CFD code, the physical problem is implemented into the mathematical problem by first making simplifying assumptions that would enable the problem to be analysed accurately. Therefore, in this stage, the computational domain is defined and it is then discretized into a number of elements, which constitute the mesh or grid. The fluid properties and the boundary conditions are then set. Since the CFD solution of a fluid dynamic problem is given locally, the accuracy of the results obtained are strongly depending on the total number of cells in the grid. In general, the larger is the number of elements, the better is the solution accuracy, even though the computational time will be higher as well. Consequently, the optimal grid should not be uniform, but finer where higher are the variables gradients and coarser in the region characterized by smooth changes in the flow. The final success of a CFD simulation strongly depends on the pre-processing and therefore a special attention might be paid to the choice of the mesh and of boundary condition.

ii. *Solver*

In the second stage, the numerical solution algorithm is the core of CFD code. All the main CFD solvers work with the following procedure:

- Modelling the problem unknown by means of simple analytical functions.

- Discretising the governing equations for the fluid flows, properly modified by substituting the former mentioned functions.
- Solving the algebraic system of equations.

Most of the commercial CFD codes (e.g. Fluent) are based on a finite volume (FV) discretization which consists of the following steps:

- Integration of the governing equations over each control volume within the computational domain.
- Discretisation – the flux terms, which deal with convection and diffusion process, are approximated with a finite differential approach as well as the source terms when being present, in order to obtain an algebraic system of equations.
- Solution of the algebraic equations by an iterative method.

The integration phase distinguishes between FV methods and other numerical techniques. By integrating the governing equations, a new set of equations is obtained, which states the conservation of the fundamental properties for each of the cells (finite control volumes) within the computational domain.

iii. *Post-processor*

Finally, in this stage, the analysis of solution results is provided. The solver output is a set of solution variable, associated to the given grid nodes or volumes. These data must be collected elaborated in the most suitable way for the analysis, in order to produce a physical representation of the solution. Some CFD software packages (like Fluent) contain a post-processing section. Other solvers need an external tool for data treatment, which can be a commercial one (several complete package exit for the scope) or a dedicated in-house code. Anyhow, one might be able to do the following post-processing operations:

- Domain and grid visualization
- Vectorial plots of solution variables
- Contour plots of solution variables
- Drawing 2D and 3D plots
- Tracking path-lines, stream traces, etc.
- Algebraic and analytical operations within the variables
- Dynamic representations, animations etc.

In general, we should refer to the solved flow field as it had been an experimental test situation. Among the given data set, we could operate as we were using real instruments, by selecting the position of "virtual" probes or control surfaces where our interest is focused.

3.2 Governing Equation

The mathematical model used to represent the fluid flow around a body is based on the principles of conservation of mass and conservation of momentum.

The conservation of mass or continuity equation is defined as,

$$\frac{\partial \rho}{\partial t} + \nabla \cdot (\rho \mathrm{v}) = 0 \tag{3.1}$$

meanwhile the conservation of momentum is described by,

$$\frac{\partial \rho \mathrm{v}}{\partial t} + \nabla \cdot (\rho \mathrm{v}\mathrm{v}) = -\nabla \mathrm{p} - \rho \mathrm{g} + \nabla \cdot \tau \tag{3.2}$$

where,

- ρ is the density of the fluid;
- v is the velocity vector;
- p is the pressure of the fluid;
- g is the acceleration due to gravity; and
- τ is the stress tensor.

Assuming the Stokes' hypothesis for Newtonian fluids which states that the components of stress are linearly related to the components of the rate of strain and that a Newtonian fluid is isotropic, the stress tensor τ in the Navier-Stokes equation is given by (Versteeg and Malalasekera, 2007),

$$\tau = \mu \left[\left(\nabla \mathrm{v} + \nabla \mathrm{v}^T \right) - \frac{2}{3} \nabla \cdot \mathrm{v} I \right] \tag{3.3}$$

where,

- μ is the molecular viscosity of the fluid; and
- I is the unit tensor.

According to Reynolds, for each of the instantaneous dependent variables in the Navier-Stokes equations a time-average and a randomly fluctuating component can be found, for instance the velocity *i*-component u_i (of velocity v) will be

$$u_i = \bar{u}_i + u'_i \tag{3.4}$$

where,

- $\bar{u}_i$ is the time-averaged component of the velocity; and
- u'_i is the fluctuating component of the velocity.

The time-averaged component of the velocity is obtained by

$$\bar{u}_i = \frac{1}{\Delta t}\int_{t_0}^{t_0+\Delta t} u_i \, dt \tag{3.5}$$

Substituting Equation (3.5) in the Navier-Stokes equation gives the incompressible time-averaged Navier-Stokes or RANS equations (in tensor notation),

$$\rho\frac{\partial \bar{u}_i}{\partial t} + \rho\frac{\partial\left(\bar{u}_i\bar{u}_j\right)}{\partial x_j} = -\frac{\partial \mathrm{p}}{\partial x_i} + \frac{\partial}{\partial x_j}\left[\mu\frac{\partial \bar{u}_i}{\partial x_j}\right] - \frac{\partial \overline{u'}_i\overline{u'}_j}{\partial x_j} \tag{3.6}$$

The last term in Eqn. (3.6) is known as the Reynolds stress. This term causes the closure problem of the Navier-Stokes equations which can only be solved by including a turbulence model to relate the Reynolds stress to the mean velocity field.

3.3 Turbulence Closure

The turbulence modelling is an approximation to seek solution of unsteady Reynolds-Averaged Navier-Stokes (URANS) equations by modelling the effect of velocity fluctuation in the flow. Hence, to obtain the close form solution the turbulence models are included to obtain the numerical solution of the URANS equations. Selection of turbulence model is highly dependent on the flow characteristics, level of accuracy required and computational power available (Ferziger and Peric, 1999). $k-\omega, k-\omega$ SST, $k-\varepsilon$, and Spalart-Allmaras (S-A) model are among the significantly researched models to model the turbulent in flow. Each of these turbulent models have its own strength and limitation.

In the present work, $k-\omega$ SST model is chosen due to its superior characteristic to accurately predict the flow separation and performance curve and to deal with the advance pressure gradients that are expected to occur over the entire cycle of oscillation airfoil.

The $k-\omega$ SST model also make use of individual strength and weakness of two turbulence models namely $k-\varepsilon$ model and $k-\omega$ turbulence model. The $k-\varepsilon$ turbulence

model has the performance limitation of modelling the viscous sub layer. This limitation has been compensated by the adoption of $k-\omega$ turbulence model in the viscous boundary layer region. Outside the boundary layer and wall boundary regions, performance of $k-\varepsilon$ turbulence model is satisfactory.

The shear-stress transport (SST) $k-\omega$ model was developed by Menter to effectively blend the robust and accurate formulation of the $k-\omega$ model in the near wall region with the free-stream independence of the $k-\epsilon$ model in the far field. The SST $k-\omega$ model is similar to the standard $k-\omega$ model, but includes a number of features that make the SST $k-\omega$ model more accurate and reliable for a wider class of flows than the standard $k-\omega$ model. The SST $k-\omega$ model equations are (Ferziger and Peric, 1999)

$$\frac{\partial}{\partial t}(\rho\kappa)+\frac{\partial}{\partial x_i}(\rho\kappa u_i)=\frac{\partial}{\partial x_j}\left(\Gamma_\kappa\frac{\partial\kappa}{\partial x_j}\right)+G_\kappa-Y_\kappa+S_\kappa \tag{3.7}$$

$$\frac{\partial}{\partial t}(\rho\omega)+\frac{\partial}{\partial x_i}(\rho\omega u_i)=\frac{\partial}{\partial x_j}\left(\Gamma_\omega\frac{\partial\omega}{\partial x_j}\right)+G_\omega-Y_\omega+D_\omega+S_\omega \tag{3.8}$$

3.4 Flow Solver

In the present work, finite volume base fluid dynamics code Ansys Fluent (V. 14.5) is used to solve the Navier-Stokes equations with the pressure-based solver using URANS. The main properties of flow were assumed by unsteady, incompressible, viscous laminar and turbulent flows.

For laminar flow fields, a second order upwind spatial discretization is done with second-order central differencing scheme. A second order implicit scheme is used to discretize time. Semi-implicit method for pressure-linked algorithm SIMPLE is used for the velocity-pressure coupling, and Gauss-Seidel linear equation solver is used for the discretized equations.

For turbulent flow fields, the turbulence modelling of two equations $k-\omega$ SST has been chosen (as mentioned in section 3.2). Again, the SIMPLE algorithm has been selected for pressure-velocity coupling, and second order schemes are used for pressure, momentum and turbulent viscosity resolution. The unsteady formulation is based on a second order implicit scheme and absolute convergence criteria of 10^{-5} are set for continuity and velocity components while 10^{-4} is used for the turbulent viscosity.

3.5 Sliding Mesh Theory

Sliding mesh model has been chosen for oscillating foil in this study due to the computational of the unsteady flow field. This model is the most accurate method for simulating flows in multiple moving reference frame in Fluent. The sliding mesh model allows the motion of multiple domains sliding relative to one another along interface boundaries. The unsteady solution which is sought in a sliding mesh simulation is time periodic. That is, the unsteady solution repeats with a period related to the speeds of the moving domains. The minimum number of cell zone that is required in sliding mesh technique is two, and each of the zones must be bounded by at least one interface zone. The interface zones of adjacent cell zones are associated with one another to form a mesh interface. The two cell zones will move relative to each other along the mesh interface.

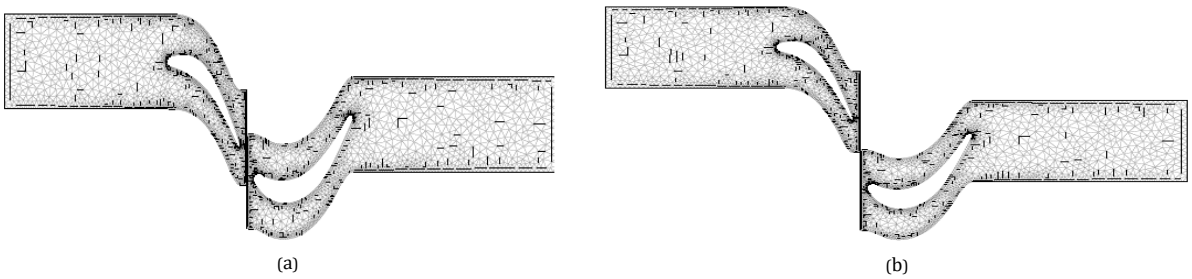

Figure 3. 1: Example of sliding mesh on interface nodes (a) initial position (b) end position (Ansys, 2005)

3.6 Grid Generation

Pointwise commercial mesh software has been used to model the simulation domain and IGES file is the compatible geometrical format required by this package. For this particular requirement, the coordinate data points of NACA profiles has been imported in the SolidWorks CAS modeller before it then saved in the IGES file format. Mesh generation has presented many difficulties owing to the different range of geometric scales, length of the domain, size of the rotor, typical chord length, and boundary layer thickness. Hence, in this study, the simulation domain was built by the structured and unstructured grid. Any domain created by the structured grid will have quadrilateral surface grid, while the domain created by the unstructured grid will contain triangular surface elements (Figure 3.2). However, even for the unstructured grid domain, we are still use the structured grid at the boundary layer for better prediction (Figure 3.3).

The structured grid control for boundary layer thickness and first cell height estimation is based on the applied velocity and the airfoil chord length. As outlined in Table 3.1, the estimation of first cell height and boundary thickness have been made for fully resolved boundary layer i.e. y^+value of 1:

Table 3. 1: Shape classification and mesh generation

Shape approximation	**Boundary layer thickness**	**First cell height**
Flat plate	$\delta = 0.370\ c\ (Re)^{-1/5}$	$\Delta y = 5.87123\ cy^{+}(Re)^{-9/10}$

where Δy defines the normal distance of first layer from the solid surface, δ denotes the boundary layer thickness value and y^+ is non-dimensional wall distance. Within the boundary layer grid, at least 60 node points are placed and the mesh expansion normal to the airfoil surface is based on the expansion ratio of 1.05 to 1.2.

Other than the boundary layer grid, the overall simulation domain consists of two different mesh zones (stationary and rotational zones) separated by a sliding interface between these zones (details given in the next chapter). The fine mesh bounded by the circular interface was set to rotate, thereby inducing the rotational pitching motion. This approach for representing the pitching motion of the airfoil ensures that the quality of the grid remains intact as the airfoil rotate.

Table 3. 2: Mesh information

Configuration	Single Airfoil			Tandem	
	NACA0012	NACA0015	NACA0018	Airfoil-airfoil	Bluffbody-airfoil
Cells	67,245	67,257	67,272	261,836	287,769
Faces	136,161	136,184	136,214	478,304	531,969
Nodes	68,077	68,089	68,104	215,519	242,935
Partitions	2	2	2	2	2
Cell zones	2	2	2	3	3
Face zones	10	10	10	15	15

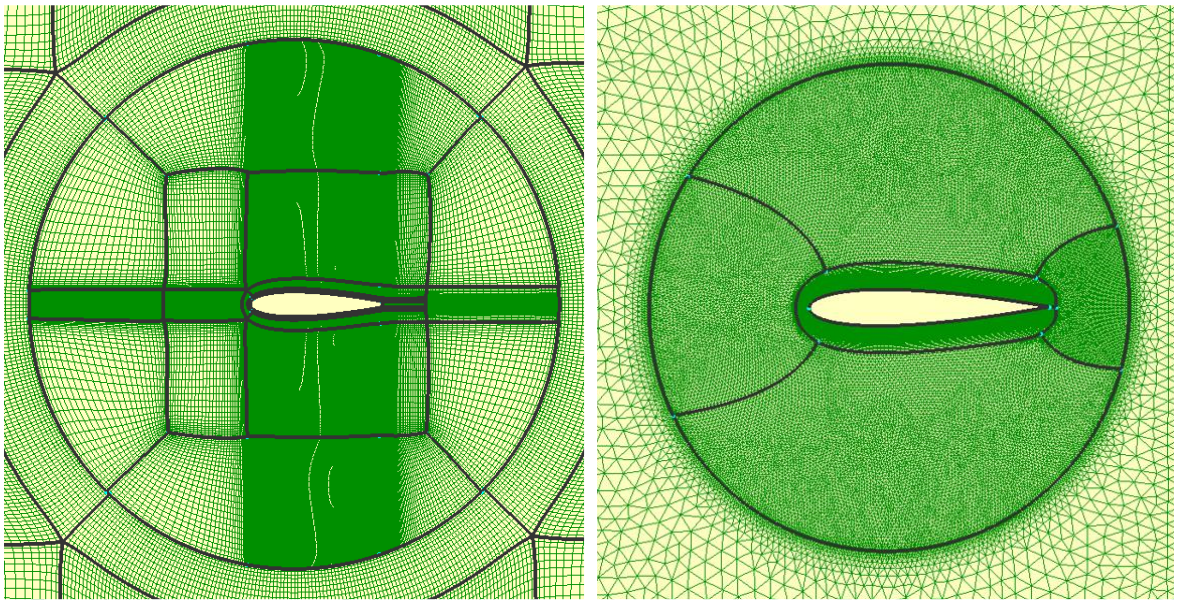

Structured grid Unstructured grid

Figure 3. 2: Types of domain grid

In 2D simulation, for the structured grid, the mesh was generated in the butterfly topology (Pointwise, 2011) (or known as "O-H" topology) which differ to the unstructured grid where triangular elements have been used. These two different meshes have been used for different cases. For all single airfoils analysis (2D and 3D cases), structured mesh has been used. Meanwhile for tandem cases (airfoil-airfoil and cylinder-airfoil), the unstructured mesh is used, as the mesh quality is found to be better within the foils' swapped regions and less difficult to generate, as compared to the structured mesh. Specifically, for the tandem cases an unstructured grid is constructed within the foils' swapped regions, while structured-boundary layer grids are adopted for each of the foils, to ensure the accuracy of the foil-forces calculation (Figure 3.3). A structured grid is then used for the rest of the calculation domain to ensure an accurate and quick simulation (Figure 4.28). This mesh is found to work well for the tandem cases. For all the meshes used in this study, the highest value of skewness fell in the range of 0.4 - 0.45 which means the mesh quality is good. In order to have high quality of mesh grid, the pointwise software has a special feature name '*Solve*' which is used to improve the grid quality of structure and unstructured domain and structure and unstructured block. Hence, this '*solve*' command has been widely used in the grid generation process.

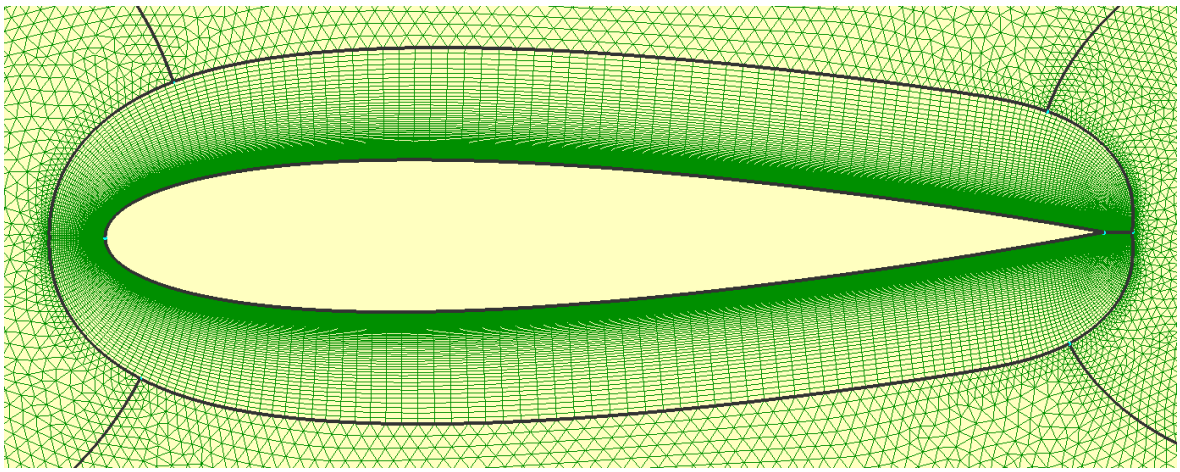

Figure 3. 3: Close-up of the boundary layer in unstructured grid

3.7 Validation Study

Fluid structure interaction study of oscillating airfoil is complex in nature due to aerodynamic behaviour of moving airfoils and resulting large flow separation over the periodic cycle of oscillation. To validate the Navier-Stokes computation, a rigorous 2D mesh sensitivity analysis together with numerical validations of similar airfoil geometry under identical case setup of (Kinsey and Dumas, 2008a, 2014, 2015) has been carried out for laminar and turbulent flow regimes. Due to time and computational resource constrains, it is not feasible to numerically resolve all the instances of parametric design space of geometric and fluid flow parameters. Therefore, to carry out this two-steps validation process, a base line NACA0015 sharp trailing edge airfoil system is selected.

First, to optimize the discretization error for both space and time and to assess the independence of the numerical solution, a set of three-structured grid were generated. For coarse, medium and fine mesh, the number of computational nodes on the airfoil surface are 250, 350 and 500 respectively. The corresponding total cells count of 2D cross sections of simulated domain are shown in Table 3.3.

The simulations were run for sufficiently large number of cycles before the targeted residual values of 10^{-5} for pressure, velocity and turbulence parameters have been achieved. Statistically averaged values of aerodynamic performance coefficients of oscillating airfoil systems, i.e. C_L and C_Y from converged solution have been setup to estimate the mesh resolution and numerical discretization errors. The Case setup involves NACA0015 undergoing sinusoidal pitching and heaving motion at Reynolds number of 1100 in order to

examine the power extraction performance, with parameters setup of $H_0 = c, \theta_0 = 76.3°$ and $f^* = 0.14$, where the dimensionless frequency is defined as $\left(f^* = \frac{f.c}{U_\infty}\right)$. These parameters values were chosen as they are found to have an optimum performance by (Kinsey and Dumas, 2008a).

Table 3. 3: Description of mesh sensitivity analysis

Mesh Resolution	**Nodes on Airfoil Profile**	**Cells**
Coarse	250	38,934
Medium	350	67,257
Refine	500	111,369

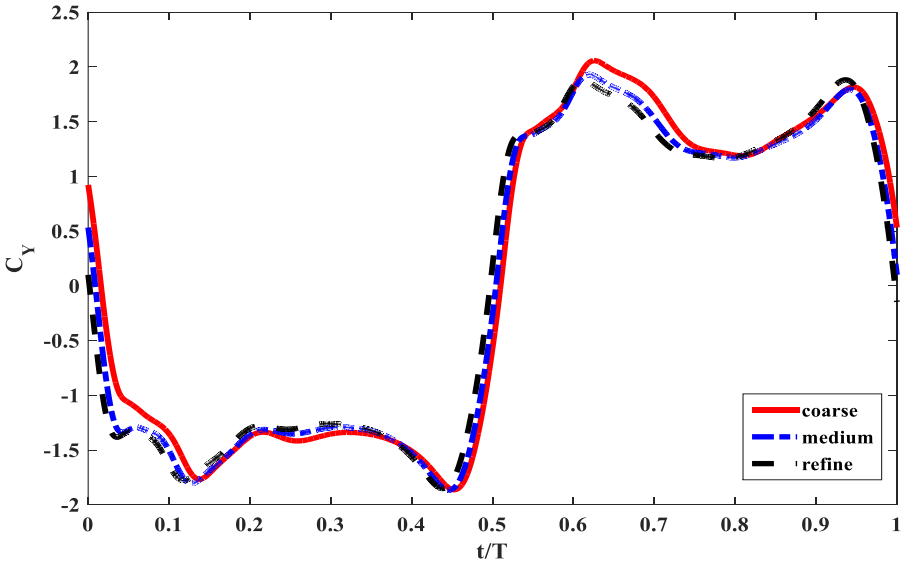

Figure 3. 4: Comparison of performance for coarse, medium and refine mesh

Figure 3.4 shows the comparison of coefficient of lift force (C_Y) performance between the coarse, medium and refine mesh. As can be seen, the medium and refine mesh show much closer results. Therefore, for further simulations run in this study, the medium mesh resolution is selected.

For the time simulation, a second-order implicit time-marching scheme was used, with 30 sub-iterations per time-step. A time refinement study with a time-step varied from 2×10^{-3}T to 1×10^{-3}T, is used which ensured a minimum number of time-steps per period while also keeping an acceptable Courant–Friedrichs–Lewy number (based on the free stream velocity) in all the cells of interest. Lower time-steps did not yield a more accurate solution. For the results in Figure 3.4 they are obtained for a time-step of 0.001.

For the second steps of the validation process, Table 3.4 shows the results for the mean values of coefficient of drag ($\bar{C}_X$), maximum values of coefficients of lift $(\hat{C}_Y)$ and moment $(\hat{C}_M)$, efficiency (η) and cycle-averaged power coefficient $(\bar{C}_P)$, while Figures 3.4 and 3.5 show the vorticity contours for two representative cases of pitching amplitude and reduced frequency (Case 1: $f^* = 0.14, \theta_0 = 76.33°$ and Case 2: $f^* = 0.18, \theta_0 = 60.0$).

Table 3. 4: Parametric study of flow over flapping NACA0015 airfoil at $Re = 1100$

Study	$\bar{C}_X$	$\hat{C}_Y$	$\hat{C}_M$	η[%]	$\bar{C}_P$
Case 1: $f^* = 0.14, \theta_0 = 76.33°, H_0 = c$					
Present	2.063	1.937	0.626	33.3	0.86
Kinsey and Dumas (2008)	2.014	1.910	0.646	33.7	0.86
Liu et al. (2016) [DVM with TEFSC]	-	-	-	-	0.86
Bryan model (2013)	-	-	-	-	0.87
Case 2: $f^* = 0.18, \theta_0 = 60.0°, H_0 = c$					
Present	0.72	1.245	0.299	11.4	0.27
Kinsey and Dumas (2008)	0.69	1.256	0.299	11.5	0.27
Liu et al. (2016) [DVM with TEFSC]	-	-	-	-	0.37
Bryan model (2013)	-	-	-	-	0.24

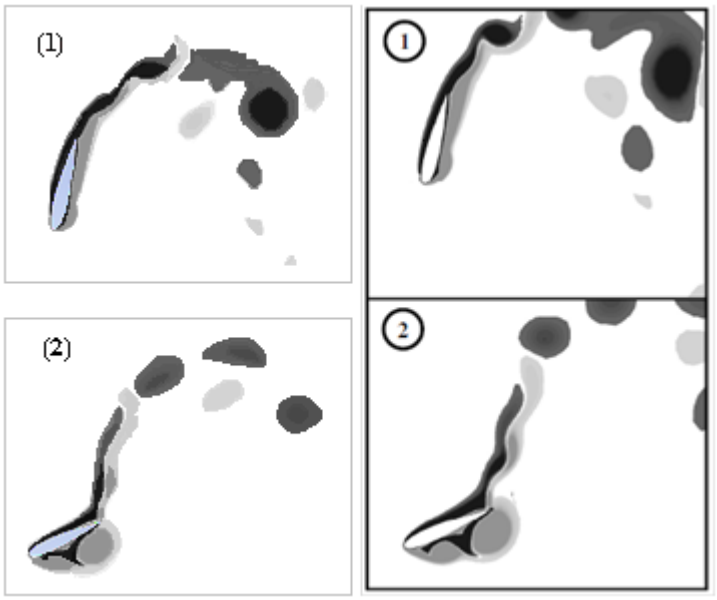

Figure 3. 5: Comparison of vorticity contour of present study (left) and Kinsey and Dumas work (right) for laminar Case 1: (1) at 0.25T and (2) at 0.45T

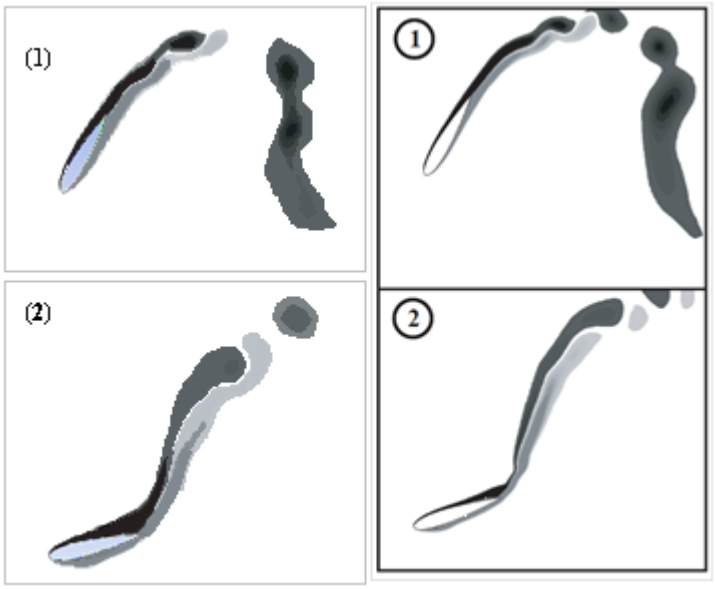

Figure 3. 6: Comparison of vorticity contour of present study (left) and Kinsey and Dumas work (right) for laminar Case 2: (1) at 0.25T and (2) at 0.45T

From the results presented in Table 3.4, and Figures 3.5 and 3.6, it is evident that the results obtained from the present study compare very well with those of Kinsey and Dumas (2008). The averaged C_p ($\overline{\boldsymbol{C}}_{\boldsymbol{P}}$) are also compared with the discrete vortex method (DVM) with TEFSC (trailing edge flow separation corrections) Liu et al.(2016) and Bryant model (2013) (using Reduced-Order Aerodynamic Modelling). Liu et al.(2016) have compared their results to Kinsey and Dumas (2008) and stated that the DVM provides better approximations of the time history of C_p to the CFD method of Kinsey & Dumas compared with the Bryant model (2013). In comparison to our work, the DVM method and the Bryan model show a very good agreement for Case 1, while for case 2 they show less accurate results (Table 3.4). This is expected as Liu et al. uses DVM method and Bryan model uses a reduced-order model with some empirical values. The % errors for averaged C_p between our present method and Liu et al. method for Case 2 is 37%, while for Bryan method it is 10%. Case 2 ($f^* = 0.18$ and $\theta_0 = 60°$) in Figure 3.6 shows a smooth aerodynamics flow with a moderate efficiency of $\eta = 11.4\%$, while Case 1 ($f^* = 0.14$ and $\theta_0 = 76.33°$) in Figure 3.5 shows a higher efficiency of $\eta = 33.3\%$ for lower reduced frequency and higher pitching amplitude. Moreover, Figure 3.5 exhibits dynamic (delayed) stall vortex shedding characterised by the delay in boundary layer separation and the formation of leading edge vortices (LEVs), which are known to play an important role in the capability of extracting energy from the flow during cycles.

In order to further test the validation of the numerical model, simulations of imposed pitching-heaving motion of NACA0015 have also been carried out in turbulence flow field regime at $Re = 5 \times 10^5$. As mentioned earlier, the turbulence model that is used in this study is the $k - \omega$ SST with low-*Re* correction. The turbulent inlet boundary condition for this model has been characterized as an intensity of 0.1% and a turbulent viscosity ratio of 0.01. These stated parameters have been chosen in order to validate the current results with the published work by (Kinsey and Dumas, 2014, 2015) for the two cases (see Table 3.5). Table 3.5 shows the comparison between the results obtained in the present study with those of Kinsey and Dumas. From this table, it can been seen that the results are in good agreement for both the forces and moment coefficients, as well as for the efficiency.

Table 3. 5: Parametric study of flow over flapping NACA0015 airfoil at $Re = 5 \times 10^5$

Study	$\overline{C}_X$	$\widehat{C}_Y$	$\widehat{C}_M$	$\eta, \%$	$\overline{C}_P$
Case 1: $f^* = 0.14, \theta_0 = 75°, H_0 = c$					
Present	1.894	2.884	0.574	40.31	1.028
Kinsey and Dumas (2015)	1.937	2.772	0.577	39.94	1.018
Study	$\overline{C}_{PY}$	$\overline{C}_{P\theta}$	-	$\eta, \%$	$\overline{C}_P$
Case 2: $f^* = 0.16, \theta_0 = 85°, H_0 = 1.5c$					
Present	2.03	-0.50	-	43.7	1.53
Kinsey and Dumas (2014)	2.07	-0.51	-	44.6	1.56

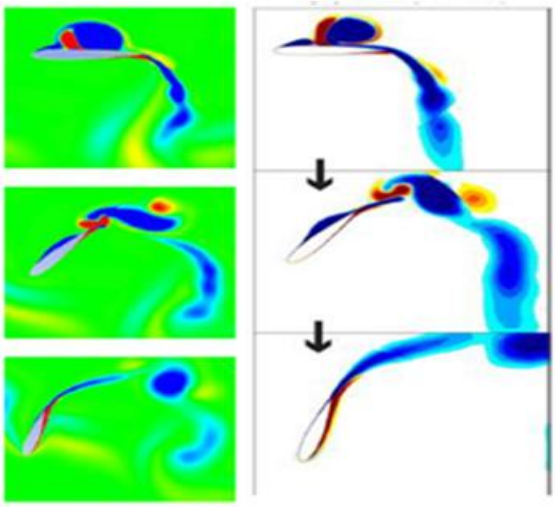

Figure 3. 7: Comparison of vorticity contour of present study (left) and Kinsey and Dumas work (right) and for turbulent Case 1: at 0T, 0.125T and 0.25T

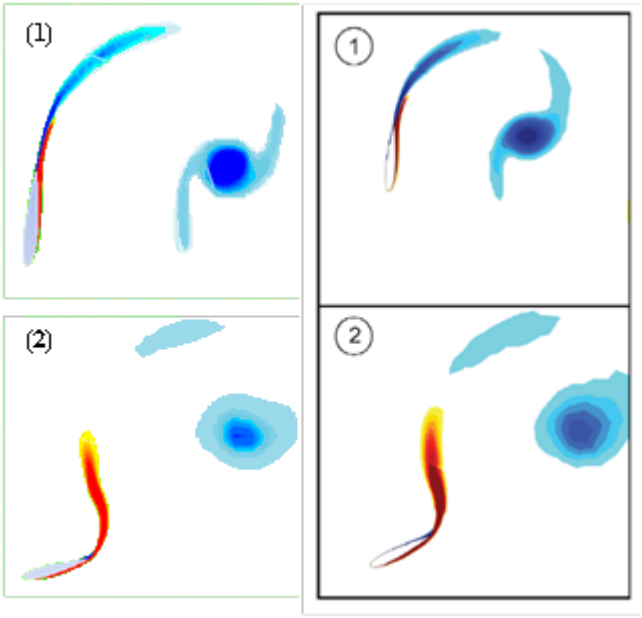

Figure 3. 8: Comparison of vorticity contour of present study (left) and Kinsey and Dumas work (right) for turbulent Case 2: (1) at 0.25T and (2) at 0.45T

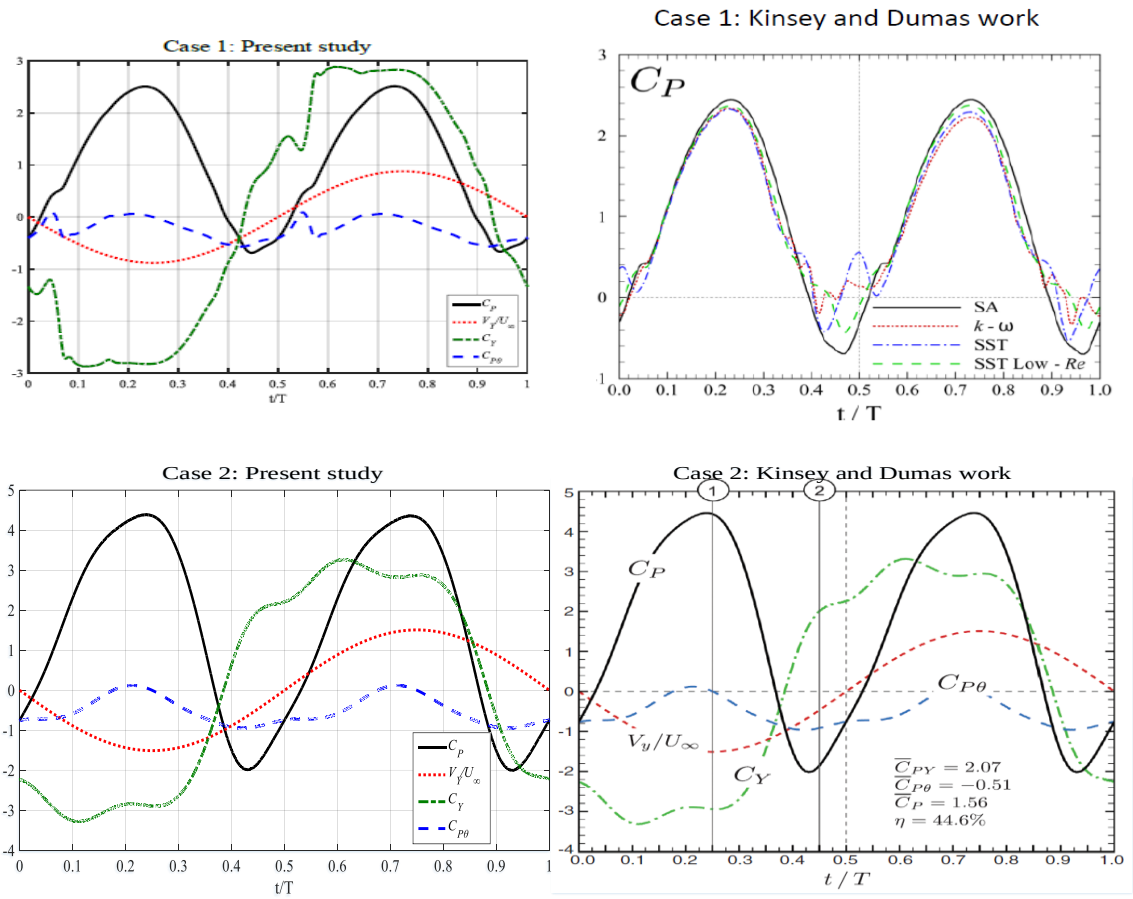

Figure 3. 9:Instantaneous vertical force C_Y, heaving velocity V_y, pitching contribution to power $C_{P\theta}$ and total power coefficient C_P over a periodic cycle of present study (left) and Kinsey and Dumas work (right) for Cases 1 and 2

Figures 3.7-3.8 show the vorticity contours, and Figure 3.9 shows the time evolution of the instantaneous vertical force C_Y, heaving velocity V_Y, pitching power, and the total power C_P. In comparison to the laminar cases, where the optimum results are characterised by the presence of dynamic stall and LEVs, the turbulent results show a different outcome, i.e. without LEVs, which are not necessary in this case to reach a high energy efficiency. This can be seen in Figure 3.8, where the vorticity contours show no LEVs but the efficiency is high (Table 3.5). This may be due to a good timing (synchronization) in the sign switch of V_Y and C_Y (exhibiting the same sign at times, Figure 3.9) with high instantaneous force coefficients (as opposed to Case 1, which have LEVs but having the instantaneous vertical force that is smaller than Case 2); which resulted in positive values of total extracted power.

In comparison to the previous work, it can be seen that from the above graphs that a good agreement is achieved in these two cases. Therefore, it can be concluded that the numerical methodology used in the present work is suitable for the current investigation.

3.8 Mesh Sensitivity Analysis

Mesh sensitivity analysis were carried out in multiple bodies analysis to ensure the numerical predictions are grid independent. Similar to Section 3.7, three grid resolution have been developed which are coarse, medium and fine. Due to the time constrain, the mesh sensitivity analysis has been conducted with two airfoils configuration only. The details of the number of cells generated are presented in Table 3.6.

Table 3. 6: Mesh sensitivity analysis for tandem case

Mesh Resolution	**Nodes on Each Airfoil Profile**	**Cells**
Coarse	350	222,196
Medium	700	261,836
Fine	1000	300,531

One of the simulation cases was selected to perform the grid independency study for the combined pitch and heave motions. The parameters used for this test case are: $Re = 5 \times 10^5, f^* = 0.14, \theta_0 = 76.3°, H_0 = c, \phi = 90°, \psi_{1-2} = 0, L_x = 2.5$

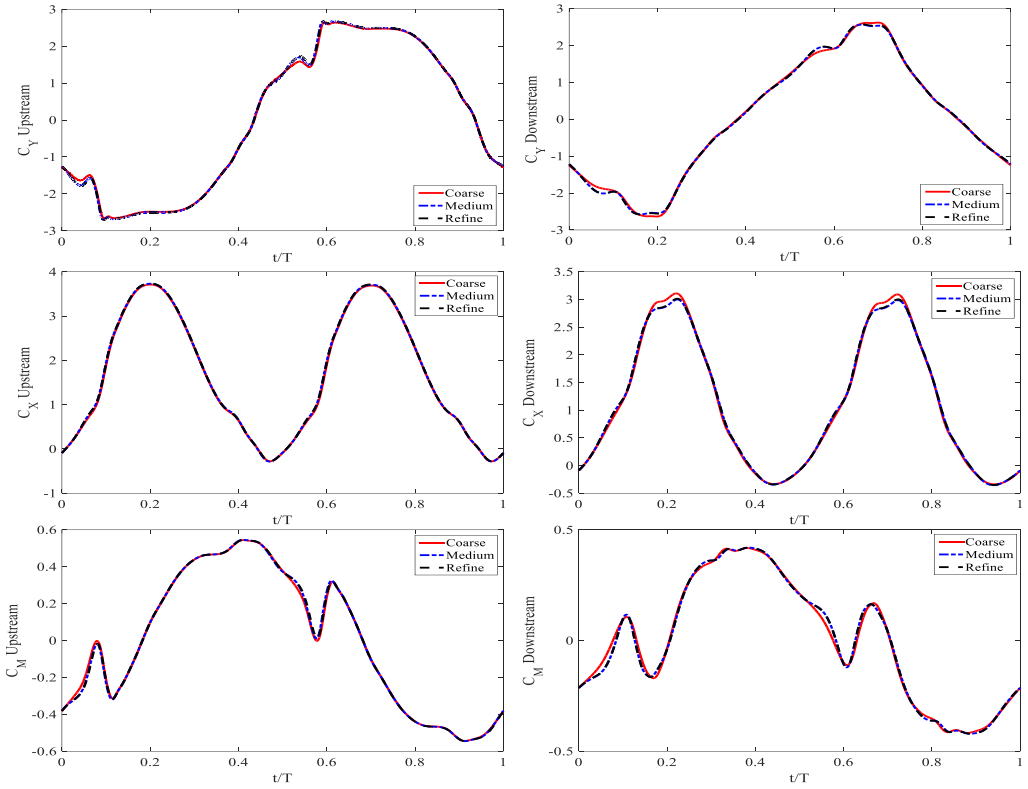

Figure 3. 10: Comparison between coarse, medium and fine mesh for upstream and downstream NACA0015 airfoil

Table 3. 7: Comparison results of grid independence study for tandem airfoil, NACA0015 (sharp edge), $Re = 5 \times 10^5, f^* = 0.14, \theta_0 = 76.3°, H_0 = c, \phi = 90°, \psi_{1-2} = 0, L_x = 2.5c$

Mesh	**Airfoil**	$\overline{C}_X$	$\widehat{C}_Y$	$\widehat{C}_M$	$\overline{C}_P$
Coarse	Upstream	1.655	2.647	0.548	0.8891
	Downstream	1.134	2.639	0.426	0.5634
	Total	2.789	/	/	1.4525
Medium	Upstream	1.671	2.676	0.550	0.8880
	Downstream	1.131	2.584	0.424	0.5612
	Total	2.802	/	/	1.4492
Fine	Upstream	1.672	2.678	0.550	0.8818
	Downstream	1.135	2.594	0.425	0.5673
	Total	2.807	/	/	1.4491

The grid independence results of the test case are presented in Figure 3.10 and Table 3.7. A difference of 0.6% and 0.2% on the total mean horizontal force ($\bar{C}_X$) are observed respectively when comparing the results of the coarse mesh and the medium mesh to the fine mesh. The total mean power extracted ($\bar{C}_P$) is essentially the same between the medium and refine meshes with a relative difference of less than 0.1%. Thus, the medium grid is appropriate to be used for the rest of the 2D tandem simulations.

Chapter 4: Effect of Geometrical Shape Modifications on Power Extraction of Single and Multiple Oscillating Bodies

This chapter explores the influence of trailing edge shape modifications, kinematics parameters, and on the power extraction efficiency performance of single and multiple oscillating bodies. For the single oscillating foil undergoing both heave and pitch motions, numerical simulations for different geometrical shape modifications and kinematics parameters have been conducted in the laminar and turbulent flow fields. For multiple oscillating bodies, simulations are focussed on different body interactions in the turbulent flow regime. The details of the simulations setup have been included in the sections below.

4.1 Single Airfoil Analysis

In this section, a single airfoil undergoing sinusoidal heave and pitch motion is considered. A selective range of parameters has been investigated (simplify in Table 4.1 & 4.2), including the airfoil geometrical parameters: thickness distribution (NACA0012, NACA0015 and NACA0018) and trailing edge shapes modification (sharp, blunt and round); the fundamental kinematics parameters: oscillating frequency ($f^* = 0.12 - 0.20$), pitching amplitude ($\theta_0 = 60°, 76.3°, 80°$ and $85°$) at fixed heaving amplitude, and the fluid physics parameters: laminar flow field (*Re* =1100) and turbulent flow field ($Re = 5 \times 10^5$). For the turbulent flow field, the highly resolved numerical simulations ($y^+ \leq 1$) are performed at high pitch angle using $k - \omega$ SST model, which is found to be well suited for separating flow and strong adverse pressure gradients (Versteeg and Malalasekera, 2007), and is of particular importance in a flatback or round airfoil wake. The power extraction efficiency has been used as the performance comparison metric to map the efficiency into the parametric space considered in this study.

Table 4. 1: Various parameters investigated in this study

Airfoil geometrical	Fundamental kinematics	Fluid physics
• Thickness distribution: NACA0012, NACA0015, NACA0018	• Oscillating frequency, f^*: $f^* = 0.12, 0.14, 0.16, 0.18, 2.0$	• Reynolds number, Re: $Re = 1100, Re = 5 \times 10^5$
• Trailing edge (TE): sharp, blunt and round	• Pitching amplitude, θ_0: $\theta_0 = 60^\circ, 76.3^\circ, 80^\circ, 85^\circ$	

Table 4. 2 : Parametric study of flow over the oscillating airfoil

	Thickness Distribution	Pitching amplitude, θ_0
$H_0 = c, f^* = 0.14$, Sharp TE $Re = 1100$ $Re = 5 \times 10^5$	NACA0012 NACA0015 NACA0018	60°, 76.3°, 80°, 85°
$H_0 = c, f^* = 0.18$, Sharp TE $Re = 1100$ $Re = 5 \times 10^5$	NACA0012 NACA0015 NACA0018	60°, 76.3°, 80°, 85°
	Trailing edge shape	Pitching amplitude, θ_0
$H_0 = c, f^* = 0.14$, NACA0018 $Re = 1100$ $Re = 5 \times 10^5$	Sharp Blunt Round	60°, 76.3°, 80°, 85°
$H_0 = c, f^* = 0.18$, NACA0018 $Re = 1100$ $Re = 5 \times 10^5$	Sharp Blunt Round	60°, 76.3°, 80°, 85°
	Fluid Physical	Oscillating frequency, f^*
$H_0 = c, \theta_0 = 76.3^\circ$ NACA0018, Blunt TE	$Re = 1100$ $Re = 5 \times 10^5$	0.12, 0.14, 0.16, 0.18, 0.20

4.1.1 Numerical Method

4.1.1.1 Computational Modelling

The airfoil investigated in this study was set to oscillate in the vertical translation reference frame. The reference frame associated with the domain was custom to follow the heaving motion described by $h(t)$ in Eqn (2.2). Based on the recommendations of the preliminary test cases, a sufficiently large computational domain with reference to the oscillating airfoil chord length 'c' is implemented in all of the simulations cases to avoid reverse flow. The upstream inlet velocity boundary and the downstream pressure outlet were located at 35c and 40c from the pitching point, respectively. The upper and lower flow boundaries were placed at 35c from the pitching point. The details of the simulation domain size is shown in Figure 4.1 (a) and the domain was then split into two zones bounded by a circular non-conformal sliding interface (the details of the sliding mesh theory is given in the previous chapter) which is located at 2c from the pitching point as shown in Figure 4.1 (b). This imply the mesh motion is necessary only for rotating (pitching) motion of the airfoil. The rotating and translating motions applied in this study were implemented via user-defined function (UDF) compiled within the solver (see, Appendix A).

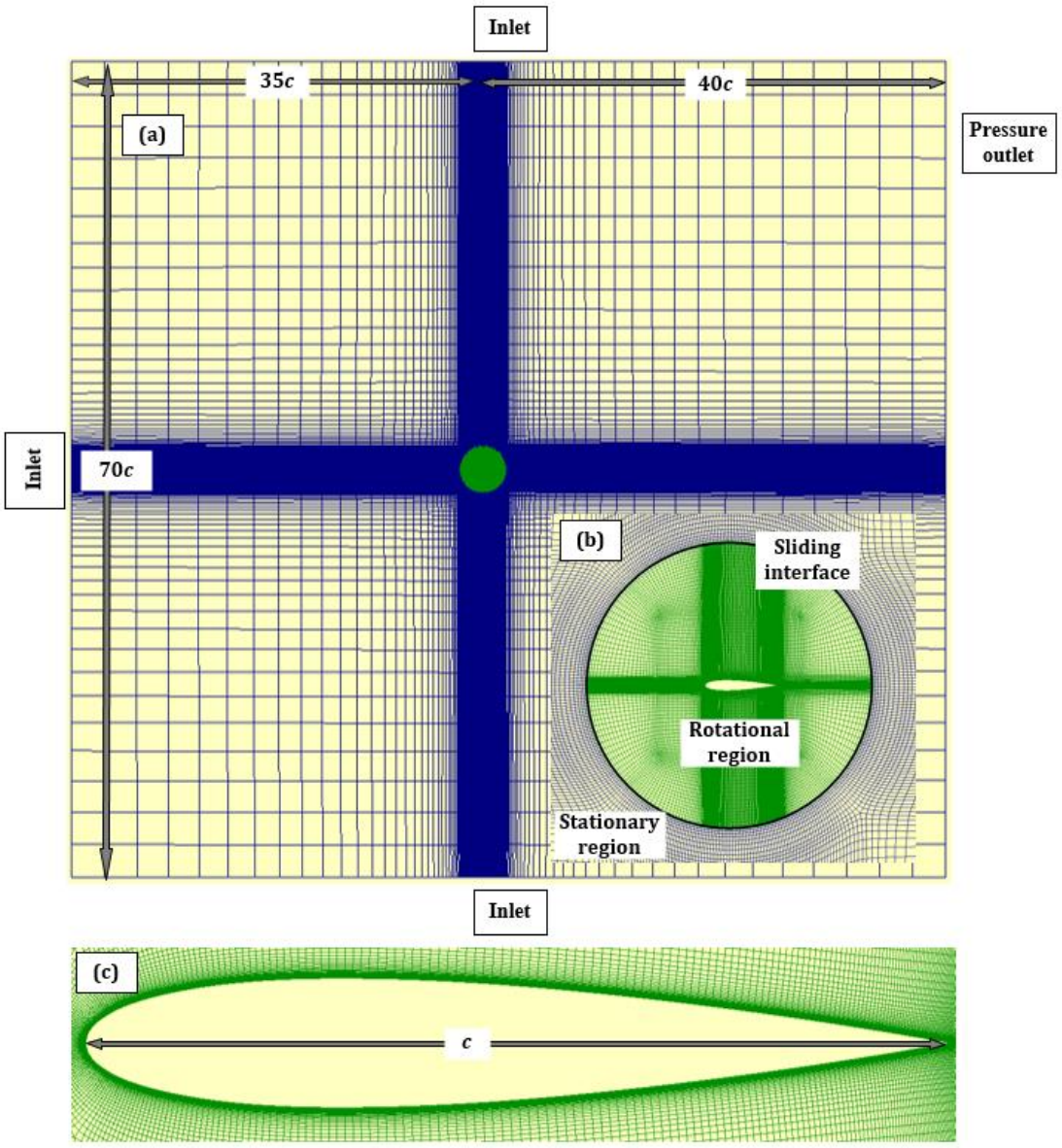

Figure 4. 1: (a) Simulation domain (b) close-up of the sliding interface and rotational region (c) close-up view near the airfoil

4.1.2 Effect of Geometrical Shape modifications on Energy Harvesting Performance Efficiency

To assess how the geometry of the airfoil influences the energy extraction efficiency of the system, investigations were carried out on the oscillating airfoils having different thicknesses distribution of 12%, 15% and 18% (i.e., NACA0012, NACA0015 and NACA0018) and different trailing edge shapes (sharp, blunt and round). The required geometrical modifications of the trailing edge shapes have been carried out in the SolidWorks environment and then exported the IGES file format into pointwise meshing tool.

The results for each geometry modifications were compiled distinctly for laminar ($Re = 1100$) and turbulent flow ($Re = 5 \times 10^5$) at reduced frequencies $f^* =$

0.14 and 0.18. These values of reduced frequencies were chosen based on the previous validation studies, which show that the maximum energy efficiency occurs when the non-dimensionalised frequency is in the range of 0.14 – 0.18. Other fluid kinematics parameters such as pitching amplitude ($\theta_0 = 60°, 76.3°, 80°$ and $85°$) and heaving amplitude, $H_0 = c$ are held constant for the simulated cases to explicitly identify the effect of geometrical parameters in different flow regimes.

4.1.2.1 Oscillating Airfoils Response to Variation of Thickness Distribution at Different Kinematics Parameters

The effect of thickness variation on three symmetrical oscillating airfoils: NACA0012, NACA0015 and NACA0018 (Figure 4.2) for energy extraction were investigated in laminar and turbulent flow regimes.

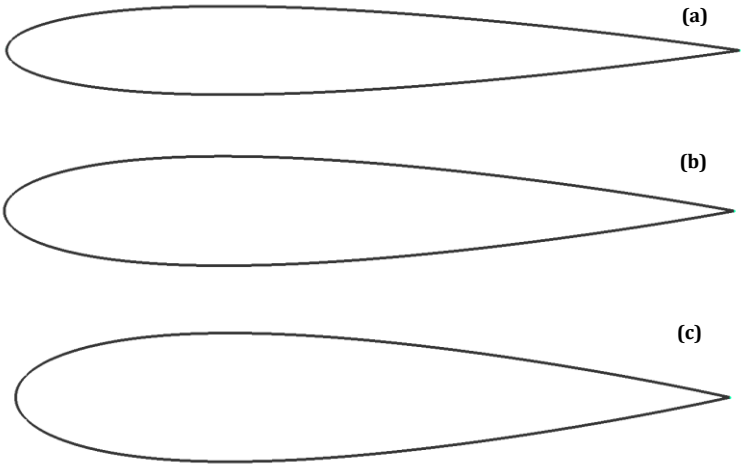

Figure 4. 2: Three different airfoils (a) NACA0012 (b) NACA0015 (c) NACA0018

Figures 4.3 and 4.4 show the result of the effect of varying the thickness distribution on the energy harvesting efficiency at different pitching amplitude and two reduced frequencies ($f^* = 0.14$ and $f^* = 0.18$) in laminar flow field.

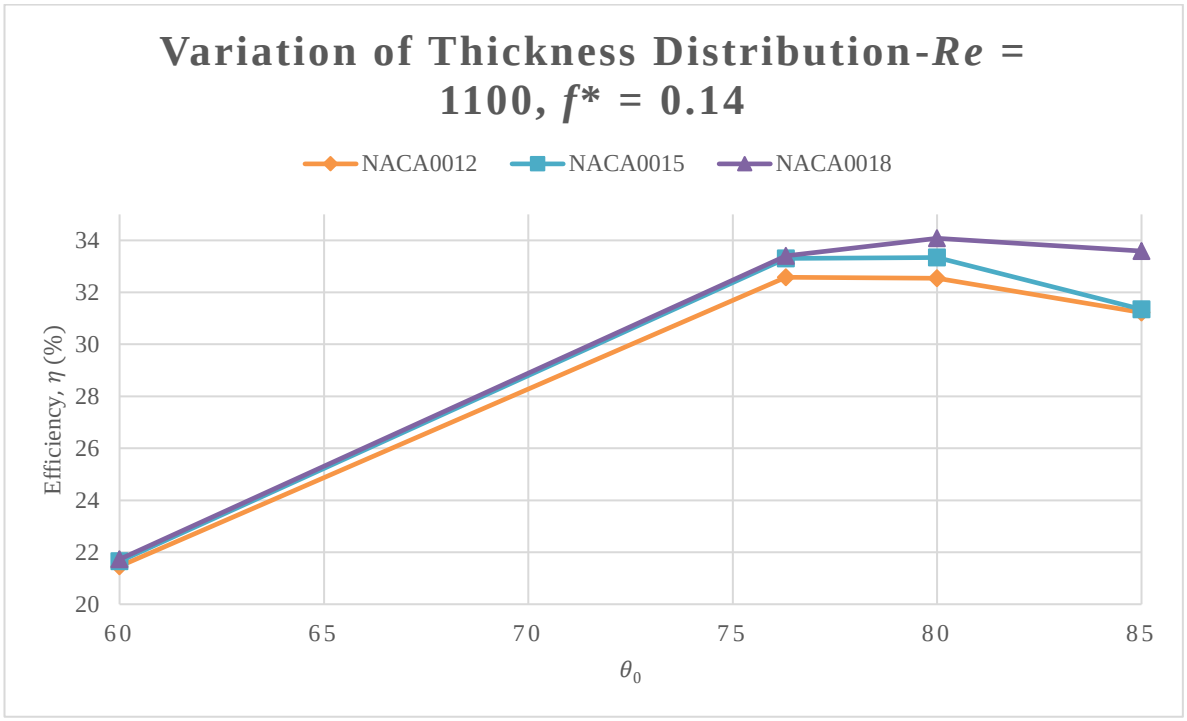

Figure 4. 3: Comparison between NACA0012, NACA0015 and NACA0018 on power extraction efficiency in laminar flow field at $f^* = 0.14, H_0 = c, x_p = {}^{c}/_{3}$

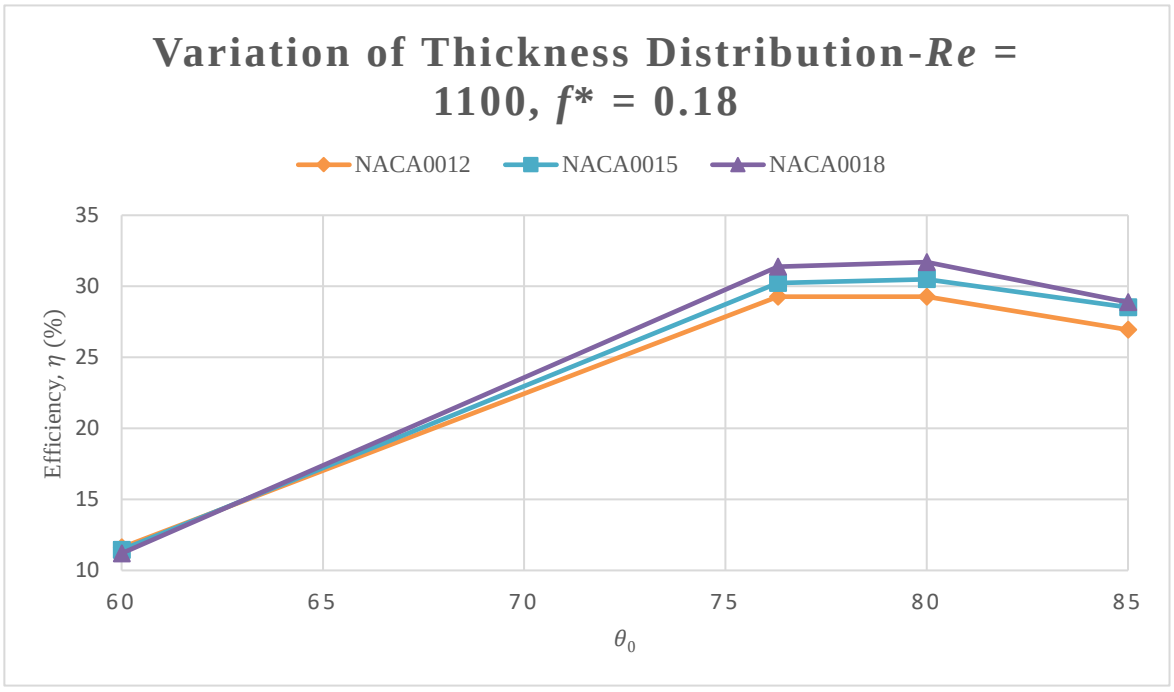

Figure 4. 4: Comparison between NACA0012, NACA0015 and NACA0018 on power extraction efficiency in laminar flow field at $f^* = 0.18, H_0 = c, x_p = {}^{c}/_{3}$

From these figures, it can be seen that for the tested frequencies ($f^* = 0.14$ and $f^* = 0.18$), as thickness increases efficiency increases, that is, NACA0018 shows higher efficiency values as compared to NACA0015 and likewise NACA0015 as compared to

NACA0012 (prominently at reduced frequency $f^* = 0.18$). Moreover, it can be seen that the peak energy harvesting efficiency occurs at pitching amplitude $\theta_0 = 80$ with 34.08% efficiency (for $f^* = 0.14$) and 31.70% efficiency (for $f^* = 0.18$), and then the efficiency starts to decrease for all the NACA profiles tested. Also, it is found that the highest percentage difference of power efficiency performance between NACA0012 and NACA0018 occurs at $\theta_0 = 80°$ and $85°$ for the frequency, $f^* = 0.14$ and 0.18, and hence showing an overall variation of around 7.7% and 7%, respectively.

Another important observation which can be drawn from Figures 4.3 and 4.4 is that the impact on the efficiency performance for different thickness distribution at low pitching amplitude was rather weak as compared to high pitching amplitude where a more significant change in the efficiency is noticed. The reason for this transition in behaviour is because of, as the pitching amplitude increases, the vortex separation on the leading edge becomes more significant (see, Figures 4.5-4.8) and therefore the effect of varying the thickness of an airfoil is different for different pitching amplitudes. In addition to that, the plot of instantaneous vertical force C_Y in Figure 4.9 emphasise that as the pitching amplitude increase, ($\theta_0 = 60^{\circ}$ and $\theta_0 = 85^{\circ}$) the difference between V_Y and C_Y of NACA0012 and NACA0018 are more obvious in both reduced frequencies tested ($f^* = 0.14$ and $f^* = 0.18$).

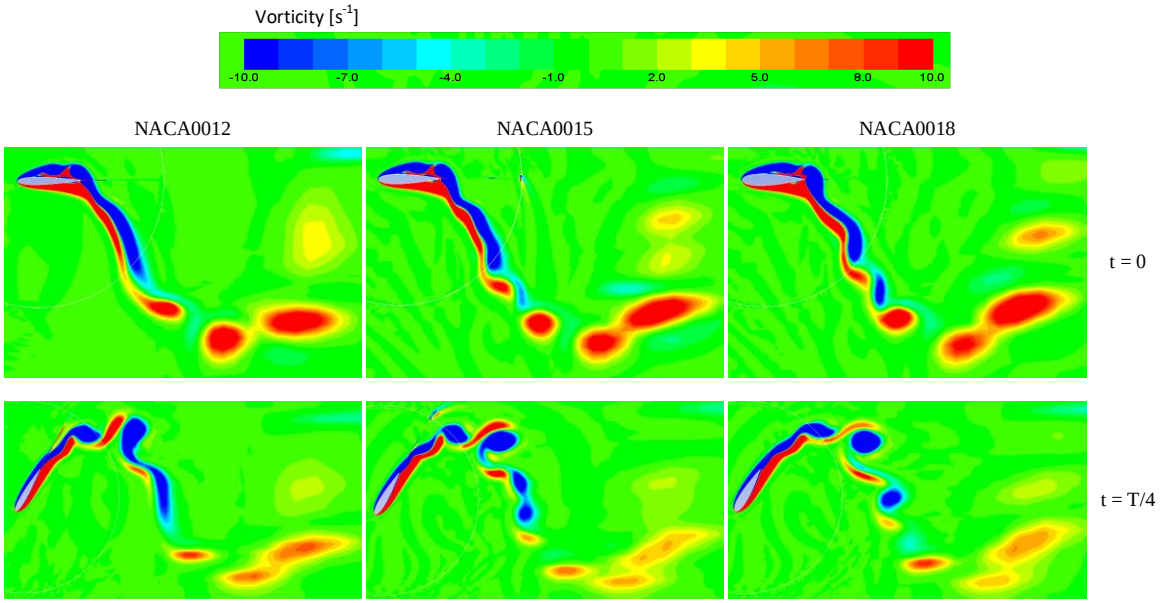

Figure 4. 5: Vorticity plot (red: counter-clockwise vorticity, blue: clockwise vorticity) in laminar flow field for NACA0012, NACA0015 and NACA0018, $f^* = 0.14, \theta_0 = 60°$ at t = 0 and 0.25T

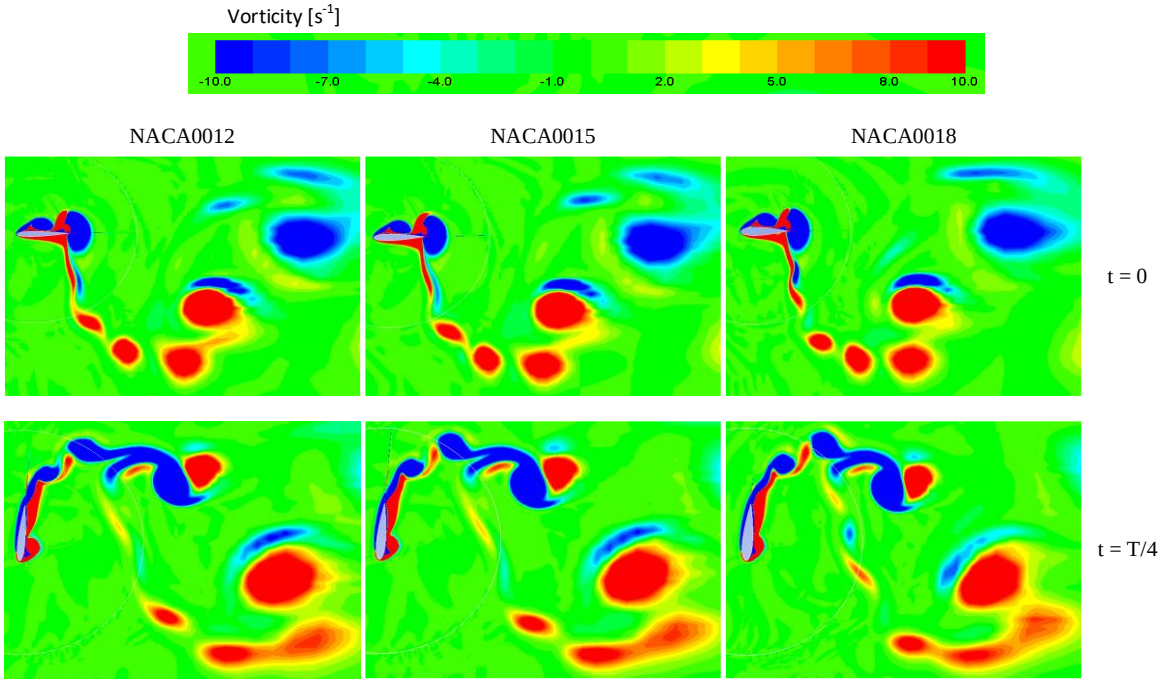

Figure 4. 6: Vorticity plot (red: counter-clockwise vorticity, blue: clockwise vorticity) in laminar flow field for NACA0012, NACA0015 and NACA0018, $f^* = 0.14, \theta_0 = 85°$ at t = 0 and 0.25T

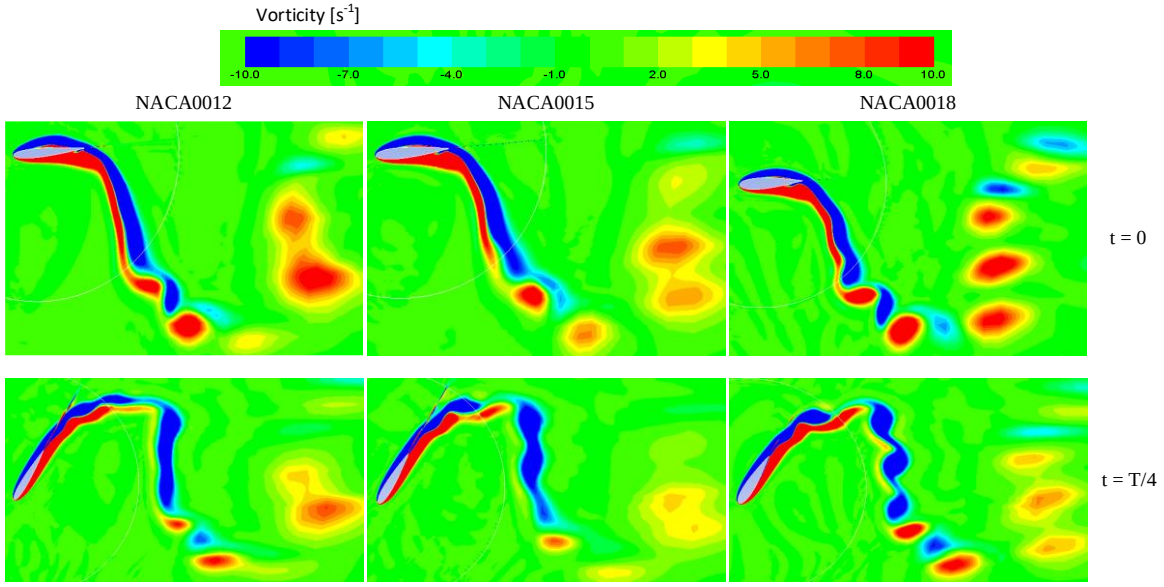

Figure 4. 7: Vorticity plot (red: counter-clockwise vorticity, blue: clockwise vorticity) in laminar flow field for NACA0012, NACA0015 and NACA0018, $f^* = 0.18, \theta_0 = 60°$ at t = 0 and 0.25T

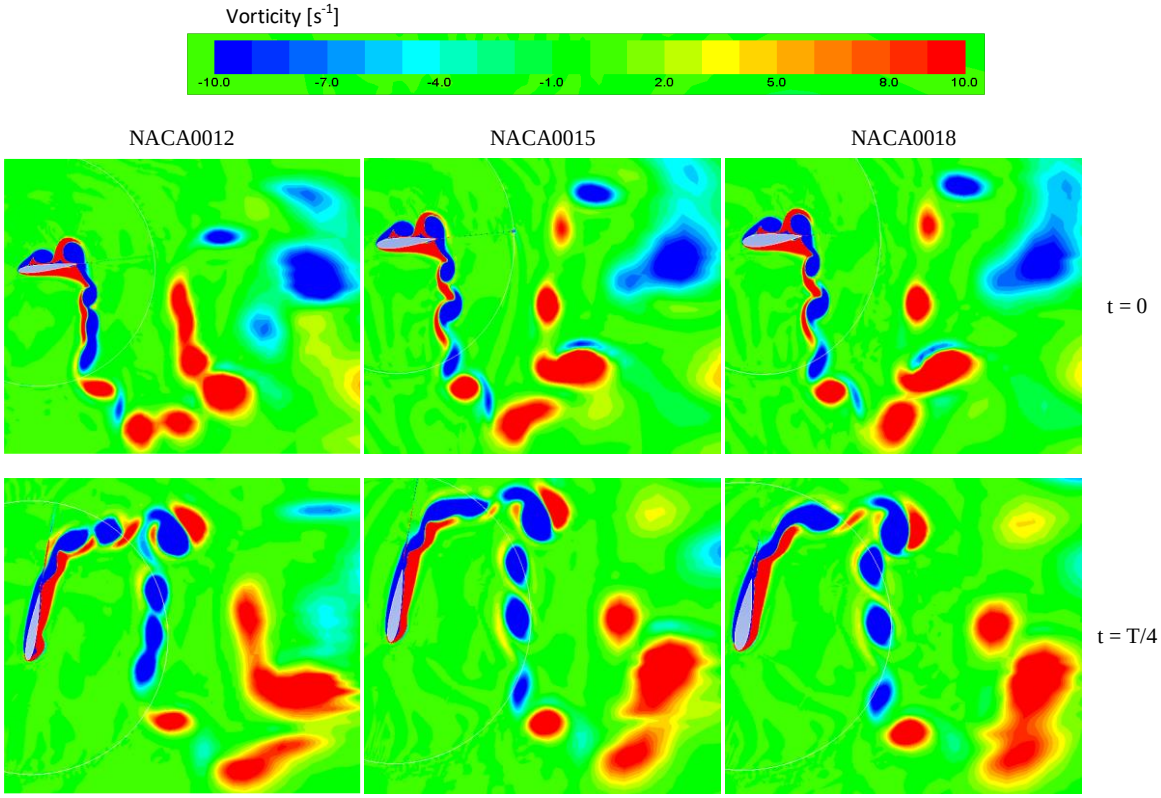

Figure 4. 8: Vorticity plot (red: counter-clockwise vorticity, blue: clockwise vorticity) in laminar flow field for NACA0012, NACA0015 and NACA0018, $f^* = 0.18, \theta_0 = 85°$ at t = 0 and 0.25T

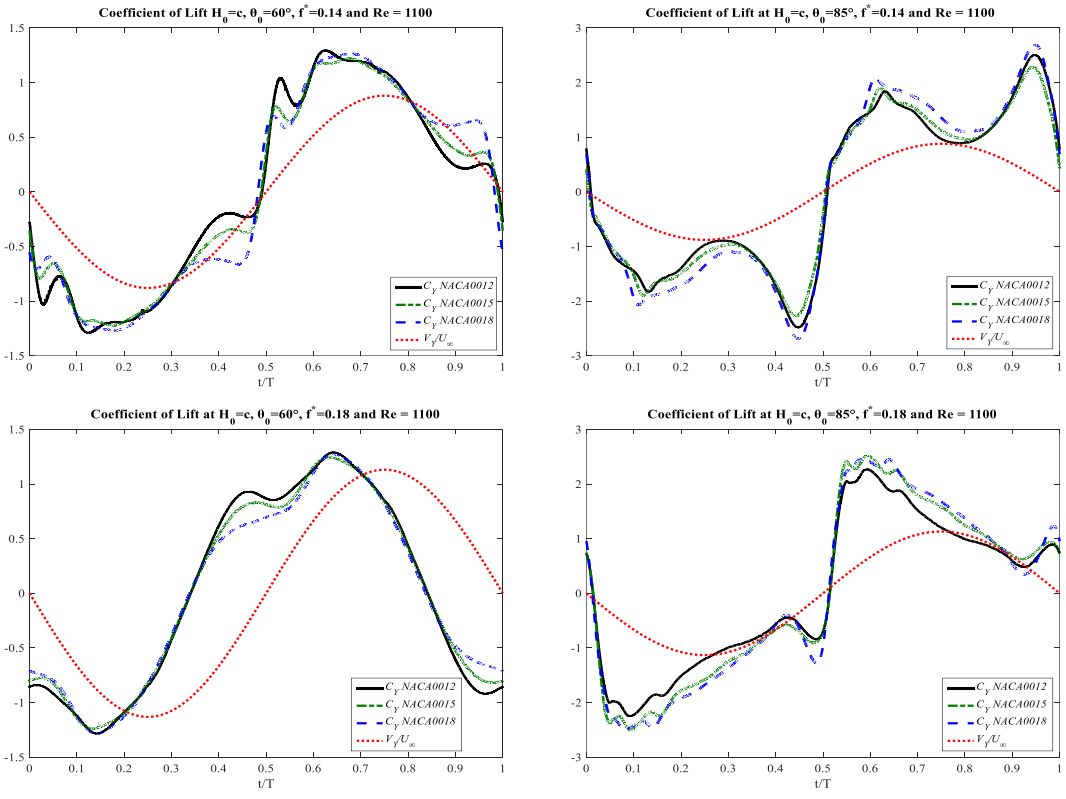

Figure 4. 9: Comparison of synchronization between heaving velocity V_Y and vertical force C_Y of NACA0012, NACA0015 and NACA0018 in laminar flow

The investigation on the variation of thickness distribution is then extended to the turbulence flow field. All of the parameters were kept the same except for the Reynolds number. Figures 4.10 and 4.11 show the results for the reduced frequency $f^* = 0.14$ and $f^* = 0.18$, respectively.

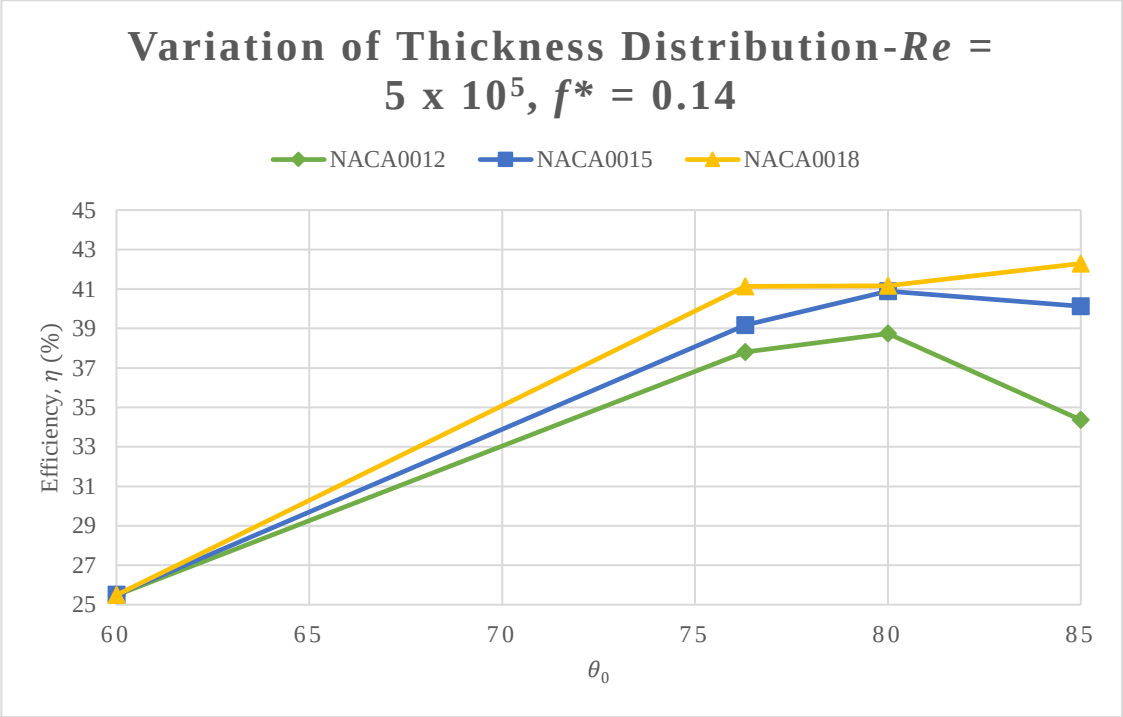

Figure 4. 10: Comparison between NACA0012, NACA0015 and NACA0018 on power extraction efficiency in turbulent flow field at $f^* = 0.14, H_0 = c, x_p = {}^{c}/_{3}$

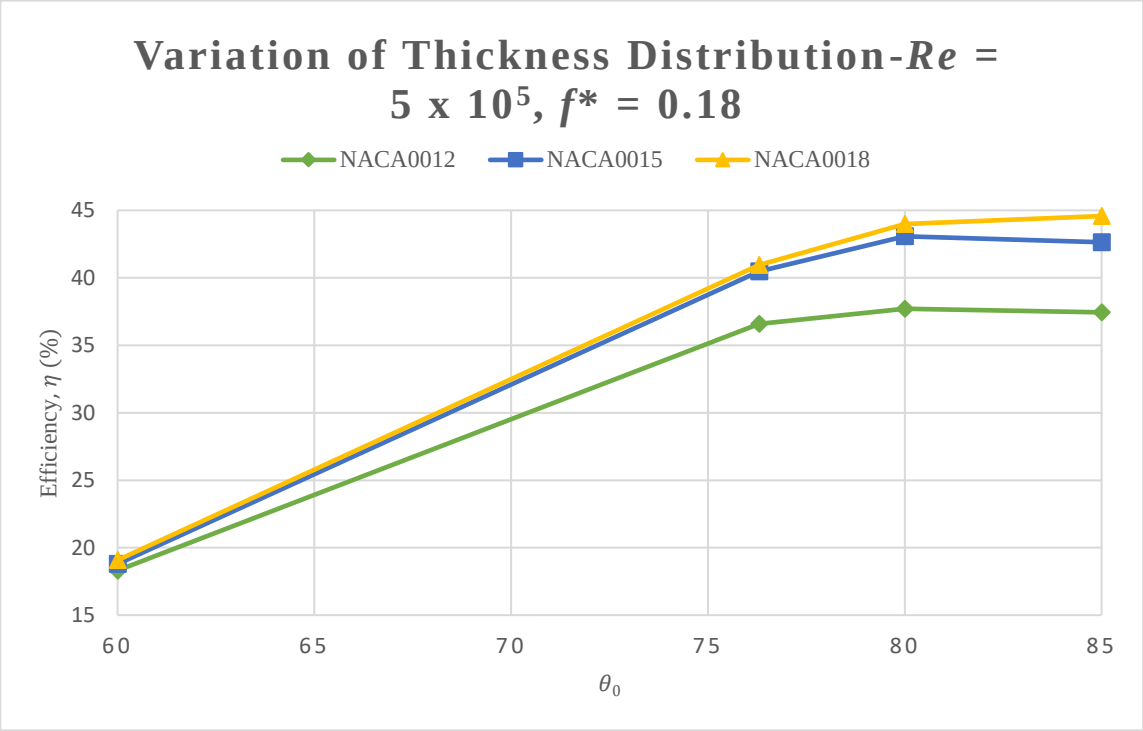

Figure 4. 11: Comparison between NACA0012, NACA0015 and NACA0018 on power extraction efficiency in turbulent flow field at $f^* = 0.18, H_0 = c, x_p = {}^{c}/_{3}$

Overall, the data presented in Figures 4.5 and 4.6 indicates a similar trend as for laminar flow field, in which the thicker airfoil l is performing better than thinner airfoils and the efficiency start to drop after the pitching amplitude reaches $\theta = 80°$ except for NACA0018. The efficiency for NACA0018 is continuously increasing for both reduced frequencies tested.

The effect of variation thickness distribution in turbulent flow is more visible than in the laminar case, in which the highest difference in efficiency is about 19% which occurs between NACA0012 and NACA0018 airfoils at reduced frequency $f^* = 0.14$ and pitching amplitude $\theta_0 = 85°$. However, for NACA0015 and NACA0018 airfoils, the difference in efficiency is not very significant as the efficiency variation between these two airfoils is less than 5%. To gain some insight into the flow behaviour as the thickness distribution varies, the contours of vorticity are displayed in Figures 4.12 - 4.15 at t = 0 and 0.25T (peak pitching amplitude) for the three airfoils and the plot of the instantaneous vertical force C_Y is shown in Figure 4.16.

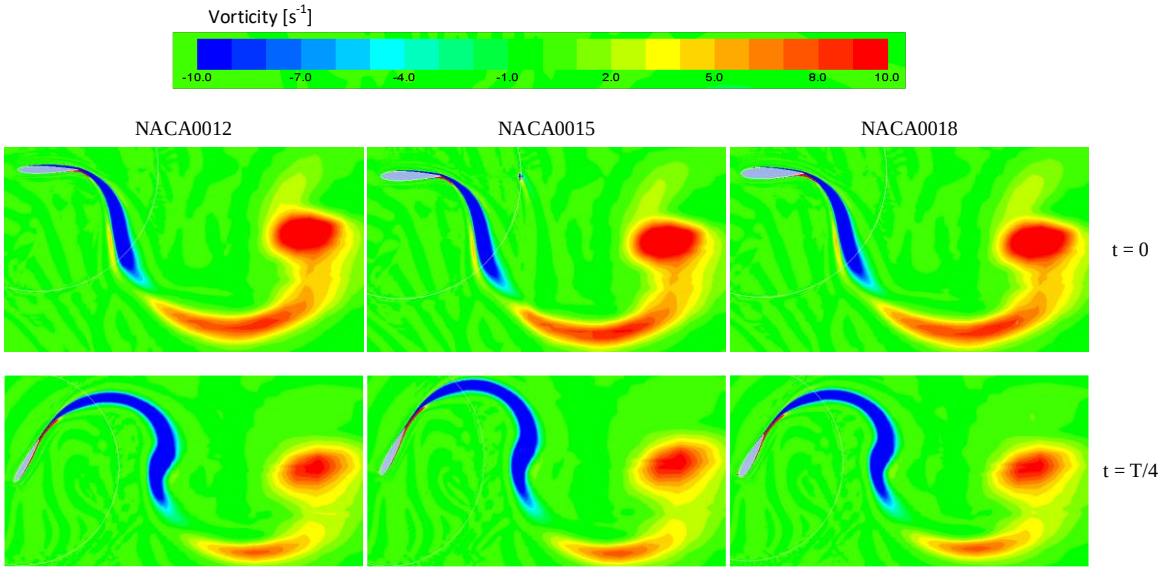

Figure 4. 12: Vorticity plot (red: counter-clockwise vorticity, blue: clockwise vorticity) in turbulent flow field for NACA0012, NACA0015 and NACA0018 $f^* = 0.14, \theta_0 = 60°$ at t = 0 and 0.25T

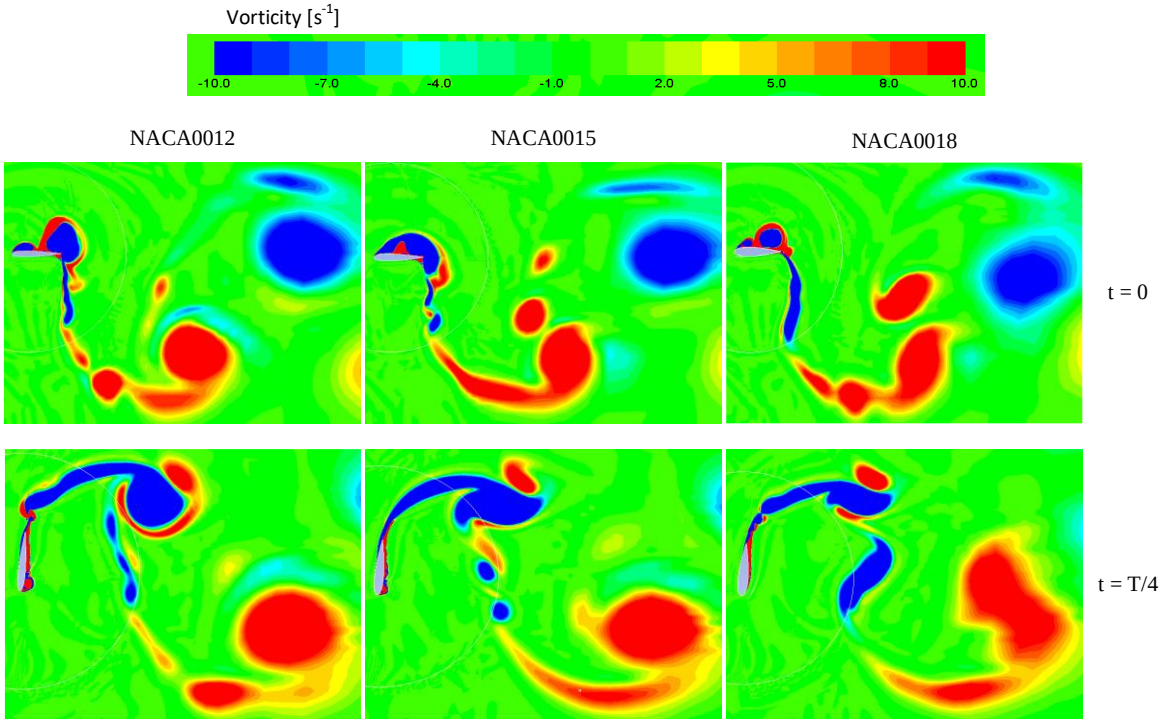

Figure 4. 13: Vorticity plot (red: counter-clockwise vorticity, blue: clockwise vorticity) in turbulent flow field for NACA0012, NACA0015 and NACA0018 $f^* = 0.14, \theta_0 = 85°$ at t = 0 and 0.25T

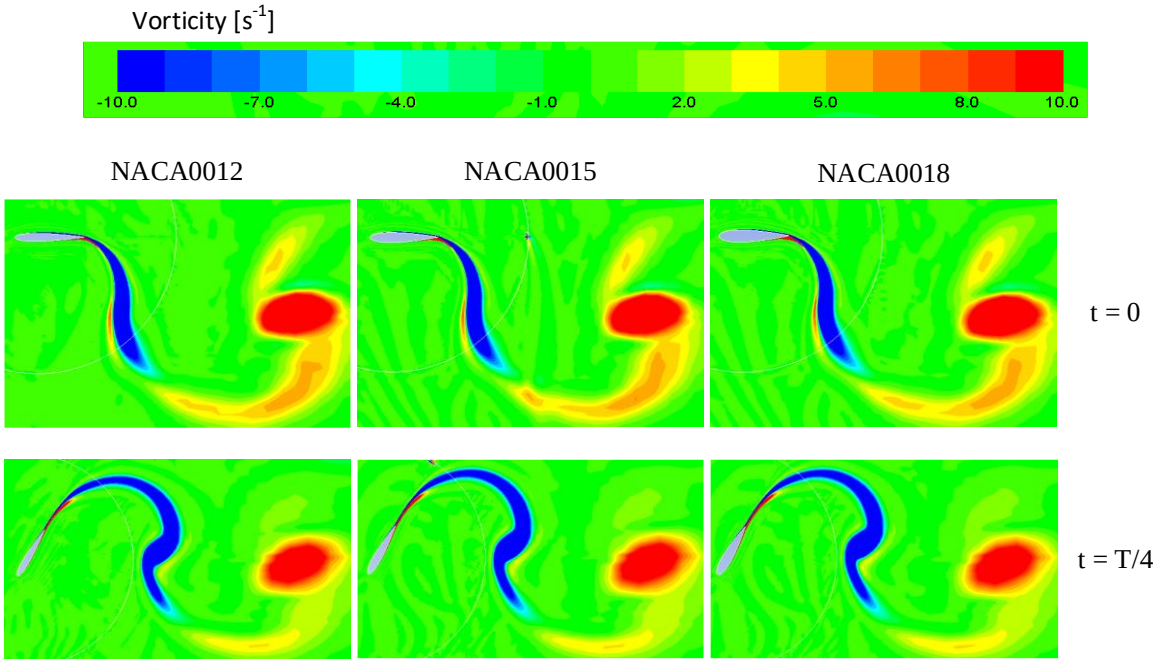

Figure 4. 14: Vorticity plot (red: counter-clockwise vorticity, blue: clockwise vorticity) in turbulent flow field for NACA0012, NACA0015 and NACA0018 $f^* = 0.18, \theta_0 = 60°$ at t = 0 and 0.25T

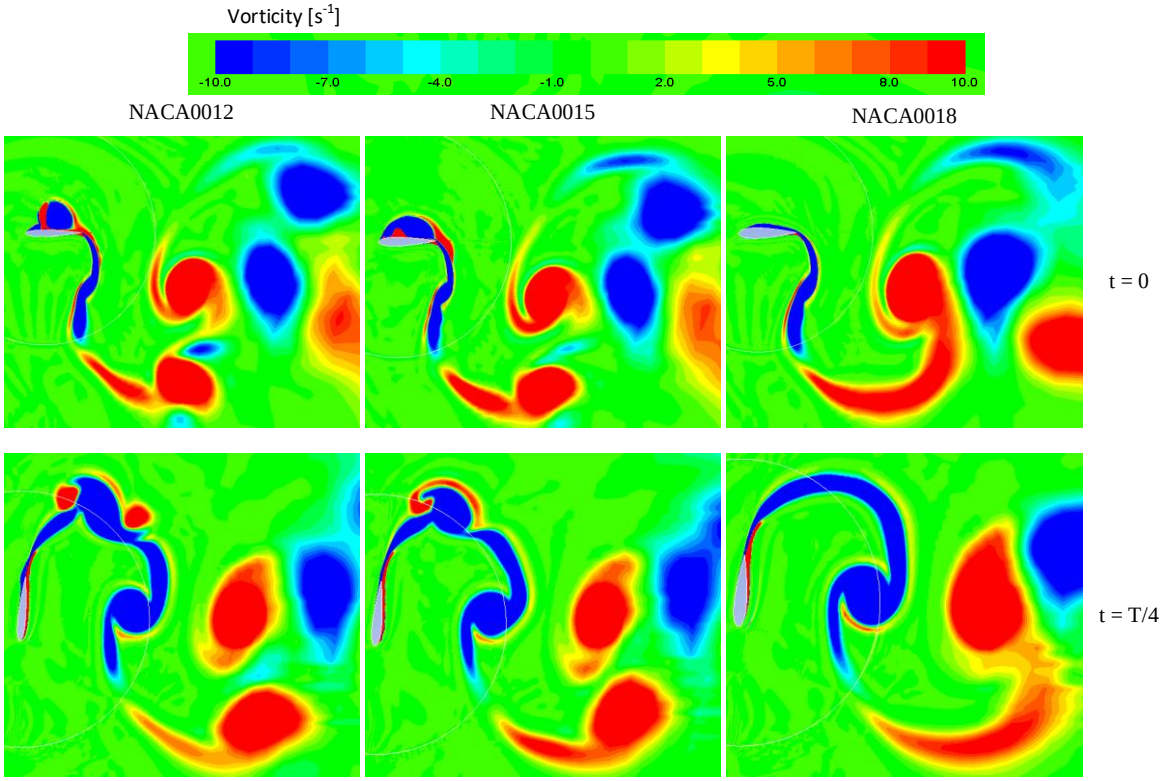

Figure 4. 15: Vorticity plot (red: counter-clockwise vorticity, blue: clockwise vorticity) in turbulent flow field for NACA0012, NACA0015 and NACA0018, $f^* = 0.18, \theta_0 = 85°$ at t = 0 and 0.25T

At low pitching amplitude, Figures 4.12 and 4.14 show smooth aerodynamics flow with low efficiency (Figures 4.10 and 4.11). However, an obvious change in the formation of leading edge vortices (LEV) and wake vortices are observed at higher pitching amplitude (Figures 4.13 and 4.15), which are closely associated with the energy extraction efficiency of the oscillating foil (Figures 4.10 and 4.11 for high pitch amplitudes). For the flow fields of NACA0012, NACA0015 and NACA0018 they show the same trends overall, i.e., without LEVs (Figures 4.12 and 4.14) for low pitching amplitudes and dynamic stall vortex shedding for higher pitching amplitudes (Figures 4.13 and 4.15). Moreover, Figure 4.16 (left hand side plots) show a poor synchronization between V_Y and C_Y (i.e., exhibiting opposite signs at times) which is causing the total power curve to go negative in some parts. On the other hand, Figure 4.16 (right-hand side plots) exhibit dynamic stall, and show good timing in the sign switch of V_Y and C_Y, resulting in positive values of total extracted power over almost all of the cycle. Moreover, it can be seen from the right-hand side plots (Figure 4.16) that the lift coefficient C_Y of NACA0018 is higher than the lift coefficients of NACA0012 and NACA0015, and as such the extracted power of NACA0018 is higher than those of NACA0012 and NACA0015 (see, Figures 4.10 and 4.11) for high pitching amplitudes.

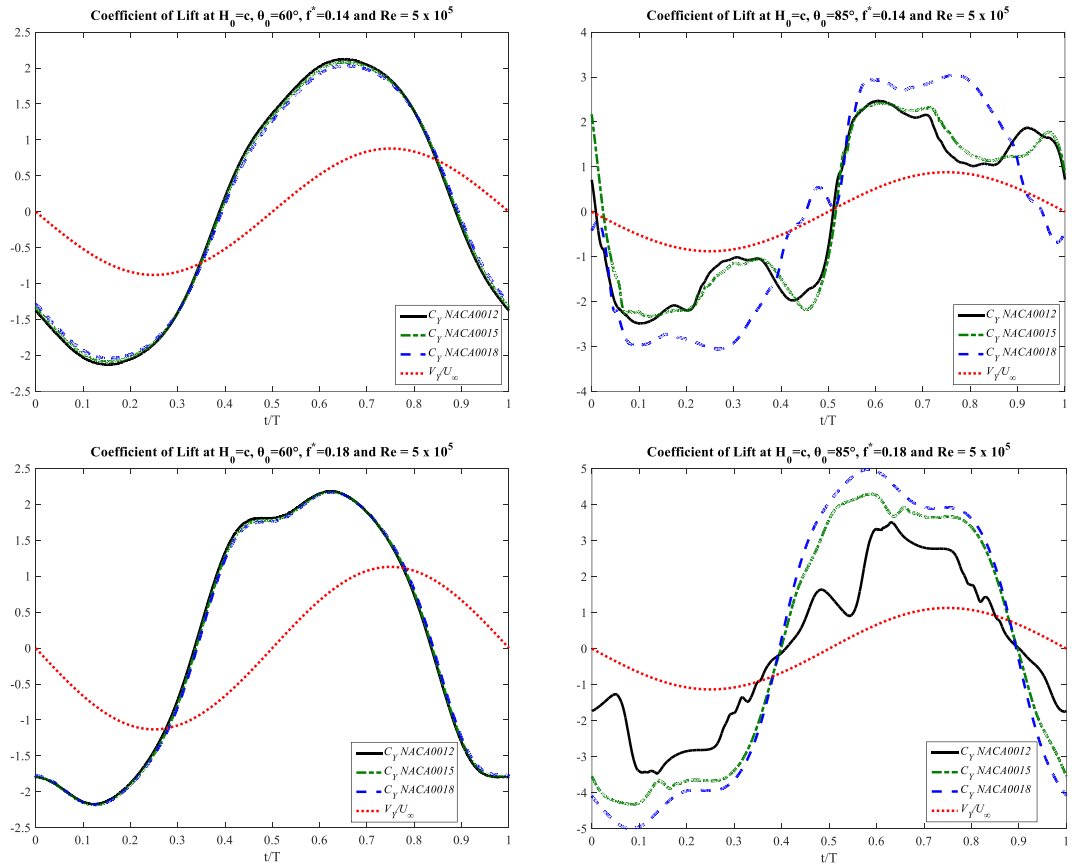

Figure 4. 16: Comparison of synchronization between heaving velocity V_Y and vertical force C_Y of NACA0012, NACA0015 and NACA0018 in turbulent flow

From all the simulations that have been carried out in this section, it can be concluded that, thickness distribution does have a positive impact on the power performance with the thicker airfoil. However, the difference between NACA0015 and NACA0018 is less in comparison to the difference between NACA0012 and NACA0018.

4.1.2.2 Oscillating Airfoils Response to Variation of Trailing Edge Shapes at Different Kinematics Parameters

In order to increase the yield of oscillating energy harvesting system, optimum geometrical combination of thickness distribution and trailing edge shapes are searched. Therefore in this section, following the conclusion from the above section (Section 4.1.2.1) that thicker airfoil has a more positive impact on the power performance, here NACA0018 was chosen for further investigation over the design space range of pitching amplitude and trailing edge configuration. Figure 4.17 shows the modified trailing edge shapes (sharp, blunt, and rounded) for NACA0018. The trailing edge modification of 3% from the airfoil length were implemented with the corresponding thickness of 0.0438m.

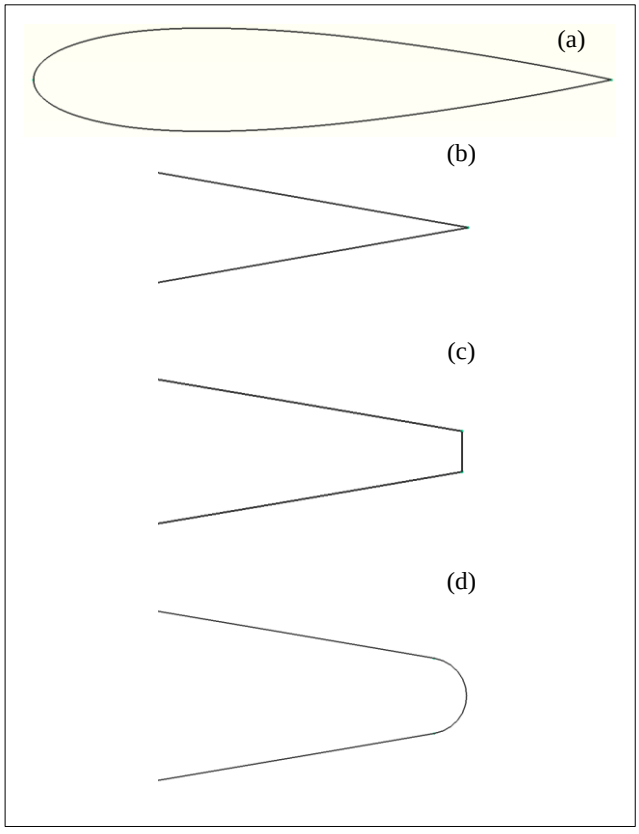

Figure 4. 17: (a) NACA0018 with different trailing edge shapes (b) close-up view of sharp edge (c) close-up view of blunt edge (d) close-up view of round edge

The energy harvesting efficiency, η for all the tested trailing edge shapes at low Reynolds numbers are presented in Figures 4.18 and 4.19.

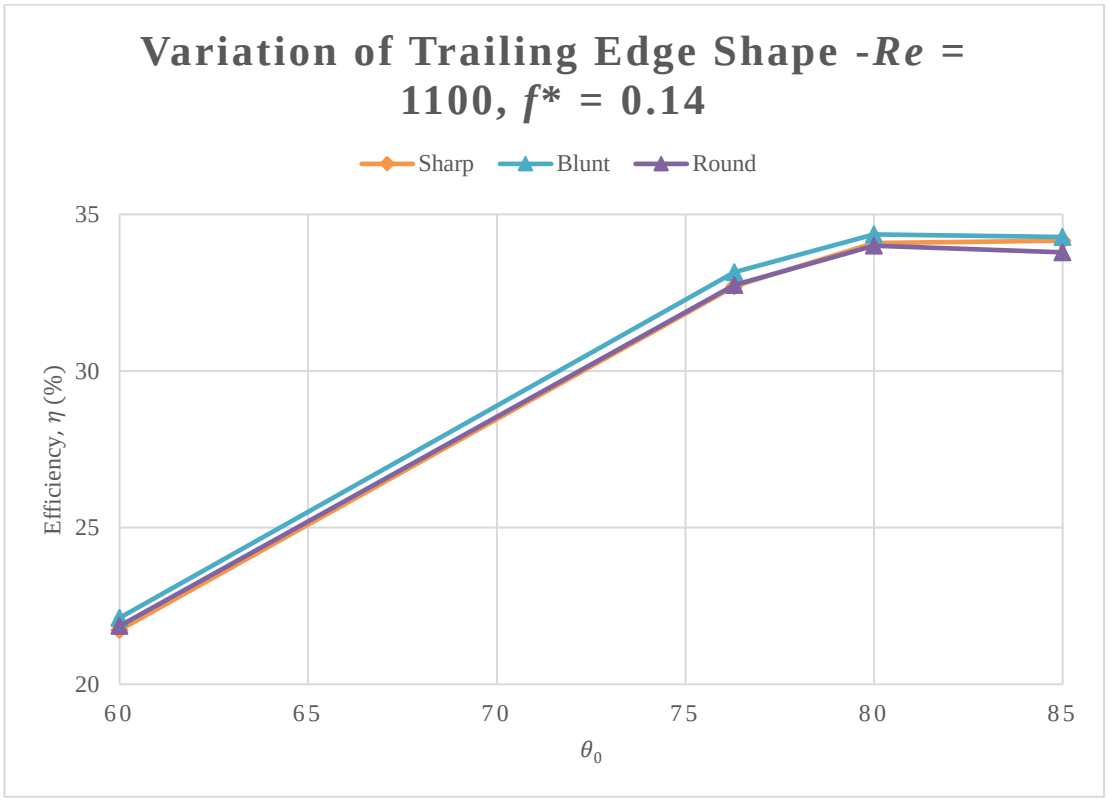

Figure 4. 18: Comparison between sharp, blunt and round trailing edge shape of NACA0018 on power extraction efficiency in laminar flow field at $f^* = 0.14, H_0 = c, x_p = {}^{c}/_{3}$

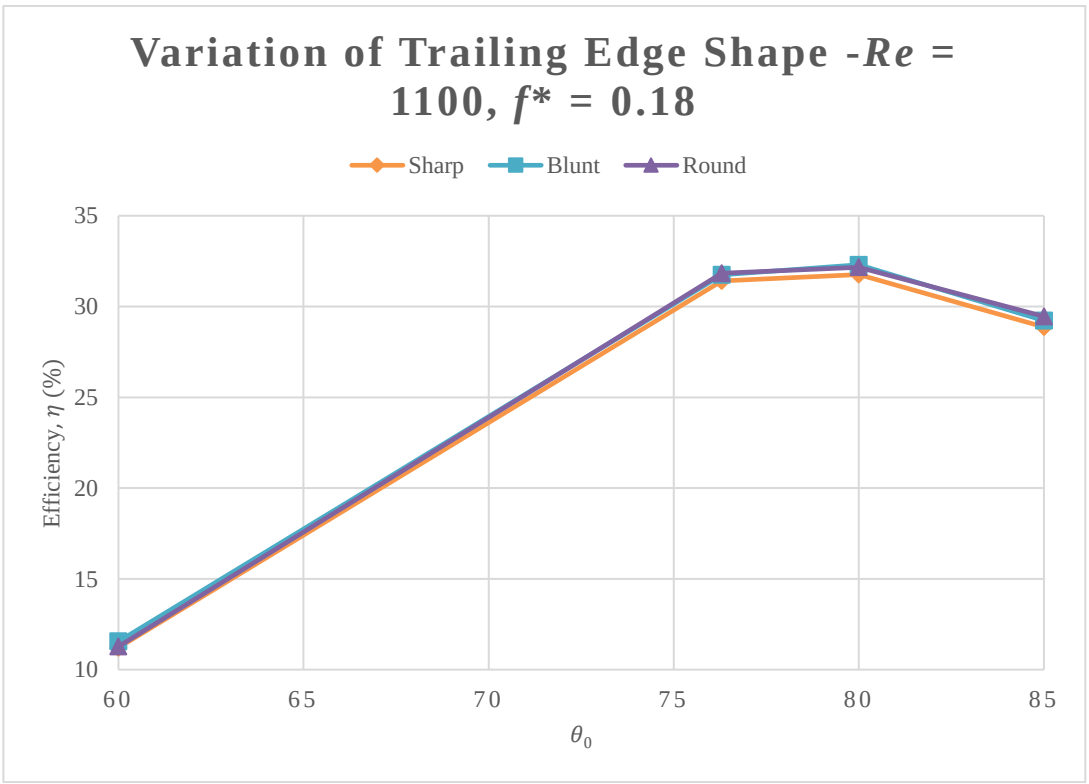

Figure 4. 19: Comparison between sharp, blunt and round trailing edge shape of NACA0018 on power extraction efficiency in laminar flow field at $f^* = 0.18, H_0 = c, x_p = {}^{c}/_{3}$

The results show that the sharp, blunt and round trailing edge shapes have similar efficiency performance overall over the range of the pitching amplitude for both reduced frequencies tested. The highest difference is only about 3% which occurs at reduce frequency $f^* = 0.14$ and pitching amplitude $\theta_0 = 76.3°$ with the blunt edge leading, followed by the sharp and rounded edges. These outcomes may be due to the laminar flow characteristic where the fluid flow is in the parallel layers with no disruption between the layers. Next, the simulations are run in turbulent flow regimes, and the results are shown in Figures 4.20- 4.21.

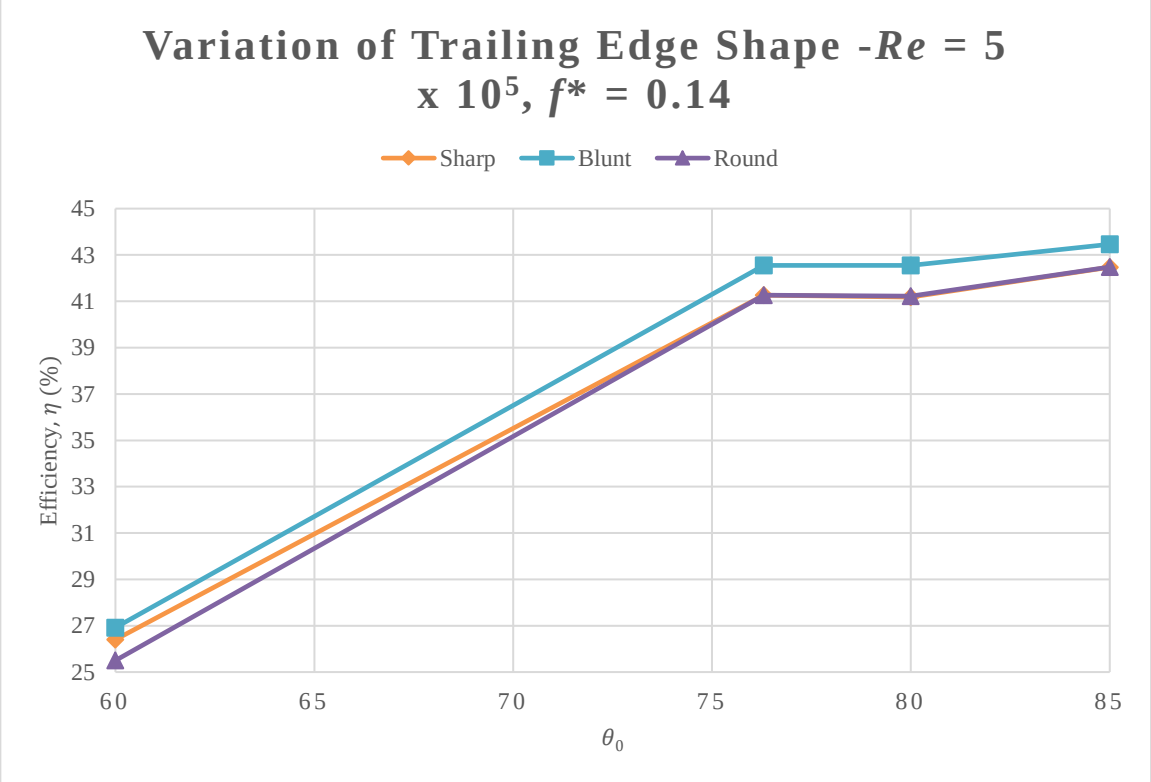

Figure 4. 20: Comparison between sharp, blunt and round trailing edge shape of NACA0018 on power extraction efficiency in turbulent flow field at $f^* = 0.14, H_0 = c, x_p = {}^{c}/_{3}$

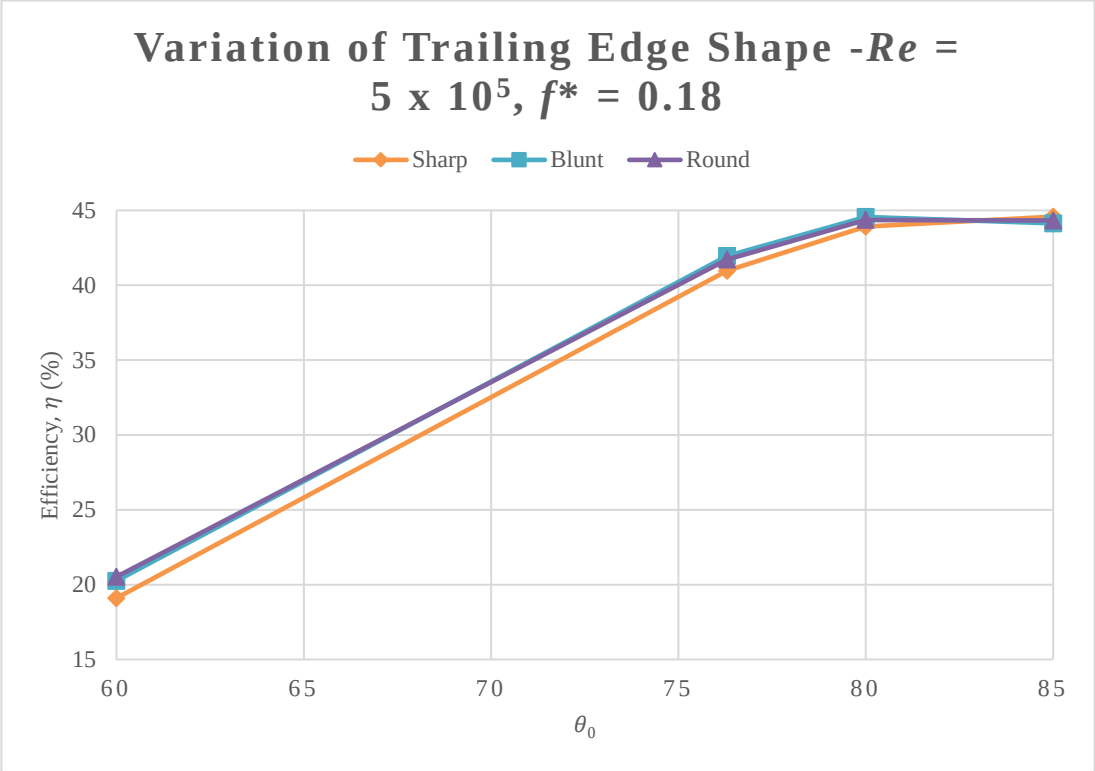

Figure 4. 21: Comparison between sharp, blunt and round trailing edge shape of NACA0018 on power extraction efficiency in turbulent flow field at $f^* = 0.18, H_0 = c, x_p = {}^{c}/_{3}$

The results in Figure 4.20 are for a range of pitching amplitude θ_0. This figure indicates that the blunt trailing edge shape steadily generates higher efficiency values as compared to sharp and rounded shapes. The highest difference in efficiency is found at pitching amplitude $\theta_0 = 76.3°$ and a low reduced frequency $f^* = 0.14$, with a 7% improvement for the blunt edge shape, while the sharp and rounded trailing edge shapes do not show any significant difference. The vorticity plot at pitching amplitude $\theta_0 = 76.3°$ is given in Figure 4.22. This figure clearly shows the formation of small vortices shedding from the trailing edge of the blunt edge; which is not the case for the sharp and round edges. By examining the plot of the synchronization between the vertical force C_Y and heaving velocity V_Y in Figure 4.23, it can be seen that the lift coefficient of the blunt edge is slightly higher than those of the sharp and round edges, and as such this contributes to a better power efficiency for the blunt edge.

For a higher reduced frequency of $f^* = 0.18$ (Figure 4.21), a similar trend as in laminar flow is observed, where the efficiency performance is found to be less sensitive to the trailing edge shape modification, which is about 3% better for the blunt edge.

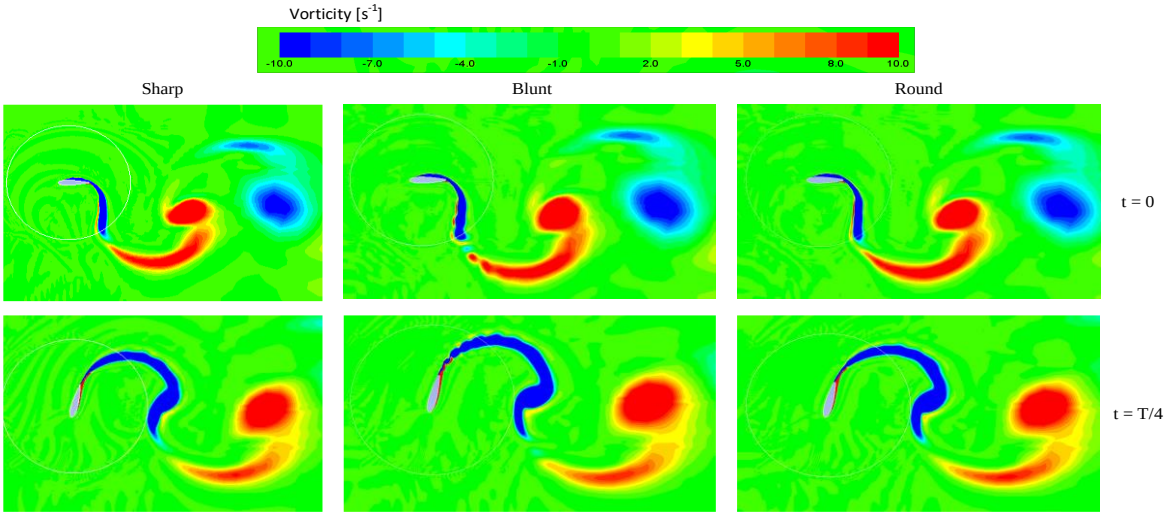

Figure 4. 22: Vorticity plot (red: counter-clockwise vorticity, blue: clockwise vorticity) in turbulent flow field for sharp, blunt and round edge for NACA0018, $f^* = 0.14, \theta_0 = 76.3°$ at t = 0 and 0.25T

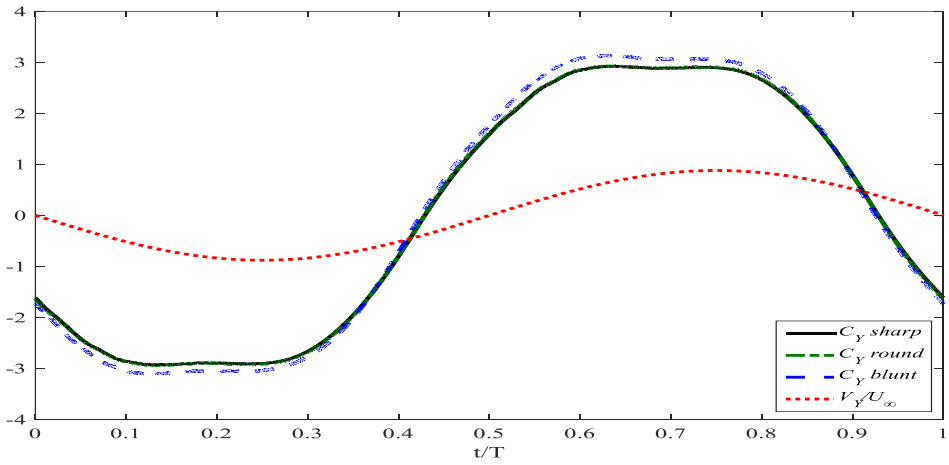

Figure 4. 23: Comparison of synchronization between vertical force C_Y of sharp, round and blunt trailing edge shape for NACA0018 and heaving velocity V_Y at $\theta_0 = 76.3°$; $f^* = 0.14$

Overall, it can be concluded that the blunt trailing edge shows positive improvement in efficiency in comparison to the sharp and rounded trailing edge shape modifications, especially at a low reduced frequency and a higher Reynolds number. Moreover, the energy efficiencies for the blunt, sharp and rounded edges are larger in the turbulent flow (high Reynolds number) than in the laminar flow.

4.1.3 Reduced Frequency and Reynolds numbers Effects on Energy Harvesting Performance Efficiency

From the presented data in Section 4.1.2, all of the numerical cases were simulated in laminar ($Re = 1100$) and turbulent ($Re = 5 \times 10^5$) flow fields. In order to evaluate the effect of

oscillating frequency on the flow behaviour and the performance efficiency, simulations of NACA0018 with blunt trailing edge shape were carried over the range of reduced frequencies and at fixed pitch and heave amplitude which are $\theta_0 = 85°$ and $H_0 = c$, in laminar and turbulent flows. These values of pitch and heave amplitudes were chosen since these parameters showed an optimal efficiency performance in Figures 4.20 and 4.21.

Comparing the results of the turbulent flow with those of laminar flow (Figure 4.24), it can be seen that the energy extraction is higher in the turbulent flow over the range of reduced frequencies. Moreover, it can be seen that for the laminar case, the efficiency increases till it reaches a maximum (about $\eta = 35\%$) which is at the reduced frequency of $f^* = 0.14$, then it reduces. For the turbulent case, the efficiency increases till it reaches the maximum at $f^* = 0.16$ ($\eta = 46\%$), then decreases. This increase in the energy extraction efficiency for the oscillating airfoil in a turbulent flow can be described by comparing the vorticity plots obtained by oscillating airfoil in a turbulent flow (Figure 4.25) with those in a laminar flow (Figure 4.26). From these plots, it can be seen that the vortices shed by the oscillating airfoil in a turbulent flow are stronger than those shed when it is oscillating in a laminar flow. This occurs because the vortices already present in the turbulent flow interact with each other and with the shed vortices, thus it resulting in increasing the vortex strength. Moreover, the graph of the synchronization between vertical force C_Y and heaving velocity V_Y in Figure 4.27 shows that the turbulent flow has a better synchronization with airfoil motion and higher lift, which result in a higher energy efficiency.

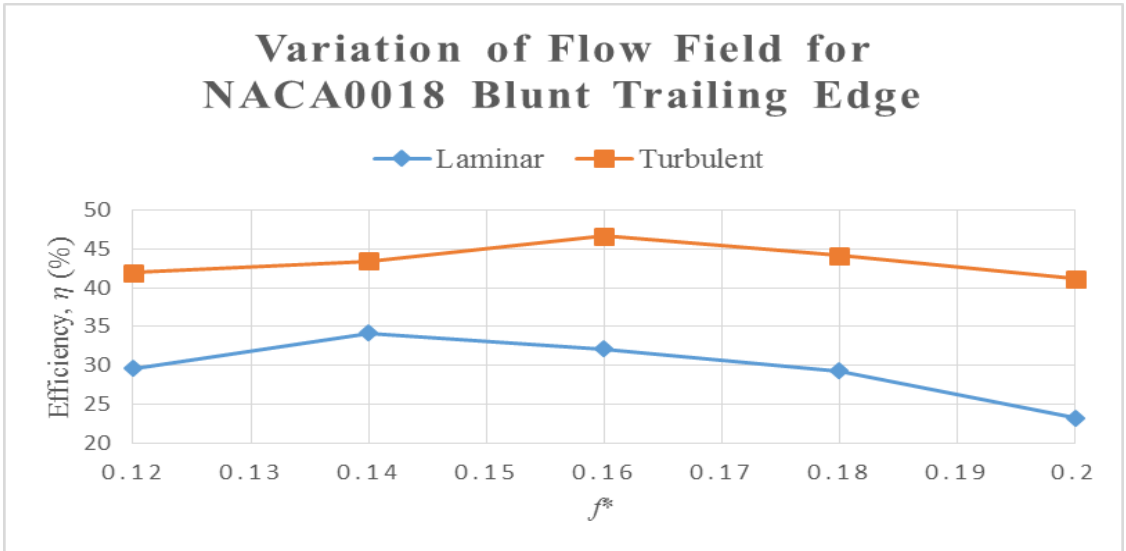

Figure 4. 24: Comparison between laminar ($Re = 1100$)and turbulent ($Re = 5 \times 10^5$) flow on power extraction efficiency at $\theta_0 = 76.3°, H_0 = c, x_p = {}^{c}/_{3}$

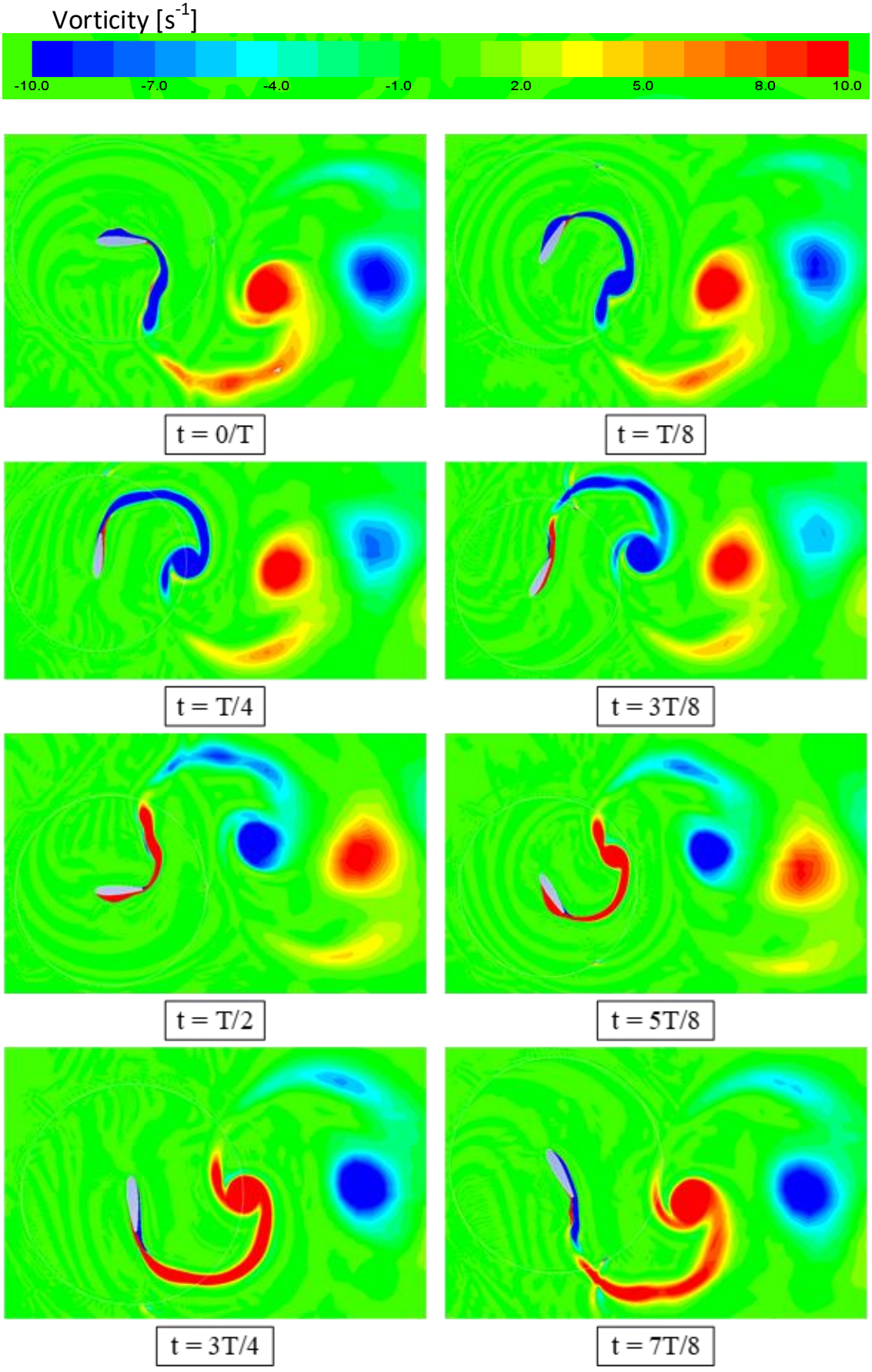

Figure 4. 25: Vorticity field for NACA0018 with blunt trailing edge shape over one cycle at $Re = 5 \times 10^5$; $\theta_0 = 85°$; $f^* = 0.16$

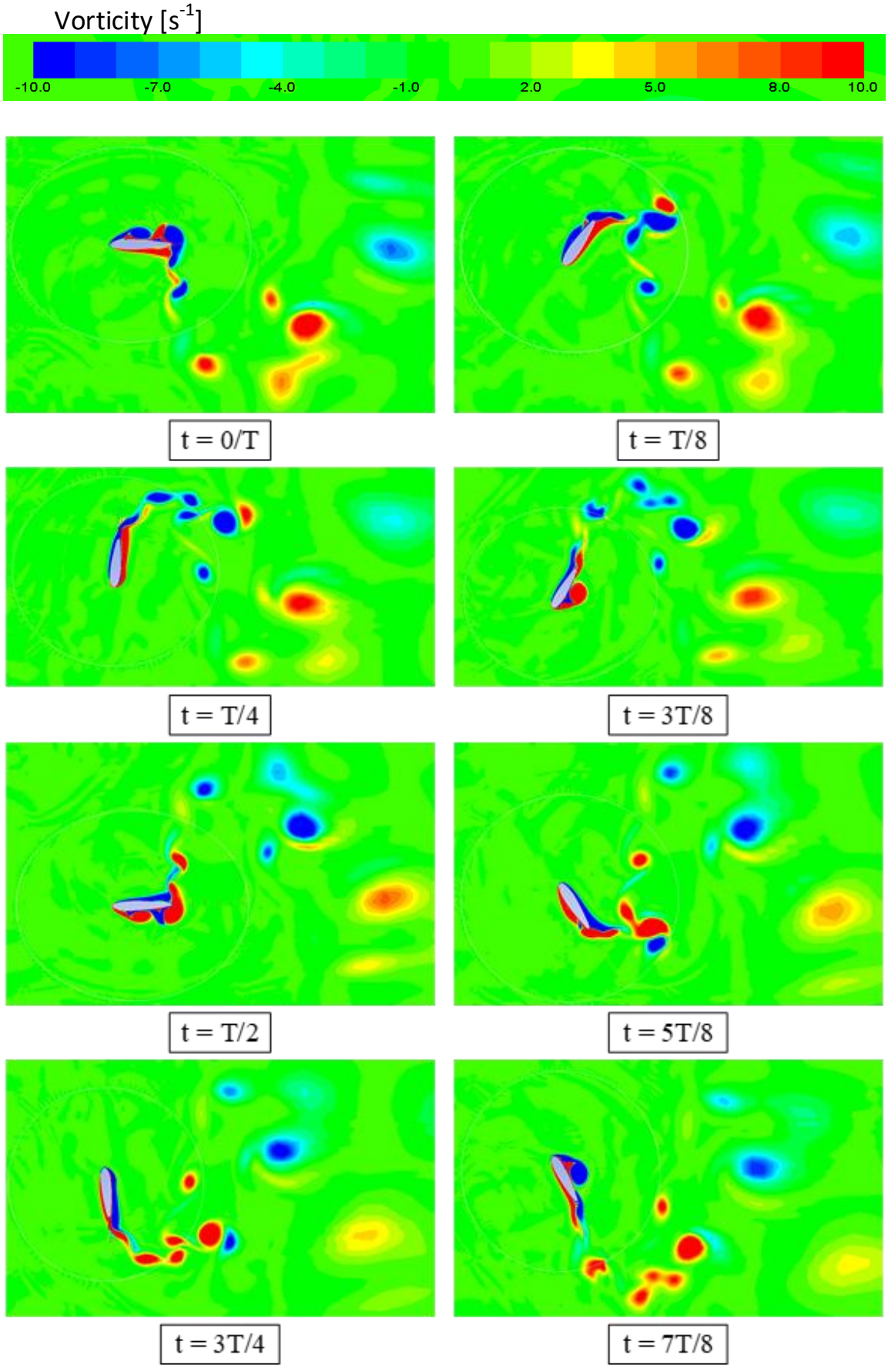

Figure 4. 26: Vorticity field for NACA0018 with blunt trailing edge shape over one cycle at $Re = 1100;\ \theta_0 = 85°;\ f^* = 0.16$

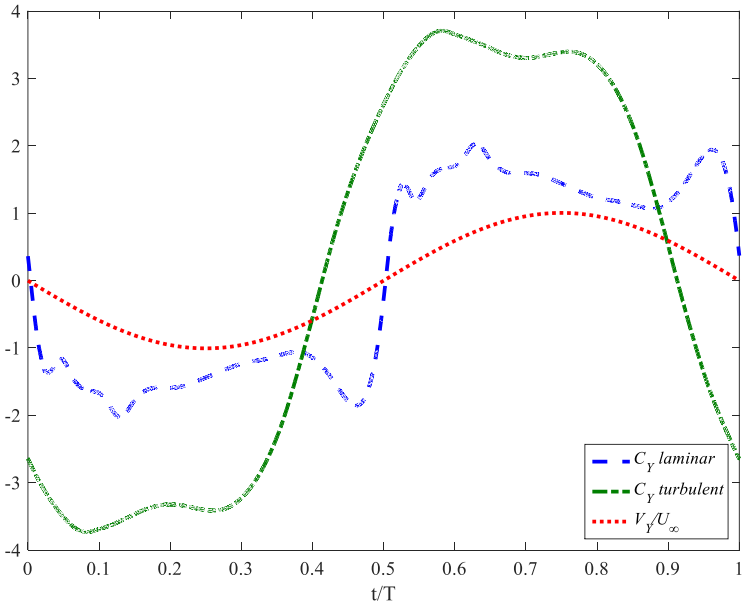

Figure 4. 27: Comparison of synchronization between vertical force C_Y for laminar and turbulent case and heaving velocity V_y at $\theta_0 = 85°$; $f^* = 0.16$ and NACA0018 blunt edge

Thus, we may conclude that, the energy efficiency increase does depend on the Reynolds number, and the reduced frequency. In addition, turbulent flow contributes to a higher efficiency than the laminar flow over a wide range of reduced frequencies. Hence, in the rest of the simulations in this study, we will just focus on the turbulent flow analysis.

4.2 Multiple Bodies Analysis

In this section, numerical simulations of oscillating bodies were focused on the multiple interactions between different bodies such that: interaction between two airfoils (airfoil-airfoil); and interaction between bluff body and an airfoil (cylinder-airfoil). A parametric design includes the oscillation motion direction, distance between two bodies ($L_x = 2.5c$ and $4c$), and kinematics parameters, i.e. reduced frequencies ($f^* = 0.12 - 0.18$) and pitching amplitude ($\theta_0 = 60° - 85°$). In this section, all of the simulated cases were run in turbulent flow field with phase angle $\psi = 0$ between the upstream and downstream bodies and a pitching motion about an axis located at $x_p = {}^{c}/_{3}$ from their respective leading edge. For the airfoils, NACA0015 with sharp trailing edge shape and NACA0018 with blunt trailing edge shape have been investigated for this multiple bodies analysis for turbulent flow.

4.2.1 Numerical Method

4.2.1.1 Computational Domain and Boundary Condition

In tandem configuration (two objects), the mesh was generated through combination of structured and unstructured grid as shown in Figure 4.28. The upstream inlet velocity and the downstream pressure outlet were located at 35*c* and 40c from the pitching point of the upstream body, respectively. The upper and lower velocity inlet were located at 35*c* from the pitching body (same as in single airfoil). The distance of the interface has been varied from 1.5*c* to 1*c* in order to investigate the effect of the distance between two bodies as highlighted in Figure 4.29. Moreover, a high grid resolution is maintained around the oscillating bodies and the inter-body region in order to accurately resolve the upstream body wake structures up to their interaction with the downstream body.

The same method as implemented in the single airfoil analysis was used in order to enable the pitching motion of the individual bodies within the system. Each body was enclosed in a circular zone and that zone was set to rotate with respect to the outer domain by using a user-defined function (UDF). The sinusoidal heave motion of the whole system was also prescribe by a UDF.

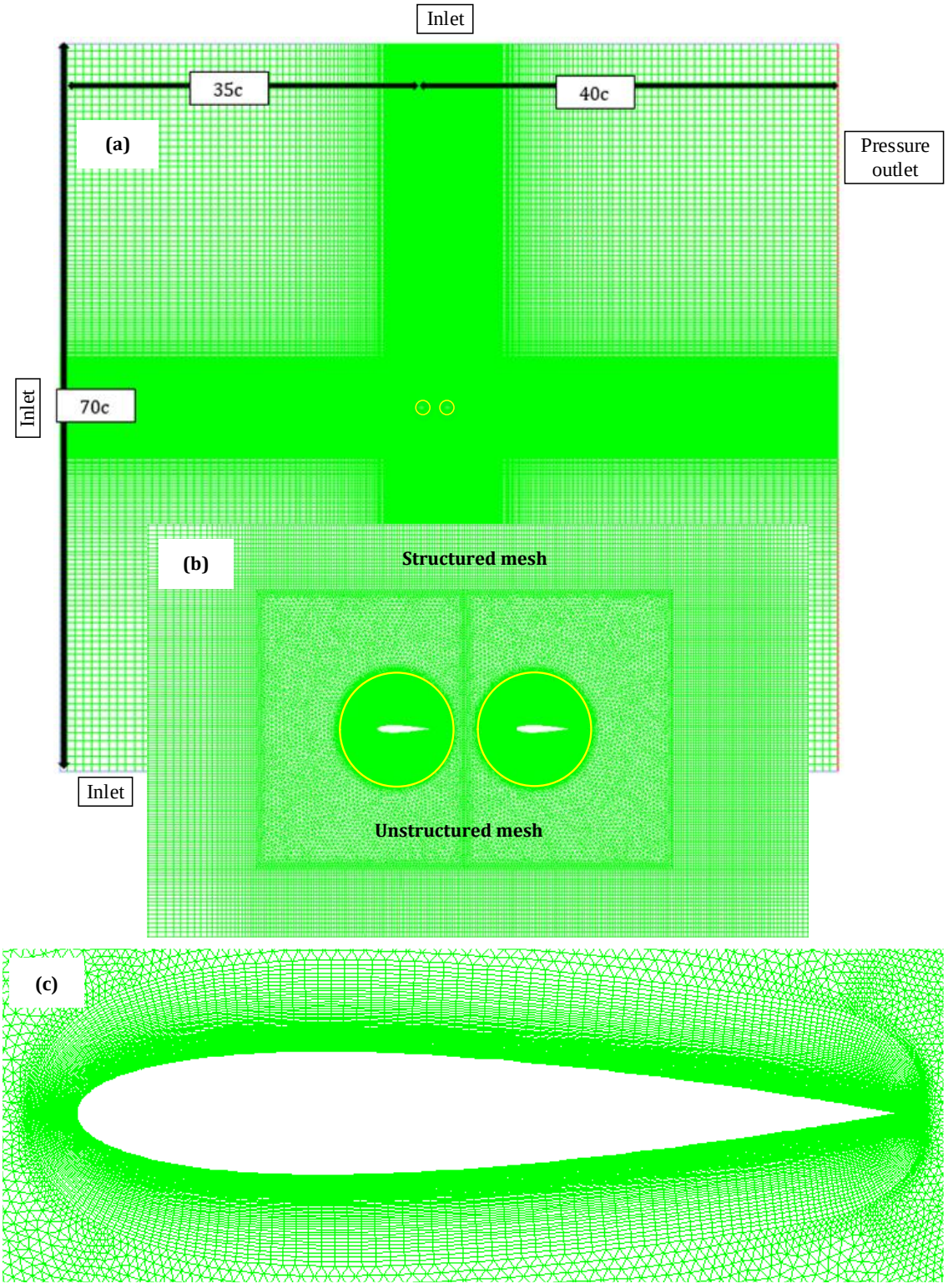

Figure 4. 28: (a) Simulation domain for tandem cases, (b) close-up view for structured and unstructured mesh (c) close-up view of the boundary layer for the NACA0015 airfoil

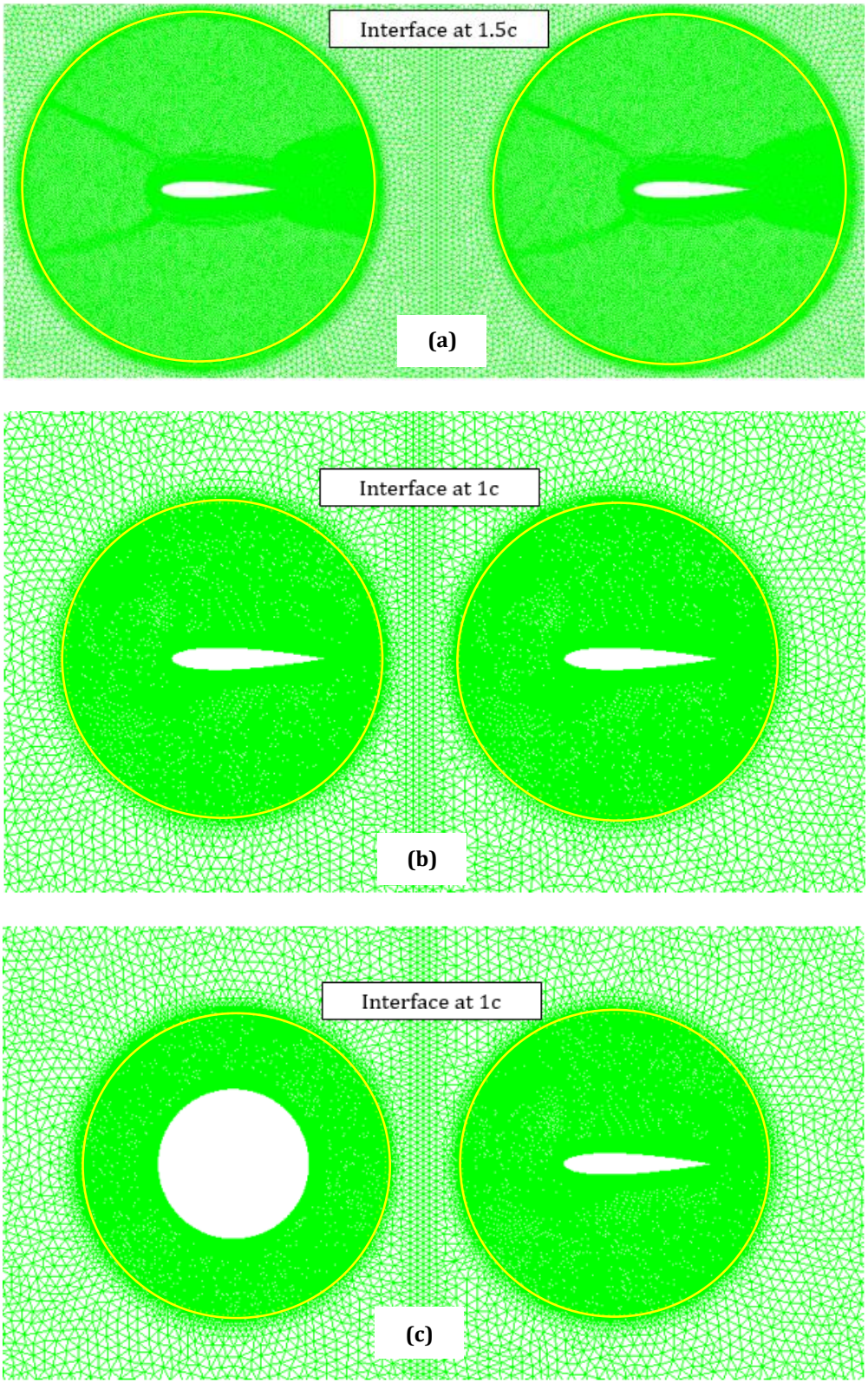

Figure 4. 29: close-up view of tandem configuration (a) two airfoils at 3 diameter interface, (b) two airfoils at 2 diameter interface, (c) cylinder and airfoil at 2 diameter interface

Three level of grid resolution have been established and the details are discussed in the previous Chapter (Section 3.8).

4.2.2 Effect of Oscillation Motion Direction on Energy Harvesting Performance Efficiency

In this section, the effect of motion direction between upstream and downstream of the oscillating airfoils in tandem configuration is studied. Two cases have been simulated. For Case 1-0, the upstream and downstream airfoils were setup to oscillate in the opposite direction, which means when the upstream airfoil starts to pitch down, the downstream airfoil will pitch up (Figure 4.31). Meanwhile for Case 2-0, both upstream and downstream airfoils will oscillate in the same direction (Figure 4.32). Simulation has been set at $Re = 5 \times 10^5, f^* = 0.14, H_0 = c, \theta_0 = 76.3°, L_x = 4c$. The results presented in this section will focus on the mean power coefficient, $\bar{C}_P$ and energy harvesting efficiency η of upstream and downstream airfoils.

Table 4. 3: Comparison of coefficient of power and energy harvesting performance efficiency on oscillating motion direction

Case	$\bar{C}_{P\,upstream}$	$\eta_{upstream}$	$\bar{C}_{P\,downstream}$	$\eta_{downstream}$	$\bar{C}_{P\,total}$	η_{total}[%]
Case 1-0	0.9048	35.31%	-0.8867	-34.60%	0.0181	0.71
Case 2-0	0.8861	34.58%	0.4452	17.37%	1.3313	51.95

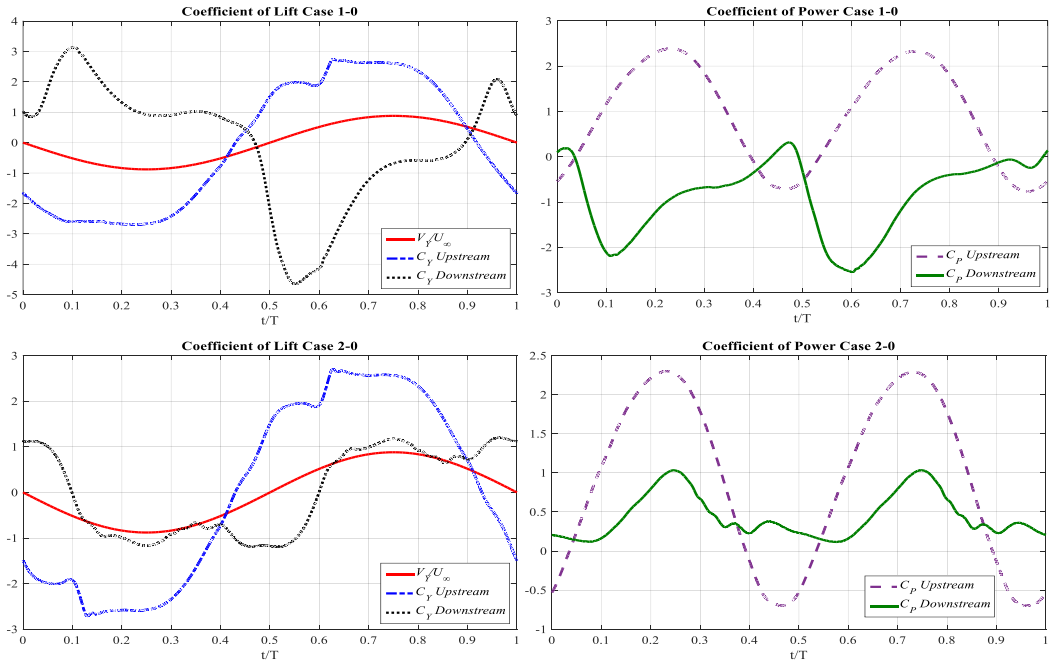

Figure 4. 30: Instantaneous vertical force C_Y over a periodic cycle, V_Y/U_∞ and coefficient of power C_P, for Case 1-0 and Case 2-0

Table 4.3 compares the power output and their respective efficiency on the two airfoils when treated individually and when considered for the whole system. About 2% difference is observed from the outcome of the upstream airfoil between Case 1-0 and 2-0. However, a marked difference results can be seen from the downstream airfoil of these two cases tested which finally making up the total coefficient of power and efficiency. For Case 1-0, the downstream airfoil contributes to the negative power to the system. This is because, from Figure 4.30 (downstream airfoil Case 1-0), it clearly shows a bad synchronization between the heaving velocity V_Y and the vertical force coefficient C_Y (i.e. they have opposite sign at a time), causing the total power curve C_P to go negative throughout the whole cycle. On the other hand, for the downstream airfoil Case 2-0, although less vertical force C_Y is generated, the phase difference between the airfoils provides better synchronization of C_Y and heaving velocity V_Y, resulting in net positive power output being maintained throughout the whole cycle.

The details of the negative power produced by the downstream airfoil of Case 1-0 are illustrated in the vorticity contours plots in Figure 4.31. The downstream airfoil exhibits dynamic-stall over the entire cycle. This shows that the downstream airfoil and the flow motion are in opposite manner. Hence, energy will be consumed in order to overcome the damping effect of the surrounding flow. Meanwhile in Case 2-0, even though the vorticity plots do show the dynamic stall (Figure 4.32), it is reattached as the airfoil flap in the cycle. The reattachment vortex increase the lift and result in positive power generation (produced the energy).

Case 2-0 is then were further investigated by varying the reduce frequency f^* and pitching amplitude θ_0 in order to observe their effects on the power generation. Other parameters i.e. Reynolds number *Re*, heaving amplitude H_0 and distance between upstream and downstream airfoil L_x were kept the same. The results were shown in Table 4.4 including the results of Case 2-0 in order to have a better comparison with the other simulation results.

From the overall results presented in Table 4.4, there are few observations which need to be emphasized. First, it is clear that the major contribution to the total power coefficient and efficiency comes from the upstream airfoil. This is because the downstream airfoil operates in the upstream airfoil velocity deficit, hence there are not much power generated. Secondly, when the pitching amplitude is fixed ($\theta_0 = 76.3°$) and the reduced frequencies are varied $f^* = 0.12 - 0.18$, the efficiency performance of the downstream airfoil drops drastically as the reduced frequency increases. On the other hand, the efficiency performance

of the upstream airfoil is slowly increasing until it achieved it maximum at reduced frequency $f^* = 0.16$ with 36.77% efficiency, then it starts to decrease. Moreover, when the reduced frequency is fixed at $f^* = 0.12$ and $f^* = 0.14$ and the pitching amplitude is varied $\theta_0 = 60° - 85°$, the performance of the upstream airfoil is improved as the pitching amplitude increases with efficiency increments of 24.9%, 5.8% and 5.4% for $f^* = 0.12$ and 29.7%, 2.6% and 6.4% for $f^* = 0.14$. Conversely, the performance of the downstream airfoil decreases significantly as the pitching amplitude increases for both reduced frequencies tested.

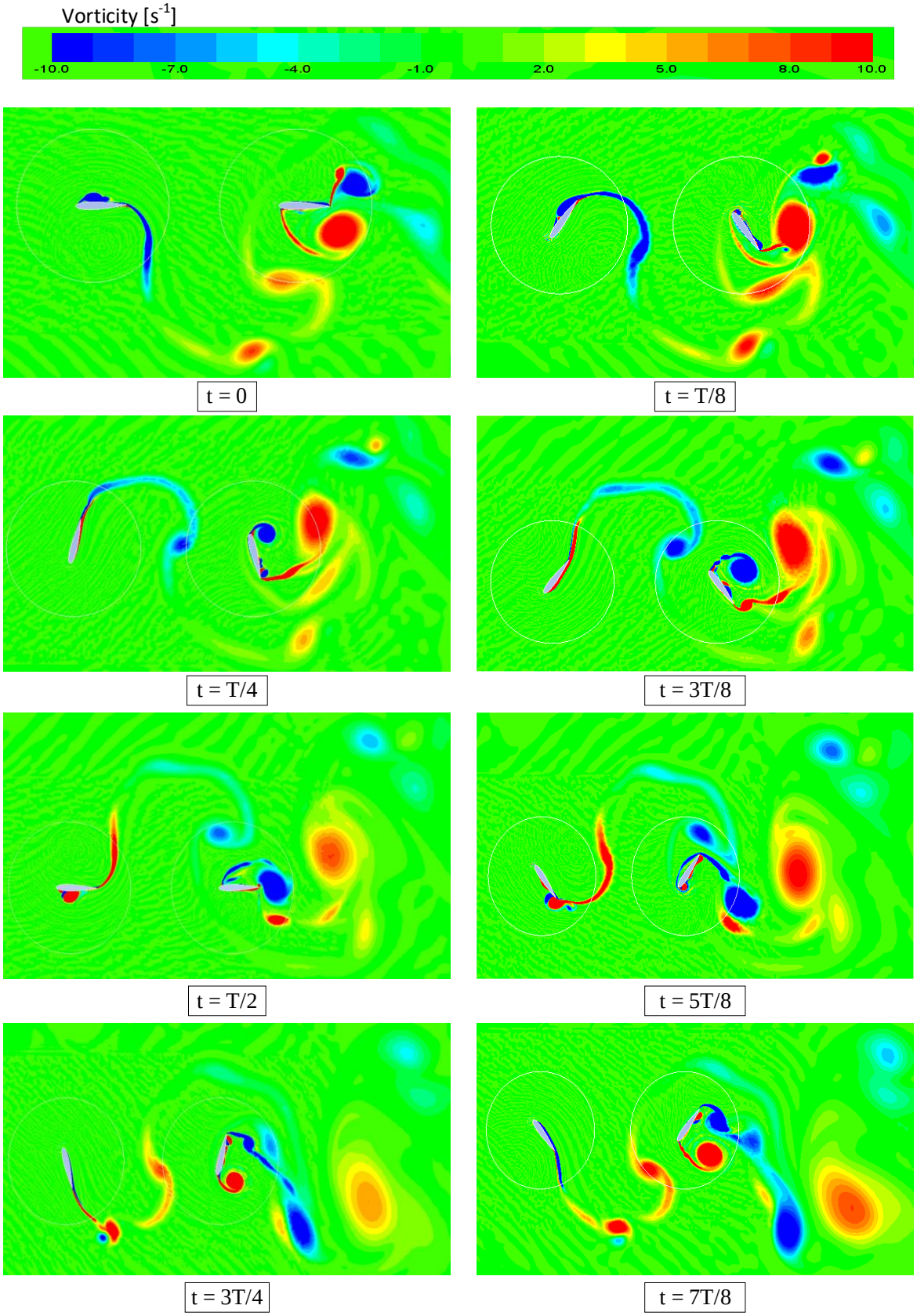

Figure 4. 31: Vorticity field for Case 1-0 over one cycle (blue: clockwise, red: counter-clockwise)

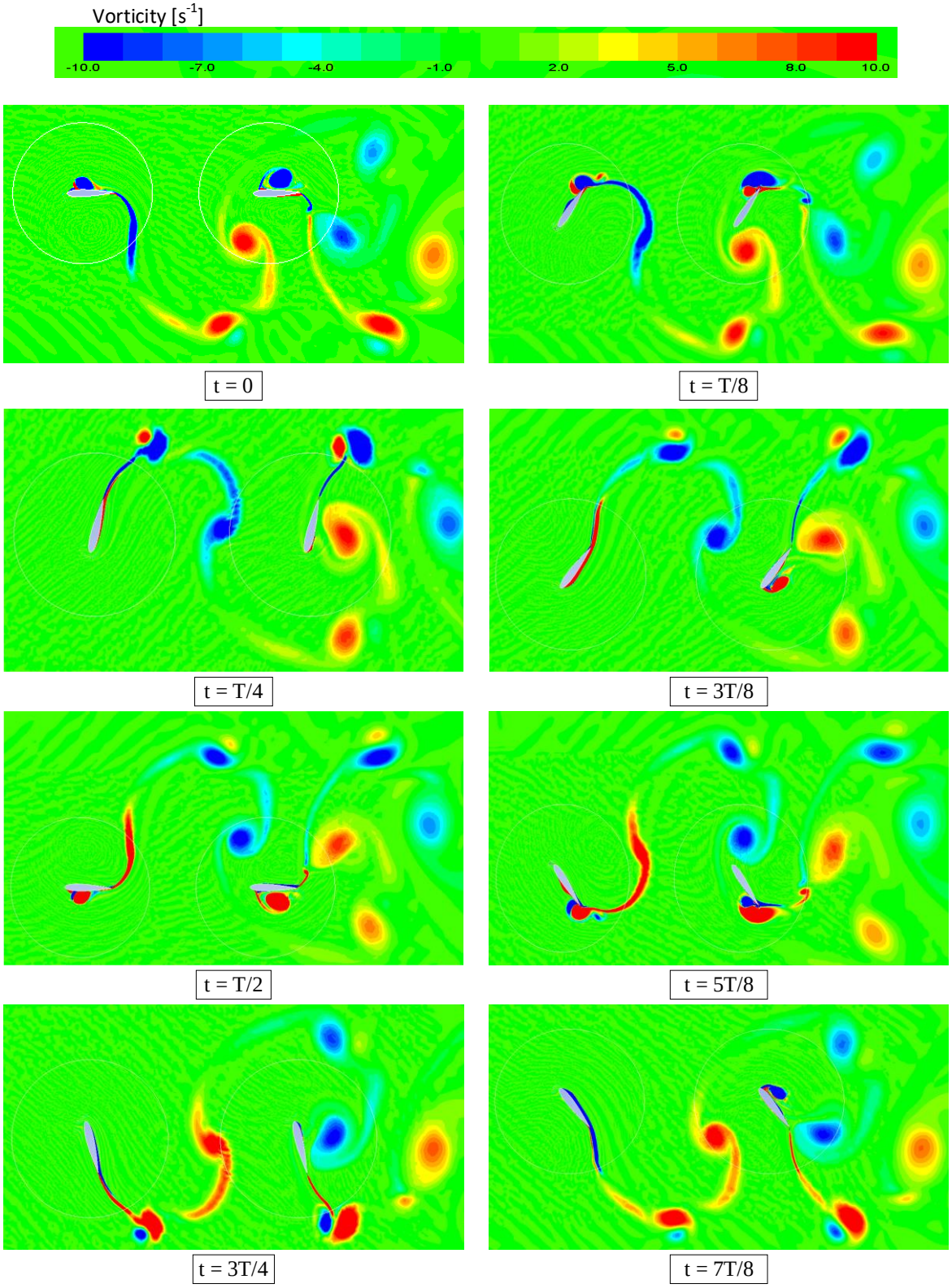

Figure 4. 32: Vorticity field for Case 2-0 over one cycle (blue: clockwise, red: counter-clockwise)

Table 4. 4: Parametric study of Case 2 over a range of reduced frequencies and pitching amplitudes

Case study	$\overline{C}_{P\,upstream}$	$\eta_{upstream}$	$\overline{C}_{P\,downstream}$	$\eta_{downstream}$	$\overline{C}_{P\,total}$	η_{total}[%]
$f^* = 0.14, \theta_0 = 76.3°$						
Case 2-0	**0.8861**	**34.58%**	**0.4452**	**17.37%**	**1.3313**	**51.95**
$f^* = 0.12, \theta_0 = 76.3°$						
Case 2-1	0.8659	33.79%	0.4408	17.20%	1.3067	50.99
$f^* = 0.16, \theta_0 = 76.3°$						
Case 2-2	0.9423	36.77%	0.326	12.72%	1.2683	49.49
$f^* = 0.18, \theta_0 = 76.3°$						
Case 2-3	0.9204	35.92%	0.1495	5.83%	1.0699	41.75
$f^* = 0.12, \theta_0 = 60°$						
Case 2-4	0.6086	25.37%	0.5446	22.70%	1.1532	48.07
$f^* = 0.14, \theta_0 = 60°$						
Case 2-5	0.5836	24.32%	0.5005	20.86%	1.0841	45.18
$f^* = 0.12, \theta_0 = 80°$						
Case 2-6	0.9316	35.87%	0.3801	14.64%	1.3117	50.51
$f^* = 0.14, \theta_0 = 80°$						
Case 2-7	0.9222	35.51%	0.3554	13.69%	1.2776	49.20
$f^* = 0.12, \theta_0 = 85°$						
Case 2-8	0.9735	36.85%	0.2509	9.50%	1.2244	46.35
$f^* = 0.14, \theta_0 = 85°$						
Case 2-9	1.0021	37.93%	0.2392	9.05%	1.2413	46.98

Overall, the peak efficiency of the oscillating airfoils in tandem configuration occurs at Case 2-0 (bold) with less than 2% difference in power efficiency, as compared to Case 2-1. In another words, it can be concluded that, the maximum energy extraction efficiency of the two airfoils in tandem configuration oscillating in the same direction happens at the reduced frequencies $f^* = 0.12 - 0.14$ and pitching amplitude $\theta_0 = 76.3°$, with 24.6% increase in power efficiency, as compared to the single airfoil.

4.2.3 Effect of the Distance between Upstream and Downstream Airfoils on Energy Harvesting Performance Efficiency

The investigation on the oscillating airfoils were further studied in order to examine the influence of the separation distance between upstream and downstream airfoil (measured between the pitching axes of the two airfoils) on the energy extraction efficiency of the system. The inter airfoil distance (L_x) of Case 2-0 has been modified from 4*c* to 2.5*c* and this new simulation setup is introduced as Case 3-0.

Table 4. 5: Comparison of coefficient of power and energy harvesting performance efficiency over the distance between upstream and downstream airfoil

Case study	$\overline{C}_{P\,upstream}$	$\eta_{upstream}$	$\overline{C}_{P\,downstream}$	$\eta_{downstream}$	$\overline{C}_{P\,total}$	η_{total}**[%]**
Case 2-0	0.8861	34.58%	0.4452	17.37%	1.3313	51.95
Case 3-0	0.8799	34.34%	0.5503	21.48%	1.4302	55.82

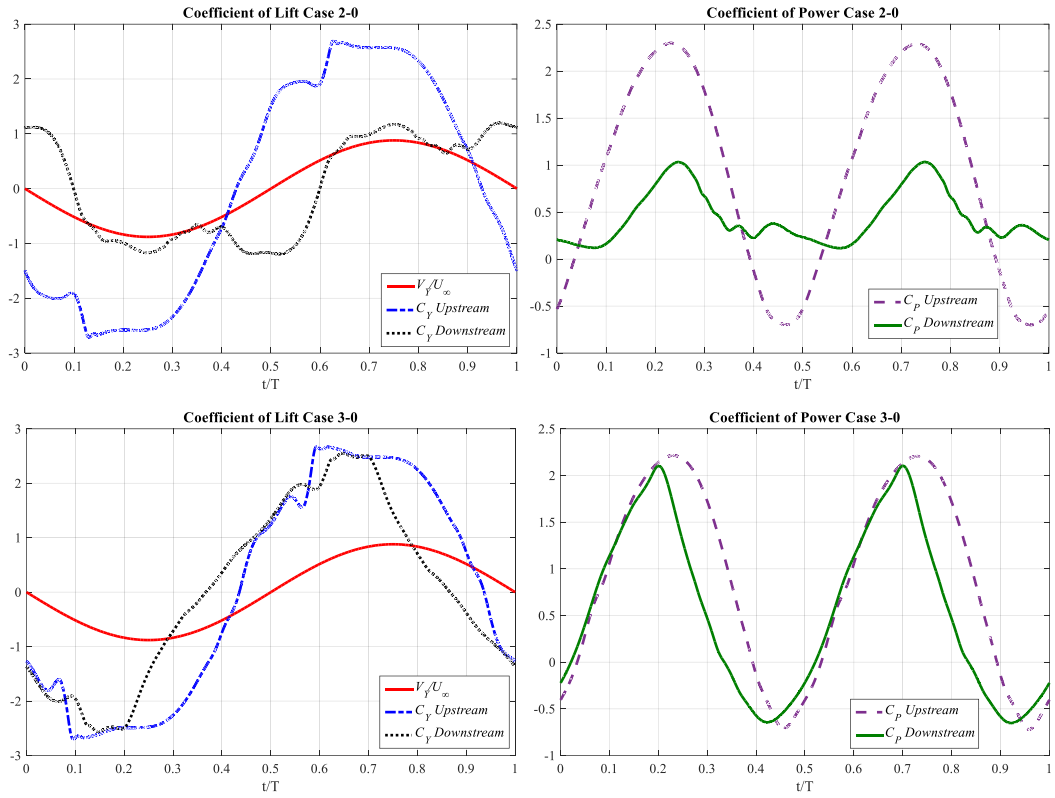

Figure 4. 33: Instantaneous vertical force C_Y over a periodic cycle, V_Y/U_∞ and coefficient of power C_P, for Case 2-0 and Case 3-0

Table 4.5 compares the power generated by two airfoils in tandem configuration and their respective efficiencies when they are placed at 4c and 2.5c apart. The results show about 7% increment in the total power generation and energy extraction efficiency of the system when the two airfoils are placed closer. This increase in the total coefficient of power of the system can be described by comparing the plot of the heaving velocity V_Y and the vertical force C_Y coefficient for each airfoil (Figure 4.33). The plot by the upstream airfoil in both tested cases shows a similar pattern however, it is not the same for the downstream airfoil. The plot by the downstream airfoil of Case 3-0 shows the vertical force C_Y is higher than the vertical force C_Y of downstream airfoil of Case 2-0, and as such the power generated by the downstream airfoil for Case3-0 is higher (see Figure 4.33, coefficient of power for Case3-0).

The vorticity plot of Case 3-0 is shown in Figure 4.34 to illustrate the flow behaviour, as compared to Case 2-0 in Figure 4.33. One obvious observation that can be seen in Figure 4.35 is the strong interaction of the wake vortices of the upstream airfoil and the downstream airfoil. In general, the strong interaction of the wake vortices from the upstream body with the downstream body in tandem configuration may lead to increase or decrease in energy performance depending on two criteria: a local rise or a local loss of available dynamic

pressure provided by the vortex-induced velocity. Hence, in this case, the strong interaction of vortices was resulting in loss of performance especially at t = T/4, when the airfoils are about to start rotating in a clockwise manner, a vortex shed from the upstream airfoil interacts with the leading edge of the downstream airfoil. A vortex, which is in a region of fluid rotating about an axis, is characterised by a region of low pressure at its centre. At t = T/4, this region of low pressure is rotating in an opposite manner to its pitching motion. Similar scenario happened at t = 3T/4 but having inverse sign. This poor synchronization of motion imposed by the shed vortices on the airfoil and its pitching motion is therefore resulting in the airfoil which would not be self-driving. Nevertheless, on most of the rest of the cycles, the synchronization happened which contributes to increase in the energy extraction efficiency of the system.

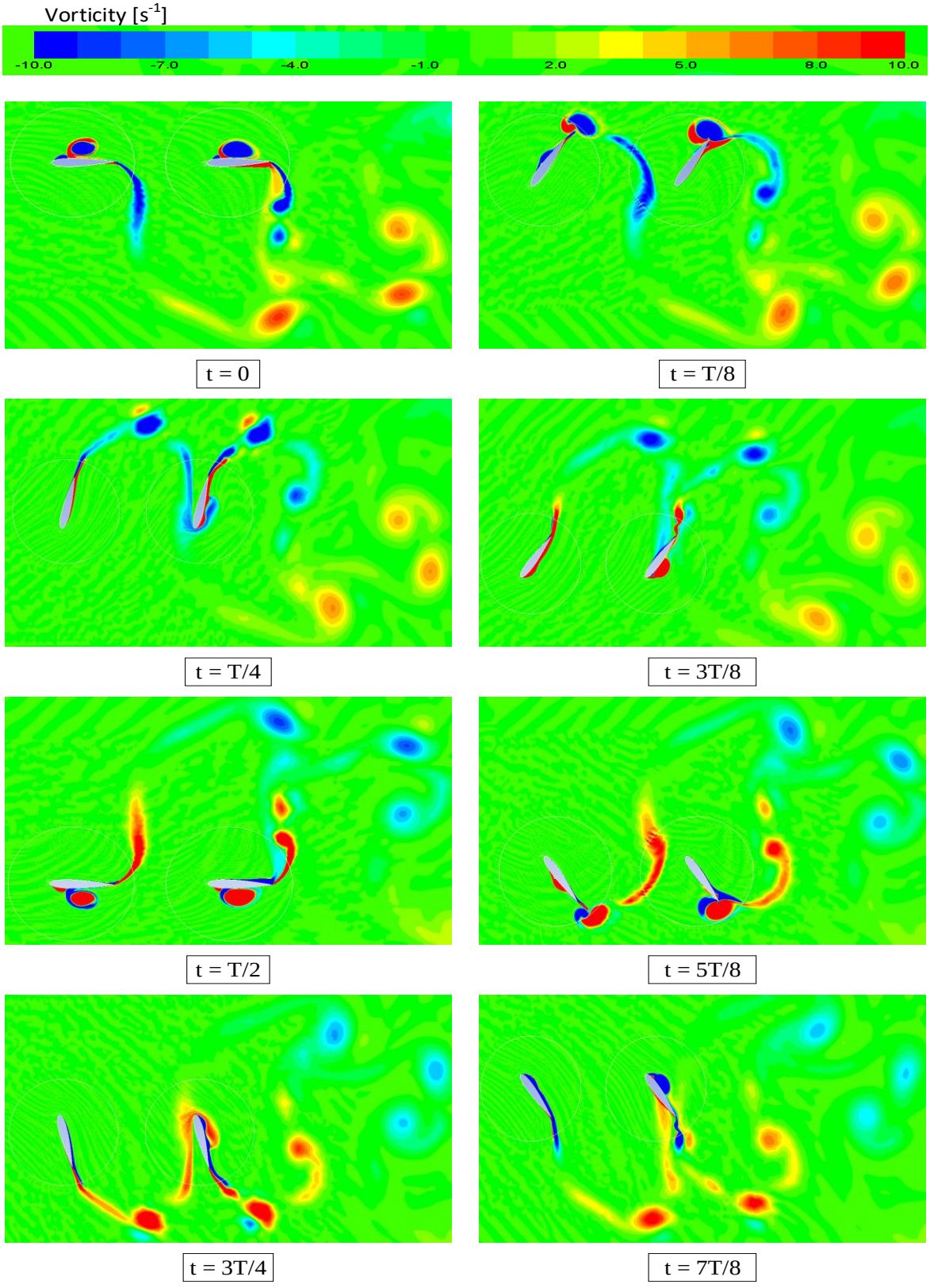

Figure 4. 34: Vorticity field for Case 3-0 over one cycle (blue: clockwise, red: counter-clockwise)

Case 3-0 has also been investigated further by varying the reduced frequency f^* and pitching amplitude θ_0 as already been done in Case 2-0, in order to have a full comparison of the effect of the distance between upstream and downstream airfoil. The results were presented in Table 4.6.

Table 4. 6: Parametric study of Case 3 over a range of reduced frequencies and pitching amplitudes

Case study	$\overline{C}_{P\ upstream}$	$\eta_{upstream}$	$\overline{C}_{P\ downstream}$	$\eta_{downstream}$	$\overline{C}_{P\ total}$	η_{total} [%]
$f^* = 0.14, \theta_0 = 76.3°$						
Case 3-0	0.8799	34.34%	0.5503	21.48%	1.4302	55.82
$f^* = 0.12, \theta_0 = 76.3°$						
Case 3-1	0.9307	36.32%	0.5654	22.06%	1.4961	58.38
$f^* = 0.16, \theta_0 = 76.3°$						
Case 3-2	0.8808	34.37%	0.5183	20.22%	1.3991	54.59
$f^* = 0.18, \theta_0 = 76.3°$						
Case 3-3	0.8686	89%	0.4891	19.09%	1.3577	52.98
$f^* = 0.12, \theta_0 = 60°$						
Case 3-4	0.6118	25.50%	0.5174	21.56%	1.1292	47.06
$f^* = 0.14, \theta_0 = 60°$						
Case 3-5	0.5781	24.09%	0.4995	20.82%	1.0776	44.91
$f^* = 0.12, \theta_0 = 80°$						
Case 3-6	0.9426	36.30%	0.5055	19.46%	1.4481	55.76
$f^* = 0.14, \theta_0 = 80°$						
Case 3-7	0.8532	32.85%	0.4671	17.98%	1.3203	50.83
$f^* = 0.12, \theta_0 = 85°$						
Case 3-8	0.9223	34.91%	0.3493	13.22%	1.2716	48.13
$f^* = 0.14, \theta_0 = 85°$						
Case 3-9	0.8882	33.62%	0.2406	9.11%	1.1288	42.73

The results presented above, showed that in most simulated cases, the shift of 4c to 2.5c distance between upstream and downstream airfoils gives a positive impact on efficiency. The highest increment is observed at $f^* = 0.18, \theta_0 = 76.3°$ where 21.2% improvement in total efficiency is achieved. Conversely, at $f^* = 0.12, \theta_0 = 60°$, $f^* = 0.14, \theta_0 = 60°$ and $f^* = 0.14, \theta_0 = 85°$ the change to 2.5c separation distance shows a decrease in energy efficiency performance by 2.2%, 0.6% and 10% respectively. Even though 10% reduction in power efficiency is a lot, however the drop of 2.2% and 0.6% difference in efficiency is negligible and in most of the other tested cases, the results show an improvement of efficiency. Hence, it can still be concluded that the change of the separating distance from 4c to 2.5c apart is beneficial on the overall power performance efficiency.

Comparing Case 3-0 – Case 3-9 in Table 4.6, it can be seen that the peak value of efficiency is obtained at $f^* = 0.12, \theta_0 = 76.3°$ (Case 3-1) which is 4.6% higher than total efficiency of Case 3-0. Moreover, it can be seen from Table 4.6 that the upstream airfoil contributes more in power generation than the downstream airfoil. Figure 4.35 shows comparison results of the time histories for upstream and downstream airfoil for the higher efficiency of Case 3-0 and Case 3-1 (Table 4.6). From this figure, it can be seen that it is mainly the downstream power of Case 3-1 which contributed to its higher power (Figure 4.35, right hand-side plots), as the upstream power is nearly the same for both cases. Moreover, Case 3-1 (Figure 4.35) shows better timing in the sign switch of V_Y and C_Y and higher C_Y over some cycles for the downstream airfoil, resulting in positive values of total extracted power of the downstream (Figure 4.35, bottom right plot).

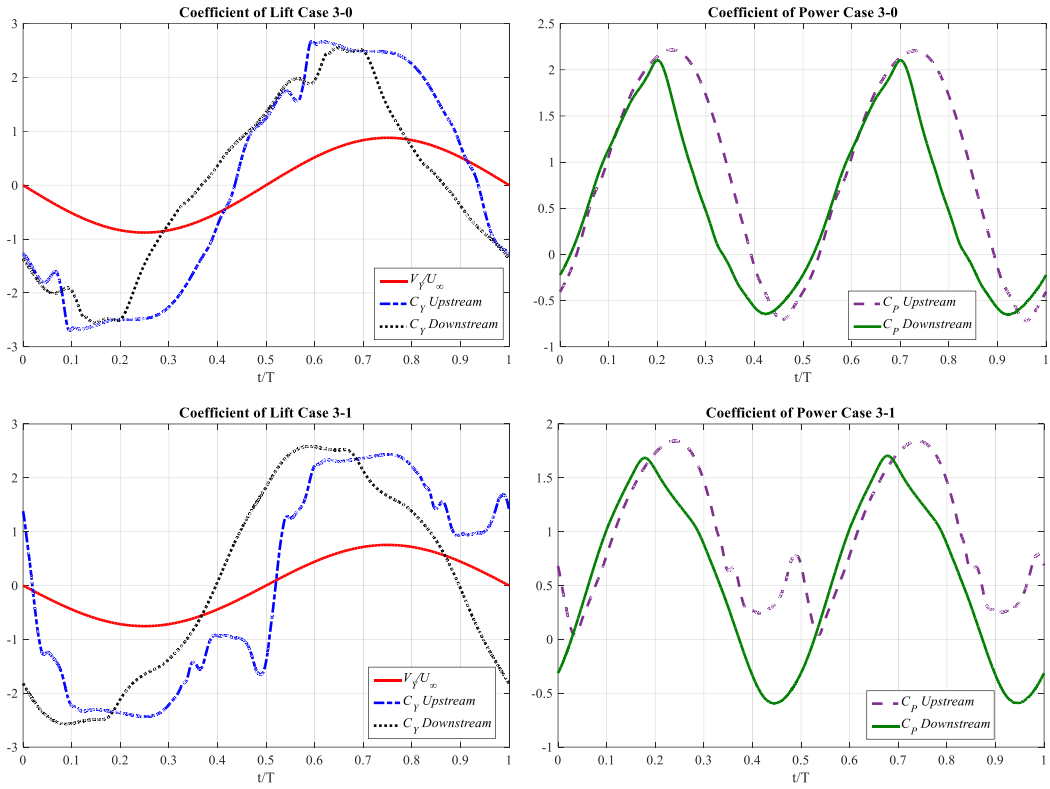

Figure 4. 35: Instantaneous vertical force C_Y over a periodic cycle, V_Y/U_∞ and coefficient of power C_P, for Case 3-0 and Case 3-1

Some insight can also be obtained by comparing the vorticity plots obtained for the system oscillating in Case 3-0 (Figure 4.34) with those obtained for the system oscillating in Case 3-1 (Figure 4.36). At t = 0, although the flow separates at the leading edge for both cases and for both airfoils, it can be observed that the flow reattachment for upstream airfoil of Case 3-1 occurs at a point further downstream of the pitching axis than that at which it occurs for Case 3-0. Because of the region of low pressure present at the core of the vortex, both airfoils are forced to rotate counter-clockwise similar to their pitching motion. Since the leading edge vortex interacts with the surface of the upstream airfoil in Case 3-1 at a point further downstream of the pitching axis than that in Case 3-0, the momentum of the upstream airfoil in Case 3-1 is actually larger than that in Case 3-0 which finally resulting in more energy extraction. A similar interaction is observed at t = T/2. Meanwhile, for the overall simulation cycle, it can be observed that the vortices shed on the two airfoils and their pitching motions of Case 3-1 are more synchronize than in Case 3-0. These results show general agreement with those obtained in Figure 4.35.

Next, additional simulations were computed at $f^* = 0.10, \theta_0 = 76.3°$ in order to find the optimum parameter of the reduced frequency for the effect of the distance between two airfoils on the energy harvesting efficiency, and this new setup is introduced as Case 3-10. The result of this simulation is presented in Table 4.7.

Table 4. 7: Parametric study of Case 3 over a range of reduced frequencies and pitching amplitudes (continued)

Case study	$\overline{C}_{P\,upstream}$	$\eta_{upstream}$	$\overline{C}_{P\,downstream}$	$\eta_{downstream}$	$\overline{C}_{P\,total}$	η_{total}[%]
			$f^* = 0.10, \theta_0 = 76.3°$			
Case 3-10	0.7797	30.43%	0.3501	13.66%	1.1298	44.09

From the above result, the same conclusion can be made as in the previous section, where the maximum energy extraction efficiency of two oscillating airfoils in tandem configuration occurs at the reduced frequencies $f^* = 0.12 - 0.14$ with pitching amplitude $\theta_0 = 76.3°$. In addition, we can observe also that, in most cases simulated in this section, the reduction of the inter airfoil distance L_x from 4c to 2.5c is beneficial to energy harvesting performance. Moreover, an increment of about 30% in energy harvesting efficiency has also been observed when compared to the single airfoil configuration at the same kinematic parameter setup. Hence, for further investigation, the simulation parameters are fixed at the inter airfoil distance $L_x = 2.5c$, reduced frequencies $f^* = 0.12$ and $f^* = 0.14$, and pitching amplitude $\theta_0 = 76.3°$.

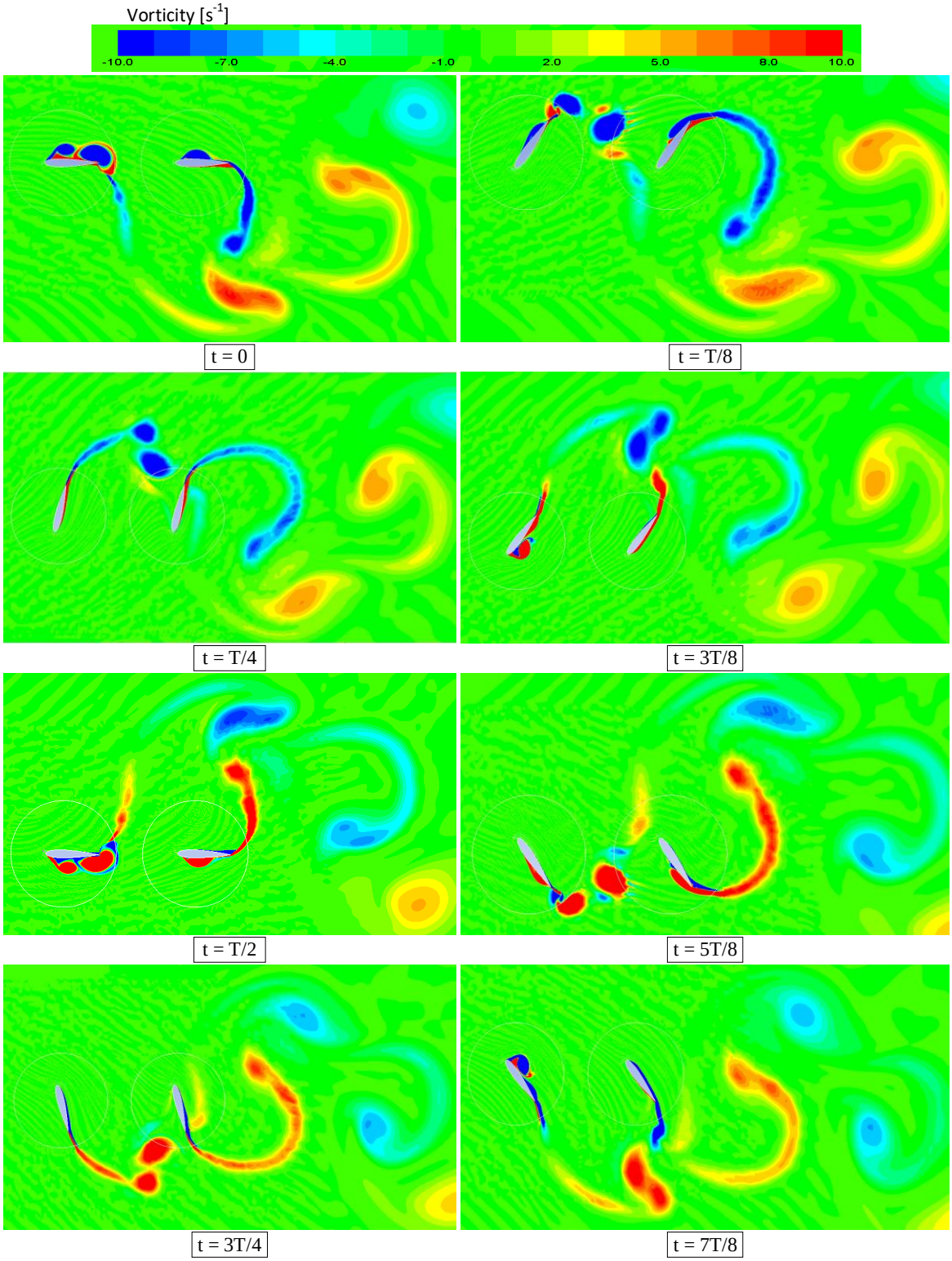

Figure 4. 36: Vorticity field for Case 3-1 over one cycle (blue: clockwise, red: counter-clockwise

4.2.4 Effect of Trailing Edge Modification on Energy Harvesting Efficiency

Apart from the conclusion that has been drawn previously, here we assess also the geometrical shape modification influence on the efficiency performance for the most optimum tandem configuration. From the previous simulations, we have observed that Case 3-1 has the highest efficiency. Hence, comparisons have been made between NACA0018 with blunt trailing edge (the most optimum geometry in single simulation) and NACA0015 with sharp trailing edge (Case 3-1), and the results are presented in Table 4.8 and Figures 4.37 & 4.38.

Table 4. 8: Comparison of power contribution between NACA0015 Sharp edge (Case 3-1) and NACA0018 Blunt Edge

Case study	$\overline{C}_{P\,upstream}$	$\eta_{upstream}$	$\overline{C}_{P\,downstream}$	$\eta_{downstream}$	$\overline{C}_{P\,total}$	η_{total}[%]
			$f^* = 0.12, \theta_0 = 76.3°$			
NACA0015 Sharp Edge	0.9307	36.32%	0.5654	22.06%	1.4961	58.38
NACA0018 Blunt Edge	0.8996	35.11%	0.6767	26.41%	1.5763	61.52

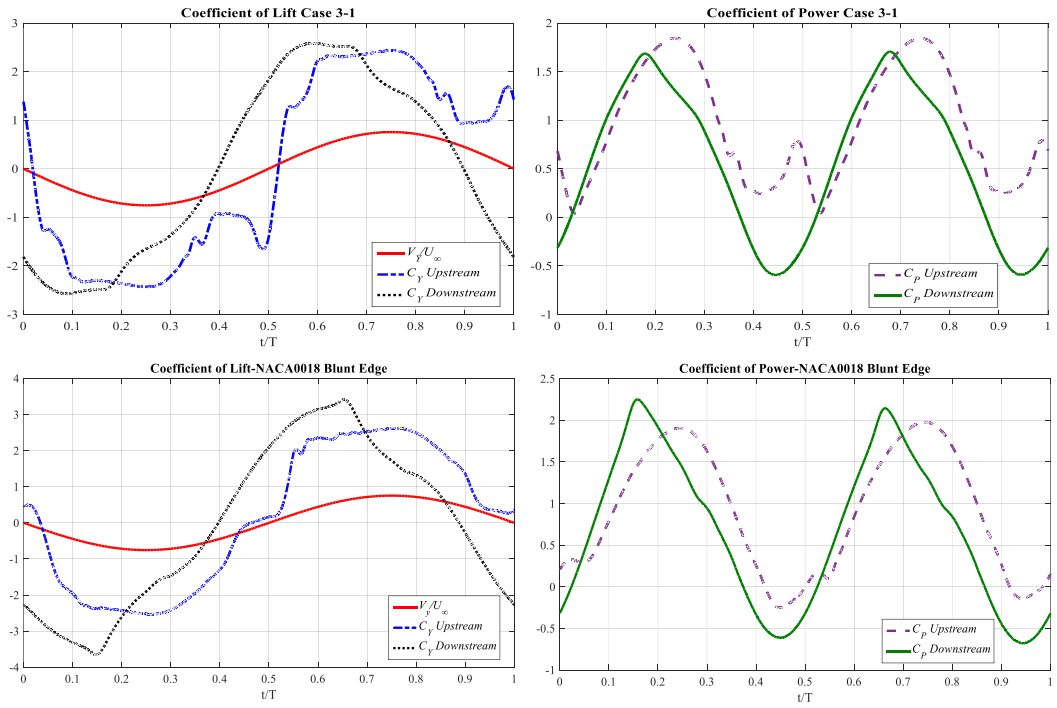

Figure 4. 37: Instantaneous vertical force C_Y over a periodic cycle, V_Y/U_∞ and coefficient of power C_P, for NACA0015 Sharp edge (Case 3-1) and NACA0018 Blunt Edge

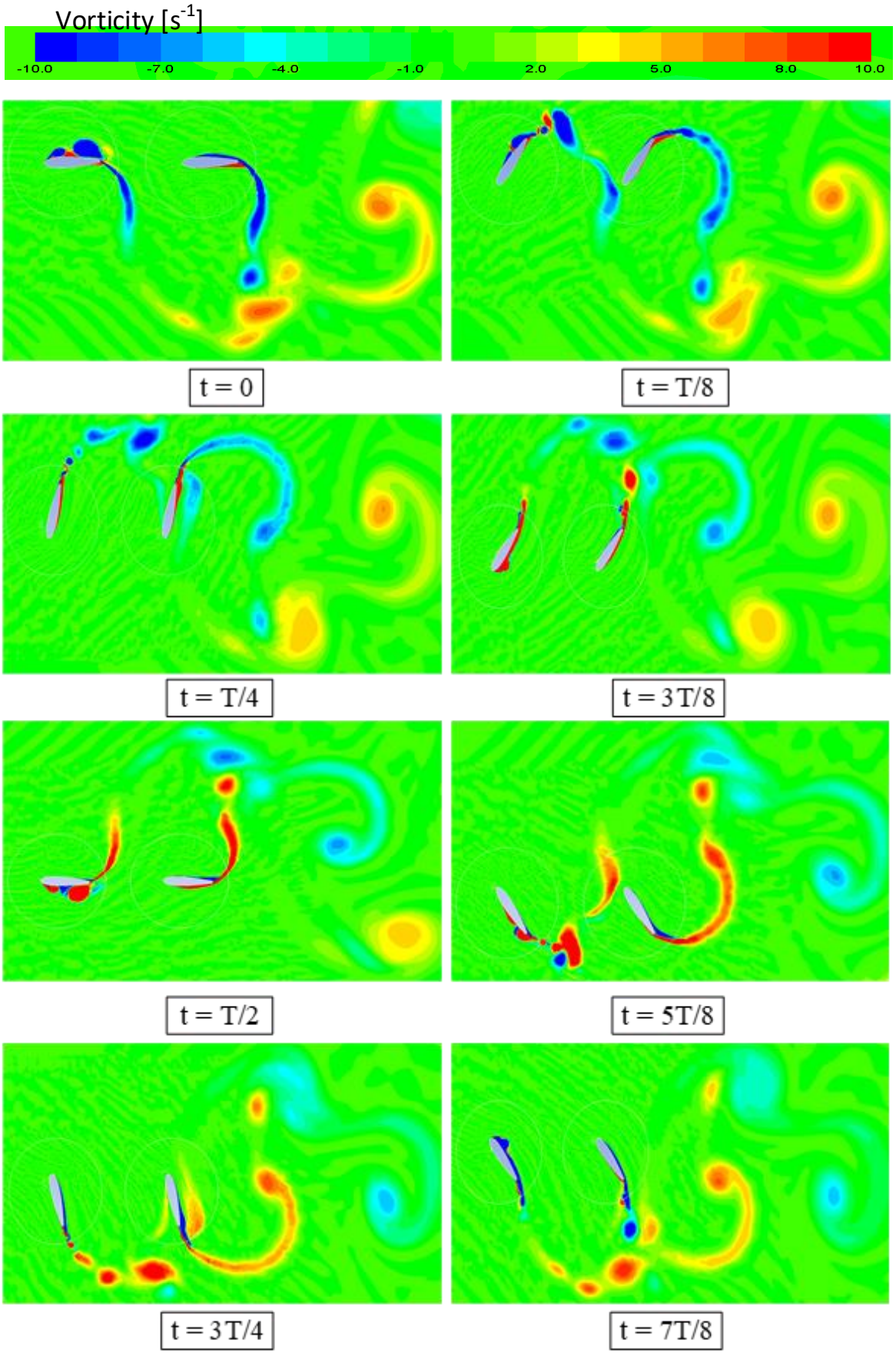

Figure 4. 38: Vorticity field for NACA0018 with blunt trailing edge shape over one cycle (blue: clockwise, red: counter-clockwise)

The presented data does shows an improvement in the power generation with the use of NACA0018 blunt trailing edge shape, as in the single blunt trailing edge airfoil. This improvement relates mainly to the downstream airfoil, with a total efficiency of more than 5% in comparison to the sharp airfoil. The flow vorticity also shows the vortex of the downstream airfoil is always attached to the airfoil surface throughout the cycle. Furthermore, the wake shedding has also contributed to the higher power generation.

4.2.5 Effect of Bluff Body on Oscillating Airfoil Energy Harvesting Efficiency

In this section, the study of the oscillating airfoil system was further extended to explore the interaction of the oscillating airfoil (NACA0015 sharp edge) with the bluff body (cylinder) on the energy harvesting efficiency. The upstream airfoil from the previous cases (Section 4.2.3) has been replaced with the cylinder and the rest of the simulations setup were remain the same. Based on the conclusion that have been made from the previous section, the simulations were narrow down and the investigation were carried out at reduced frequencies $f^* = 0.12$ and $f^* = 0.14$ and pitching amplitude $\theta_0 = 76.3°$. These simulations are referred as Case 4-0 and Case 4-1 for reduced frequencies $f^* = 0.12$ and $f^* = 0.14$, respectively.

Table 4. 9: Parametric study of Case 4 over two reduced frequencies and pitching amplitude

Case study	$\overline{C}_{P\,upstream}$	$\eta_{upstream}$	$\overline{C}_{P\,downstream}$	$\eta_{downstream}$	$\overline{C}_{P\,total}$	η_{total}[%]
			$f^* = 0.12, \theta_0 = 76.3°$			
Case 4-0 C1	0.3321	11.07%	0.5510	21.50%	0.8831	32.57
Case 4-0 C2	0.3155	10.52%	0.6509	25.40%	0.9664	35.92
Case 4-0 C3	0.3300	11.00%	0.6549	25.56%	0.9849	36.56
Case 4-0 C4	0.3579	11.93%	0.5207	20.32%	0.8786	32.25
			$f^* = 0.14, \theta_0 = 76.3°$			
Case 4-1	0.4594	15.31%	0.4908	19.15%	0.9502	34.46

From the results in Table 4.9, a special behaviour has been observed in Case 4-0, where a periodicity occurred after fourth cycle. The C1, C2, C3 and C4 are referred to cycle one,

two, three and four respectively. Figure 4.39 shows the vertical force C_Y of upstream and downstream bodies of Case 4-0 in eight cycle. It can be clearly seen that, the same curve is repeated after four cycle. Contrary to Case 4-1, a periodicity happens after each cycle (Figure 4.40). This shows that the reduced frequency has an expectedly strong effect on flow dynamics.

One similarity that can be observed from these two cases which differ from the case of the interaction between two airfoils is, the downstream body is generating more power as compared to the upstream body.

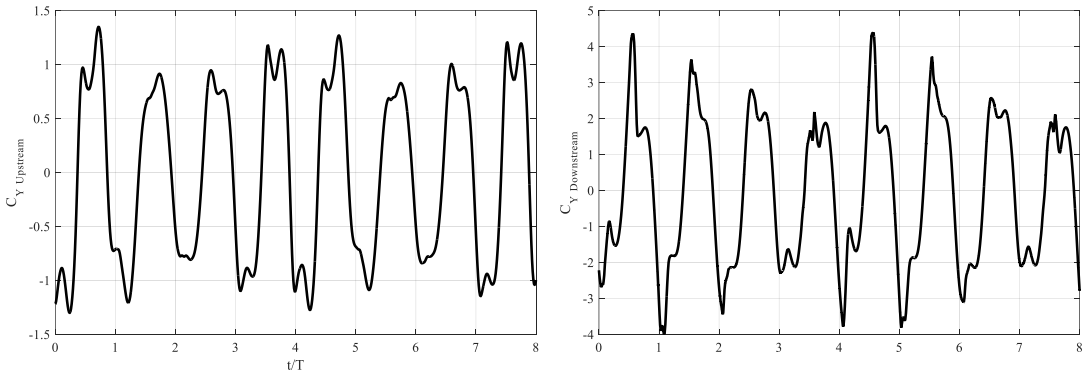

Figure 4. 39: Instantaneous vertical force C_Y of upstream and downstream bodies of Case 4-0 over eight cycle

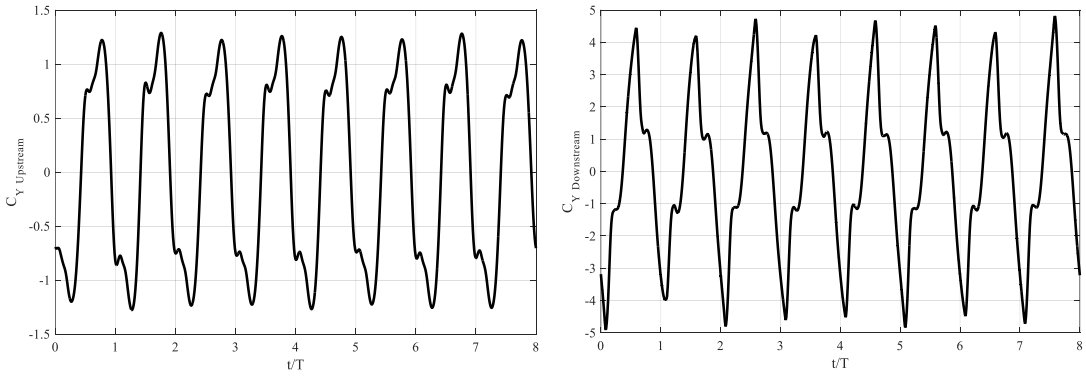

Figure 4. 40: Instantaneous vertical force C_Y of upstream and downstream bodies of Case 4-1 over eight cycle

In order to clearly examine the physics of the power generation, the instantaneous force and power coefficients are phase-averaged. Figures 4.41 and 4.46 show time histories of the heaving, pitching and total power coefficient for upstream and downstream bodies. It can easily seen that the downstream airfoil reaches higher vertical force values compared to the

upstream cylinder. This scenario is due to the aerodynamic shape that the airfoil has. The aerodynamic shape of the airfoil was chosen to provide advantages to the high lift generation.

Another observation from Figures 4.41 and 4.46 that can be stressed is the synchronization between the vertical force and the heaving velocity curve. By looking at the vertical force curve in Figure 4.48 (Downstream Airfoil Case 4-0 C1 & Downstream Airfoil Case 4-0 C3), it is clear that the vertical force of cycle one reached higher value as compared to cycle three, however cycle three generates more power and reached higher efficiency than cycle one. The same situation happened at Case 4-1 and Case 3-0 where the vertical force of the downstream airfoil Case 4-1 achieved higher value than vertical force of downstream airfoil in Case 3-0 but downstream airfoil in Case 3-0 achieved higher efficiency. This occurs because although more vertical force value is attained, yet the synchronization of the vertical force and the heaving velocity is imperfect.

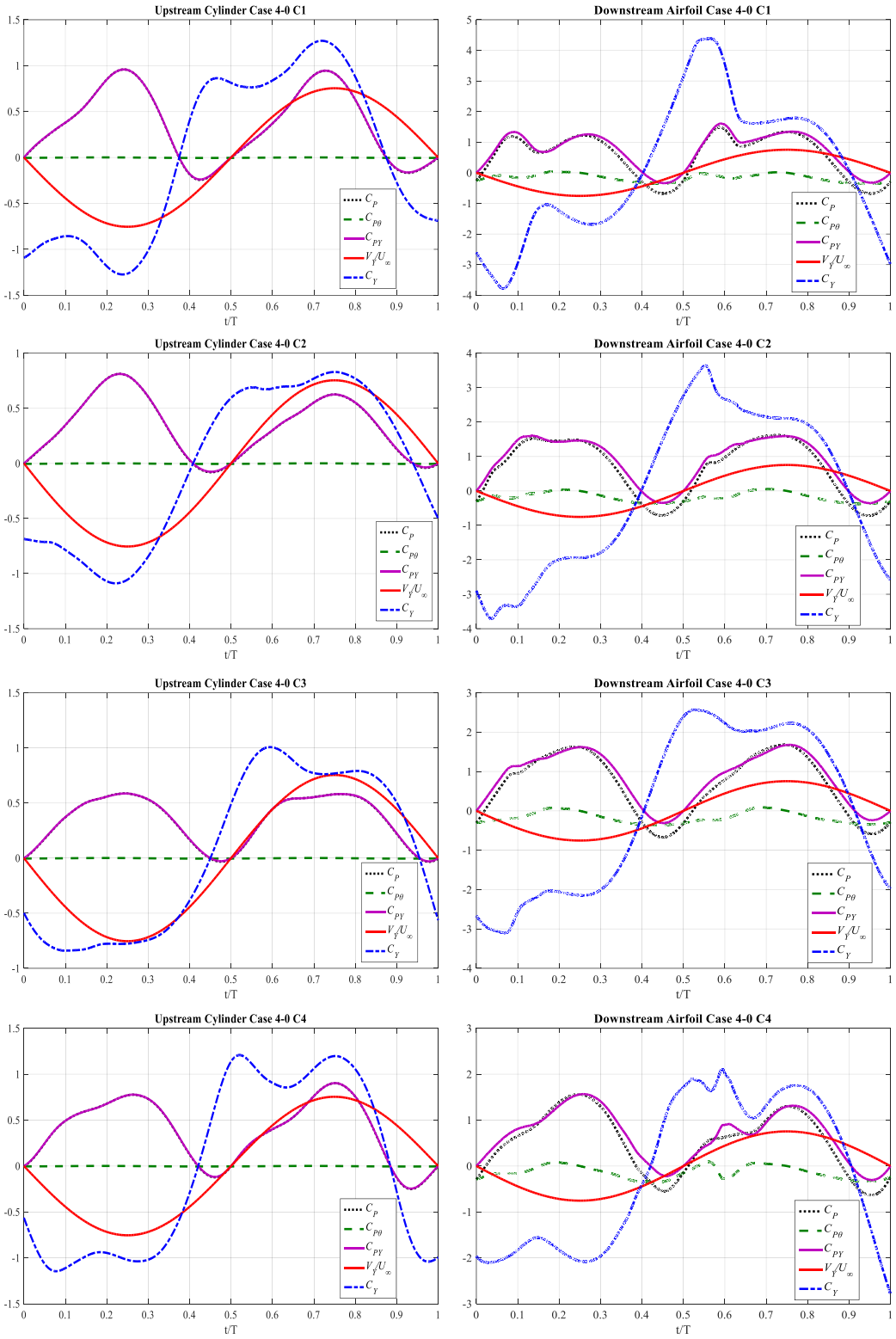

Figure 4. 41: Total power coefficient C_P, pitching contribution to power C_{P_θ},heaving contribution to power C_{P_Y}, V_Y/U_∞, and instantaneous vertical force C_Y over a periodic cycle for Case 4-0

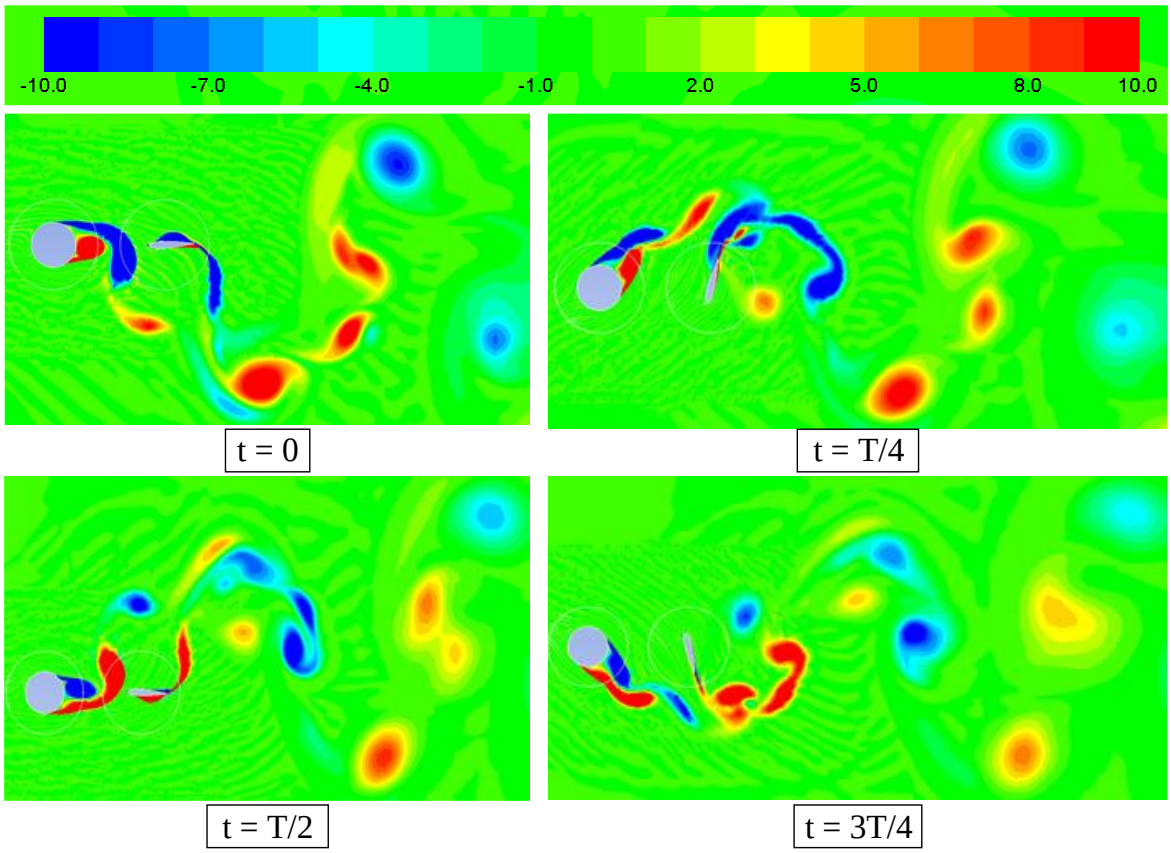

Figure 4. 42: Vorticity field for Case 4-0 C1 (blue: clockwise, red: counter-clockwise)

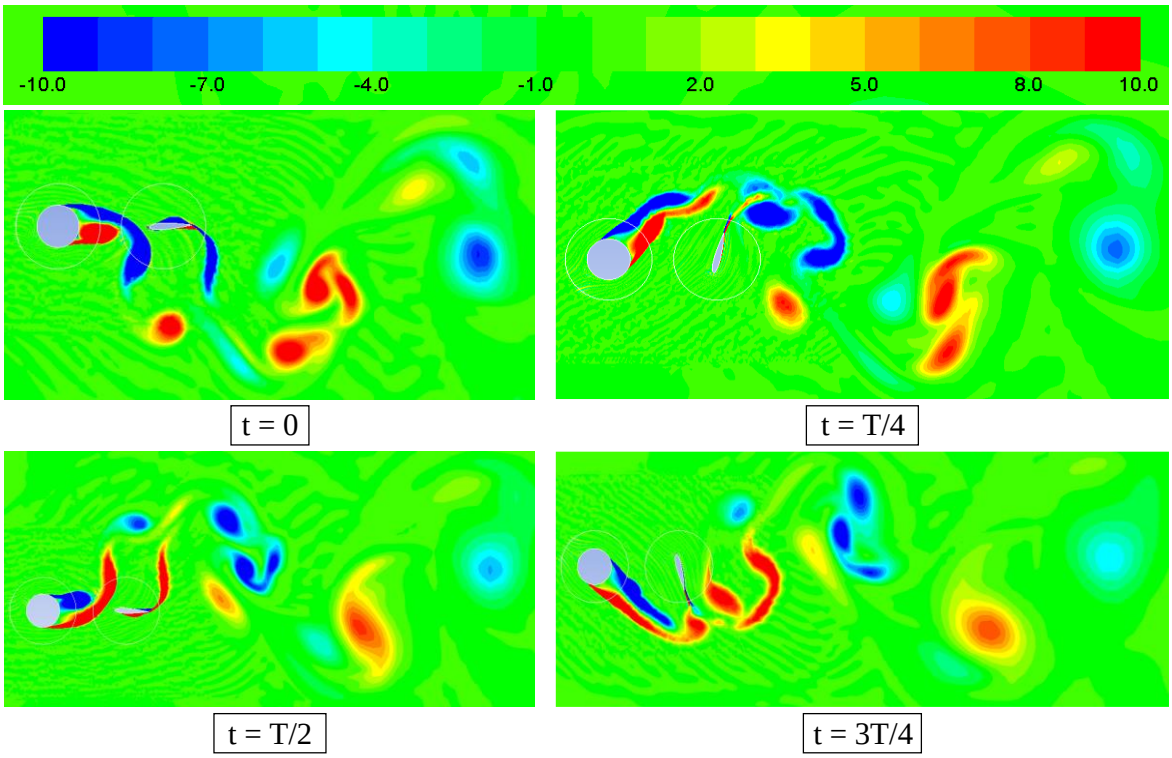

Figure 4. 43: Vorticity field for Case 4-0 C2 (blue: clockwise, red: counter-clockwise)

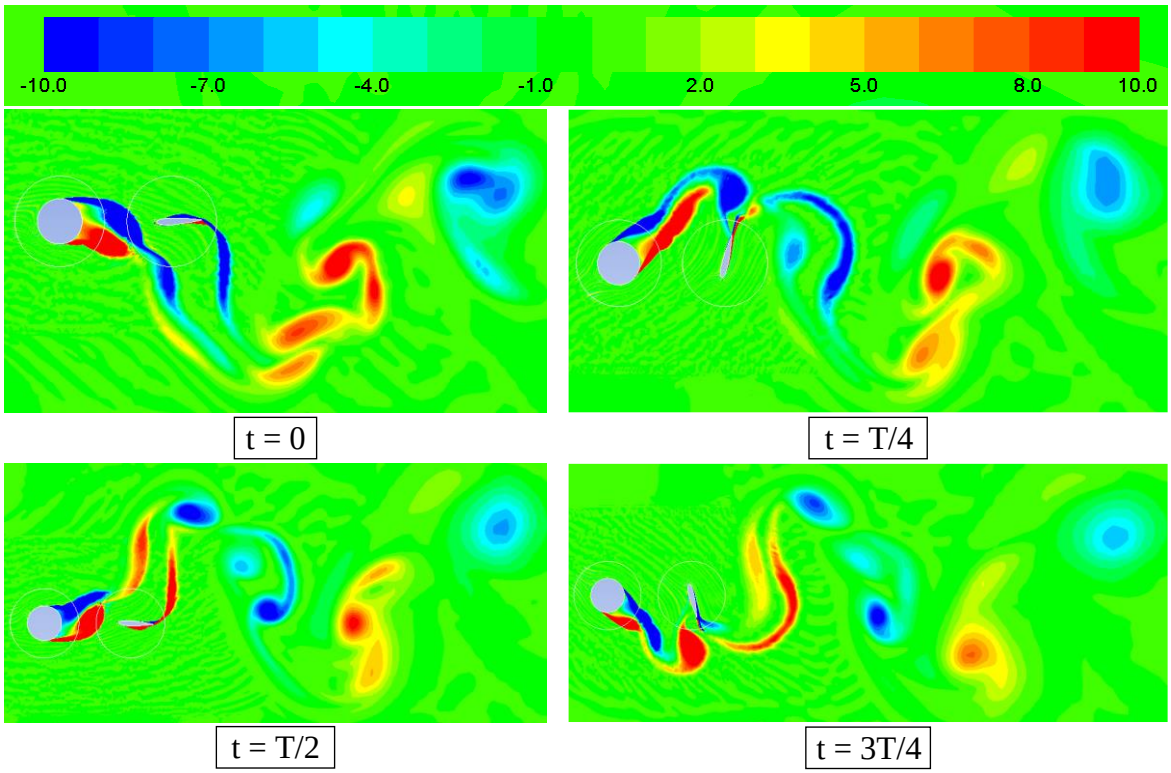

Figure 4. 44: Vorticity field for Case 4-0 C3 (blue: clockwise, red: counter-clockwise)

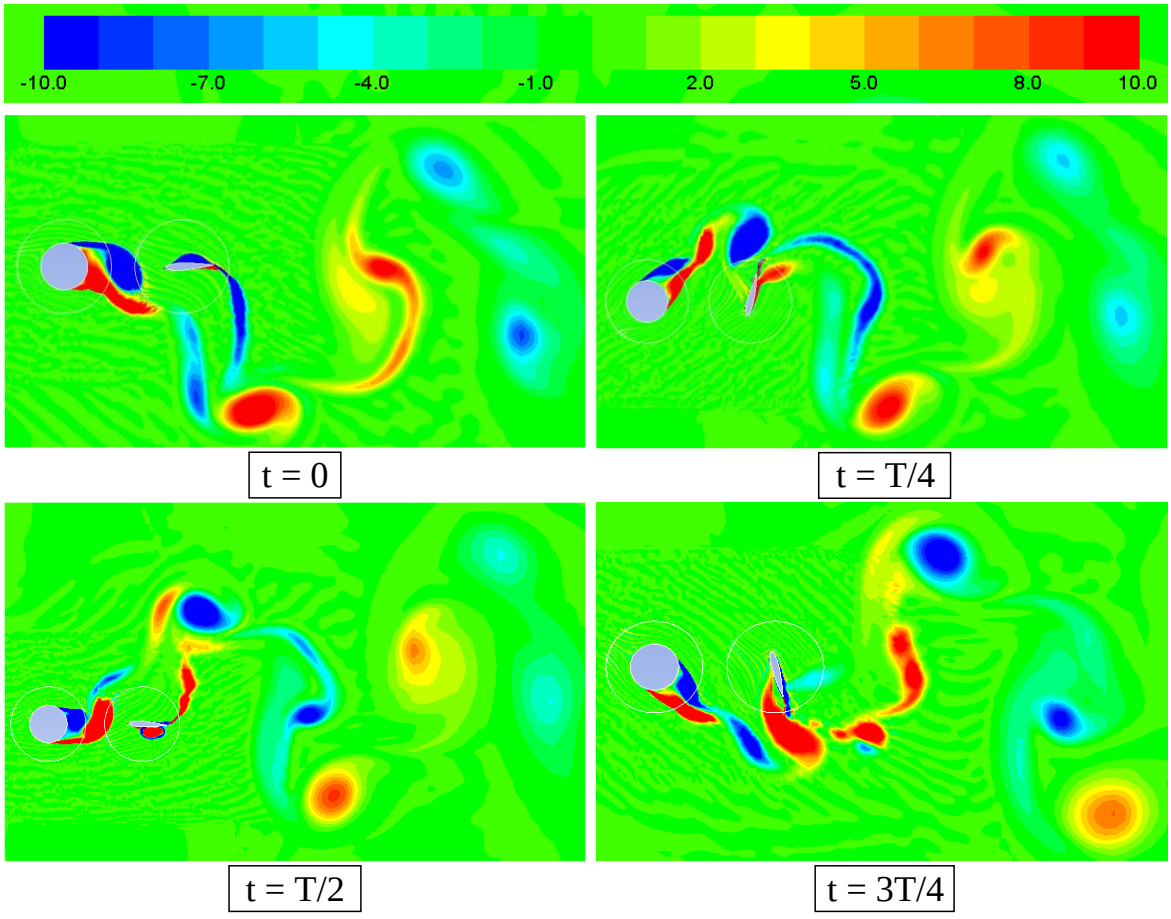

Figure 4. 45: Vorticity field for Case 4-0 C4 (blue: clockwise, red: counter-clockwise)

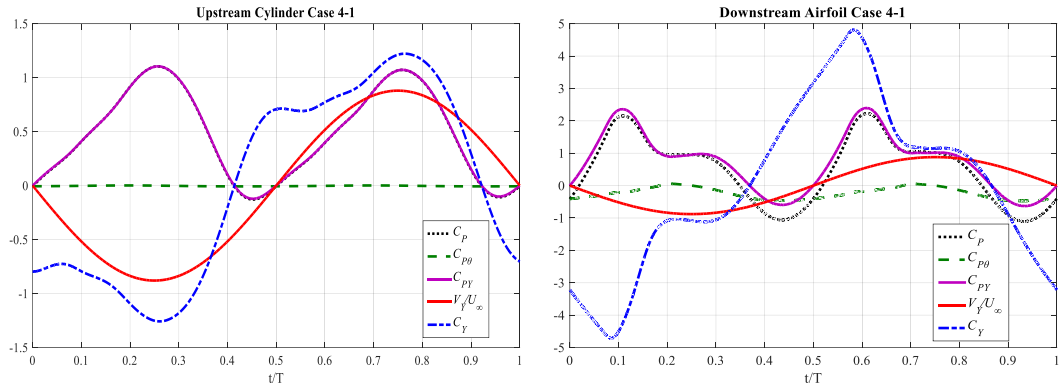

Figure 4. 46: Total power coefficient C_P, pitching contribution to power C_{P_θ},heaving contribution to power C_{P_Y}, V_Y/U_∞, and instantaneous vertical force C_Y over a periodic cycle for Case 4-1

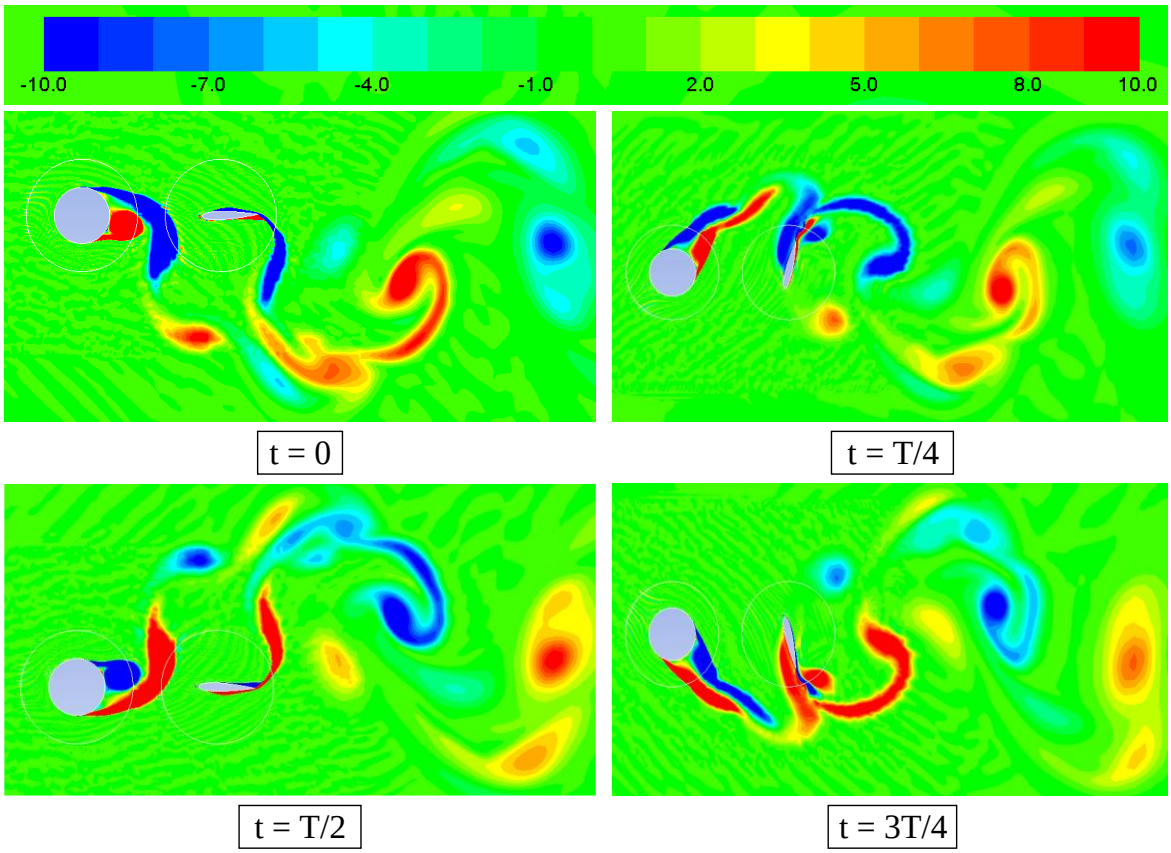

Figure 4. 47: Vorticity field for Case 4-1 over one cycle (blue: clockwise, red: counter-clockwise)

Furthermore, the vorticity plot in Figures 4.42 – 4.45 and Figure 4.47 show the strong interaction between wake vortices from the upstream cylinder and the downstream airfoil. Opposite to Case 3-0, this strong interaction of wake vortices was resulting in adding dynamic pressure to the downstream airfoil, which finally contribute to the increase performance efficiency.

4.2.5.1 Trailing Edge Modification-Bluff Body Effect on Energy Harvesting Efficiency

Here, the effect of the airfoil trailing edge modification on bluff body for possible energy harvesting improvements has been investigated by replacing NACA0015 sharp edge with NACA0018 blunt edge; as the blunt edge showed improvement in efficiency performance when two blunt edge airfoils are used (Table 4.8). The results of the new simulations (denoted Case 5) have been compiled and presented in Table 4.10, and Figures 4.48-4.49.

Table 4. 10: Parametric study of NACA0018 blunt edge

Case study	$\overline{C}_{P\,upstream}$	$\eta_{upstream}$	$\overline{C}_{P\,downstream}$	$\eta_{downstream}$	$\overline{C}_{P\,total}$	η_{total}[%]
			$f^* = 0.12, \theta_0 = 76.3°$			
Case 5-0 C1	0.3713	12.38%	0.5771	22.52%	0.9484	34.90
Case 5-0 C2	0.3582	11.94%	0.6621	25.84%	1.0203	37.78
Case 5-0 C3	0.3292	10.97%	0.6805	26.55%	1.0097	37.52
Case 5-0 C4	0.4199	14.00%	0.6645	25.93%	1.0844	39.93
			$f^* = 0.14, \theta_0 = 76.3°$			
Case 5-1	0.4849	16.16%	0.4994	19.49%	0.9843	35.65

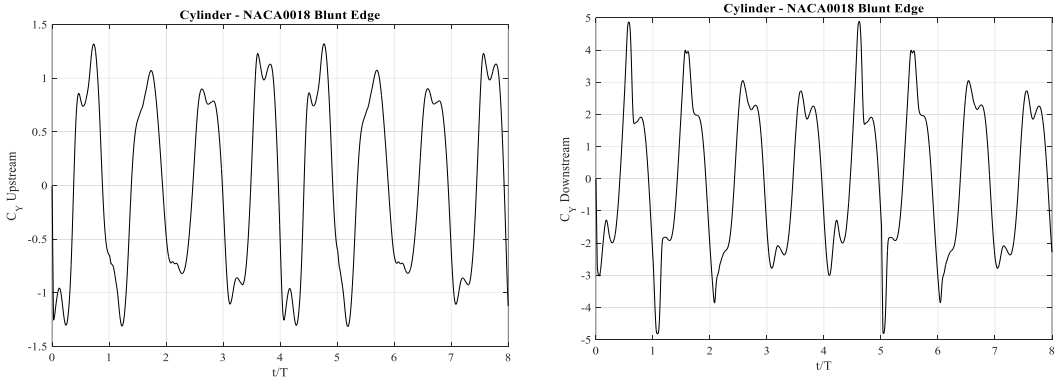

Figure 4. 48: Instantaneous vertical force C_Y of upstream and downstream bodies of Case 5-0 over eight cycle

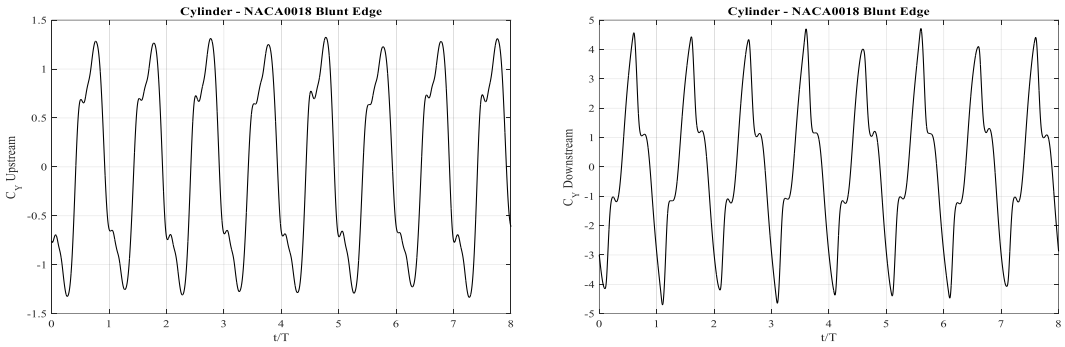

Figure 4. 49: Instantaneous vertical force C_Y of upstream and downstream bodies of Case 5-1 over eight cycle

Figures 4.48 and 4.49 show similar trends to Figures 4.39 and 4.40, respectively. However, the efficiency performance is slightly different with positive improvement in the new simulations.

Hence, we can conclude that, apart from the aerodynamic shape of an airfoil which contributes to the higher power generation, the airfoil's geometrical shape (i.e., thickness and trailing edge shape) does also play an important role in the improvement of the energy harvesting performance. Moreover, the dynamic pressure provided in the wake vortices is also important for the downstream airfoil to reach high vertical force value.

4.3 Summary

This chapter has focused on investigating the efficiency performance of energy harvesting system of single and multiple oscillating bodies. For single oscillating airfoils, simulations have been carried out for laminar and turbulent flows, and for multiple oscillating bodies they were carried out only in turbulent flow field.

For single oscillating airfoils, the investigations of energy harvesting efficiency were focused on the effect of the geometrical shape modifications for different thickness distribution (NACA0012, NACA0015 and NACA0018) and trailing edge shape modifications. For the thickness distribution, it is found that the highest difference in the efficiency performance between NACA0018 and NACA0012 airfoils is about 8% and 19% for laminar and turbulent flow fields, respectively. Hence, NACA0018 is used for further investigation on the influence of trailing edge shape modifications for energy harvesting. The modified trailing edge profiles applied to the oscillating airfoil are blunt, sharp and rounded. Modifying the airfoil trailing edge is found to have influence on the lift coefficient, especially for high a Reynolds number. From the results, it is observed that the blunt trailing

edge has a better efficiency than the sharp and rounded trailing edges. About 3% and 7% difference in performance efficiency between blunt, sharp and rounded edges occurred in laminar and turbulent flow field, respectively, with the blunt edge leading followed by sharp and rounded edges. Moreover, for all simulation cases that have been carried out for the single oscillating airfoils, the highest efficiency performance is found to occur at reduced frequencies $f^* = 0.14 - 0.18$.

For multiple oscillating bodies, simulations have been carried out for a range of parameters, such as the oscillation direction motion, the inter airfoil distance, airfoil trailing edge modification, and the interaction of bluff body with an airfoil, to investigate their effects on energy harvesting efficiency. For the two airfoils arranged in tandem configuration with 4*c* apart and are set to oscillate in the opposite direction, the negative energy has been produced, while when the same airfoils are forced to oscillate in the same direction, 24% increment in energy harvesting performance has been observed, as compared to the single oscillating airfoil produced energy. Secondly, when the separation distance of the two airfoils is shifted to 2.5*c* apart, an increase of 7% in efficiency has been observed as compared to 4*c* distance, and an increase of 30% in efficiency as compared to the single oscillating airfoil. The effect of trailing edge modifications on the efficiency performance for the multiple oscillating bodies has also investigated. Both the NACA0015 sharp trailing edge and the NACA0018 blunt trailing edge have been used, and it is found that there is an improvement in efficiency for the thicker and modified blunt trailing edge airfoil, with a total efficiency of more than 5% in comparison to the sharp airfoil-airfoil.

The investigation of multiple oscillating bodies is then extended to explore the effect of bluff body-airfoil interaction on the efficiency performance. From this study, a special behaviour has been observed at reduced frequency $f^* = 0.12$ where the periodicity happens at every four cycles. However, the efficiency performance is found to decrease when compared to the interaction between two airfoils (at 2.5*c* apart) with the loss of 37% - 45% at reduced frequency $f^* = 0.12$ and 38% at reduced frequency $f^* = 0.14$. When compared to single oscillating airfoils, at reduced frequency $f^* = 0.12$, the efficiency increases between 0.7% to 12%, but at reduced frequency $f^* = 0.14$ the efficiency drops by 12%. Simulations of bluff body were again run with NACA0018 blunt edge and a positive improvement in efficiency is attained. Thus, in summary, for the cylinder-airfoil interaction, the efficiency performance is found to decrease when compared to the two airfoils interaction; and for a better energy harvesting of two oscillating bodies in tandem the use of airfoil-airfoil interaction with blunt trailing edge is to be recommended.

Chapter 4

Chapter 5: Effect of Near Ground on Power Extraction

Two distinctly known research areas i.e. oscillating airfoils, and airfoil in ground effect when studied together, oscillating airfoils in ground effect reveal a novel line of research. Studies on oscillating airfoils investigate the exceptional aerodynamic and navigating abilities shown by fish swimming and flying insects while in-flight or hovering motions (Wu,2011 Platzer,2008). An inverted airfoil operating under the influence of ground is known as wing in ground effect (WIG). Under the influence of the ground, the oncoming flows compared to free stream produce a higher lift and reduction in the induced drag.

Inspired from the advantages of ground effect on lift enhancement for fixed wings, in this section we explore the effect near ground on the potential energy extraction of oscillating airfoils. This chapter investigates the aerodynamic performance and energy harvesting of oscillating wings in ground effect. It has been found that flow separation is promoted in ground effect. Its underlying mechanism is that the pressure on lower surface of the wing increases when the distance between the wing and the ground is below a critical value. The WIG effect has been successfully applied to the racing cars and wing-in-ground aircraft. However, the studies on the ground effect were mainly concentrated on the fixed wing. Very limited information is available on the ground effect related to flapping wings.

The present study aims to investigate the flow of flapping foils NACA0015 in ground effect for potential energy harvesting increase. Their flapping motion modes were induced through synchronous harmonic plunge and pitch rotation, on which the first type of existing flapping type energy generators is based. The effects of Reynolds numbers at laminar and turbulent flows, the location of airfoil pitching axis, the distance between the airfoil pitching axis and the ground, the amplitude and frequency of oscillation on power extraction by the flapping wing were examined using URANS. Based on the numerical results obtained, the evaluation of ground effect on the force behaviour as well as power extraction performance of the flapping wing were conducted.

5.1 Problem Description and Methodology

In this study, a NACA0015 airfoil were used to model the wing cross-section with the flapping motion. The most common NACA0015 is used for a validation process. As shown

in Figure 5.1, the foil which was placed in proximity to the ground experienced synchronous pitching and heaving motions.

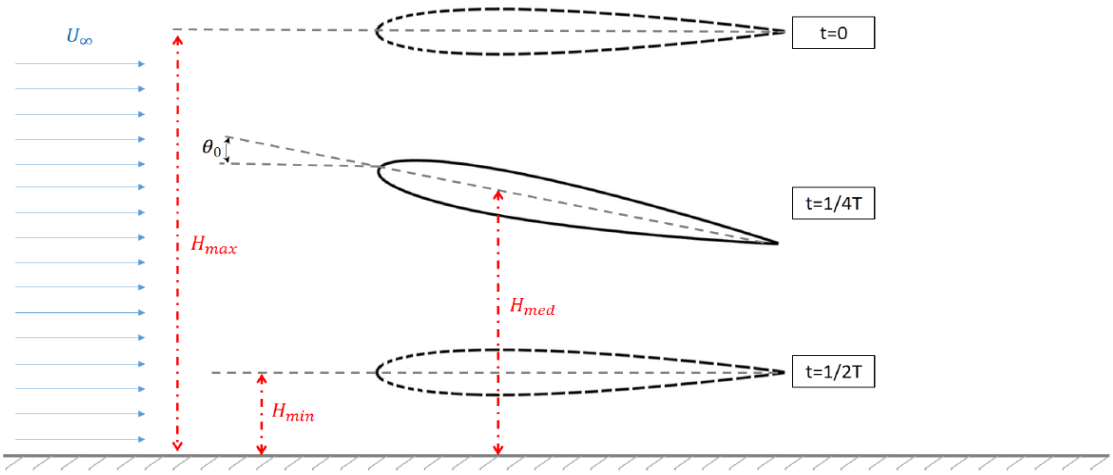

Figure 5. 1: Schematic of an airfoil in ground effect at different position over the cycle

During this process, the actuating mechanism in the system was neglected, which implies that the power was totally extracted from the kinetic energy of flow. Similar to the previous studies (Kinsey and Dumas, 2008; Xiao et al., 2012; Liu et al., 2013), the flapping motion of the foil was enforced and controlled. A simple harmonic motion mode was employed in this study. In the current study, the airfoil pitching axis was located at one third of the chord length from the leading edge and (ϕ) was fixed at 90 degrees. The parameter *c* was the chord of the airfoil.

One important parameter in ground effect is the height from the ground. Figure 5.1 shows a schematic of an airfoil in ground effect during half of the cycle. It can be seen that the minimum distance from the group occurs at $t = 1/2T$, whereas the maximum distance happens at $t = 0$. Hence, the equation describing the heaving motion is redefined to include the height, as shown in Eqn. 5.1.

$$h(t) = H_{med} + H_0 \sin(2\pi f t + \phi) \tag{5.1}$$

where H_{med} represents the medium height of the heaving oscillation and H_0 the amplitude of the heaving oscillation.

5.2 Numerical Method

In this work, the unsteady flow-fields of oscillating airfoil in ground effect were simulated using a 2D unsteady Reynolds-averaged Navier-Stokes (URANS) equations

with Menter's shear-stress transport k-w turbulence model. This model has been widely used for industrial and academic purposes and is well known to be able to deliver good predictions for flows involving a strong adverse pressure gradient and separation, which are usually the case for flows in ground effect. This has been also shown to work by previous studies for oscillating foils in freestream, for examples as in [Kinsey and Dumas, 2008, Kinsey *et al.*, 2011]. The iterative solution algorithm to solve these equations consisted of an initial approximation of the velocities, a Poisson equation for the pressure correction, followed by velocity correction that allows the computation of the new velocity and pressure fields. The governing equations are solved at the cell centers by a finite volume method. Second-order upwind discretization was used for the convection terms, and a second-order central difference scheme was used for the diffusion terms. The convection terms are interpolated at the cell faces through a Taylor series expansion. A first-order implicit time-marching scheme was used, with 30 sub-iterations per time-step. A time refinement study suggested that the optimal non-dimensional time step depends on the frequency. The time-step varied from 2×10^{-3}T to 1×10^{-3}T. That ensured a minimum number of time steps per period while also keeping an acceptable Courant–Friedrichs–Lewy number (based on the free stream velocity) in all the cells of interest. Lower time-steps did not yield a more accurate solution.

5.2.1 Grid Structure

The mesh is based on structured block around the airfoil and ground and an additional structured block 0.72c above the airfoil, extending up to the symmetry plane. The mesh was C-shaped, with 500 points around the airfoil and 30 points inside the boundary layer. The initial cell spacing normal to the surface was such that the wall - $y^+ = 1$ was close to unity. A mesh refinement study yielded a 151,000-point grid with a grid convergence index (Roache, 2013) of 0.26% in C_Y. The grid extended 10c upstream and downstream of the airfoil and10.5c above the airfoil. The distance to the ground was set according to the different ride heights studied. In the case of the airfoil out of the ground effect, the domain was extended $10.5c$ below the airfoil, and an additional unstructured block was inserted and the dynamic motion was implemented by rotating and vertically moving the airfoil (see section 5.2). The dynamic motion was implemented by allowing the cells around the airfoil and boundary layer to deform as the airfoil moves. A combination of smoothing and layering on the cells proved successful in keeping excellent aspect ratio and skewness on all cells throughout all the simulation. The edges between nodes behave as springs that are free to

adapt to the new boundaries. The deformation of the idealized springs results in imaginary forces at the nodes. At each time step, the condition of net force equal to zero at each node gives an iterative equation for the displacement of the interior nodes that must be solved. Using the displacements at the boundaries as the boundary conditions, it was found that 750 iterations were required to obtain a smooth deformation of the nodes. Figure 5.2 shows how the quality of the mesh is maintained at various incidences.

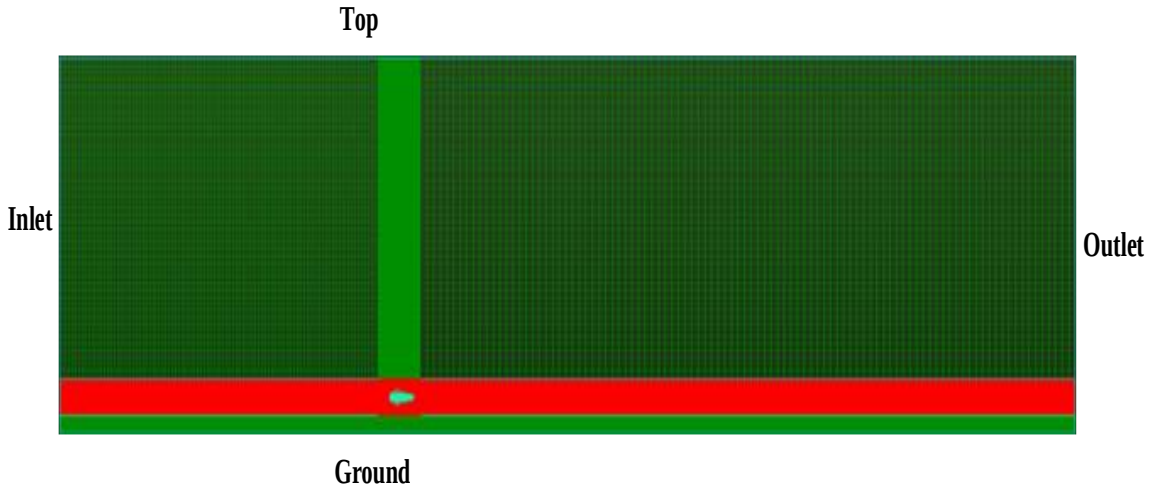

Figure 5. 2: Ground effect grid structure

5.2.2 Mesh Sensitivity Analysis

In this work, a mesh-independence study was conducted. This is because, at the moment there is no available published data that can be used to benchmarking our results. Hence, a rigorous grid resolution has been built in order to have a confident in our numerical simulation.

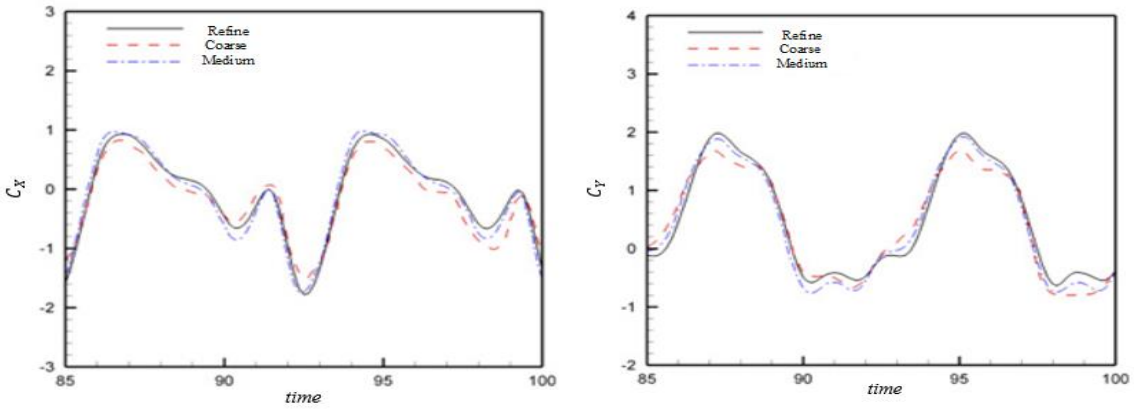

Figure 5. 3: Grid sensitivity analysis

Figure 5.3 highlights the convergence of the lift and drag coefficients over an oscillating cycle. The convergence study was carried out for NACA 0015 sharp trailing edge airfoil. Three discrete mesh resolutions namely coarse, medium and fine were tested subject to parameters plunging amplitude $H_0 = c$, f^*=0.18, and the airfoil pitching axis located at 1/3 of chord location. The instantaneous value of performance coefficients are throughout consistent for various mesh spacing, and this indicate that the medium spacing grid resolution is sufficiently refined, which enables accurate solutions to be obtained for this research work. Therefore, for the rest of the simulations the medium mesh resolution grid is selected to investigate the influence of the ground on the aerodynamic performance of foil oscillating at various ride heights for the sharp trailing edge shape for NACA0015. Table 5.1 shows the vertical and the horizontal force coefficients at two reduced frequencies, $f^* = 0.18$ and 0.14. The cycle average value of lift and drag coefficients indicate less than 2 percent variation for selected range of grid spacing resolutions.

Table 5. 1: Comparison results of vertical and horizontal forces

Operating parameters $H_0 = c \;\; H_{med} = c$	Mesh resolution					
	Coarse		Medium		Refine	
	$\hat{C}_Y$	$\bar{C}_X$	$\hat{C}_Y$	$\bar{C}_X$	$\hat{C}_Y$	$\bar{C}_X$
$f^* = 0.18$	0.462	1.21	0.495	1.243	0.502	1.245
$f^* = 0.14$	0.381	1.527	0.387	1.531	0.389	1.530

5.3 Results and Discussion

The numerical model is investigated for the sharp trailing edge NACA 0015. In these investigations the parametric study is focussed on the variation of reduced frequency, f^*, plunging amplitude, H_0 and mean, H_{med} ride hide while keeping the other kinematic and geometrical parameters as constant.

5.3.1 Ground Effect on Aerodynamic Coefficient and Efficiency

Under the influence of the ground the behaviour of oscillating airfoil is discussed here. In these simulations the plunging amplitude and the medium plunging amplitude are varied at c and $1.5c$ to model the influence of the ground for range of reduced frequency values. Figure 5.4 below shows the mean values of coefficients of vertical and drag forces. In order to compare the results, the standard free stream configuration placed far enough from the ground is taken as the benchmark to highlight the ground influence.

Moving closer to the ground has a positive impact on the energy extraction behaviour of the oscillating airfoil as shown in Figures 5.4 and 5.5. Similarly, the increase in effective angle of attack indicates gain in vertical lift force over the simulated range of reduced frequency values. As the mean ride height is decreased from $1.5c$ to c, the venture effect results in higher velocities through the section between ground and airfoil and consequently the lower surface of the oscillating airfoil experiences higher pressure force. For the simulated range, by gradually reducing the mean ride height increases this pressure and hence the vertical force coefficient also increases as expected, and a similar trend in the value of vertical force coefficient C_Y is seen over the experimented range of the reduced frequency.

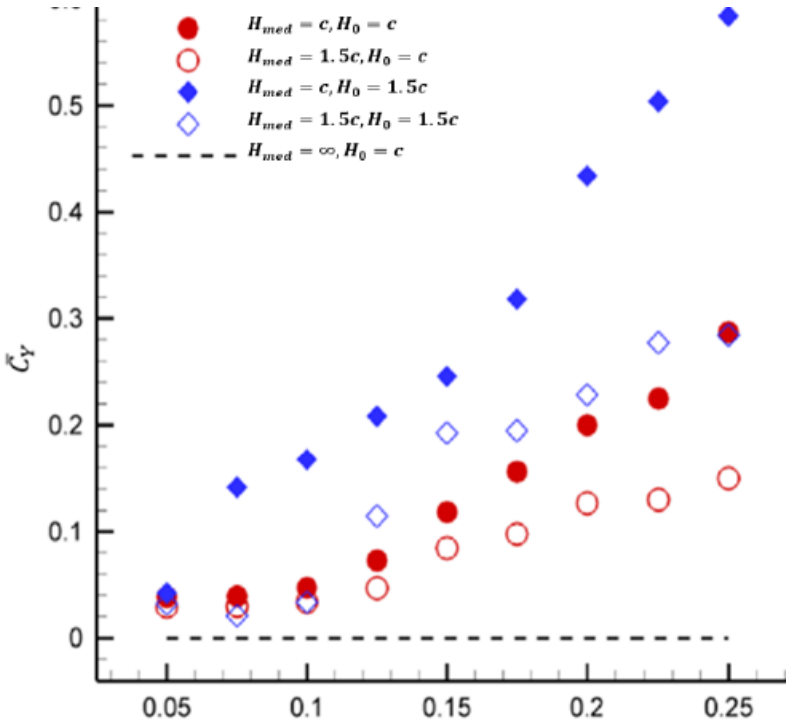

Figure 5. 4: Comparison of the mean vertical lift coefficient

Parametric variation of the mean moment coefficient is shown in Figure 5.6 for $H_0 = c$ and $1.5c$. The moment coefficients follow similar trends, i.e. ground proximity result in larger magnitudes of the moment coefficients. Although effective angles of attack are lower, the moment coefficient value is negative with reference to the benchmarked free stream case.

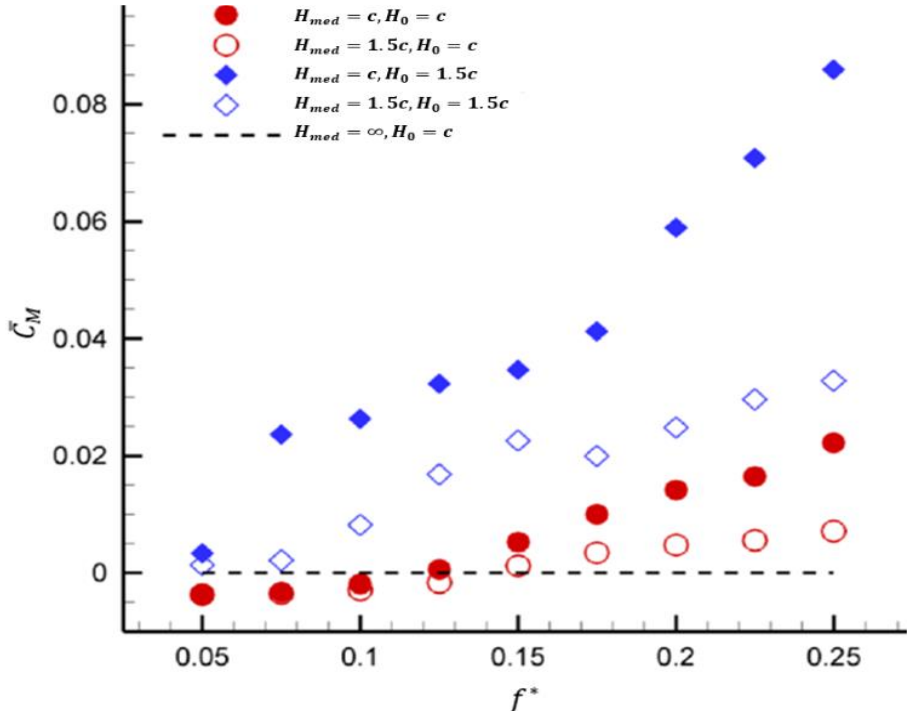

Figure 5. 5: Comparison of the mean moment coefficient

5.3.2 Performance Coefficient and Efficiency

In this section, the power coefficient and system efficiency are discussed. Following similar trends as in case of aerodynamic coefficients these two parameters also show positive influence of the ground proximity for energy extraction applications and shown in Figures 5.6 and 5.7. The maximum gain in power coefficient while reducing the mean ride height from $1.5c$ to $1c$ occurs at reduced frequency value of 0.18. The plots of power coefficient also indicate that at a particular mean ride height and a higher incidence angle value this result in a higher gain of power coefficient, irrespective of the reduced frequency used. Moreover, the improvement obtained in ground effect depends mainly on the perfect synchronization of the heaving velocity and the instantaneous lift which happen at $0.12 < f^* < 0.20$. For mean ride height equal to 1c, varying the effective angle of attack from 10 to 20^0 modifies the system efficiency value from 10.2% to approximately 24%. Power coefficient variable also follow a similar pattern in variation against the change in effective angle of attack at a specific mean ride height.

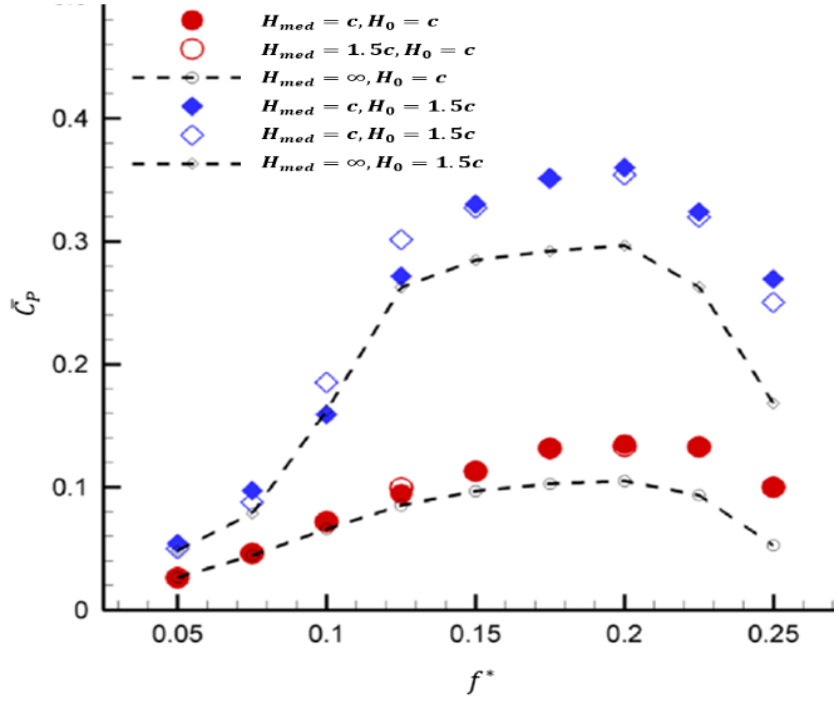

Figure 5. 6: Comparison of the power coefficient

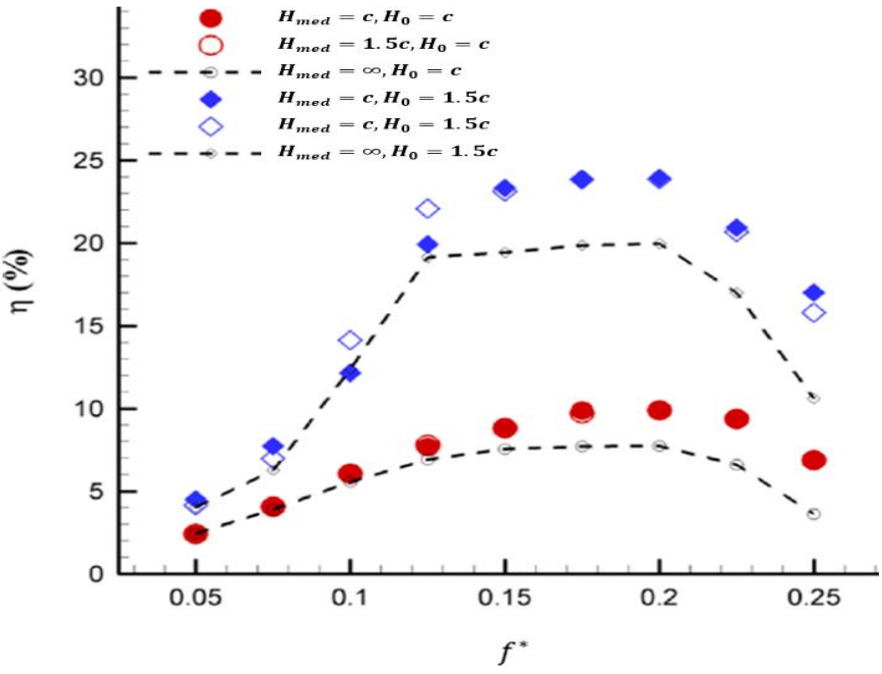

Figure 5. 7: Comparison of the efficiency

5.3.3 Parametric Analysis of Influence of Ground

In order to further investigate the ground effect on the vertical force and mean value of power coefficient another set of simulation is carried out. The mean ride height distance for this investigation is varied from $H_{med} = 1c$ to $5c$ while fixing the other applied condition of effective angle of attack at 10° and plunging amplitude $H_0 = 0.5c$. The response of the vertical force coefficient and power coefficient are plotted in Figures 5.8 and 5.9.

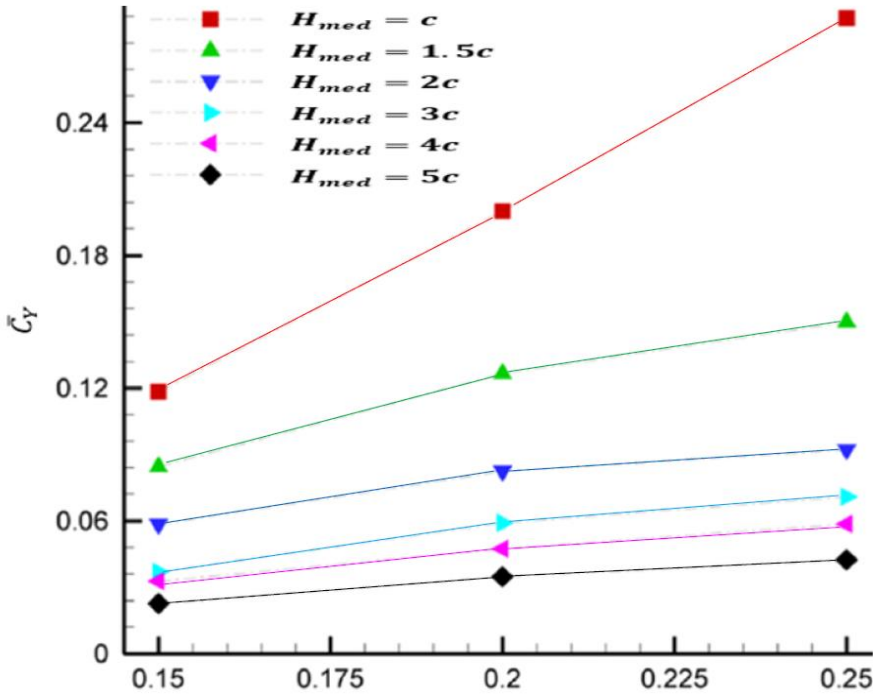

Figure 5. 8: Response of vertical lift coefficient for $H_0 = 0.5c$ and $H_{med} = c \; to \; 5c$

In case of vertical lift coefficient, the value of the parameter increases almost linearly as the influence of the ground is increased by reducing the mean ride height from 5c to 1c**.** On the other hand, the values of power coefficients as highlighted in Figure 5.10 show that the efficiency values decrease after attaining their peak values which correspond to a reduced frequency value of 0.2. This is due to the motion of the airfoil and the forces are not well synchronized for $f^* > 0.2$. For both parameters, power and vertical lift coefficients, the ground has a stronger influence against mean ride height range of 1c to 2c, and as such, values of these parameter show sharp variation. Whereas for the remaining simulated range of mean ride height values 2c to 5c, the response of power and vertical force coefficients show relatively less variation.

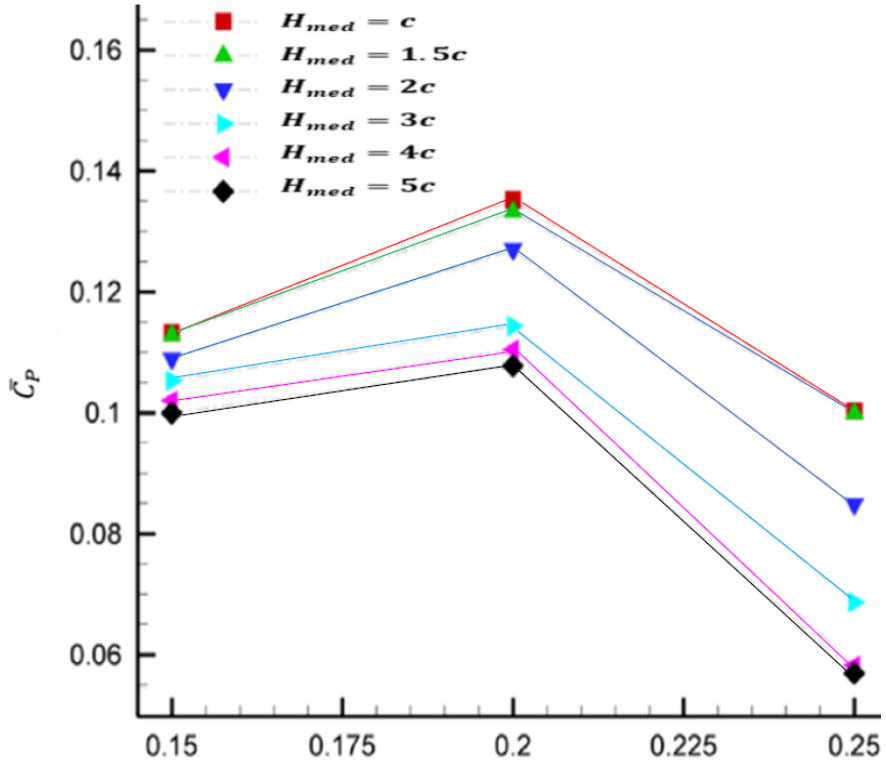

Figure 5. 9: Response of power coefficient for $H_0 = 0.5c$ and $H_{med} = c\ to\ 5c$

5.3.4 Effect of Pitching Amplitudes and the Oscillating Frequencies on the Energy Harvesting of Oscillating Foil in Ground Effect

To investigate the influence of the ground effect on the energy harvesting efficiency, in this section the airfoil is forced to oscillate at $Re = 1100, H_0 = c, H_{med} = 2c$ and $x_p = {}^{c}/_{3}$ and different pitching amplitude and oscillating frequencies. The reduced frequencies were chosen as 0.08, 0.10, 0.12, 0.14, 0.16, 0.20 and 0.25, at two different pitching amplitudes $(\theta_0 = 70°\ and\ 80°)$. These were the same data used in the free-stream simulation. Table 5.2 shows the results obtained for these operation values, together with those obtained for the free-stream case.

Looking at Table 5.2, it is clear that there was an increase in the peak lift coefficient $(\hat{C}_Y)$, for all the cases tested in ground effect, and with the peak lift coefficient showing the increment in percentage to be as high as 25.10%. However, in some cases, although there was an increase in the peak lift coefficient, a small reduction is obtained in the efficiency. Moreover, the improvement in power efficiency in ground effect is found to be depended mainly on the perfect synchronization of the heaving velocity and the instantaneous lift that happens at $0.12 < f^* < 0.2$. For lower and higher reduced frequencies, the increase in lift from ground effect is not always reflected in a better power efficiency (Table 5.2). From Table 5.2, the highest efficiency in ground effect is 36.92% which is found at $f^* =$

$0.16\ for\ \theta_0 = 80°$, and this corresponds to an improvement of about 8% in comparison to the freestream case. Figure 5.10 and 5.11 show the increase in the lift coefficient and also the mean lift coefficient ($\overline{C_Y}$) and mean moment coefficient ($\overline{C_M}$) over one cycle. Since the C_Y and C_M are symmetric for the free-stream cases, it is logical to assume that the $\bar{C}_Y$ and $\bar{C}_M$ are zero for the case far from the ground. Nonetheless, these coefficients become asymmetric when they oscillate near to the ground, as shown in these figures. Moreover, it can be seen that the mean lift coefficient increase consistently until $f^* = 0.15$ for $\theta_0 = 70°$ and $f^* = 0.20$ for $\theta_0 = 80°$, and then there is a decrease after this point. On the other-hand, for $\theta_0 = 70°$ the mean moment coefficient does not shown a clear trend, and for $\theta_0 = 80°$ the trend follows the same as observed for the lift coefficient.

Analysing Figure 5.10a and Figure 5.11b, it can be seen that there is an improvement in the efficiency for cases where the reduced frequency is in the range of 0.12 to 0.20 ($0.12 < f^* < 0.20$). In order to better understand why there is a slight reduction in the efficiency of the harvested energy for the others non-dimensional frequencies, a plot showing the instantaneous coefficients for those cases is presented. The first case corresponds to $f^* = 0.14$ and $\theta_0 = 80°$, where there is an improvement from 33.92% to 36.22%, while the second case corresponds to $f^* = 0.10$ and $\theta_0 = 80°$, with a reduction from 21.39% to 19.81%. Figures 5.12 and 5.13 show the first and second cases, respectively.

Examining Figure 5.12a, it is evident that there is increase in the lift coefficient in the last half of the cycle. Interestingly, in the first half of the cycle, when the airfoil undergoes its downward motion, there is a reduction in the lift coefficient. To illustrate this point, a sequence of instantaneous vorticity and pressure coefficient contours are shown in Figures 5.14-5.15 and discussed at this end of this section. The largest reduction experienced in the first half of the cycle (around t/T = 0.45), happens a little before the heaving velocity is changing signs (becoming positive), therefore, its magnitude is small. As such, the reduction of lift in this point of the cycle does have a small impact on the lift power coefficient, as it can be seen in the graph. However, for the second half of the stroke, the increase experience in the instantaneous lift coefficient is seen over the entire half cycle, not only on the peak. Therefore, the lift power coefficient for the case close to the ground shows a significant improvement.

Table 5. 2: Results of the oscillating NACA0015 at $Re = 1100, H_0/c = 1, H_{med}/c = 2$

f^*	$\overline{C}_X$	$\widehat{C}_Y$	$\widehat{C}_M$	$\eta(\%)$	$\overline{C}_X$	$\widehat{C}_Y$	$\widehat{C}_M$	$\eta(\%)$	$\Delta\eta$ relative to Freestream[%]
	Free-stream $\theta_0 = 80°$				**Ground effect $\theta_0 = 80°$**				
0.08	1.802	2.275	0.359	11.60	1.824	2.608	0.409	11.20	-3.45
0.10	2.206	2.103	0.646	21.39	2.180	2.471	0.611	19.81	-7.37
0.12	2.322	1.988	0.694	29.64	2.422	2.443	0.864	30.23	1.99
0.14	2.237	2.232	0.741	33.92	2.385	2.427	0.880	36.22	6.78
0.16	2.040	2.192	0.576	33.72	2.319	2.563	0.781	**36.46**	8.13
0.20	2.130	2.540	0.622	26.84	2.204	3.178	0.700	28.86	7.53
0.25	2.195	3.384	1.141	12.50	2.147	3.636	1.130	10.08	-19.36
	Free-stream $\theta_0 = 70°$				**Ground effect $\theta_0 = 70°$**				
0.08	1.636	2.040	0.593	16.18	1.618	2.260	0.441	15.42	-4.70
0.10	1.781	1.948	0.648	24.69	1.788	2.177	0.571	23.40	-5.22
0.12	1.835	1.741	0.521	30.13	1.836	2.100	0.639	31.54	4.70
0.14	1.591	1.732	0.382	30.46	1.671	1.984	0.504	32.62	7.09
0.16	1.493	1.862	0.366	29.20	1.565	2.078	0.371	31.20	6.85
0.20	1.337	2.136	0.493	20.70	1.384	2.333	0.487	22.45	8.45
0.25	1.199	2.881	0.793	3.99	1.231	3.066	0.771	4.56	14.29
	$\theta_0 = 70°$ $\widehat{C}_Y$				**$\theta_0 = 80°$** $\widehat{C}_Y$				

f^*	f. -stream	g. effect	(%)[$\Delta \widehat{\boldsymbol{C}}_{\boldsymbol{Y}}$]	f. -stream	g. effect	(%) [$\Delta \widehat{\boldsymbol{C}}_{\boldsymbol{Y}}$]
0.08	2.040	2.260	10.78	2.275	2.608	14.66
0.10	1.948	2.177	11.78	2.103	2.471	17.51
0.12	1.741	2.100	20.64	1.988	2.443	22.91
0.14	1.732	1.984	14.57	2.232	2.427	8.74
0.16	1.862	2.078	11.58	2.191	2.563	16.96
0.20	2.136	2.333	9.25	2.540	3.178	25.10
0.25	2.881	3.066	6.43	3.384	3.636	7.44

The differences shown in the drag coefficient (Figure 5.12b) are related to the fact that for the freestream case, the first and second half of the cycle always exhibited equal curves. However, in the cases when the airfoil is flapping in the proximity of the ground, the second half of the curve is no longer equal to the first half. This behaviour is related to the differences in the pressure around the airfoil as it moves close to the ground.

Comparing the curves in the Figure 5.12c, it can be seen that although the presence of the ground has changed the instantaneous moment coefficient at some points, its effect is compensated over the cycle. This can be seen when the efficiency is divided between the two motions (heaving and pitching). In the free-stream case, for this frequency and heaving amplitude, from a total of 33.92% efficiency, 31.08% were obtained from the heaving motion and 2.84% from the pitching motion, whereas in ground effect, from the total of 36.22% efficiency, 33.25% were obtained from the heaving motion and 2.97% from the pitching motion. Thus, the efficiency improvement is mainly obtained from the increase in the heaving component of the power extraction coefficient rather than on the pitching component. Similar trends were observed by (Wu et al. 2015) for different combinations of f^*, θ_0 , H_0/c, using the immersed boundary − lattice Boltzmann method for laminar flow.

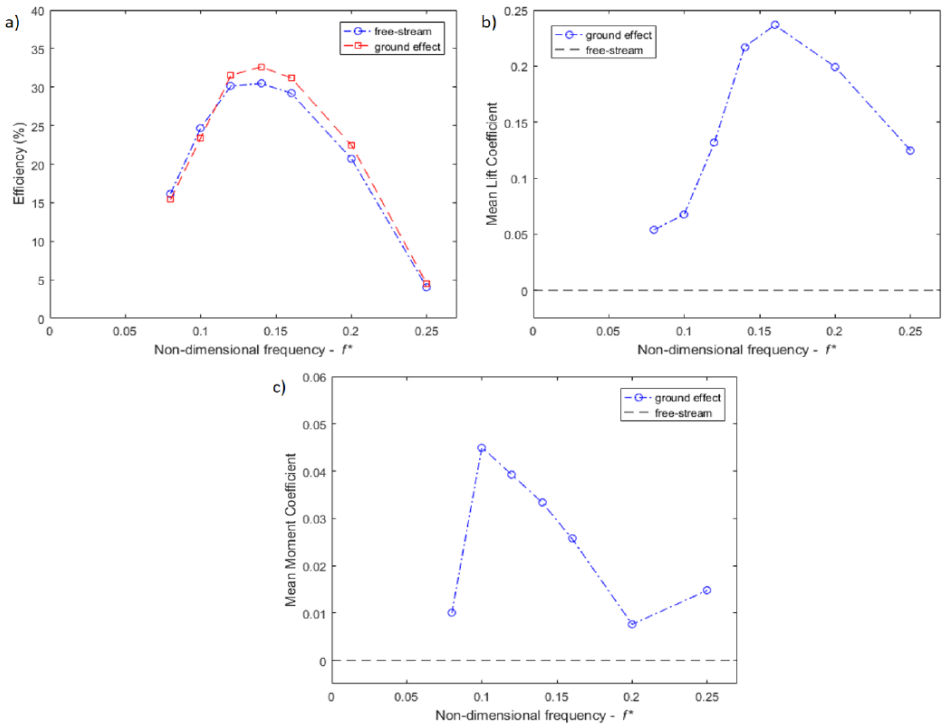

Figure 5. 10: Comparison of (a) efficiency, (b) mean lift coefficient and (c) mean moment coefficient for $Re = 1100, H_0/c = 1, H_{med}/c = 2, x_p/c = 1/3\ \theta_0 = 70°$

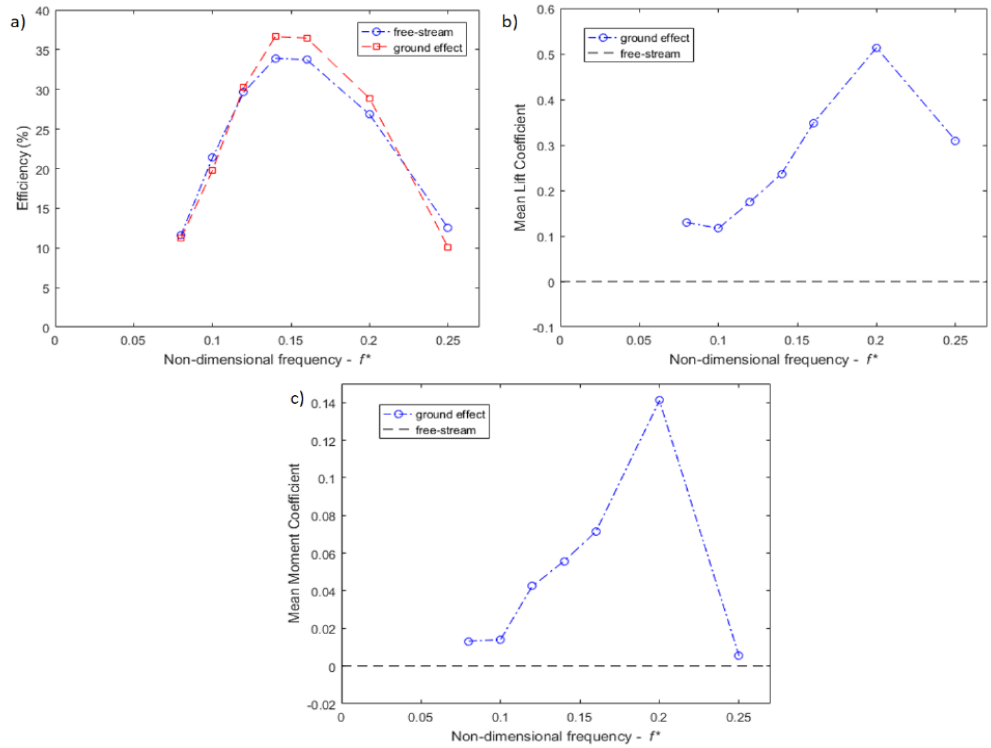

Figure 5. 11: Comparison of (a) efficiency, (b) mean lift coefficient and (c) mean moment coefficient for $Re = 1100, H_0/c = 1, H_{med}/c = 2, x_p/c = 1/3\ \theta_0 = 80°$

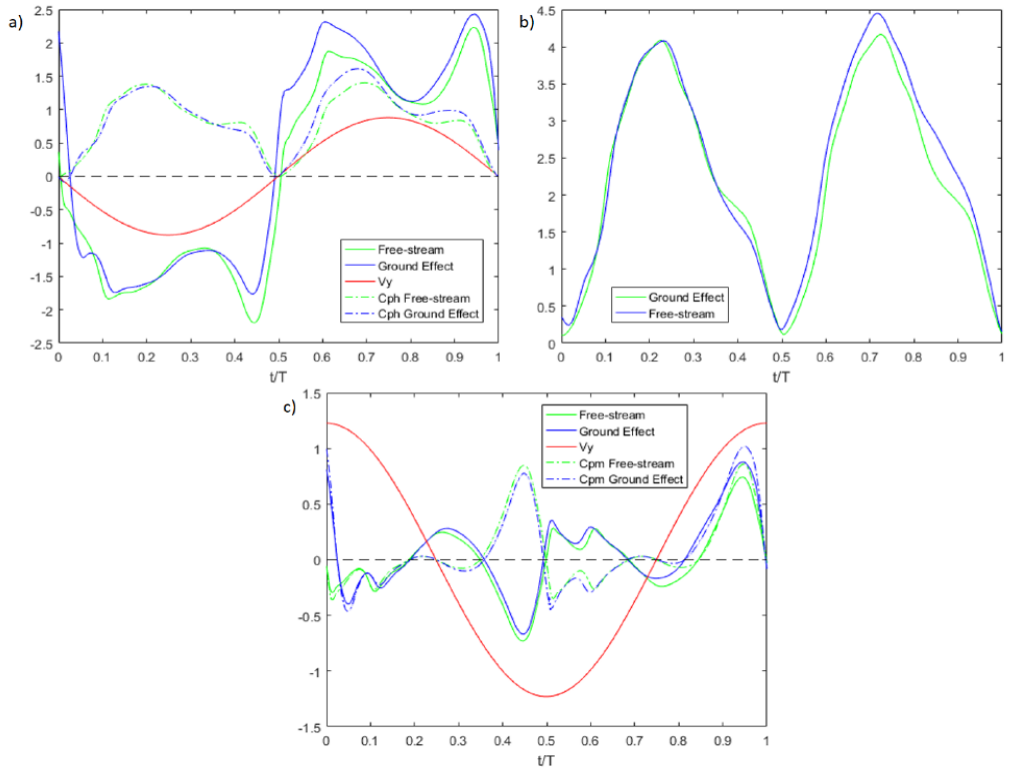

Figure 5. 12: Instantaneous coefficient (a) lift coefficient, (b) drag coefficient and (c) moment coefficient for $Re = 1100, H_0/c = 1, H_{med}/c = 2, x_p/c = 1/3, f^* = 0.14 \;\; \theta_0 = 80$

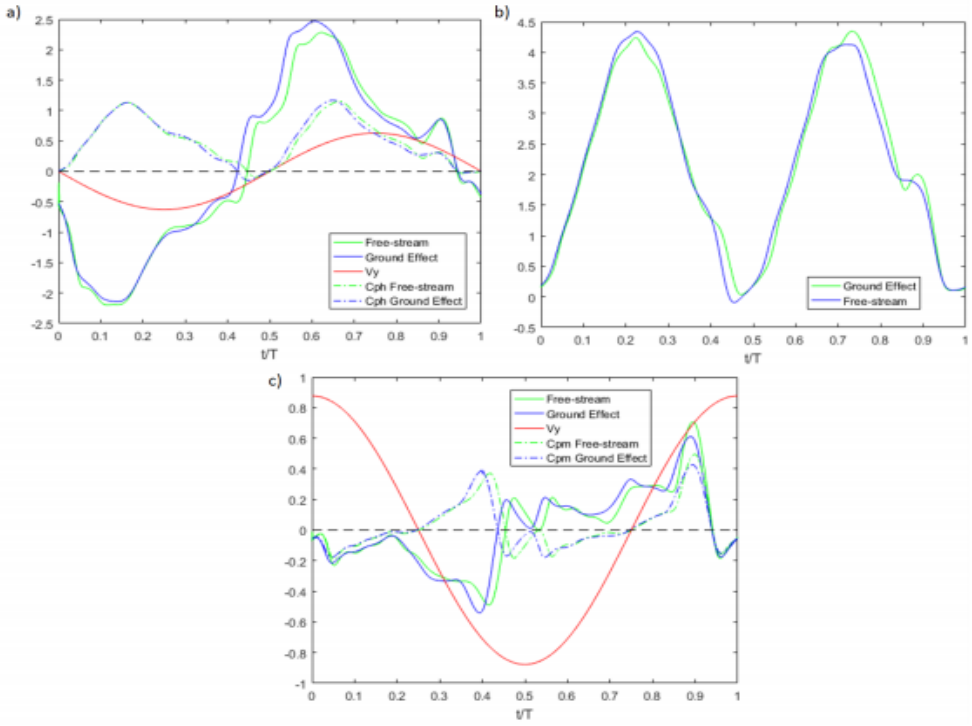

Figure 5. 13: Instantaneous coefficient (a) lift coefficient, (b) drag coefficient and (c) moment coefficient for $Re = 1100, H_0/c = 1, H_{med}/c = 2, x_p/c = 1/3, f^* = 0.10 \;\; \theta_0 = 80$

Evaluating Figure 5.13a, a similar trend as in Figure 5.12a case is obtained here, that is, there is a reduction in peak lift coefficient on the first half of the cycle and an increment in the peak lift coefficient on the second half of the stroke. However, as it is quite different than the previously case, the lift coefficient in the ground effect is smaller than the one obtained for the free-stream case over the whole second half of the cycle. Additionally, as there is not a perfect synchronization between the heaving velocity and the lift coefficient for this combination of f^* and θ_0 (a negative lift power coefficient takes place around t/T=0.45), if the lift coefficient is increased in this portion of the cycle, there will be a negative impact on the heaving power coefficient. This can be seen as the portion of the negative heaving power coefficient is higher for the ground effect case. Therefore, adding this two negative differences, a slight reduction is seen, which is about 1.58% in the efficiency. This lead to the conclusion that cases which deviate from the perfect synchronization between the motion and the force coefficient for a constant θ_0, tend to experience lower improvement or even worse efficiencies than the free-stream cases. This is observed for $f^* = 0.08, 0.10$ and 0.25 for $\theta_0 = 80°$ and $f^* = 0.08$ and 0.10 for $\theta_0 = 70°$. These observations can also be seen in Figures 5.10 and 5.11, for cases where there was an improvement due to the ground effect they happened around $f^* = 0.14$.

In order to further investigate the reason of the force coefficients' differences in free-stream (i.e., out of ground effect) and in ground effect cases, Figures 5.14 and 5.15 show the vorticity contours and the pressure coefficient, respectively, with plots over one whole cycle around the flapping airfoil. First, by analysing the vorticity plots (Figure 5.14), it is possible to identify the presence of the leading edge vortices (LEV) as a consequence of the dynamic stall, as it was explained previously. At t=2/8T, it is possible to see the formation of LEV, which at t=3/8T is already formed an is transferred along the airfoil surface. Also at t=3/8T, a stronger LEV in the free-stream case can be seen. This is the reason why it is possible to identify a more negative lift coefficient for the free-stream case around t=0.4T in Figure 5.12a. On the other hand, at t=6/8T and t=7/8T, the LEV formed in the ground effect case is stronger than in the free-stream. Moreover, this difference is also noted in the Figure 5.12a, where around this time of the period, the ground effect shows a higher instantaneous lift coefficient.

Examining Figure 5.15, the differences observed in the instantaneous force coefficients can also be seen in the pressure plots. The most evident difference is seen when the airfoil is moving away from the ground, at t=5/8T and t=6/8T. At these points, it is clear that the pressure under the airfoil is higher in ground effect case. These differences in the

pressure distribution around the airfoil can be explained by the venturi effect, which is formed when the airfoil is close to the ground, due to the differences in the area ratio formed from the ground to the leading-edge and to trailing edge. As the area ratio is changing, the pressure under the airfoil is also modified.

Thus, it can be concluded that the differences in the lift coefficient between the free-stream and the ground effect case are the result of two behaviours. Firstly, the interaction of the vortices with the ground and with the different pressure distribution generated by the presence of the ground. Secondly, the venturi effect that is observed in the points where the airfoil is closer to the ground and there is area ratio formed from the ground to the leading-edge and to trailing edge.

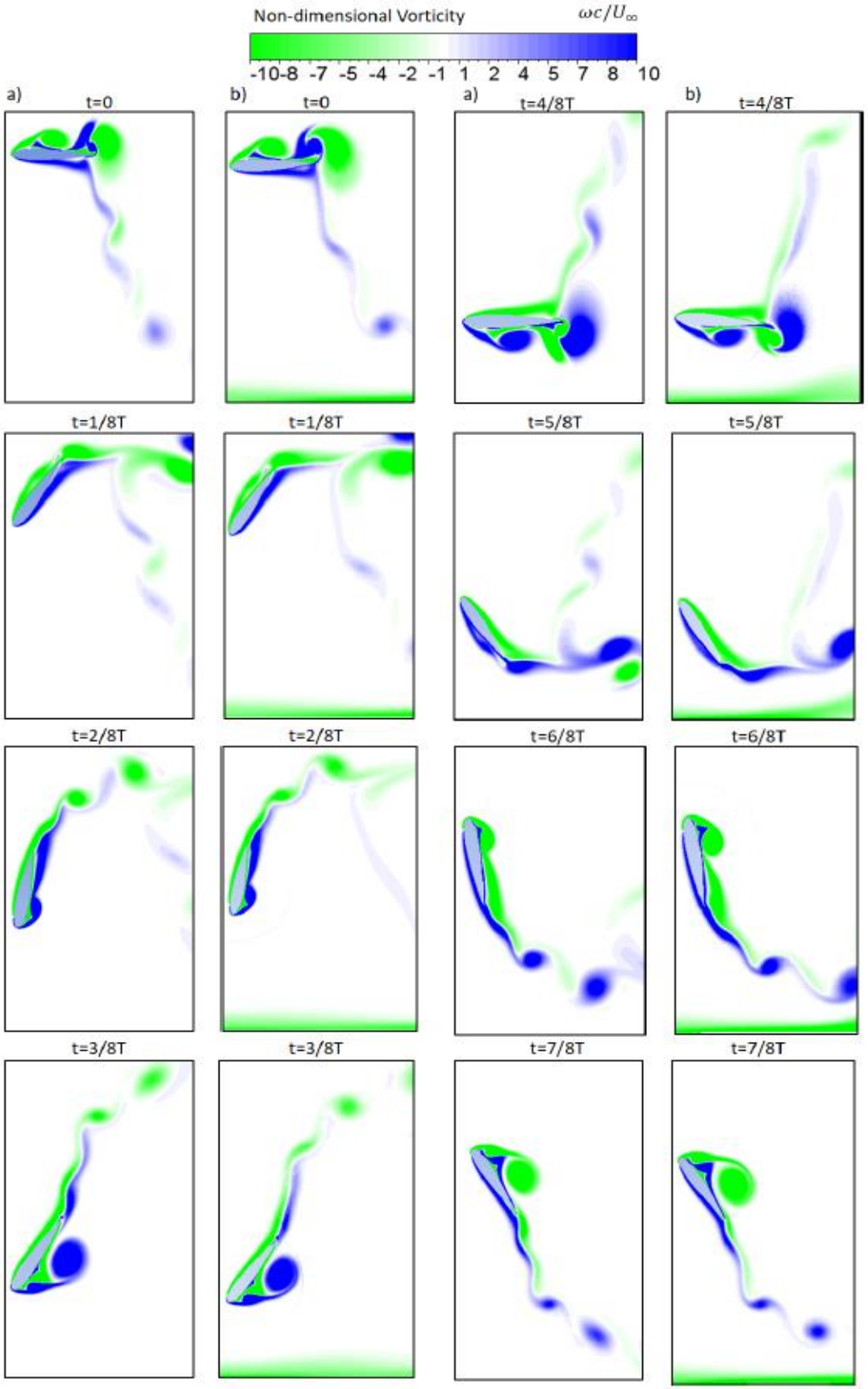

Figure 5. 14: Comparison of the vorticity plot for NACA0015 oscillating at $Re = 1100, H_0/c = 1, H_{med}/c = 2, x_p/c = 1/3, f^* = 0.14$ $\theta_0 = 80°$ for (a) free-stream and (b)ground effect

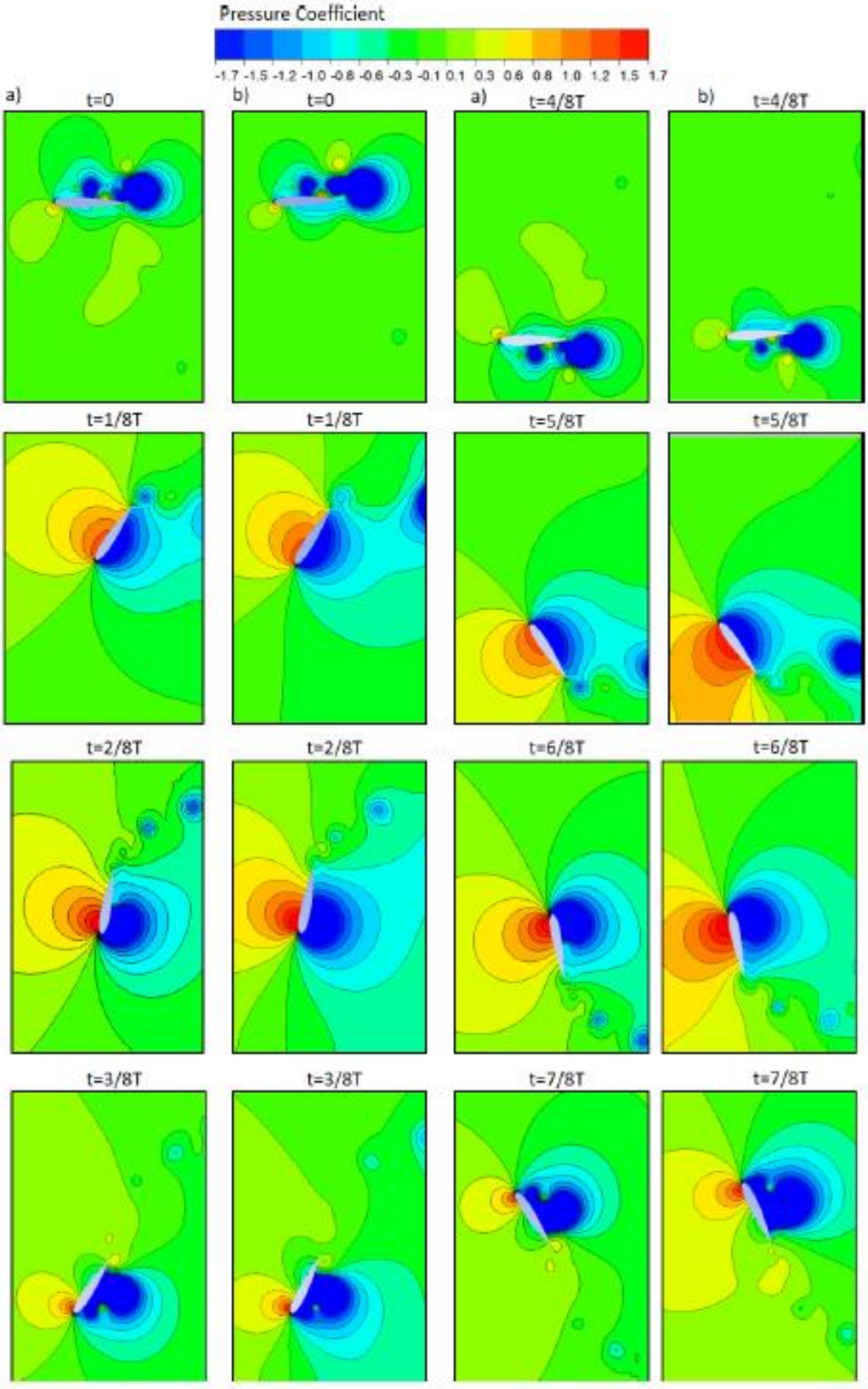

Figure 5. 15: Comparison of the pressure coefficient plot for NACA0015 oscillating at $Re = 1100, H_0/c = 1, H_{med}/c = 2, x_p/c = 1/3, f^* = 0.14$ $\theta_0 = 80°$ for (a) free-stream and (b) ground effect

5.3.5 Effect of Height

In the previous section, only one value of $H_{med}/c = 2$ was used during the investigation. Thus, to investigate the effect of changing the distance from the ground, numerical simulations were performed by varying this parameter. The mean height (H_{med} in Figure 5.1) was varied from $H_{med}/c = 2, 3, 4, 5, 6, 7 \text{ and } 8$ at $Re = 1100, H_0/c = 1,\ x_p/c = 1/3, f^* = 0.2\ \ \theta_0 = 70°$, for a NACA0015 oscillating airfoil. Figure 5.10 shows the peak, mean lift coefficient and efficiency as the airfoil is moved away from the ground, keeping all others parameters constant.

From Figure 5.16, it can be seen that as the airfoil is set to oscillate further from the ground, the lift coefficient and the efficiency values tend to the free-stream ones. It is worth mentioning though, that the drop in the efficiency is not as sharp as expected, thus a high performance of energy harvesting can be obtained for a wider range of heights. The reason is that the enhancements of the LEVS and the venturi effect become less noticeable as the distance from ground is increased.

Figure 5.17 shows the instantaneous lift coefficient over a whole cycle for different heights and free-stream. From figure 5.17, it can be seen that the curves tend to follow the free-stream, as the airfoil is oscillating away from the ground. Another relevant observation is that the C_Y improvement is usually found in parts of the cycle that are close to the peak portions of the curve, which is different than the case shown in Figure 5.12 for $f^* = 0.14$ and $\theta_0 = 80°$, where the increase in C_Y is found to be better spread along the cycle.

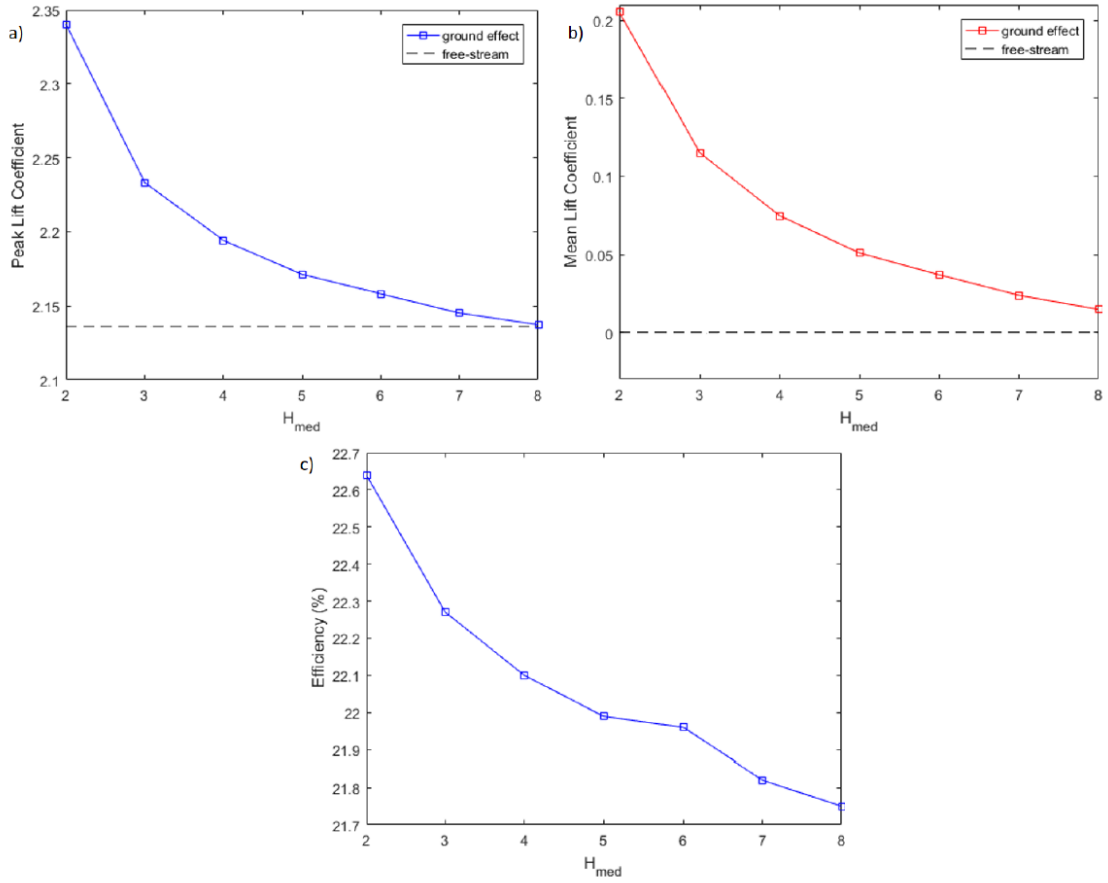

Figure 5. 16: Effect of the distance from the ground on the (a) peak lift coefficient, (b) mean lift coefficient and (c) efficiency for $Re = 1100, H_0/c = 1, x_p/c = 1/3, f^* = 0.12 \;\; \theta_0 = 70°$

5.3.6 Effect of the Reynolds Number

Finally, the effect of a higher Reynolds number (turbulent flow) on the energy harvesting efficiency in ground effect was investigated. Here, an airfoil was forced to oscillate in a turbulent flow with a Reynolds number of 5×10^5. The other parameters were kept constant as $H_0/c = 1, H_{med}/c = 2, x_p/c = 1/3, f^* = 0.14 \;\; \theta_0 = 76.3°$, and they were the same parameters as those used in the free-stream turbulent case. The turbulence model used is the $k - \omega$ SST with low-Reynolds correction, as in the free-stream turbulence case. The turbulent inlet boundary condition at the inlet is set to 0.1% and the turbulent viscosity ratio to 0.01. The initial cell spacing normal to the surface was such that the wall $y^+ = 1$ was close to unity.

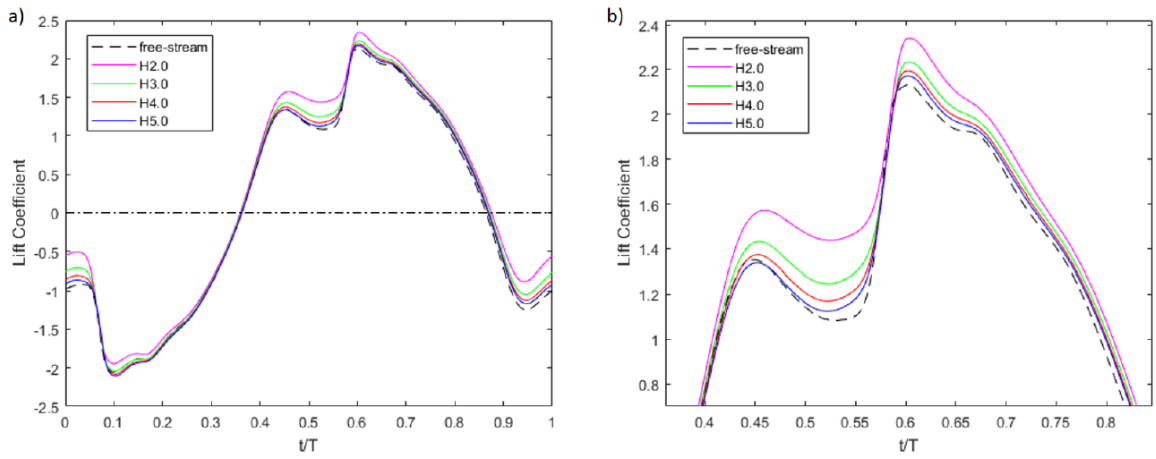

Figure 5. 17: Comparison of the (a) instantaneous lift coefficient over a whole cycle for different heights and (b) detail of one peak for $Re = 1100, H_0/c = 1, H_{med}/c = 2, x_p/c = 1/3, f^* = 0.12 \;\; \theta_0 = 70°$

Table 5. 3: Comparison of NACA0015 at $Re = 5 \times 10^5, H_0/c = 1, H_{med}/c = 2, x_p/c = 1/3\,, f^* = 0.14 \; and \; \theta_0 = 76.3°$

Source	$\bar{C}_X$	$\hat{C}_Y$	$\hat{C}_M$	$\bar{C}_P$	$\eta(\%)$	$\Delta\eta$ relative to Freestream[%]
Turbulent – freestream	1.775	2.916	0.523	0.998	39.12	-
Turbulent- ground effect	2.008	3.129	0.527	1.085	42.34	8.23

Table 5.3 shows the results obtained for the turbulent case in ground effect, together the free-stream case for comparison. In comparison to the freestream turbulence, the efficiency in ground effect has been increased by 8.23% (Table 5.3), i.e., slightly larger than the improvements observed in the laminar cases (Table 5.2). Moreover, the efficiency for the turbulent freestream in ground effect is 42.34% (Table 5.3), whereas for the laminar case in ground effect the maximum efficiency is found to be 36.46% (Table 5.2). This corresponds to an efficiency improvement of more than 16%. Compared with the laminar cases, the improvement in peak lift coefficient of 7.3% (Table 5.3 for $\hat{C}_Y$) is below the average obtained of 14.2% (Table 5.2). In spite of this, there is an improvement in the average power coefficient, which is reflected in the increase in the efficiency.

To better understand the differences not only on the peak and mean coefficients, but also along the whole cycle, Figure 5.17 shows the evolution of the instantaneous lift coefficient, drag coefficient and moment. In those graphs, it has been also included the heaving velocity, angular velocity, lift power coefficient and moment power coefficient. Initially, inspecting the coefficients related to the heaving motion (Figure 5.17a), it can be seen that there is improvement in the lift peak coefficient in the second half of the cycle. Moreover, it can also be seen that this enhancement is maintained for the whole range after the second half of the cycle. As it was seen for laminar cases, there is also a reduction in the lift coefficient in the first half of the cycle. The improvement however in the second half overcomes the reduction in the first half, and this is reflected in the improvement of the efficiency. This can also be seen by observing the difference between the lift power coefficient curves for the free-stream and ground effect.

Figure 5.18b shows the instantaneous drag coefficient both in freestream and ground effect. Differently than the laminar case (Figure 5.17b), the drag coefficient for the turbulent in ground effect is higher at the two peaks. Aside from the peak, the main differences are present in the second half of the cycle, as happened for the laminar in ground effect. In Figure 5.18b, the average drag coefficient $\bar{C}_X$ is positive, which indicates a net drag cycle. Since the airfoil is actually not moving horizontally, but only heaving and pitching into a uniform flow from left to right of speed U_∞, hence only the lift force (vertical component) contributes to the power extraction. However, while the drag does not directly influence the power extraction capabilities, the drag on the foil is an important design consideration, as it will influence how the device is mounted. Although it may yield optimal power, a large relative angle of attack increases the drag forces significantly since the foil is acting like a bluff body for much of its stroke, presenting significant structural engineering challenges.

Finally, from Figure 5.18c it can be seen that the moment coefficients for the cases in ground effect and free-stream are quite similar (i.e., small difference between them). Examining the time history of the moment coefficient, it can see that the main discrepancies take place around t/T=0.6 and t/T=0.95, i.e., regions where the angular velocity has low magnitude. As such, this does not have a large effect on the moment power coefficient. In free-stream, the moment power coefficient was -9.12%, whereas for the ground effect, the moment power coefficient is -8.23%. As already mentioned, the negative value of efficiency means that in the majority of the cycle the moment coefficient and the angular velocity have opposite signs, thus, instead of harvesting energy, work is being done over the flow (transfer energy to the flow).

From the analysis conducted for turbulent flows, it can be concluded that the ground effect can also be used to enhance the energy extraction efficiency for turbulent flows. However, although the peak lift coefficient had a lower improvement when compared to the laminar cases, for the case analysed in the present study, it seems that turbulent flow have a slightly larger potential of enhancing the energy efficiency. Thus, it would be interesting to further investigate this potential for a wider variety of pitching amplitudes and frequencies for turbulent flow.

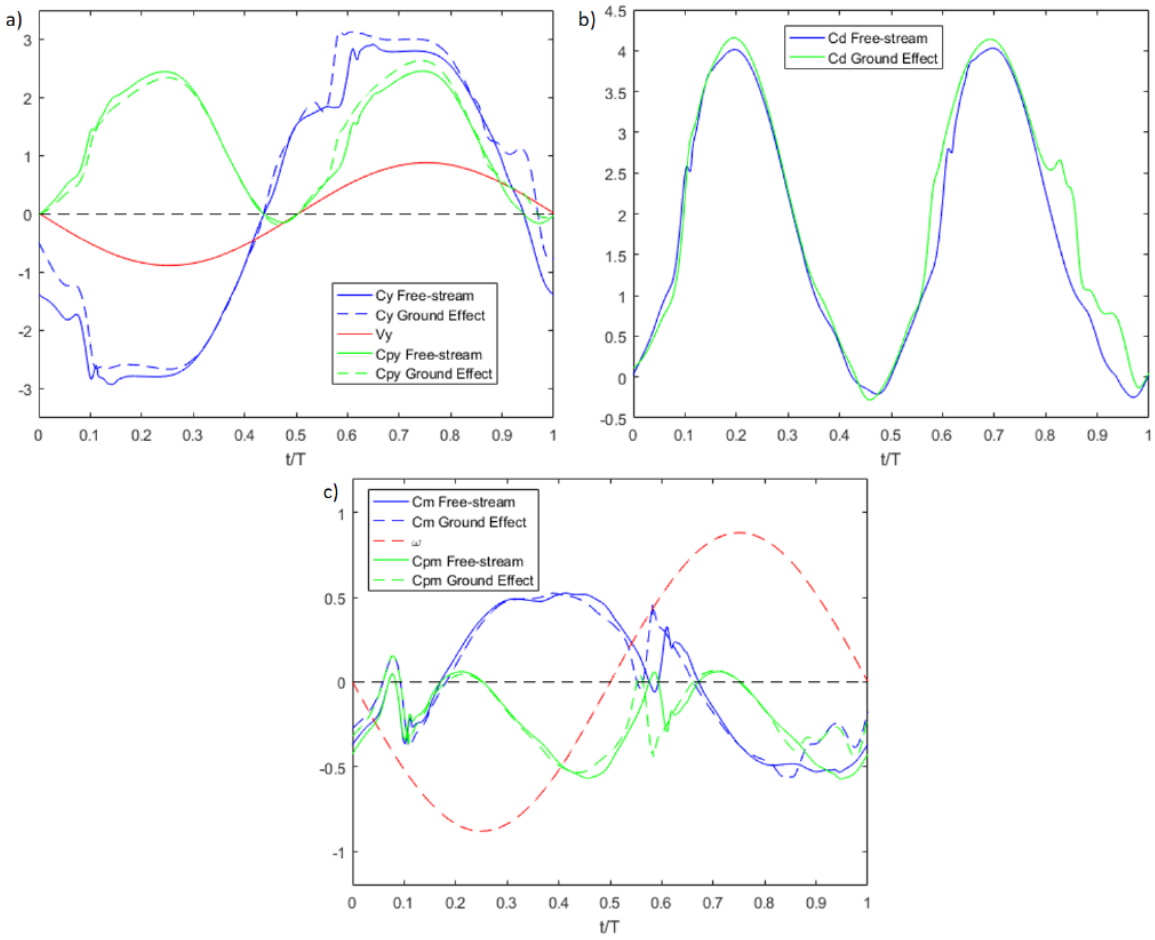

Figure 5. 18: Comparison of NACA0015 at $Re = 5 \times 10^5, H_0/c = 1, H_{med}/c = 2, x_p/c = 1/3\,, f^* = 0.14\ and\ \theta_0 = 76.3°$ in ground effect and free-stream for the (a) lift coefficients, (b) drag coefficients and (c) moment coefficients

5.3.7 Comparison of the Airfoil Flapping in and out of ground effect for Energy Harvesting

In this study, the results obtained show that airfoils flapping in ground effect for the investigated cases, have larger peak lift coefficients than those ones obtained for free-stream. This improvement is due to the venturi effect and the LEV's modification that is observed

when the airfoil is flapping close to the ground. Though, these improvements have been observed in all the cases tested, the power coefficient, and consequently, the energy efficiency, have not always been increased. For some cases, there was even a slight reduction in the efficiency. From the analysis conducted, it can be concluded that the improvement obtained in ground effect depends mainly on the synchronization of the heaving velocity and the instantaneous lift coefficient. If these increase in the lift coefficient occurs in a point of the cycle where the heaving velocity and the lift have different signs, instead of increasing the energy efficiency, there will be a reduction. This reduction has been observed for the cases where the oscillating frequency is further from the perfect synchronization that happens at $0.14 < f^* < 0.16$ for the two pitching amplitudes tested ($\theta_0 = 70°$ and $80°$). The highest efficiency improvement was obtained for the case where the airfoil was flapping at $f^* = 0.16$ and $\theta_0 = 80°$, from 33.72% to 36.46% (Table 5.2). It has also been observed that this improvement is primarily due to the enhancement of the heaving component rather than the pitching component.

As expected, varying distance from the ground has been shown to have an impact on the peak coefficients and on the efficiency. Moreover, as the airfoil is set to flap further from the ground, it tends to have the same results as of the free-stream case. The present study is constrained by the minimum distance from the ground (H_{min}) of one chord because of the numerical approach used. Thus, it would be of interest to investigate how the efficiency would change for H_{min} lower than one chord. Moreover, it is worth mentioning that it would not be possible to reach much lower values, as a collision between the ground and the airfoil would occur.

Finally, a turbulent case with a higher Reynolds number was also evaluated in ground effect. Comparing to the turbulent case in freestream, a slight improvement was observed in the energy efficiency, from 39.19% to 42.34% for $f^* = 0.14$ and $\theta_0 = 76.3°$, which corresponds to about 8% increment in efficiency. Following on this, it would be interesting to investigate the effect of different pitching amplitudes and frequencies on the enhancement of the energy efficiency.

5.4 Summary

In this chapter, a parametric study on the ground effect has been conducted to optimise the power efficiency. The effects of Reynolds numbers at laminar and turbulent flows, the location of airfoil pitching axis, the distance between the airfoil pitching axis and the ground, the amplitude and frequency of oscillation on power extraction by the flapping wing were

examined using URANS. From this study, it is found that in all the cases there is an increase in the peak lift coefficient, as height decreases. However, the improvement in power efficiency in ground effect is found to be depended mainly on the perfect synchronization of the heaving velocity and the instantaneous lift that happens. Moreover, it has also been observed that this improvement is primarily due to the enhancement of the heaving component rather than the pitching component. For the laminar flow, the maximum efficiency in ground effect is 8.13% more than the freestream (Table 5.2). Finally, a turbulent case with a higher Reynolds number was also evaluated in ground effect, and it found that an improvement of 8.23% in the energy efficiency was observed in comparison to its freestream case (Table 5.3).

Chapter 6: 3D effects and Geometry variation influence on Energy Harvesting Efficiency

The flow around oscillating devices involves three-dimensionality, turbulence transition, and unsteady flow separation associated with large-scale vortex structures. All these aspects are difficult to investigate computationally and experimentally. Thus, due to the complexities of three-dimensional flow, the studies of foils are still focused on two-dimensional structures at low or moderate Reynolds number. This has been far from the real applications, where the effects of three-dimensionality, free stream turbulence and high Reynolds numbers should be considered.

In this Chapter, the 2D numerical simulations have been further extended to 3D study to investigate the 3D effects, geometry shape variation, and aspect ratios on energy harvesting efficiency for oscillating wings in laminar and turbulent flows. For the 3D simulations with varying aspect ratios, most of the previous studies focused mainly on the thrust/propulsion, i.e., to understand how flapping low-aspect-ratio foils work for propulsion (Triantafyllou et al. 1991, Dong et al. 2006, Bleischwitz et al. 2015), as opposed to energy extraction from the flow. For the energy harvesting, only few studies were conducted in 3D. Kim et al. (Kim et al. 2017) investigated the energy harvesting performance and the flow structures of a 3D hydrofoil oscillating in pitch and heave experimentally in a water flume for different aspect ratios, Kinsey et al. (Kinsey *et al.*, 2011b) designed, built and experimentally tested a hydrokinetic turbine using oscillating hydrofoils to extract energy from water currents/tidal, and Deng et al. (Deng et al. 2015) investigated numerically the effect of variation of the aspect ratio and the structure of pitching motions on the energy extraction efficiency and wake topology of flapping hydrofoils in laminar flow.

In this study, two NACA profiles have been considered, which are NACA0015 with sharp trailing edge and NACA0018 with blunt trailing edge. NACA0015 has been used for experimental study by (Kinsey *et al.*, 2011b), and choosing this will be consistent for the validation process in 3D studies. NACA0018 is used later for the study of geometrical effect in 3D. This is because, from the conclusion in Chapter 4, the 2D NACA0018 with blunt trailing edge shows the higher energy efficiency value as compared to other NACA profiles. For the numerical simulations, to reduce the computational time the spanwise extension has been reduced to a half of the size by using the symmetry plane, and we also narrowed down the simulations that will be carried out in this 3D study to the optimum set of parameters

from the 2D simulation (which have a high energy efficiency, Chapter 4), and two different aspect ratios (with low and high aspect ratios, i.e., 3.5 and 7). The previous study of (Kinsey *et al.*, 2011b) has used aspect ratio 7 and choosing this aspect ratio in current study is necessary for the validation process. However, it is of interest to investigate how much the efficiency will be drop if a low aspect ratio is used. For example, due to the expensive cost and practical limitations (e.g., only small devices can be build), then the question is how efficient this device will be affected by three-dimensionality as we reduce the foil aspect ratio. For practical applications, one can design a variable wing using actuator (as in the case of spanwise morphing wing) which can be used, e.g., in shallow water (e.g., with a low aspect ratio) and in deep sea with a high aspect ratio. To investigate the effect of a low aspect ratio, this study simply reduce the aspect ratio to half the size than the one we validated, as usually aspect ratios of below 4 are considered to be low. Therefore, aspect ratio 3.5 has been chosen. Moreover, in this study the effect of 3D geometry shape variation on the energy harvesting was investigated.

6.1 Three-Dimensional Simulation Setup

For the 3D grid generation, the 2D grid was extended in spanwise 1.75c and 3.5c, as shown in Figures 6.1(b)-(c). Figure 6.2 shows the overall mesh of 3D study and the mesh details are given in Table 6.1. In these cases, only half of the spanwise has been extended due to the implementation of the symmetry plane (Figure 6.3) that allows us to model only half of the problem. Figure 6.4 shows the close-up view of the two airfoils at different aspect ratios with the end plates. These end plates have been used here to be matched with the geometry that has been used in the experimental study. Moreover, the end plates are also found to be beneficial in reducing the loss of efficiency at the wingtip (Kinsey and Dumas, 2012). For the solver setup, a similar approach that has been used in 2D simulation has been implemented here: Unsteady RANS with combined pitch-heave motions, and the non-conformal sliding interface (Figure 6.5), which appears as a closed cylinder around the airfoil with sealed at a half-chord distance farther from the endplate. This distance is used to avoid interfaces interruption to occur at the wingtip plane. Figure 6.6 shows the 3D wing parameters with the symmetry line.

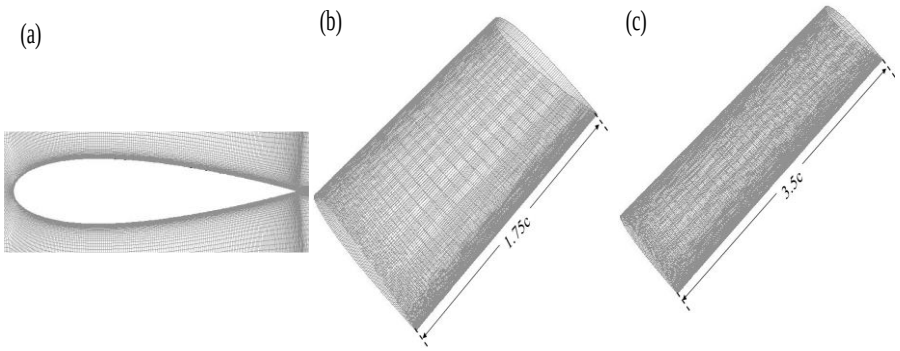

Figure 6. 1: (a) Close-up view of 2D grid (b) half airfoil span for 3D computation of *AR* = 3.5 (c) half airfoil span for 3D computation of *AR* = 7

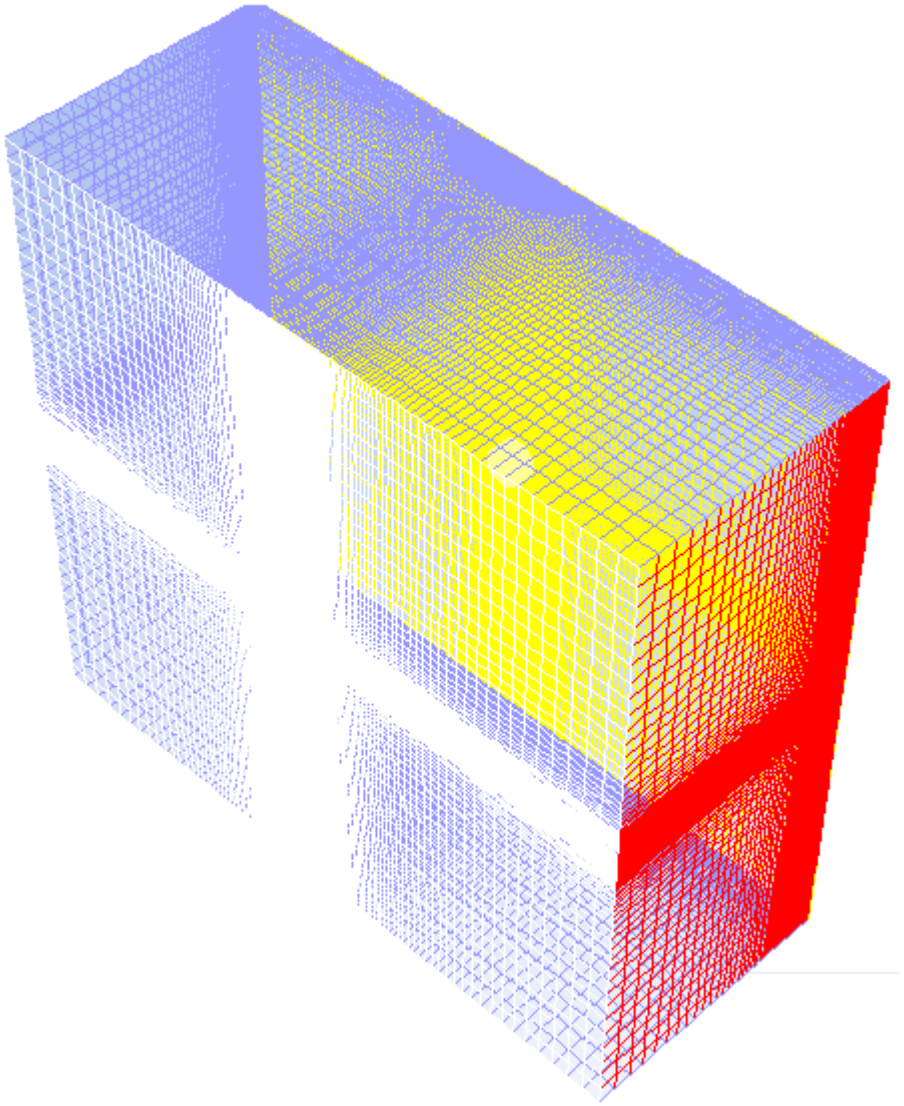

Figure 6. 2: Overall view of 3D mesh

Table 6. 1: Mesh information

	Aspect Ratio = 3.5	Aspect Ratio = 7
Cells	3,874,192	4,774,997
Faces	11,062,523	13,581,399
Nodes	3,203,205	3,913,253
Partitions	2	2
Cell zones	2	2
Face zones	19	19

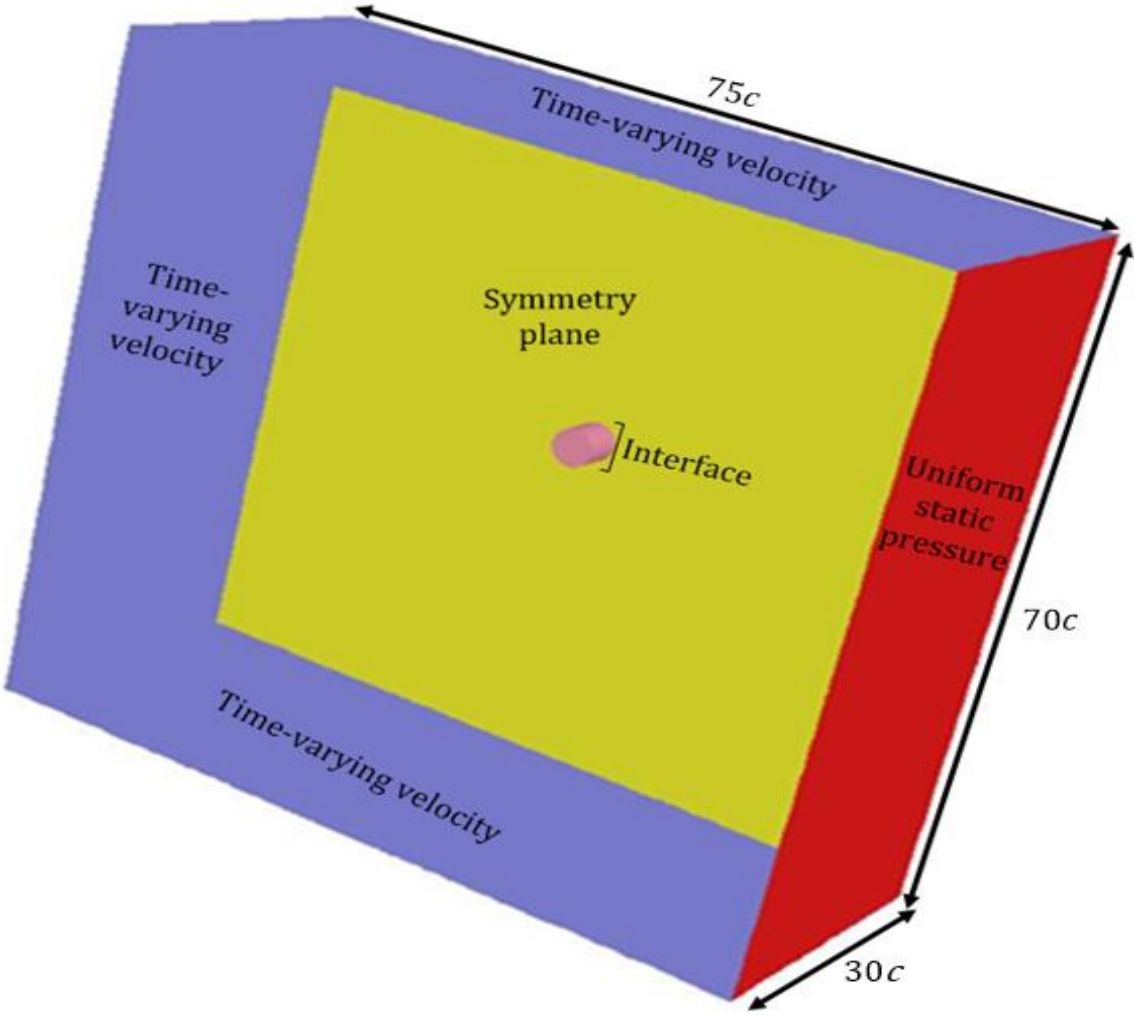

Figure 6. 3: Domain size and boundary condition types for the 3D numerical simulation

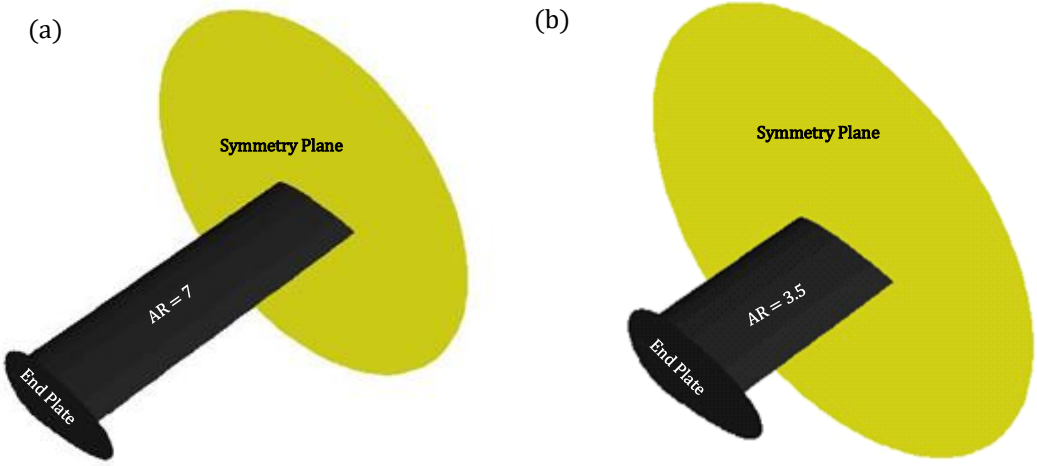

Figure 6. 4: Airfoil with end plate at different aspect ratio

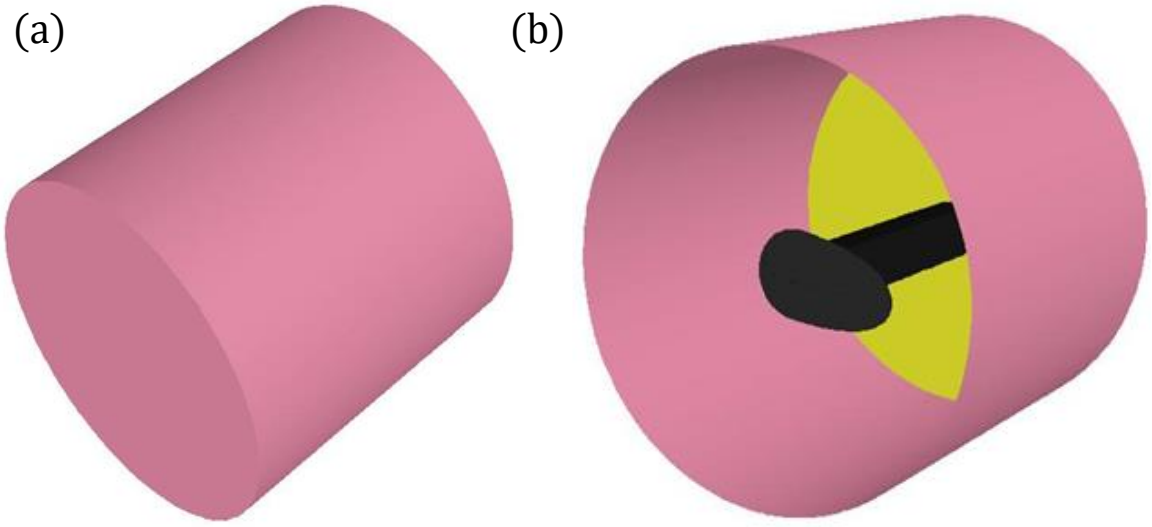

Figure 6. 5: (a) close-up view of the interface, (b) inside the interface, the airfoil equipped with the endplates (same as on the experimental prototype)

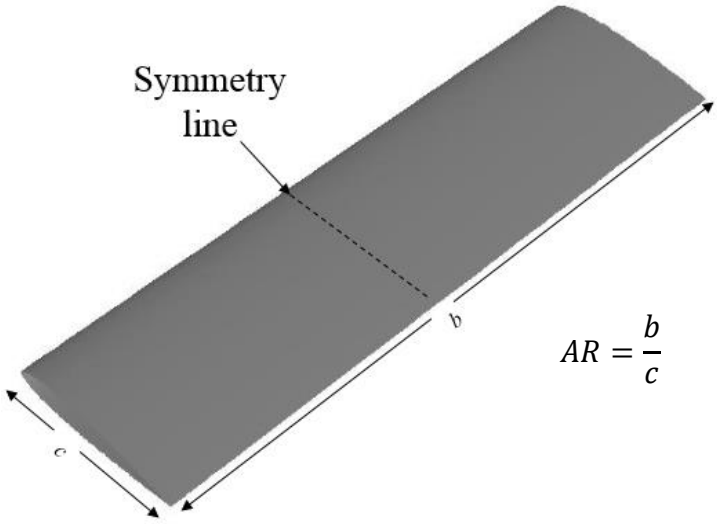

Figure 6. 6: 3D airfoil parameters (c is chord length and b is airfoil span)

6.2 Grid Independency Study

Before we start the validation process, the grid and time independence study have been carried out. Two sets of grid refinements have been built in the spanwise direction for each aspect ratio tested (Table 6.2) and the chosen grid was run in three different time refinements (Table 6.3). Then, the validation process begin by comparing the present results with the published study of (Kinsey & Dumas 2012b, Kinsey et al. 2011b)) for the 2D case.

Table 6. 2: Grid independence study

	AR = 3.5		*AR* = 7.0	
	Total cells	Nodes on airfoil	Total cells	Nodes on airfoil
Set 1	3,874,192	500 x 26	4,774,997	500 x 52
Set 2	4,253,189	500 x 30	5,153,994	500 x 60

Table 6. 3: Time independence study

	AR = 3.5	*AR* = 7.0
ts/cycle	2381	2381
	3000	3000
	7143	7143

The results of the grid and time independence studies are shown in Figures 6.7 and 6.8, respectively for both aspect ratios tested ($AR = 3.5$ and $AR = 7$).

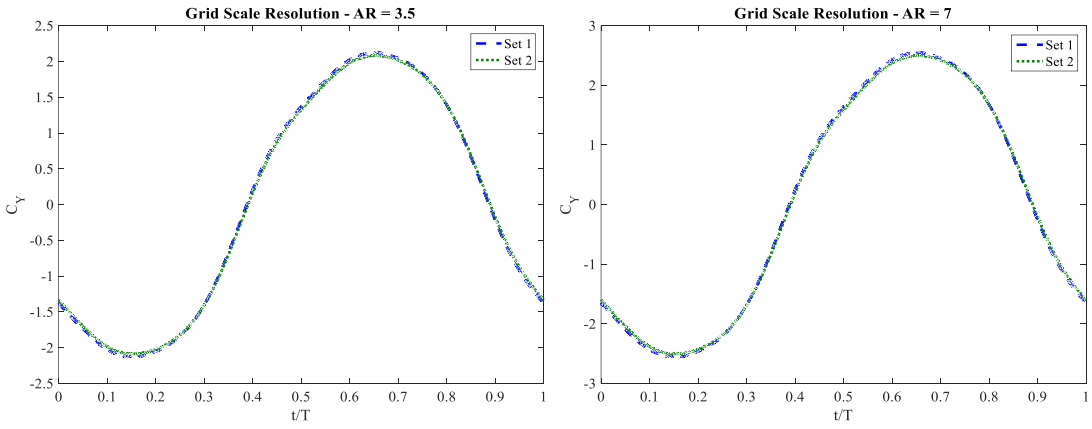

Figure 6. 7: Grid refinement results for *AR* = 3.5 and *AR* = 7 at ts/cycle = 2381 ($f^* = 0.14, \theta_0 = 75°, H_0 = c, Re = 5 \times 10^5$)

From Figure 6.7, both grid refinement sets show a good agreement. Hence, grid refinement of Set 1 with a smaller number of cells has been selected for further test at smaller time steps.

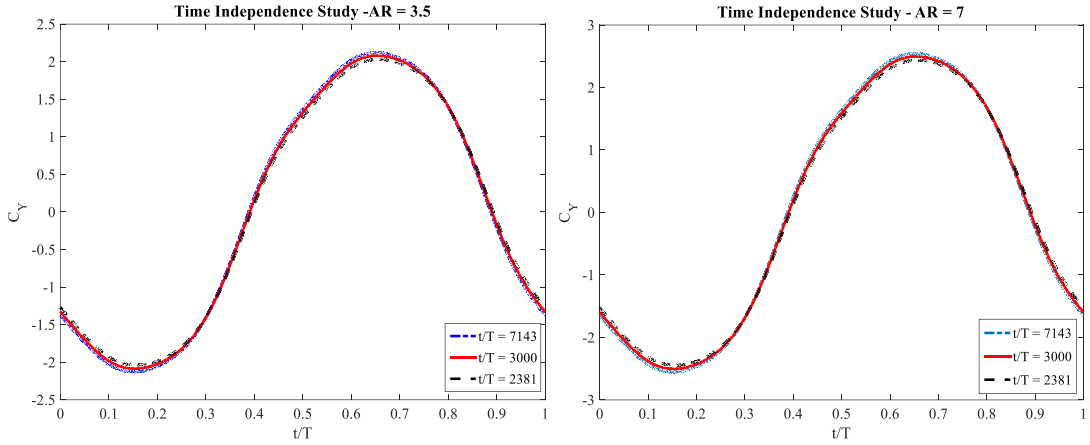

Figure 6. 8: Time independence study for AR = 3.5 and AR = 7

$(f^* = 0.14, \theta_0 = 75°, H_0 = c, Re = 5 \times 10^5)$

Again, a very good agreement has been obtained for the time independence study, with a difference of less than 0.1% between the largest and smallest time-steps used (0.003 and 0.001, respectively). Therefore, it can be concluded that the current mesh is space and time independent, and consequently this mesh has been used for further validation.

For the second step validation process, the overall dimension of oscillating airfoil geometry and endplate used in the present study are the same as the one used in the experimental study of (Kinsey et al. 2011b). Table 6.4 summarizes the parameters as well as the airfoil size that has been used in the experimental study.

Motion phase (ϕ)	90°

Table 6. 4: Oscillating airfoil turbine parametric details (Kinsey *et al.*, 2011b)

Airfoil profile	NACA0015
Chord length (c)	0.24m
Span(b)	1.68m
Pitching axis (x_p)	c/3
Heaving amplitude (H_0)	c
Pitching amplitude (θ_0)	75°

Eight cycles were performed with a time steps size of 0.003 and periodicity from cycle to cycle was excellent. Table 6.5 shows a comparison of our numerical simulations with the published work. A difference of less than 5% has been observed between the results. Figure 6.9 shows the plots of the vertical and horizontal force coefficients (C_Y and C_X), and the power coefficient (C_P), and as can be seen good agreements were obtained with the published work. Hence, it can be concluded that, the 3D approach in this study has been successfully validated and the results obtained are reliable.

Table 6. 5: Comparison results of the numerical simulation and the published study for $Re = 5 \times 10^5, f^* = 0.14, \theta_0 = 75°, H_0 = c$

Study	$\bar{C}_P$	Efficiency, η[%]
Present	0.806	31.58
(Kinsey *et al.*, 2011b)	0.844	33.10

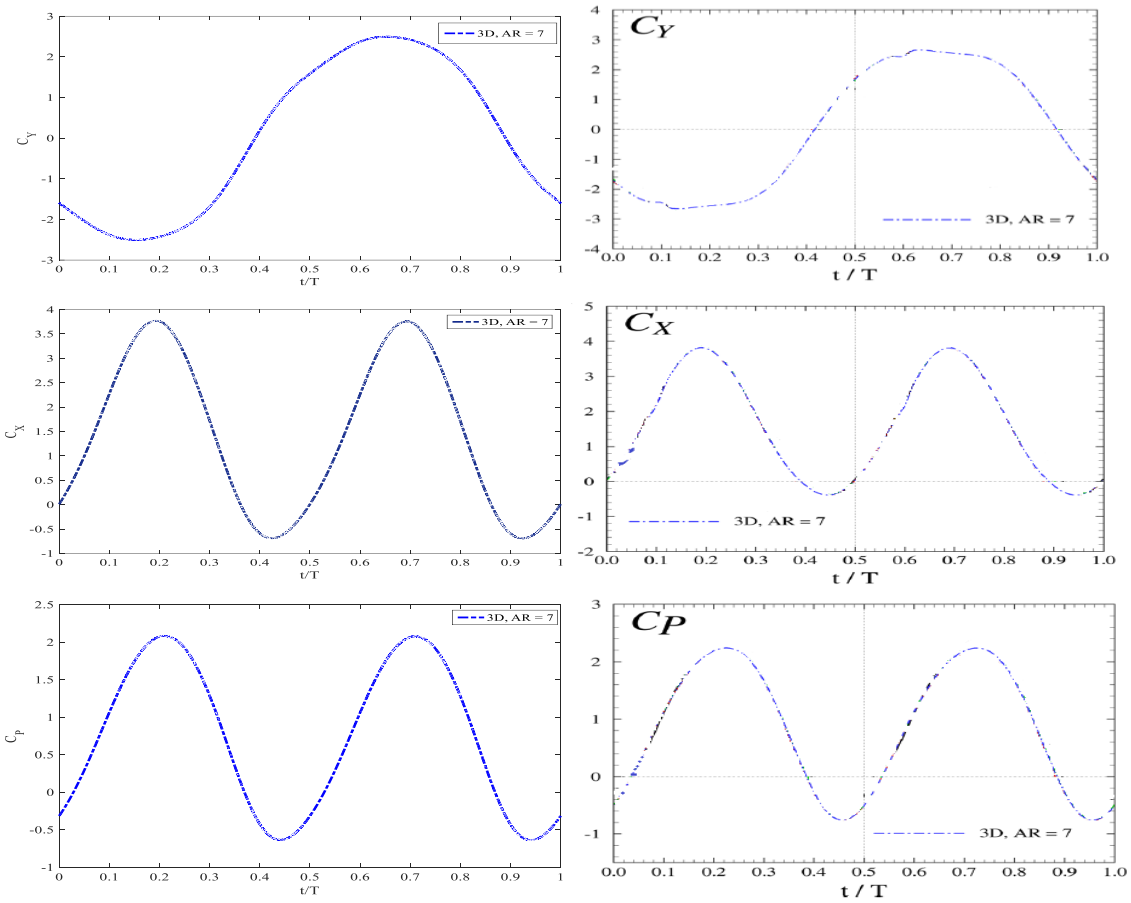

Figure 6. 9: Comparison plot between present study (left) and published study (Kinsey and Dumas, 2012) (right)

6.3 Comparison of 2D and 3D Results

In this study, the 3D effects on the potential power extraction of oscillating wing is considered in laminar and turbulent flows and compared to the 2D case. In this section, only optimum cases (with largest energy harvest efficiencies) obtained for 2D NACA0015 with sharp trailing edge in Chapter 4 (single airfoil analysis) have been considered for the oscillating 3D wing. In laminar flow field (with $Re = 1100$), the simulations have been conducted at a reduced frequency $f^* = 0.14$, pitching amplitude $\theta_0 = 76.3°$ and heaving amplitude $H_0 = c$, while for turbulent flow field ($Re = 5 \times 10^5$), the reduced frequency, the pitching amplitude, and the heaving amplitude are taken to be as $f^* = 0.18$, $\theta_0 = 80°$ and $H_0 = c$, respectively (from Chapter 4).

The results obtained from these simulations are presented in Table 6.6 and Figure 6.10 for laminar case, and Table 6.7 and Figure 6.11 for turbulent case. From these results, it can be seen that the 2D case overestimates the power efficiency as compared to the 3D cases, as this does not take into account the 3D effects. The power efficiency of the 3D case for aspect ratio 7 is higher than the one for aspect ratio 3.5. These results agree with the other studies on the aspect ratios where, as the aspect ratio increases, the lift force performance improves, and which in turn can enhance the energy harvest performance.

Comparing the results of 2D and 3D cases, we can observe that, there is about 22% and 10% efficiency drop in laminar case for aspect ratio 3.5 and 7 respectively, whereas in turbulent flow, there is about 25% and 11% performance decrease. These efficiencies drop is primary coming from the heaving contribution, and the percentage drop of the cycle averaged coefficient of power from heaving motion is more significant as compared to the pitching motion for both fluid flows. Indeed, one finds in this study that for the cases studied, the heaving contribution significantly dominates the pitching contribution, especially for the laminar case (Table 6.6). For the pitch contribution, it can be seen that the energy consumption properties of the pitch motion are very different (Tables 6.6 and 6.7), and that for the turbulent case the contribution from the pitching is quite significant as compared to laminar case which is low.

The plots of the vertical and horizontal forces (C_Y and C_X), pitching moment (C_M) and coefficient of power (C_P) in laminar flow (Figures 6.10) show similar trends between the 2D and the 3D curves but with higher peaks for the lift force and pitching moment coefficients in 2D characterised by the presence of dynamic stall and LEVs; and which is not the case for turbulent flow (Figure 6.11), especially for the vertical force and pitching moment. Moreover, it can be seen from the power coefficients (Figures 6.10-6.11) that these

peaks are lower for the low aspect ratio, followed by the larger aspect ratio, and then the 2D (infinite aspect ratio), which in turn contribute to a higher power efficiency. The vertical force and pitching moment in 3D cases of turbulent flow show higher values and better synchronization than the corresponding 3D laminar flow cases, resulting in a better power efficiency. For the high aspect ratio, the efficiency results of the 3D are quite similar to the 2D case (i.e., infinite aspect ratio) as expected, while for the low aspect ratio there is a significant difference between the 3D and 2D results, where the 2D results are over-predicted, and drop in efficiency is about 22% for aspect ratio 3.5 and 10% for aspect ratio 7 for the laminar case (Table 6.6), and 24.5% . Thus, it can be concluded that to limit 3D losses is to increase the foil aspect ratio.

Table 6. 6: Cycle-averaged power coefficients and efficiencies for 2D and 3D oscillating airfoils in laminar flow field

Dimension	AR	$\bar{C}_{P_Y}$	$\bar{C}_{P_\theta}$	$\bar{C}_P$	Efficiency, $\eta[\%]$	$\Delta\eta$ relative to 2D[%]
2D	-	0.8171	0.0458	0.8629	33.25	-
3D	3.5	0.6433	0.0209	0.6642	25.89	22
3D	7	0.7273	0.0279	0.7551	29.87	10

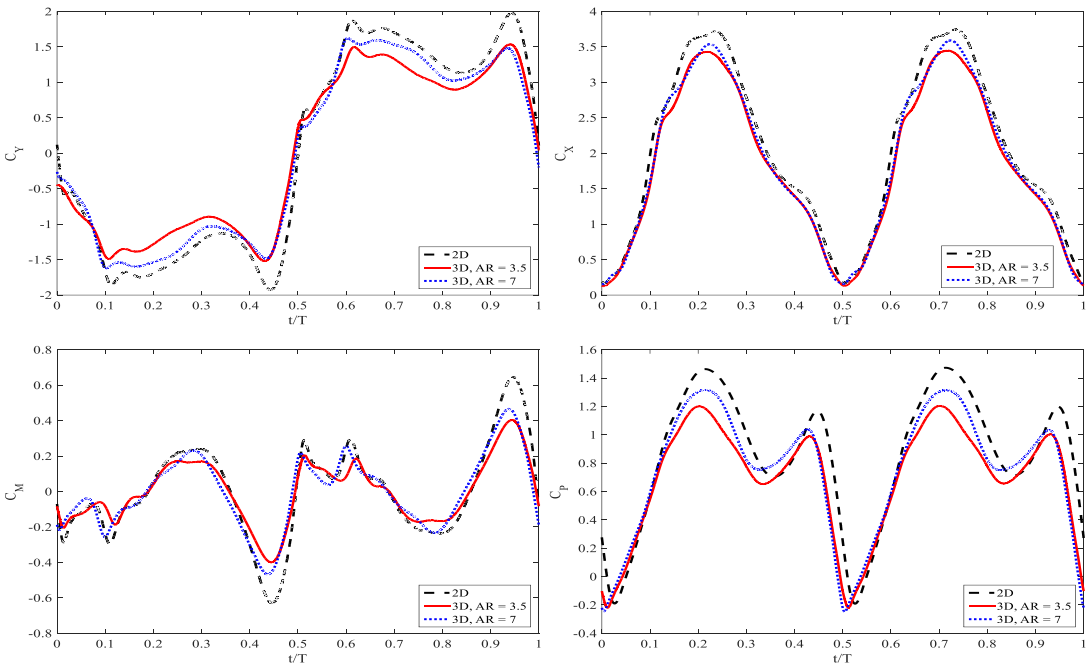

Figure 6. 10: Comparison of instantaneous forces, moment and power coefficient between 2D and 3D simulations and different aspect ratios, $Re = 1100, f^* = 0.14,\ \theta_0 = 76.3°, H_0 = c$

Table 6. 7: Cycle-averaged power coefficients and efficiencies for 2D and 3D oscillating airfoils in turbulent flow field

Dimension	AR	$\bar{C}_{P_Y}$	$\bar{C}_{P_\theta}$	$\bar{C}_P$	Efficiency, $\eta[\%]$	$\Delta\eta$ [%]
2D	-	1.7098	-0.5911	1.1187	43.08	-
3D	3.5	1.5128	-0.6861	0.8267	32.52	24.5
3D	7	1.5953	-0.6833	1.0120	38.30	11

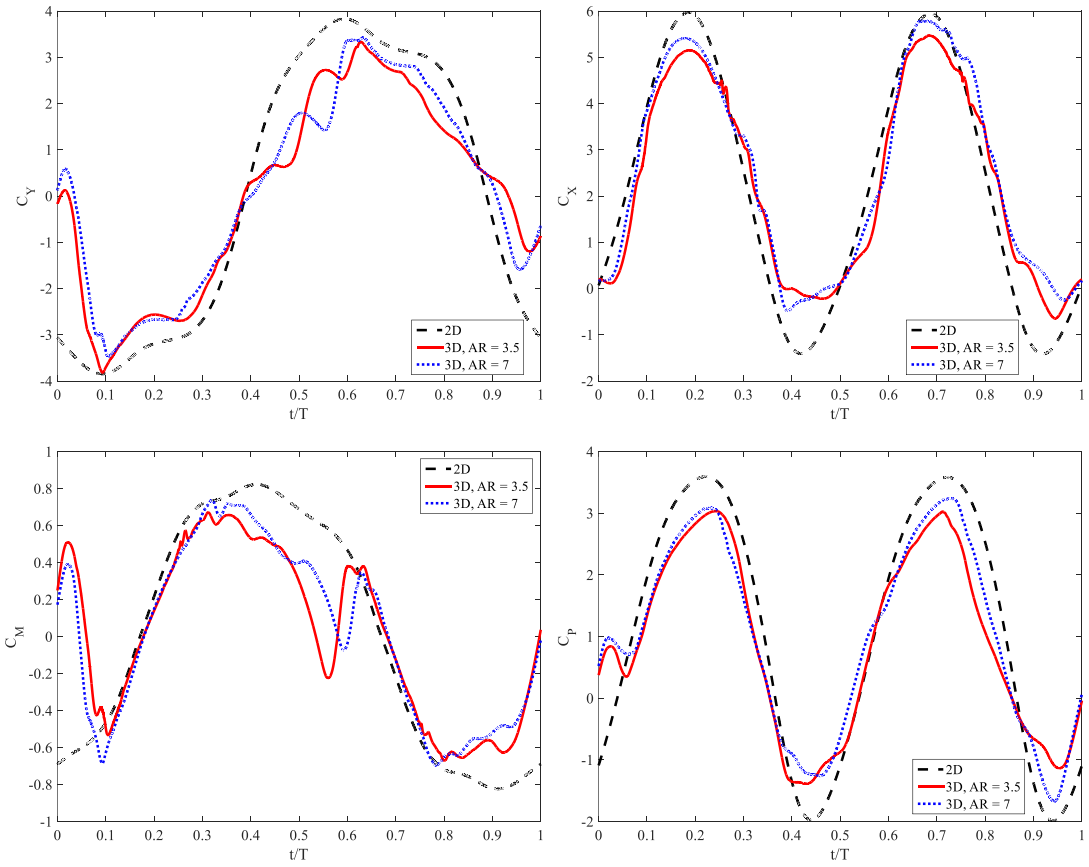

Figure 6. 11: Comparison of instantaneous forces, moment and power coefficient between 2D and 3D simulations and different aspect ratios, $Re = 5 \times 10^5, f^* = 0.18,$ $\theta_0 = 80°, H_0 = c$

Figure 6.12 shows the vorticity contours for the 3D and 2D for $Re = 5 \times 10^5, f^* = 0.18,$ $\theta_0 = 80^o, H_0 = c$. At $t/T = 0$, it can be seen clearly that the shed vortex in 3D is not perfectly correlated along the spanwise direction. At the midspan location, the 3D vortex

looks similar to the corresponding 2D vortex but towards the wingtip of the airfoil it can be seen that there is a significant difference between the 3D and the 2D shed vortex. At $t/T = 0.75$, the flow is mostly attached and the shed vortex of 3D and 2D plots look quite similar along the chord line. Taking into account the 3D effect, the global performance namely cycle-averaged lead to different results, as shown in Table 6.6-6.7 and Figures 6.10-6.11. These differences will be even more for the low aspect ratio.

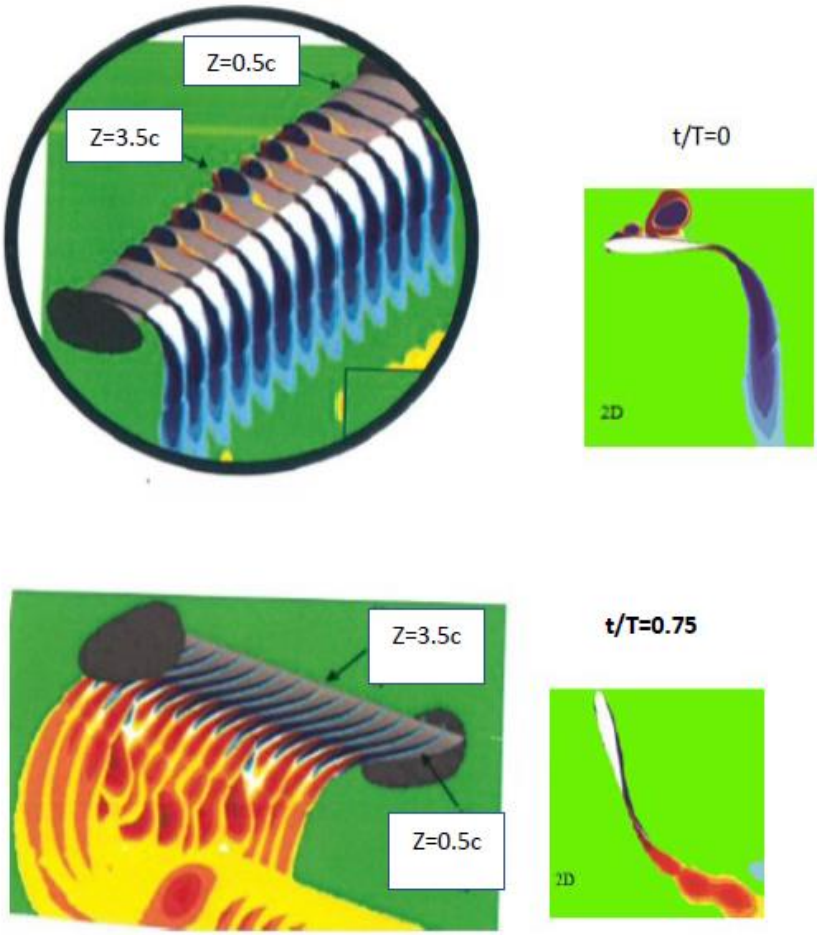

Figure 6. 12: Comparison of vorticity contour for 3D and 2D studies at $Re = 5 \times 10^5, f^* = 0.18, \theta_0 = 80^\circ, H_0 = c$

6.4 Geometrical Effect in 3D Studies

In this section we compare the results of power efficiency with the best geometrical shape found in 2D studies. It is best to study this geometrical effect in 3D, hence NACA0018 with blunt trailing edge has been selected and the results compared with standard NACA0015 sharp trailing edge. We run the simulation in both laminar and turbulent flow

with fixed aspect ratio equal to 7 (which is found to have the best efficiency for the 3D sharp trailing edge). The results are shown in Table 6.8-6.9 and Figure 6.13-6.14.

Table 6. 8: Cycle-averaged power coefficients and efficiencies for NACA0015 sharp trailing edge and NACA0018 blunt trailing edge in laminar flow field

	$\bar{C}_{P_Y}$	$\bar{C}_{P_\theta}$	$\bar{C}_P$	Efficiency, η[%]
NACA0015 Sharp edge	0.7273	0.0279	0.7551	29.87
NACA0018 Blunt edge	0.7385	0.0328	0.7713	30.63

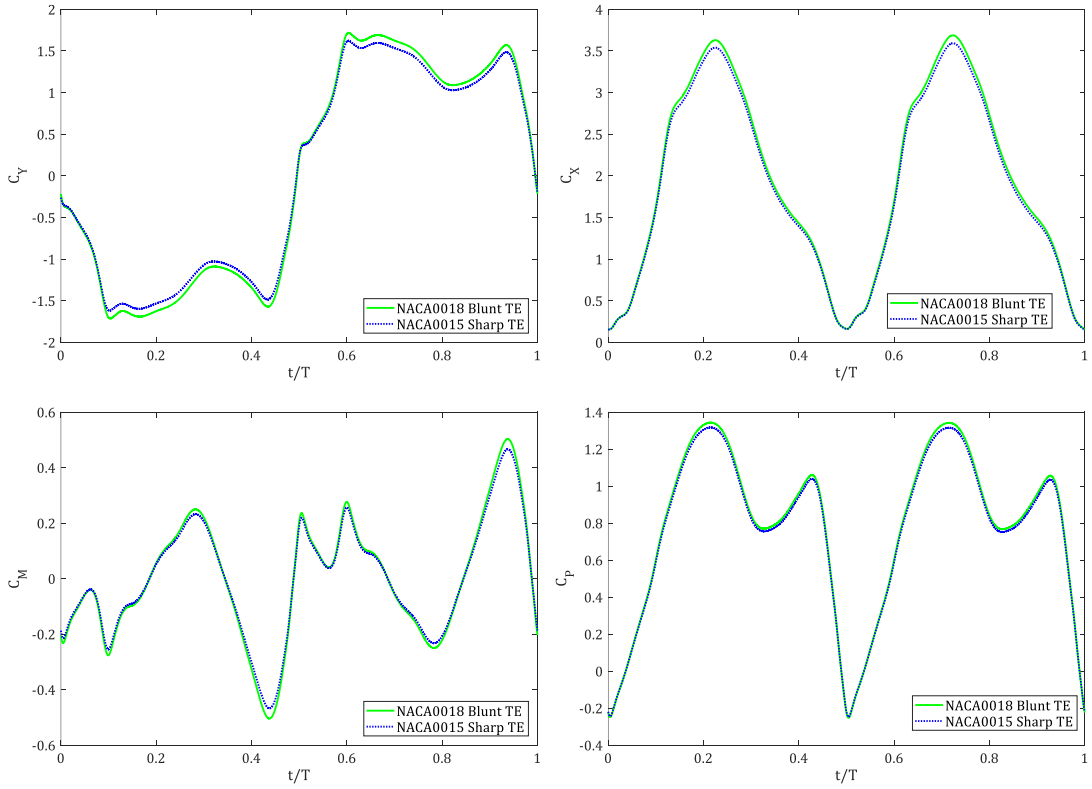

Figure 6. 13: Comparison of instantaneous forces, moment and power coefficient for AR = 7, at $Re = 1100, f^* = 0.14, \theta_0 = 76..3^\circ, H_0 = c$

Table 6. 9: Cycle-averaged power coefficients and efficiencies for NACA0015 sharp trailing edge and NACA0018 blunt trailing edge in turbulent flow field

	$\bar{C}_{P_Y}$	$\bar{C}_{P_\theta}$	$\bar{C}_P$	Efficiency, η[%]
NACA0015 Sharp edge	1.5953	-0.6833	1.0120	38.30
NACA0018 Blunt edge	1.6486	-0.6160	1.0326	39.23

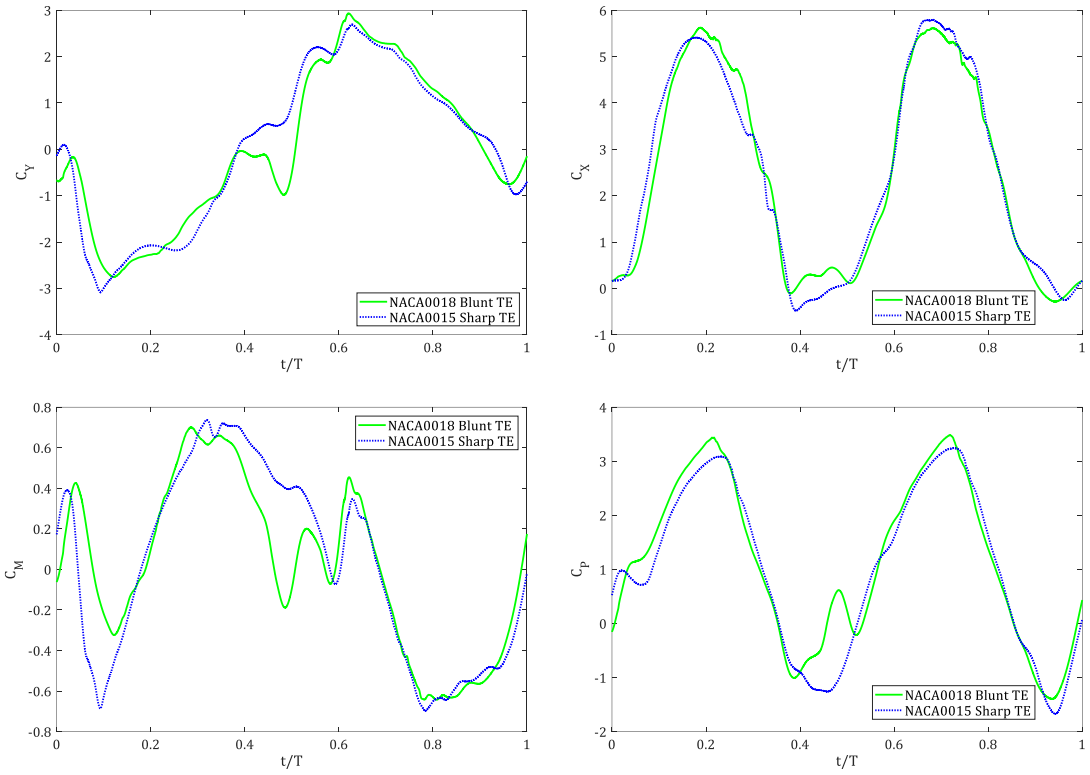

Figure 6. 14: Comparison of instantaneous forces, moment and power coefficient for AR = 7, at $Re = 5 \times 10^5, f^* = 0.18, \theta_0 = 80^\circ, H_0 = c$

From the results presented in Table 6.8 and 6.9, we can observe that the turbulent flow have a better efficiency than the laminar flow. For NACA0015 sharp edge, the efficiency is 29.87% for the laminar case, while for the turbulent case it is 38.3%. For NACA0018 blunt edge the efficiency is 30.63% for the laminar case, and 39.23% for the turbulence case. Comparing NACA0018 blunt edge to NACA0015 sharp edge, it can be seen that there is slight increments in overall numbers. In laminar flow, the increment in efficiency performance for the blunt is 2.54% in comparison to the sharp edge, while for turbulent flow

the increment is 2.43%. From practical application, using a blunt NACA0018 in turbulence flow instead of NACA0015 sharp edge in laminar flow, will give an improvement of efficiency of 31.34%. Figure 6.13 for laminar flow field shows a clear slight difference between the two NACA profiles with NACA0018 blunt edge shows an advance performance, however this is not evident for turbulent flow case (Figure 6.14). Similar trends were found for a lower aspect ratio of 3.5 between blunt and sharp edges, with a slight increment in performance for the blunt edge.

In Chapter 4, it is found for the 2D cases that the blunt trailing edge has a better efficiency (7% improvement) than the sharp and rounded trailing edges, for a high Reynolds number. In 3D cases, it can be seen that the efficiency improvements are lower than the 2D cases. This suggests that the implementation of efficiency improvement strategies obtained by two-dimensional studies should be treated with caution when extended to real three-dimensional flows. To limit the 3D losses and increase the 3D efficiency, a way is to increase the foil aspect ratio and use the blunt edge shape.

6.5 Summary

In this chapter, the 3D effect and aspect ratios on oscillating wing for energy extraction have been considered, and compared to the 2D airfoil case. Moreover, the effect of geometrical shape variation has been on energy harvesting has been investigated. The accuracy of the proposed 3D method has been validated first, and the results show a good agreement. Then, the 3D model has been successfully applied to the symmetrical airfoil with two different aspect ratios, which are 3.5 and 7. Numerical simulations of NACA0015 with sharp trailing edge have been conducted at laminar and turbulent flows, where in laminar flow the chosen reduced frequency, heave and pitch amplitudes are 0.14, c and 76.3°, while in turbulent flow the simulation parameters are chosen as $f^* = 0.18, H_0 = c$ and $\theta_0 = 80°$. The simulation then been proceeded with comparing the results with NACA0018 blunt edge at aspect ratio 7 in both laminar and turbulent flow.

From these simulations, it is found that the 2D case overestimates the power efficiency as compared to the 3D cases, as this does not take into account the 3D effect like tip vortex. The relative drops of efficiency from 2D predictions for the aspect ratios of 3.5 and 7, were found to be 22% and 10%, respectively for the laminar case, and 24.5% and 11% for the turbulent case. Thus, as the aspect ratio increases, the difference in the 2D and 3D results are small, while for a lower aspect ratio, there are significant differences between the 2D and

3D results for both laminar and turbulent flows, as expected. The 3D case results of turbulent flow show higher values and better synchronization for the vertical force and pitching moment than the laminar flow cases, and thus resulting in a better power efficiency. The geometrical effect in 3D study still have similar conclusion with 2D study in which 3D NACA0018 blunt trailing edge give a slightly better efficiency compared to 3D NACA0015 sharp trailing edge, but again with a significant drop in efficiency as compared to the 2D cases. From this study, it may be concluded that the 3D effect and aspect ratios do have influence on power generation for the oscillating wing and the geometrical shape of the oscillating airfoil contribute to the better performance. To limit the 3D losses and increase the 3D efficiency, this could be achieved by increasing the foil aspect ratio and using a blunt edge shape.

.

Chapter 6

Chapter 7: Conclusion and Future Work

7.1 Conclusion

In this study, numerical simulations have been carried out on oscillating bodies in 2D and 3D to reveal the flow aerodynamics and their potential for power extraction efficiency. The aim is to analyse the flow around oscillating bodies and determine under which conditions the system extracts the maximum amount of energy from the surrounding flow. To achieve this aim, rigorous simulations had been conducted using computational fluid dynamics software Fluent in laminar and turbulent flows.

Computational studies were first carried out to validate the proposed method and the results have been compared with the published literature, and good agreements were obtained. The effect of geometrical shape modification on energy harvesting performance of 2D oscillating airfoils were then investigated. A selective range of parameters have been investigated for symmetrical airfoils (NACA0012, NACA0015, and NACA0018), including the airfoil geometrical parameters: thickness distribution and trailing edge shapes modification (sharp, blunt and round); kinematics parameters, i.e. frequency oscillation (f*=0.10-0.20) at fixed heaving and pitching amplitudes, and the effect of fluid physics at low and high Reynolds numbers (laminar flow at Re = 1100 and turbulent flow at Re = 5x105). For the turbulent simulations, the highly resolved numerical simulations (y+ ~ 1) are performed at high pitch angles using the k-w SST turbulence model, and are found to model the flow separation effectively. The power-extraction efficiency has been used as the performance comparison metric to map the performance into the parametric space considered in this study. For the thickness distribution, it is found that the thicker airfoil (NACA0018) gives a better power efficiency (that is, increasing the thickness increases the power efficiency), and the effect of thickness variation is found to be more visible in turbulent case than in the laminar case; where the highest difference in efficiency is found to be about 19% which occurs between NACA0012 and NACA0018 airfoils at reduced frequency $f^* = 0.14$ and pitching amplitude $\theta_0 = 85°$. Moreover, for the cases studied, it is found that the highest efficiency is 34.1% for laminar flow, and 44.5% for the turbulent flow, for the clean NACA0018 airfoil (sharp trailing edge). Modifying the airfoil trailing edge shape is found to have influence on the lift coefficient, especially for the high Reynolds number. And it is observed that the blunt trailing edge has a better efficiency that the sharp and rounded trailing edges. About 3% and 7% difference in performance efficiency between blunt, sharp and rounded edges occurred in

laminar and turbulent flow field, respectively, with the blunt edge leading followed by sharp and rounded edges. Furthermore, for all simulations that have been carried out for the 2D single oscillating airfoils, the highest efficiency performance is found to occur at reduced frequencies $f^* = 0.14 - 0.18$. The increase in efficiency is mainly due to the LEVs (leading edge vortices) and a better synchronization between C_Y and V_Y (i.e., good timing in the sign switch of C_Y and V_Y).

The simulations were then extended to investigate the performance efficiency of multiple oscillating bodies. In this configuration, a parametric study involving the inter airfoil distance, oscillating motion and the interaction of bluff body-airfoil is conducted in order to quantify the effects of these parameters on the power extraction efficiency.

The results showed that, when the two airfoils (airfoil-airfoil) in tandem configuration are set to oscillate in different direction, the system will not produce energy but rather consumes energy. However, the same airfoils can generate 24% more energy than the single airfoil when both of them oscillate in the same direction with 4c distance. Besides, the higher increment in efficiency was also observed when the distance between two bodies was reduced, that is, when the separation distance of the two airfoils is shifted to 2.5*c* apart, the increase of 7% and 30% in efficiency has been observed as compared to 4*c* distance and the single oscillating airfoil, respectively. The effect of trailing edge modifications on the efficiency performance for the two oscillating airfoils has also been investigated for the NACA0015 sharp trailing edge and the NACA0018 blunt trailing edge. From the results, it is found that there is an improvement in efficiency for the thicker and modified blunt trailing edge airfoil, with a total efficiency of more than 5% in comparison to the sharp airfoil-airfoil.

Next, the effect of a bluff body (cylinder) with an airfoil in tandem configuration on the energy harvesting efficiency is investigated. From this study, it is found that the efficiency performance of the bluff body-airfoil is lower as compared to the airfoil-airfoil interaction. Nonetheless, the comparison of efficiency performance of cylinder-airfoil and airfoil-airfoil interaction is at cylinder-airfoil interaction, where the downstream body is generating more power than the upstream body, which is in contradiction with the airfoil-airfoil interaction. This is due to the weak geometry design of bluff body which is not of aerodynamics shape. Moreover, since the bluff body is in the upstream position, the vortex formulation is bigger and the contact with the downstream airfoil increases the lift force, which finally benefit in the power generation. When compared to the single oscillating airfoils, at reduced frequency $f^* = 0.12$, the efficiency increases between 0.7% to 12%, but at a reduced frequency $f^* = 0.14$ the efficiency drops by 12%. Simulations of bluff body

were again run with NACA0018 blunt edge and a positive improvement in efficiency is attained. For the multiple oscillating bodies, it maybe concluded that the use of airfoil-airfoil interaction with blunt trailing edge is recommended for a better energy harvesting of two oscillating bodies in tandem.

Next, a parametric study has been conducted to investigate the power efficiency in ground effect. The effects of Reynolds numbers at laminar and turbulent flows, the location of airfoil pitching axis, the distance between the airfoil pitching axis and the ground, the amplitude and frequency of oscillation on power extraction by the flapping wing were examined using URANS. From this study, it is found that in all the cases there is an increase in the peak lift coefficient, as height decreases. However, the improvement in power efficiency in ground effect is found to be depended mainly on the perfect synchronization of the heaving velocity and the instantaneous lift that happens at $0.12 < f^* < 0.2$. For lower and higher reduced frequencies, the increase in lift is not always reflected in a better power efficiency, as the motion of the airfoil and the forces are not well synchronized. Finally, a turbulent case with a higher Reynolds number was also evaluated in ground effect, and it found that in comparison to the laminar case, an improvement of more than 8% in the energy efficiency was observed.

Finally, 3D effects on oscillating wing has been considered for power extraction, and then compared to the 2D airfoil case. The parameters change in this 3D numerical study were the aspect ratio and the fluid flow. Aspect ratio 3.5 and 7 had been considered in laminar and turbulent flow. From these simulations, it is found that the 2D case over-predict the power efficiency as compared to the 3D cases, and this may be due to the well-known limits of the 2D models which do not take into account the 3D effects like tip vortex. For a higher aspect ratio, the difference in the 2D and 3D results are small as expected, but for a lower aspect ratio significant differences exist between the 2D and 3D results for both laminar and turbulent flows. And it is found that there is a drop of about 22% efficiency for aspect ratio 3.5, and only 10% for aspect ratio 7 in laminar flow. Turbulent flow also shows a similar efficiency drop in both aspect ratios. Comparing the 3D results of turbulent flow to the corresponding 3D laminar flow, it shows a higher power efficiency for the former, as higher values and better synchronization for the vertical force and pitching moment are obtained in the turbulent case. Thus, it may be concluded that, the aspect ratio and 3D effects affect the power efficiency in both laminar and turbulent flows, with a significant drop in efficiency in both fluid flows, as compared to the 2D case. Also, this suggests that the efficiency improvement obtained by the 2D studies should be treated with caution when extended to

3D flows. The geometrical shape variation has also been included in this 3D study, where the results of NACA0015 sharp trailing edge has been compared to NACA0018 blunt trailing edge in both laminar and turbulent flow. The results of the study agree with the 2D results where NACA0018 blunt trailing edge gives better efficiency.

From this research, it maybe concluded that the use of geometry shape variation (blunt edge foil), multiple foils configuration, ground effect, and high aspect wing ratios, in turbulent flow, improve the power efficiency of flapping foils. These results give important insight for both the fundamental flow physics of oscillating foils and the design of a more efficient foil device for energy harvesting. For industrial applications, designing, for example, high aspect ratio blunt edge flapping foils for multiple configurations (optimised for use in arrays), and operating in near ground effect (e.g. for tidal energy harvesting), could improve the device' efficiency and pave the way for a development of a new system device which may be commercially profitable.

7.2 Future Work

The research presented in the current thesis provide the following insights for future research:

- In this study, both the heaving and pitching motion of the airfoil were prescribed to follow a sinusoidal motion. Hence, further work should take into account the actuation mechanism that can induce the motion of the airfoil. The energy extraction efficiency calculated from this system would give a better overview of the net power generated as some of the power generated can be used by the actuating system.
- The other important and critical area that needs to be explored is the study of oscillating airfoil at the laminar to turbulent transition. This transition time is expected to play crucial role as the details of the laminar-turbulent transition can have a large influence on the size, location and timing of shedding vortices consequently affecting aerodynamic forces.
- Another approach for future work is the extension of ground effect and flexibility/morphing study to 3D simulation of oscillating foils, i.e., to explore these effects (ground effect and flexibility/morphing) on the potential increase of power efficiency, as has been seen for the 2D simulations in ground effect (Chapter 5).
- At the moment the majority of studies are concentrated on single foil devices. Few works discussed the multiple foils in tandem or parallel configuration. Future

research could explore other multiple configurations, including in arrays (e.g., hydrofoil arrays for tidal energy harvesting), to find the ideal placement of a trailing edge foil to optimise the energy density of the system by comparing it to the efficiency of the individual foil, in both 2D and 3D.

- LES and DES approach could be used to improve the prediction of flow especially in a deep dynamic stall configuration (which is found to contribute to performance enhancement). However, at the moment studies on pitching/heaving with LES or DES approach are rare, as they are computationally very expensive.
- Compared with rotary turbines, the flapping foil designs have some advantages: simple structure and easy manufacture, less noise and environment-friendly, etc. However, a systematic comparison between the rotary systems and the flapping foil systems has not yet been investigated. The different wake structures may cause the differences in energy harvesting efficiency. Further researches can perform specific quantitative analysis between the two systems.
- Carry out experiments on oscillating foils for energy harvesting to inform the modelling capabilities, and further validate the results obtained.

Bibliography

Abdelkefi, A. (2016) ‘Aeroelastic energy harvesting : A review’, *International Journal of Engineering Science*. Elsevier Ltd, 100, pp. 112–135. doi: 10.1016/j.ijengsci.2015.10.006.

Abiru, H., Yoshitake, A. (2011) ‘Study on a Flapping Wing Hydroelectric Power Generation System’, *Journal of Enviromental Engineering*, 6, pp. 178–186.

Andersen, A., Bohr, T., Schnipper, T., Walther, J.H., (2017), 'Wake structure and thrust generation of a flapping foil in two-dimensional flow', *J. Fluid Mech.* 812, R4.

Anderson, J. M. *et al.* (1998) ‘Oscillating foils of high propulsive efficiency’, *Journal of Fluid Mechanics*, 360(April 1998), pp. 41–72. doi: 10.1017/S0022112097008392.

Ansys, I. (2005) ‘ANSYS Modeling and Meshing Guide’.

Ashraf, M. A., Young, J., Lai, J. C. S. (2009) ‘Numerical simulation of flow driven oscillating airfoil power generator’, in *6th Asian Pasific Conference on Aerospace Technology and Science (APCATS), Beijing, China*.

Ashraf, M. a. *et al.* (2011) ‘Numerical Analysis of an Oscillating-Wing Wind and Hydropower Generator’, *AIAA Journal*, 49(7), pp. 1374–1386. doi: 10.2514/1.J050577.

Ashraf, M. A. *et al.* (2009) ‘Numerical simulation and multi-objective design of flow over oscillating airfoil for power extraction’, in *Conference on modelling fluid flow (CMFF09), 14th international conference on fluid flow technologies, Budapest, Hungary*.

Ashraf, M. A. (2010) *NUMERICAL SIMULATION OF THE FLOW OVER FLAPPING AIRFOILS IN PROPULSION AND POWER EXTRACTION REGIMES*.

Ashraf, M. a., Young, J. and Lai, J. C. S. (2011) ‘Reynolds number, thickness and camber effects on flapping airfoil propulsion’, *Journal of Fluids and Structures*. Elsevier, 27(2), pp. 145–160. doi: 10.1016/j.jfluidstructs.2010.11.010.

Ashraf, M. a., Young, J. and S. Lai, J. C. (2012) ‘Oscillation Frequency and Amplitude Effects on Plunging Airfoil Propulsion and Flow Periodicity’, *AIAA Journal*, 50(11), pp. 2308–2324. doi: 10.2514/1.J051374.

Bibo, A. and Daqaq, M. F. (2013) ‘Energy harvesting under combined aerodynamic and base excitations’, *Journal of Sound and Vibration*. Elsevier, 332(20), pp. 5086–5102. doi: 10.1016/j.jsv.2013.04.009.

Bleischwitz, R., Kat, R. De and Ganapathisubramani, B. (2015) ‘Aspect-Ratio Effects on Aeromechanics of Membrane Wings at Moderate Reynolds Numbers’, 53(3), pp. 20–22. doi: 10.2514/1.J053522.

Bleischwitz, R., Kat, R. De and Ganapathisubramani, B. (2016) ‘Aeromechanics of Membrane Wings in Ground- Effect’, (February). doi: 10.2514/6.2015-2764.

Boiron, O., Guivier-Curien, C., Bertrand, E., (2012), 'Study of the hydrodynamic of a flapping foil at moderate angle of attack', *Comput. Fluid* 59, 117–124.

Bryant M., Gomez J.C., Garcia E. (2013), 'Reduced-Order Aerodynamic Modelling of Flapping Wing Energy Harvesting at Low Reynolds Number', *AIAA Journal* 51(12): 2771-2782.

Campobasso, M. S. *et al.* (2013) 'Turbulent Navier – Stokes analysis of an oscillating wing in a power-extraction regime using the shear stress transport turbulence model', *COMPUTERS AND FLUIDS*. Elsevier Ltd, 88, pp. 136–155. doi: 10.1016/j.compfluid.2013.08.016.

Campobasso, M. S. and Drofelnik, J. (2012) 'Compressible Navier–Stokes analysis of an oscillating wing in a power-extraction regime using efficient low-speed preconditioning', *Computers & Fluids*. Elsevier Ltd, 67, pp. 26–40. doi: 10.1016/j.compfluid.2012.07.002.

Carcangiu, C. E. (2008) *CFD-RANS Study of Horizontal Axis Wind Turbines Thesis for the degree of Doctor of Philosophy*.

Cleaver, D. J. *et al.* (2014) 'Thrust enhancement due to flexible trailing-edge of plunging foils'.

Cui, E. and Zhang, X. (2010) 'Ground Effect Aerodynamics', *Fluid Dynamics and Aerothermodynamics Incompressible Flows and Aerodynamics.*

D., jones K. and F, P. M. (1997) 'Numerical computation of flapping-wing propulsion and power extraction', *AIAA Journal*.

Deng, J., L. Teng, D. Pan, and X. Shao (2015), 'Inertial effects of the semi-passive flapping foil on its energy extraction efficiency, *Physics of Fluids* (1994-present) 27(5), 053103.

Dessi, D. and Mazzocconi, S. (2015) 'Aeroelastic behavior of a flag in ground effect', *Journal of Fluids and Structures*. Elsevier, 55, pp. 303–323. doi: 10.1016/j.jfluidstructs.2015.03.006.

Dickinson, M. H., Farley, C. T., Full, R. J., Koehl, M. A. R., Kran, R. and Lehman, S. (2000) 'How animals move: an integrative view. *Science,* 288,100 -106.

Dippold, V. F. (2003) 'Numerical Assessment of the Performance of Jet-Wing Distributed Propulsion on Blended-Wing-Body Aircraft'.

Dong, H., Mittal, R., Najjar, F.M., (2006), 'Wake topology and hydrodynamic performance of low-aspect-ratio flapping foils', *J. Fluid Mech.* 566, 309.

Dumas, G., Kinsey, T. (2006) 'Eulerian simulations of oscillating airfoils in power-extraction regime', in *Proceeding in Advances in Fluid Mechanics VI, WIT Press*, pp. 245–254.

Ferziger, J. H. and Peric, M. (1999) *Computational Methods for Fluid Dynamics*. Springer-Verlag: Berlin.

Gao, T. *et al.* (2008) 'Insect normal hovering flight in ground effect', *Physics of Fluids*, 087101(20). doi: 10.1063/1.2958318.

Ghasemi, A., Olinger, D.J. and Tryggvason, G. (2016) 'A nonlinear computational model of tethered underwater kites for power generation', *Journal of Fluids Engineering* 138(12), 121401.

Gomez, A. and Pinilla, A., 2006, 'Aerodynamic characteristic of airfoils with blunt trailing edge', *In Revista de Ingeria*, pages 23-33.

Green, M.A., Rowley, C.W., Smits, A.J., (2011), 'The unsteady three-dimensional wake produced by a trapezoidal pitching panel', *J. Fluid Mech.* 685, 117–145.

Grue, J., Mo, A. and Palm, E. (2006) 'Propulsion of a foil moving in water waves.', *Journal of Fluid Mechanics*, 186(1), p. 393. doi: 10.1017/S0022112088000205.

Guglielmini, L. & Blondeaux, P. (2004) "Propulsive efficiency of oscillating foils", *Euro. J. Mech. B/Fluids* 23, 255.

Harbig, R.R., Sheridan, J., Thompson, M.C., (2013), 'Reynolds number and aspect ratio effects on the leading-edge vortex for rotating insect wing planforms', *J. Fluid Mech*. 717, 166–192.

Heathcote, S., Martin, D. and Gursul, I. (2004) 'Flexible Flapping Airfoil Propulsion at Zero Freestream Velocity', 42(11). doi: 10.2514/1.5299.

Hejlesen, M.M., Koumoutsakos, P., Leonard, A., Walther, J.H., (2015), 'Iterative Brinkman penalization for remeshed vortex methods', *J. Comput. Phys*. 280, 547–562.

Huxham, G. H., Cochard, S. and Patterson, J. (2012) 'Experimental Parametric Investigation of an Oscillating Hydrofoil Tidal Stream Energy Converter', in *18th Australa-sian fluid mechanics conference*.

IPCC (2014) *Climate Change 2014 Synthesis Report Summary for Policymakers*. Technical Report, Intergovernmental Panel on Climate Change.

Isogai, K., Yamasaki, M., Matsubara, M., Asaoka, T. (2003) 'Design Study of Elastically Supported Flapping Wing Power Generator', in *Proceedings of the international forum on aeroelasticity and structural dynamics*.

Javed, A., Djidjeli, K., Naveed, A. and Xing, J.T. (2018), 'Low Reynolds Number Effect on Energy Extraction Performance of Semi-Passive Flapping Foil', *Journal of Applied Fluid Mechanics* 11(6), 1613-1627.

Jones, K., Platzer, M., (1997) 'Numerical computation of flapping-wing propulsion and power extraction', In: *Aiaa Aerospace Sciences Meeting and Exhibit*.

Jones, K.D., Platzer, M.F., (1999), 'An experimental and numerical investigation of flapping-wing propulsion', In: *AIAA Aerospace Sciences Meeting & Exhibit.*

Jones, K. D., Linsey, K., Platzer, M. F. (2003) *An investigation of the fluid-structure interaction in an oscillating-wing micro-hydropower generator*.

Jones, K. D., Davids, S. and Platzer, M. F. (1999) 'Oscillating-wing power generation', *ASME/JSME Joint Fluids Engineering Conference, San Francisco, California, July 1999*.

Karbasian, H. R., Esfahani, J. A. and Barati, E. (2016) 'The power extraction by flapping foil hydrokinetic turbine in swing arm mode', *Renewable Energy*. Elsevier Ltd, 88, pp. 130–142. doi: 10.1016/j.renene.2015.11.038.

Karakas, F. and Fenercioglu, I. (2017) 'Effect of phase angle on tandem flapping-wing power generation', *International Journal of Energy Production and Management* 2, http://dx.doi.org/10.2495/EQ-V2-N1-95-105.

Kaya, M., Tuncer, I.H., (2007), 'Nonsinusoidal path optimization of a flapping airfoil', *AIAA J.* 45, 2075– 2082.

Von Karman, T., Burgers, J. M. (1934) *Aerodynamic theory*. Berlin: Springer.

Kim, D. *et al.* (2017) ‘Energy harvesting performance and flow structure of an oscillating hydrofoil with fi nite span’, *Journal of Fluids and Structures*, 70(February), pp. 314–326. doi: 10.1016/j.jfluidstructs.2017.02.004.

Kinsey, T. (2011) *ANALYSIS , OPTIMIZATION AND DEMONSTRATION OF A NEW CONCEPT OF HYDROKINETIC TURBINE BASED ON OSCILLATING HYDROFOILS*, PhD thesis, 2011.

Kinsey, T. *et al.* (2011a) ‘Prototype testing of a hydrokinetic turbine based on oscillating hydrofoils’, *Renewable Energy*. Elsevier Ltd, 36(6), pp. 1710–1718. doi: 10.1016/j.renene.2010.11.037.

Kinsey, T. *et al.* (2011b) ‘Prototype testing of a hydrokinetic turbine based on oscillating hydrofoils’, *Renewable Energy*. Elsevier Ltd, 36(6), pp. 1710–1718. doi: 10.1016/j.renene.2010.11.037.

Kinsey, T. and Dumas, G. (2008a) ‘Parametric Study of an Oscillating Airfoil in a Power-Extraction Regime’, *AIAA Journal*, 46(6), pp. 1318–1330. doi: 10.2514/1.26253.

Kinsey, T. and Dumas, G. (2008b) ‘Parametric Study of an Oscillating Airfoil in a Power-Extraction Regime’, *AIAA Journal*, 46(6), pp. 1318–1330. doi: 10.2514/1.26253.

Kinsey, T. and Dumas, G. (2012) ‘Three-Dimensional Effects on an Oscillating-Foil Hydrokinetic Turbine’, 134(July 2012), pp. 1–11. doi: 10.1115/1.4006914.

Kinsey, T. and Dumas, G. (2014) ‘Optimal Operating Parameters for an Oscillating Foil Turbine at Reynolds Number 500,000’, *AIAA Journal*, 52(9), pp. 1885–1895. doi: 10.2514/1.J052700.

Kinsey, T. and Dumas, G. (2015) ‘Computational Fluid Dynamics Analysis of a Hydrokinetic Turbine Based on Oscillating Hydrofoils’, 134 (February 2012), pp. 1–16. doi: 10.1115/1.4005841.

Kumar, A., Bhardwaj, R. and Sheridan, J. (2015) ‘Flow-induced deformation of a flexible thin structure as manifestation of heat transfer enhancement’, *International Journal of Heat and Mass Transfer*. Elsevier Ltd, 84, pp. 1070–1081. doi: 10.1016/j.ijheatmasstransfer.2015.01.048.

Larsen, A., Walther, J.H., (1997), 'Aeroelastic analysis of bridge girder sections based on discrete vortex simulations', *J. Wind Eng. Ind. Aerodyn.* 67–68, 524–543.

Law, S.P. and Gregorek, G.M. (1987) 'Wind Tunnel Evaluation of a Truncated NACA 64-621 Airfoil for Wind Turbine Applications'.

Le, T. Q., Ko, J. H. and Byun, D. (2013) ‘Morphological effect of a scallop shell on a flapping-type tidal stream generator’, *Bioinspiration & Biomimetics*, 8(3)(036009).

Lefrancois, J., (2008), 'Optimisation de rendement d'une turbine multi-ailes a I'aide d'une methode Iagrangienner par particules vortex', *M.S. thesis. Laval University, Quebec City, Canada.*

Legrand, C. and Ltd., B. & V. (2009) ‘Assessment of Tidal Energy Resource’, *Marine Renewable Energy Guides. Ed. by The European Marine Energy Centre Ltd. London, UK: BSI.*

Lehmann, F. (2009) ‘Wing – wake interaction reduces power consumption in insect tandem

wings', pp. 765–775. doi: 10.1007/s00348-008-0595-0.

Lentink, D., Muijres, F. T., Donker-Duyvis, F. J. & van Leeuwen, J. L. (2008), 'Vortex-wake interactions of a flapping foil that models animal swimming and flight', *The Journal of Experimental Biology* 211, 267–273.

Linsey, K. (2002) *A feasibility study of oscillating-wing power generators*, *M. Sc. Thesis*. doi: 10.1109/37.642974.

Liu, W., Xiao, Q. and Cheng, F. (2013) 'A bio-inspired study on tidal energy extraction with flexible flapping wings.', *Bioinspiration & biomimetics*, 8(3), p. 036011. doi: 10.1088/1748-3182/8/3/036011.

Liu, Zhengliang, Lai, Joseph C.S., Young, J. and Tian, Fang-Bao (2016), 'A Discrete vortex method for flapping foil power generator modelling at low Reynolds numbers', XXIV ICTAM, 21-26 August 2016, Montreal, Canada

Lu, K., Xie, Y.H., Zhang, D., (2013), 'Numerical study of large amplitude, nonsinusoidal motion and camber effects on pitching airfoil propulsion', *J. Fluids Struct*. 36, 184–194.

Lu, K., Xie, Y.H., Zhang, D., Lan, J.B., (2013), 'Numerical investigations into the asymmetric effects on the aerodynamic response of a pitching airfoil', *J. Fluids Struct*. 39, 76–86.

Lu, K. *et al.* (2015) 'Systematic investigation of the fl ow evolution and energy extraction performance of a fl apping-airfoil power generator', *Energy*. Elsevier Ltd, 89, pp. 138–147. doi: 10.1016/j.energy.2015.07.053.

Lu, K., Xie, Y. and Zhang, D. (2014a) 'Nonsinusoidal motion effects on energy extraction performance of a fl apping foil', *Renewable Energy*. Elsevier Ltd, 64, pp. 283–293. doi: 10.1016/j.renene.2013.11.053.

Lu, K., Xie, Y. and Zhang, D. (2014b) 'Numerical Investigations into the Nonsinusoidal Motion Effects on Aerodynamics of a Pitching Airfoil', *Energy Procedia*. Elsevier B.V., 61, pp. 2497–2500. doi: 10.1016/j.egypro.2014.12.031.

Ma, P. *et al.* (2017) 'Energy extraction and hydrodynamic behavior analysis by an oscillating hydrofoil device', *Renewable Energy*. Elsevier Ltd, 113, pp. 648–659. doi: 10.1016/j.renene.2017.06.036.

Ma, P., Wang, Y., Xie, Y., Han, J., Sun, G. and Zhang, J. (2019), 'Effect of wake interaction on the response of two tandem oscillating hydrofoils', *Energy Science & Engineering 7*, http://dx.doi.org/10.1002/ese3.286.

Mazaheri, K. *et al.* (2012) 'Performance Analysis of a Flapping-Wing Vehicle Based on Experimental Aerodynamic Data', 25(January), pp. 45–50. doi: 10.1061/(ASCE)AS.1943-5525.

McKinney, W., DeLaurier, J. (1981) 'The Wingmill: An Oscillating-Wing Windmill', *Journal of Energy*, 5.2, pp. 109–115.

Medjroubi, W., Stoevesandt, B., Carmo, B., Peinke, J., (2011), 'High-order numerical simulations of the flow around a heaving airfoil', *Comput. Fluid* 51 (1), 68–84.

Medjroubi, W., Stoevesandt, B., Peinke, J., (2012), 'Wake classification of heaving airfoils using the spectral/hp element method', *J. Comput. Appl. Math*. 236 (15), 3774–3782.

Mivehchi, A., Dahl, J. and Licht, S. (2016) 'Heaving and pitching oscillating foil propulsion in ground effect', *Journal of Fluids and Structures*. Elsevier, 63, pp. 174–187. doi: 10.1016/j.jfluidstructs.2016.03.007.

Molina, J. and Zhang, X. (2011) 'Aerodynamics of a Heaving Airfoil in Ground Effect', *AIAA Journal*, 49(6). doi: 10.2514/1.J050369.

Molina, J., Zhang, X. and Alomar, A. (2016) 'Aerodynamics of a Pitching and Heaving Airfoil in Ground Effect', *AIAA Journal*. doi: 10.2514/1.J053350.

Moryossef, Y. and Levy, Y. (2004) 'Effect of Oscillations on Airfoils in Close Proximity to the Ground', *AIAA Journal*, 42(9). doi: 10.2514/1.6380.

Münch, C., Ausoni, P., Braun, O., Farhat, M., Avellan, F., (2010), 'Fluid–structure coupling for an oscillating hydrofoil', *J. Fluids Struct.* 26 (6), 1018–1033.

Murcia, J.P., and Pinilla, A., (2011), 'CFD Analysis of Blunt Trailing Edge Airfoils Obtained with Several Modification Methods', *rev.ing.* [online], 33, pp.14-24.

Oueslati, M. M., Dahmouni, A. W. and Nasrallah, S. Ben (2017) 'Effects of sudden change in pitch angle on oscillating wind turbine airfoil performances', *Engineering Analysis with Boundary Elements*. Elsevier Ltd, 81(March), pp. 21–34. doi: 10.1016/j.enganabound.2017.03.014.

Pan, D. *et al.* (2014) 'Simulations of passive oscillation of a flexible plate in the wake of a cylinder by immersed boundary method', *European Journal of Mechanics B/Fluids*. Elsevier Masson SAS, 46, pp. 17–27. doi: 10.1016/j.euromechflu.2014.02.001.

Peng, J. and Chen, G. S. (2012) 'Flow-Oscillating Structure Interactions and the Applications to Propulsion and Energy Harvest', *Applied Physics Research*, 4(2), pp. 1–14. doi: 10.5539/apr.v4n2p1.

Peng, Z. and Zhu, Q. (2009) 'Energy harvesting through flow-induced oscillations of a foil', *Physics of Fluids*, 21(12), p. 123602. doi: 10.1063/1.3275852.

Platzer, M.F., Young, J., Lai, J. L. C. (2008) 'Flapping-wing technology: The potential for air vehicle propulsion and airborne power generation', in *26th International congress of the aeronautical science (ICAS), Anchorage, Alaska*.

Platzer, M. F. *et al.* (2008) 'EXTRACTING POWER IN JET STREAMS : PUSHING THE PERFORMANCE OF FLAPPING WING TECHNOLOGY', pp. 1–10. Pointwise (2011) 'Pointwise User Manual'.

Ramjee, V., Tulapurkara, E., Balabaskaran, V. (1986), 'Experimental and theoretical study of wings with blunt trailing edges', J *Aircr*aft 23(4):349–352

Rasmussen, J.T., Hejlesen, M.M., Larsen, A., Walther, J.H., (2010), 'Discrete vortex method simulations of the aerodynamic admittance in bridge aerodynamics', *J. Wind Eng. Ind. Aerodyn*. 98 (12), 754–766.

Read, D.A., Hover, F.S., Triantafyllou, M.S. (2003) 'Forces on oscillating foils for propulsion and maneuvering', J. Fluids Struct 17(1), pp. 163–183

Ribeiro, R., Frank, S.L., Franck, J.A., (2018), 'Vortex dynamics and Reynolds number effects of an oscillating hydrofoil in energy harvesting mode', Physics Fluid Dyn.

Richards, A.J. (2013),'Tuning the passive structural response of an oscillating-foil propulsion mechanism for improved thrust generation and efficiency. PhD thesis, University of Victoria.

Rohr, J.J. and Fish, F.E. (2004), 'Strouhal numbers and optimization of swimming by odontocete cetaceans', Journal of Experimental Biology, vol. 207, no. 10, pp. 1633, 1642.

Saadat, M, Fish, F.E., Domel, A., Di Santo, V., Lauder, G., and Haj-Hariri,H. (2017), 'On the rules for aquatic locomotion', Physical Review Fluids, vol. 2, no. 8,p. 083102.

Shimizu, E., Isogai, K. and Obayashi, S. (2008) 'Multiobjective Design Study of a Flapping Wing Power Generator', *Journal of Fluids Engineering*, 130(2), p. 021104. doi: 10.1115/1.2829580.

Shyy, W. and Liu, H. (2007) 'Flapping Wings and Aerodynamic Lift: The Role of Leading-Edge Vortices', *AIAA Journal*, 45(12), pp. 2817–2819. doi: 10.2514/1.33205.

Simpson, B.J. (2009),'Experimental studies of apping foils for energy extraction', PhD thesis, Massachusetts Institute of Technology.

Simpson, B. *et al.* (2008) 'PAPER NUMBER OMAE-2008-58043'.

Thaweewat, N., Bos, F. M., van Oudheusden, B. W. & Bijl, H. (2009), 'Numerical study of vortex-wake interactions and performance of a two-dimensional flapping foil', *in* 47th AIAA Aerospace Sciences Meeting, Orlando, 2009-791.

Thompson, B. and Whitelaw, J., 1988, 'Flow-around airfoils with blunt, round, and sharp trailing edges', *Journal of aircraft*, 25(4):334-342.

Tian, X., Tao, L., Li, X., Yang, J., 2017 'Hydrodynamic coefficients of oscillating flat plates at 0.15 KC 3.15.', *J. Mar. Sci. Technol.* 22 (1), 101–113.

Tian, X., Xiao, L., Zhang, X., Yang, J., Tao, L., Yang, D., 2017 'Flow around an oscillating circular disk at low to moderate Reynolds numbers', *J. Fluid Mech.* 812, 1119–1145.

Triantafyllou, M.S., Triantafyllou, G.S., Gopalkrishnan, R., (1991), 'Wake mechanics for thrust generation in oscillating foils', *Phys. Fluids A Fluid Dyn.* 3 (12), 2835–2837.

Triantafyllou, M. *et al.* (2008) 'Experiments in direct energy extraction through flapping foils', (May).

Truong, T. Van *et al.* (2013) 'Aerodynamic forces and flow structures of the leading edge vortex on a flapping wing considering ground effect', *Bioinspiration & Biomimetics*, 036007(8). doi: 10.1088/1748-3182/8/3/036007.

Tuncer, I.H., Kaya, M., (2005), 'Optimization of flapping airfoils for maximum thrust and propulsive efficiency', *AIAA J.* 43 (11), 2329–2336

Ulrich, X. and Peters, D. (2014) 'Loads and propulsive efficiency of a flexible airfoil performing sinusoidal deformations', *Journal of Fluids and Structures*. Elsevier, 45, pp. 15–27. doi: 10.1016/j.jfluidstructs.2013.11.017.

Usoh, C. O. *et al.* (2012) 'Numerical Analysis of a Non-Profiled Plate for Flapping Wing

Turbines', in *18th Australasian Fluid Mechanics Conference, Launceston, Australia*, pp. 3–6.

Versteeg, H. K. and Malalasekera, W. (2007) *An Introduction to Computational Fluid Dynamics*. Second Edi. Pearson Education.

Wang, Q., Goosen, J.F.L., van Keulen, F., (2016), 'A predictive quasi-steady model of aerodynamic loads on flapping wings', *J. Fluid Mech.* 800, 688–719.

Wang, Y. *et al.* (2017) 'Research on the mechanism of power extraction performance for fl apping hydrofoils', *Ocean Engineering*. Elsevier, 129(November 2016), pp. 626–636. doi: 10.1016/j.oceaneng.2016.10.024.

Walther, J.H., Larsen, A., (1997), 'Two dimensional discrete vortex method for application to bluff body aerodynamics', J. *Wind Eng. Ind. Aerodyn*. 67–68, 183–193.

Westwood, A. (2004) 'Ocean power wave and tidal energy review', *Refocus*, 5(5), pp. 50–55.

'World Energy Resources 2016' (2016).

Wu, J., Qiu, Y., Shu, C., and Zhao, N. (2014) 'Pitching-motion-activated flapping foil near solid walls for power extraction: A numerical investigation', *Physics of Fluids* (1994-present) 26(8).

Wu, J., Qiu, Y. L., Shu, C., Zhao, N. and Wang, X. (2015) 'An adaptive immersed boundary-lattice Boltzmann method for simulating a flapping foil in ground effect', 106, pp. 171–184. doi: 10.1016/j.compfluid.2014.10.003.

Wu, J., Yang, S. C., *et al.* (2015) 'Ground effect on the power extraction performance of a flapping wing biomimetic energy generator', *Journal of Fluids and Structures*, 54, pp. 247–262. doi: 10.1016/j.jfluidstructs.2014.10.018.

Wu, J., Qiu, Y. L., Shu, C., Zhao, N., Wu, J., *et al.* (2015) 'Pitching-motion-activated flapping foil near solid walls for power extraction : A numerical investigation', *Physics of Fluids*, 083601(2014), pp. 0–19. doi: 10.1063/1.4892006.

Wu, J., Zhan, J. P., *et al.* (2015) 'Power extraction efficiency improvement of a fully-activated flapping foil : With the help of an auxiliary rotating foil', 57, pp. 219–228. doi: 10.1016/j.jfluidstructs.2015.06.013.

Wu, J., Chen, Y.L., Zhao, N., (2015a), 'Role of induced vortex interaction in a semi-active flapping foil based energy harvester', *Phys. Fluids* 27 (9), 093601.

Wu, J., Shu, C., Zhao, N., Tian, F.B., (2015b), 'Numerical study on the power extraction performance of a flapping foil with a flexible tail', *Phys. Fluids* 27 (1), 013602.

Wu, J., Wu, J., Tian, F.B., Zhao, N., Li, Y.D., (2015c), 'How a flexible tail improves the power extraction efficiency of a semi-activated flapping foil system: a numerical study', *J. Fluids Struct.* 54, 886–899.

Xiao, Q. *et al.* (2012) 'How motion trajectory affects energy extraction performance of a biomimic energy generator with an oscillating foil ?', *Renewable Energy*. Elsevier Ltd, 37(1), pp. 61–75. doi: 10.1016/j.renene.2011.05.029.

Xiao, Q. and Zhu, Q. (2014) 'A review on flow energy harvesters based on flapping foils', *Journal of Fluids and Structures*. Elsevier, 46, pp. 174–191. doi:

10.1016/j.jfluidstructs.2014.01.002.

Xie, Y. H. *et al.* (2016) 'Numerical investigation into energy extraction of flapping airfoil with Gurney flaps', 109, pp. 694–702. doi: 10.1016/j.energy.2016.05.039.

Xie, Y., Lu, K. and Zhang, D. (2014) 'Investigation on energy extraction performance of an oscillating foil with modi fi ed fl apping motion', 63, pp. 550–557. doi: 10.1016/j.renene.2013.10.029.

Yilmaz, T.O., Rockwell, D., 2012, 'Flow structure on finite-span wings due to pitch-up motion', *J. Fluid Mech.* 691, 518–545.

Young, J., Ashraf, M. A., Lai, J. C. S., Platzer, M. F. (2010) 'Numerical simulation of flow-driven flapping-wing turbines for wind and water power generation', in *17th Australasian fluid mechanics conference, Ackland, New Zealand*.

Young, J. *et al.* (2013) 'Numerical Simulation of Fully Passive Flapping Foil Power Generation', *AIAA Journal*, 51(11), pp. 2727–2739. doi: 10.2514/1.J052542.

Yang, J., Tian, X., Li, X., 2014 ' Hydrodynamic characteristics of an oscillating circular disk under steady in-plane current conditions'. *Ocean Eng.* 75, 53–63.

Young, J. (2017) 'Investigation Investigation of of Oscillating-Foil Oscillating-Foil Power Power Generation Generation in in Constrained Constrained Flow Flow', *Procedia Engineering*. Elsevier B.V., 199, pp. 3450–3455. doi: 10.1016/j.proeng.2017.09.450.

Yu, D. *et al.* (2017) 'Numerical study of the effect of motion parameters on propulsive efficiency for an oscillating airfoil', 68(516), pp. 245–263. doi: 10.1016/j.jfluidstructs.2016.10.009.

Yu, M.L., Hu, H., Wang, Z.J., (2012), 'Experimental and numerical investigations on the asymmetric wake vortex structures around an oscillating airfoil', *Tech. Report Ieice Sdm* 108 (236), 1–6.

Yu, M.L., Wang, Z.J., Hu, H., (2013), 'High fidelity numerical simulation of airfoil thickness and kinematics effects on flapping airfoil propulsion', *J. Fluids Struct.* 42, 166–186.

Zhang, J., (2017), 'Footprints of a flapping wing', *J. Fluid Mech*. 818, 1–4.

Zhu, Q. (2011) 'Optimal frequency for flow energy harvesting of a flapping foil', *Journal of Fluid Mechanics*, 675, pp. 495–517. doi: 10.1017/S0022112011000334.

Zhu, Q. (2012) 'Energy harvesting by a purely passive flapping foil from shear flows', *Journal of Fluids and Structures*. Elsevier, 34, pp. 157–169. doi: 10.1016/j.jfluidstructs.2012.05.013.

Zhu, Q., Haase, M. and Wu, C. H. (2009a) 'Modeling the capacity of a novel flow-energy harvester', *Applied Mathematical Modelling*. Elsevier Inc., 33(5), pp. 2207–2217. doi: 10.1016/j.apm.2008.05.027.

Zhu, Q., Haase, M. and Wu, C. H. (2009b) 'Modeling the capacity of a novel flow-energy harvester', *Applied Mathematical Modelling*. Elsevier Inc., 33(5), pp. 2207–2217. doi: 10.1016/j.apm.2008.05.027.

Zhu, Q. and Peng, Z. (2009) 'Mode coupling and flow energy harvesting by a flapping foil', *Physics of Fluids*, 21(3), p. 033601. doi: 10.1063/1.3092484.

Zhu, Q., (2011), 'Optimal frequency for flow energy harvesting of a flapping foil', *J. Fluid Mech*. 675, 495–517.

Zhu, Q., (2012), 'Energy harvesting by a purely passive flapping foil from shear flows', *J. Fluids Struct.* 34, 157–169.

Zhongying Xiong, Xiaomin Liu, Dian Li, *and* Yuanying Wang, (2019), 'Numerical investigation on flapping hydrofoil for optimal propulsion performance using a very large eddy simulation method', *AIP Advances* **9**, 045208.

Publications

Abdullah Sani, S.A., Djidjeli, K. and Xing, J.T. (2016). Geometrical Shape Influence on Energy Harvesting Performance of Oscillating Airfoil. *Proceedings of Sustainable Development Conference 2016,* p 120-136, 7 – 9 July 2016; Malaysia.

Abdullah Sani, S.A., Djidjeli, K. and Xing, J.T. Numerical Investigation of Trailing Edge Modifications and Ground effect influence on Energy Extraction of Oscillating Foils. Renewable Energy Journal, to be submitted.

Appendix A

I. UDF for Single Airfoil

```
# include "udf.h"
DEFINE_ZONE_MOTION(plunge,omega,axis,origin,velocity,time,dtime)
{
  real w = 2.0*M_PI*0.14;
  real wt = w*time;
  real y, yd, ydd;
  y = sin(wt-1.5708);
  yd = w*cos(wt-1.5708);
  ydd = -w*w*y;
  *origin = 0;
  velocity[1] = -yd;
}

# include "udf.h"
DEFINE_PROFILE(bc_u,thread,position)
{
  face_t f;
  real time = CURRENT_TIME;
  real xf[ND_ND];

  begin_f_loop(f,thread)
  {
    F_CENTROID(xf,f,thread);
    F_PROFILE(f,thread,position) = 1;
  }
  end_f_loop(f,thread)
}

# include "udf.h"
DEFINE_PROFILE(bc_v,thread,position)
{
  face_t f;
  real y, yd, ydd;
  real time = CURRENT_TIME;
  real xf[ND_ND];
  real w = 2.0*M_PI*0.14;
  real wt = w*time;
  y = sin(wt-1.5708);
  yd = w*cos(wt-1.5708);
  ydd = -w*w*y;
  begin_f_loop(f,thread)
 {
    F_CENTROID(xf,f,thread);
    F_PROFILE(f,thread,position) = -yd*0;
 }
 end_f_loop(f,thread)
}

# include "udf.h"
DEFINE_ZONE_MOTION(pitch,omega,axis,origin,velocity,time,dtime)
```

```
{
  real w = 2.0*M_PI*0.14;
  real wt = w*time;
  real th, thd, thdd;
  th = 1.33221*sin(wt);
  thd = 1.332*w*cos(wt);
  thdd = w*w*th;
  *origin = 0;
  *omega = thd;
}

#include "udf.h"
DEFINE_SOURCE(source_ymom,c,t,dS,eqn)
{
  real source;
  real y, yd, ydd;
  real time = CURRENT_TIME;
  real dens = C_R(c,t);
  real xc[ND_ND];
  real w = 2.0*M_PI*0.14;
  real wt = w*time;
  y = sin(wt-1.5708);
  yd = w*cos(wt-1.5708);
  ydd = -w*w*y;
  C_CENTROID(xc,c,t);
  source = -dens*ydd;
  dS[eqn] = 0.0;
  return source;
}
```

II. UDF for Tandem Airfoil

```
# include "udf.h"
DEFINE_ZONE_MOTION(plunge,omega,axis,origin,velocity,time,dtime)
{
  real w = 2.0*M_PI*0.14;
  real wt = w*time;
  real y, yd, ydd;
  y = sin(wt-1.5708);
  yd = w*cos(wt-1.5708);
  ydd = -w*w*y;
  *origin = 0;
  velocity[1] = -yd;
}

# include "udf.h"
DEFINE_PROFILE(bc_u,thread,position)
{
  face_t f;
  real time = CURRENT_TIME;
  real xf[ND_ND];
```

```
  begin_f_loop(f,thread)
  {
    F_CENTROID(xf,f,thread);
    F_PROFILE(f,thread,position) = 1;
  }
  end_f_loop(f,thread)
}

# include "udf.h"
DEFINE_PROFILE(bc_v,thread,position)
{
  face_t f;
  real y, yd, ydd;
  real time = CURRENT_TIME;
  real xf[ND_ND];
  real w = 2.0*M_PI*0.14;
  real wt = w*time;
  y = sin(wt-1.5708);
  yd = w*cos(wt-1.5708);
  ydd = -w*w*y;
  begin_f_loop(f,thread)
 {
    F_CENTROID(xf,f,thread);
    F_PROFILE(f,thread,position) = -yd*0;
 }
 end_f_loop(f,thread)
}

# include "udf.h"
DEFINE_ZONE_MOTION(pitch1,omega,axis,origin,velocity,time,dtime)
{
  real w = 2.0*M_PI*0.14;
  real wt = w*time;
  real th, thd, thdd;
  th = 1.33221*sin(wt);
  thd = 1.33221*w*cos(wt);
  thdd = -w*w*th;
  *origin = 0;
  *omega = thd;
}

# include "udf.h"
DEFINE_ZONE_MOTION(pitch2,omega,axis,origin,velocity,time,dtime)
{
  real w = 2.0*M_PI*0.14;
  real wt = w*time;
  real th, thd, thdd;
  th = 1.33221*sin(wt);
  thd = 1.33221*w*cos(wt);
  thdd = -w*w*th;
  *origin = 2.5;
  *omega = thd;
```

```
}

#include "udf.h"
DEFINE_SOURCE(source_ymom,c,t,dS,eqn)
{
  real source;
  real y, yd, ydd;
  real time = CURRENT_TIME;
  real dens = C_R(c,t);
  real xc[ND_ND];
  real w = 2.0*M_PI*0.14;
  real wt = w*time;
  y = sin(wt-1.5708);
  yd = w*cos(wt-1.5708);
  ydd = -w*w*y;
  C_CENTROID(xc,c,t);
  source = -dens*ydd;
  dS[eqn] = 0.0;
  return source;
}
```